Three-dimensional fluid-driven frictional ruptures: theory and applications

Alexis Alejandro SÁEZ URIBE

Abstract

Fluid-driven frictional ruptures are important in a broad range of subsurface engineering technologies and natural earthquake-related phenomena. Some examples of subsurface operations where borehole fluid injections can induce frictional slip are deep geothermal energy, CO_2 and hydrogen geological storage, and wastewater disposal from oil and gas production, among many others. On the other hand, natural phenomena such as seismic swarms, aftershock sequences, and slow earthquakes, are often associated with transients of pore-fluid pressure and fault slip. Motivated by the aforementioned applications and phenomena, this doctoral thesis aims to mechanistically understand how pre-existing geological structural discontinuities such as fractures and faults slide due to the pressurization of pore fluids, in a three-dimensional configuration that can be used for quantitative comparisons with field observations and preliminary engineering designs.

We first develop a numerical solver for frictional slip and fault opening along pre-existing networks of discontinuities in 3D elastic media. We then examine a model with Coulomb's friction to reproduce the initiation, propagation, and arrest of fluid-driven stable frictional ruptures. We show that a dimensionless number containing information about the initial stress state of the fault and the intensity of the injection governs the dynamics and shape of the ruptures in all its stages. Next, we extend the model to account for a friction coefficient that weakens with slip. This results in a broader range of fault slip behaviors, from unconditionally stable slip to dynamic instabilities. We quantify the conditions controlling both the propagation of stable slip and the nucleation of earthquakes. It is shown that the Coulomb's friction model is both an early-time and late-time asymptotic solution of the more general slip-weakening model. After, we generalize some important fault rupture regimes to account for fairly arbitrary fluid injections. In particular, the connection between the expansion rate of the slipping surface and the history of injection volume rate is established.

Using field observations, we then apply and explore the implications of our modeling results to injection-induced seismicity —a critical concern in the geo-energy industry. We show how the history of injection rate may control the migration patterns of micro-seismicity, and how these patterns may contain important information about in-situ conditions such as the fault stress state. Further, we elaborate on how post-injection pulses of stable slip can continue triggering seismicity due to stress-transfer effects, long after fluid injections stop. Finally,

we propose a theoretical scaling relation for the maximum magnitude of injection-induced slow slip events, which sheds light on how aseismic motions release potential energy during injection operations.

This doctoral research offers for the first time a quantitative and conceptual framework for understanding various subsurface and earthquake-science problems associated with frictional ruptures induced by fluid injections. While some implications of our findings are already explored in detail here, this work opens the possibility of understanding a much broader range of field observations. Moreover, our research paves the way for designing laboratory experiments, which is the next step to ground the theory we develop.

Key words: Fracture, friction, geological material, injection-induced aseismic slip, geo-energy applications, injection-induced seismicity, post-injection seismicity, earthquake swarms, geothermal energy, hydraulic stimulation technique.

Résumé

Les ruptures frictionnelles induites par les fluides jouent un rôle important dans un large éventail de technologies d'ingénierie souterraine et de phénomènes sismiques naturels. Parmi les exemples d'opérations souterraines où les injections de fluide peuvent induire un glissement frictionnel, citons l'énergie géothermique profonde, le stockage géologique de CO_2 et d'hydrogène, et l'élimination des eaux usées issues de la production de pétrole et de gaz. D'autre part, des phénomènes naturels tels que les essaims sismiques, les séquences de répliques et les tremblements de terre lents sont souvent associés à des variations transitoires de pression du fluide interstitiel et de glissement de faille. Motivée par les applications et les phénomènes susmentionnés, cette thèse de doctorat vise à comprendre mécaniquement comment les discontinuités structurales géologiques préexistantes, telles que les fractures et les failles, glissent du fait de la pressurisation des fluides interstitiels, dans une configuration tridimensionnelle qui peut être utilisée pour des comparaisons quantitatives avec les observations de terrain et permettre un dimensionnement préliminaires des opérations d'ingénierie.

Nous développons d'abord un code numérique pour le glissement frictionnel le long de discontinuités préexistantes dans un milieu élastique 3D. Nous examinons ensuite un modèle avec frottement de Coulomb pour reproduire l'initiation, la propagation et l'arrêt de ruptures frictionnelles stables induites par les fluides. Nous montrons qu'un nombre sans dimension contenant des informations sur l'état de contrainte initial de la faille et l'intensité de l'injection régit la dynamique et la forme des ruptures. Ensuite, nous étendons ce modèle pour tenir compte d'un coefficient de frottement qui s'affaiblit avec le glissement. Cela se traduit par une gamme plus large de comportements de glissement de faille, allant du glissement stable inconditionnel à l'initiation d'instabilités dynamiques. Nous quantifions les conditions contrôlant à la fois la propagation du glissement stable et la nucléation des séismes. Il est montré que le modèle de frottement de Coulomb est à la fois une solution asymptotique à petits et grands temps du modèle plus général d'affaiblissement du glissement. Ensuite, nous généralisons certains régimes importants de rupture de faille pour tenir compte d'injections de fluide arbitraires en temps. En particulier, le lien entre le taux d'expansion de la surface de glissement et l'historique du volume injecté est établi.

À l'aide d'observations effectuées sur le terrain, nous explorons les implications de nos résultats de modélisation à la sismicité induite par l'injection —une préoccupation majeure

dans la pratique. Nous montrons comment l'historique du taux d'injection peut contrôler la migration de la microsismicité, et comment cette migration peut contenir des informations importantes sur les conditions in situ telles que l'état de contrainte de la faille. De plus, nous montrons comment les impulsions de glissement stable post-injection peuvent continuer à déclencher la sismicité en raison d'effets de transfert de contrainte, longtemps après l'arrêt de l'injection de fluides. Enfin, nous proposons une relation d'échelle théorique pour la magnitude maximale des événements de glissement lent induits par l'injection, ce qui éclaire la façon dont les mouvements asismiques libèrent l'énergie pendant les opérations d'injection. Cette recherche doctorale présente pour la première fois un cadre quantitatif et conceptuel pour comprendre divers problèmes associés à des ruptures frictionnelles induites par des injections de fluides. Bien que certaines implications de nos résultats soient explorées en détail ici, ce travail ouvre la possibilité de comprendre un éventail beaucoup plus large d'observations de terrain. De plus, notre recherche ouvre la voie à la conception d'expériences de laboratoire, qui est la prochaine étape pour valider la théorie développée.

Mots clefs : Fracture, friction, matériau géologique, glissement aséismique induit par injection, sismicité induite par injection, sismicité post-injection, essaims de séismes, énergie géothermique, technique de stimulation hydraulique.

Contents

List of Figures

List of Tables

1 Introduction

1.1 Background and motivation

1.1.1 Subsurface engineering applications

In the context of subsurface industrial operations, it has been known since the Denver earthquakes in the 1960s, USA (Healy et al., 1968), that borehole fluid injections can induce fault slip that is sufficiently fast to radiate detectable elastodynamic waves (earthquakes). Soon after the Denver earthquakes, it also became clear that subsurface fluid injections can induce slow, sometimes called aseismic[1] slip (Hamilton & Meehan, 1971), which is generally more difficult to detect by classical monitoring networks. Since then, an increasing number of studies have inferred the occurrence of both seismic and aseismic slip as a result of industrial fluid injections (Scotti & Cornet, 1994; Cornet et al., 1997; Bourouis & Bernard, 2007; Wei et al., 2015; Eyre et al., 2022), with recent in-situ experiments in shallow natural faults providing direct evidence and measurements of injection-induced fracture slip (Guglielmi et al., 2015; Cappa et al., 2019; Cappa et al., 2022).

The reactivation of fractures and faults is particularly important for various applications in the geo-energy industry. For instance, hydraulic stimulation techniques are commonly used with the aim of increasing the permeability and fracture surface of deep, otherwise tight geothermal reservoirs in order to achieve economical flow rates (Figure 1.1). The permeability increase is expected to be attained by shear dilating pre-existing fractures (the so-called self-propping effect) or creating new ones. The occurrence of predominantly aseismic rather than seismic slip in these operations is considered a highly favorable outcome, as earthquakes of relatively large magnitude can pose a significant risk to the success of these projects (Deichmann & Giardini, 2009; Ellsworth et al., 2019). The challenge is then to engineer the fluid injection to induce fault slip while keeping the magnitude of seismic events within acceptable levels. This

---

[1]In this thesis, we use the terms: fast slip, seismic slip, dynamic slip, and unstable slip, as nearly synonymous. Similarly, we consider that the terms: slow slip, aseismic slip, quasi-static slip, and stable slip, have nearly the same meaning. The distinction between both modes of sliding is commonly understood in the geophysics literature by a threshold for the slip rate ~ 1 cm/s.
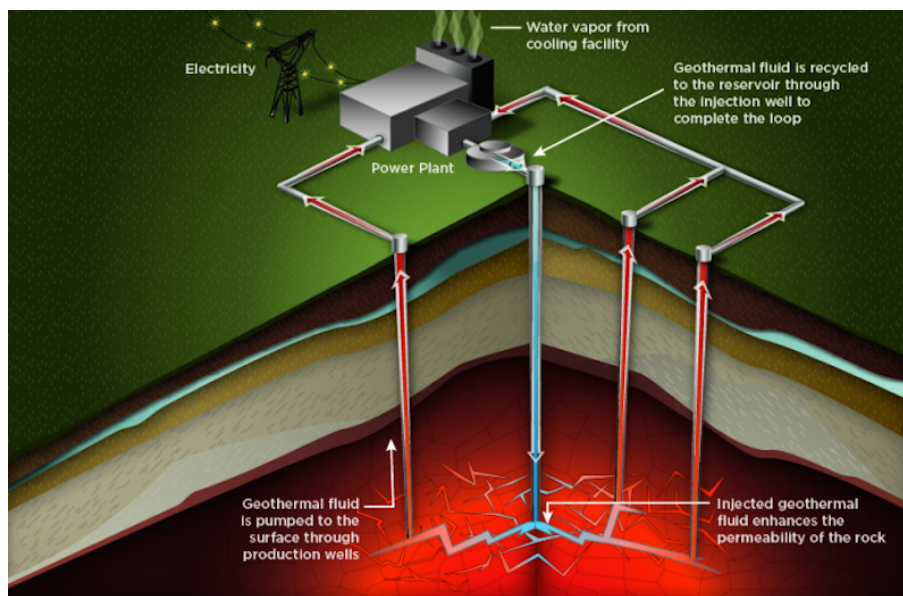
Figure 1.1: Schematics of hydraulic stimulation technique and steady operation of a geothermal power plant. Source: Department of Energy of the United States of America, Geothermal Technologies Program.

requires a mechanistic understanding of how the multi-physical processes at play interact, so that the link between important quantities for engineering design such as the volume and rate of injection, the in-situ conditions, and the resulting reactivated fracture surface and permeability changes, can be effectively established. Just as important is to understand the physical mechanisms that trigger seismicity and what controls the size of these events.

Injection-induced fault slip and, in particular, induced seismicity, is also relevant for various other geo-energy applications. For example, intensified industrial activities associated with the injection of oil wastewater into permeable reservoirs have resulted in a sudden increase in seismicity rates in the central and eastern United States (Ellsworth, 2013). Similarly, hydraulic fracturing operations in unconventional oil and gas reservoirs have led to elevated seismic activity in western Canada (Bao & Eaton, 2016). Injection-induced seismicity is also an important concern in geological carbon sequestration (Zoback & Gorelick, 2012; Vilarrasa & Carrera, 2015). These examples highlight the importance of developing a comprehensive understanding of the mechanics of injection-induced fault slip and the seismic implications associated with injection processes in various geo-energy contexts.

1.1.2   Natural earthquake-related phenomena

Fluid-driven fault slip occurs also due to natural processes in the Earth's crust. For instance, seismic swarms and aftershock sequences are often attributed to being driven by natural fluid injections (Miller et al., 2004; Parotidis et al., 2005) or the propagation of aseismic slip (Lohman & McGuire, 2007; Perfettini & Avouac, 2007), with recent studies suggesting that
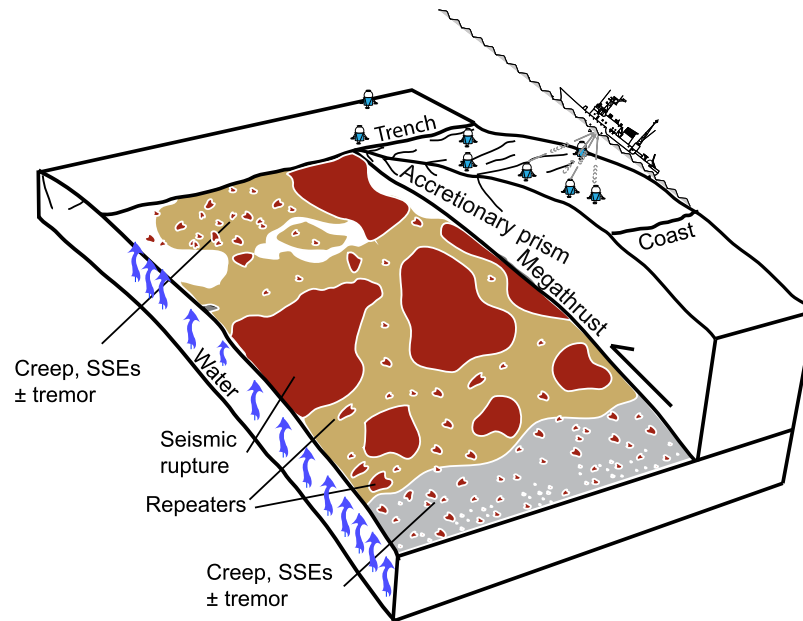
Figure 1.2: Schematics of a subduction zone. Modified from Bürgmann (2018).

the interplay between both mechanisms may be indeed responsible for the occurrence of some seismic sequences (Z. Ross et al., 2017; Sirorattanakul et al., 2022; Yukutake et al., 2022; Nishimura et al., 2023). In a similar manner, low-frequency earthquakes and tectonic tremors are commonly considered to be driven by slow slip events (Figure 1.2) occurring downdip the seismogenic zone in subduction zones (Rogers & Dragert, 2003; Shelly et al., 2006), where systematic evidence of overpressurized fluids has been found (Shelly et al., 2006; Kato et al., 2010; Behr & Bürgmann, 2021), with recent works suggesting that the episodicity and some characteristics of slow slip events may be explained by fluid-driven processes (Warren-Smith et al., 2019; Zhu et al., 2020; Perez-Silva et al., 2023). Metamorphic dehydration reactions occurring within the oceanic slab (Peacock, 2009) and fault-valving behavior (Sibson, 2020) are the two common candidates to explain this inferred over-pressurization and also the very nature of pore pressure transients along the subduction plate interface (Figure 1.2).

1.2   Objectives

The main goal of this doctoral thesis is to mechanistically understand how pre-existing geological structural discontinuities such as fractures and faults slide due to the pressurization of pore fluids, in a three-dimensional configuration that can be used for quantitative comparisons with field observations as well as preliminary engineering designs. Additionally, we aim to explore the implications of our modeling results to the phenomenon of injection-induced seismicity.

The following specific questions are systematically investigated throughout this thesis:

1. How do the in-situ conditions and parameters of the injection control the reactivation of aseismic slip on fractures and faults?

2. How does aseismic slip propagate and ultimately arrest upon the stop of fluid injections? How seismicity may be triggered due to post-injection aseismic slip?

3. How does frictional weakening affect the propagation of aseismic slip and promote the nucleation of earthquakes?

4. How do arbitrary injection rate histories control the dynamics of aseismic slip growth? How do the temporal patterns of aseismic slip relate to observations of seismicity induced by fluid injections?

5. What controls the maximum size and moment magnitude of injection-induced slow slip events?

1.3 Research approach

In this thesis, we combine analytical and numerical techniques to understand from first principles of continuum (solid and fluid) mechanics the hydro-mechanical behavior of fractures and faults subjected to fluid injections. A key part of our research approach involves using models that are a simplified version of nature, rather than trying to replicate all of its complexity. We therefore construct models that allow for profound analysis including the derivation of scaling relations, analytical solutions, and the exploration of their entire dimensionless parameter space via fully resolved numerical simulations. We gradually add complexity as we better understand the problem. This helps us choose the next physical component that is most likely to be important. Models including higher levels of complexity such as material and stress heterogeneities and intricate geometry are extremely valuable for site-specific case studies, among other applications. In this investigation, we attempt to provide a fundamental understanding of the phenomenon at hand, not restricted to any specific case or application.

1.4 Organization of this manuscript

Following the guidelines of the doctoral school, this thesis is organized as a compilation of scientific articles. As such, almost every chapter corresponds to a paper that is either published, under review, or about to be submitted for consideration to a scientific journal. This organization style may result in some redundancy between chapters.

The thesis is structured as follows.

- In Chapter 2, we develop a three-dimensional mechanical solver able to simulate the propagation of frictional slip and fault opening on pre-existing discontinuities of arbitrary shape. These localized deformations are driven by variations in interfacial fluid

pressure and/or total stresses applied either on the discontinuities' faces or the far field. This chapter is an early, significant milestone of this doctoral research, as it concerns the numerical tool that allows us to efficiently resolve the dynamics of the physical models we investigate in all of the subsequent chapters of this thesis. Additional information about the numerical solver is described in Appendix A.

- In Chapter 3, we investigate the propagation of aseismic slip due to fluid injection on a planar fault embedded in an infinite three-dimensional linearly elastic domain. We consider fluid injections conducted at a constant volumetric rate and a constant overpressure. It is assumed that the fault interface is governed by a constant friction coefficient, thus focusing on the effect of long-range elastic interactions and the way the injection is performed, in the propagation of aseismic ruptures. Analytical solutions for the case of circular shear ruptures are derived, whereas the more general case of non-circular ruptures is solved via numerical modeling. In addition, the fundamental problem of the equilibrium shape of three-dimensional shear cracks is addressed.

- In Chapter 4, we examine the further propagation and ultimate arrest of aseismic slip upon the stop of fluid injections. We consider the same fault model as in the previous chapter and focus on the particular case of injection at a constant volumetric rate, which is then suddenly stopped. The exact conditions determining when and where aseismic ruptures arrest are established. Furthermore, based on our physical model and field observations, we elaborate on how post-injection aseismic slip may trigger seismicity after shut-in; a critical concern in the geo-energy industry.

- In Chapter 5, we extend the fault model of Chapter 3 to account for a friction coefficient that weakens with slip. We focus on the simpler yet insightful case of axisymmetric circular shear ruptures and quantify the effect of frictional rheology in aseismic slip propagation. Aseismic slip can take place in two distinct modes in this model: as an interfacial rupture that is unconditionally stable, or as the quasi-static nucleation phase of an otherwise dynamic rupture. We therefore examine both, the conditions controlling the propagation of aseismic slip, and the conditions leading to the nucleation of earthquakes.

- In Chapter 6, we generalize some important regimes of propagation of aseismic slip to account for fairly arbitrary injection rate histories. The history of injection has a strong effect on the temporal patterns of slip growth. Moreover, we use our physical model in combination with field observations of anthropogenic seismic swarms to understand how different migration patterns of seismic swarms can emerge from a fluid injection that activates fault slip. The model offers a unified framework for seismic swarms driven by the combined effect of pore pressure diffusion and aseismic slip transients resulting from fluid injections.

- In Chapter 7, we study the conditions that control the maximum size and moment magnitude of injection-induced slow slip events. In particular, we examine how the in-situ conditions (stress state, fault frictional and hydraulic properties) and fluid injection

operational parameters such as the accumulated volume of injected fluid, determine an upper bound for the maximum size of episodes of injection-induced aseismic slip.

- Finally, in Chapter 8, we provide some general conclusions and perspectives for future works.

2 A fast boundary-element-based solver for frictional slip and fault opening along pre-existing discontinuities in 3D elastic media

In this chapter, we develop a boundary-element-based solver for frictional slip and fault opening along pre-existing discontinuities of arbitrary shapes and orientations in a three-dimensional linearly elastic medium. Spatial discretization of the quasi-static elastic equilibrium is performed via a collocation boundary element method. The resulting dense boundary element matrix is compressed through a hierarchical low-rank approximation technique. Time integration is conducted via a fully implicit scheme employing a Newton-Raphson procedure. We use an elastoplastic-like split of the displacement discontinuities with a non-associated flow rule. Integration of the constitutive interface laws is performed locally via an elastic predictor-plastic corrector algorithm, to which analytical expressions for the so-called plastic multiplier and consistent tangent operator are provided.

Contributions of Alexis Sáez (CRediT author statement)

Conceptualization, Methodology, Software, Validation, Formal analysis, Investigation, Writing - Original Draft, Writing - Review & Editing, Visualization, Funding acquisition.

2.1 Problem formulation

Consider a Cartesian reference system $\{\mathbf{0}; \boldsymbol{e}_1, \boldsymbol{e}_2, \boldsymbol{e}_3\}$ and its corresponding coordinate system $\{\mathbf{0}; x_1, x_2, x_3\}$, such that the coordinate vector $\boldsymbol{x}$ can be written in index notation as $\boldsymbol{x} = x_i \boldsymbol{e}_i$. Let Σ be a set of pre-existing discontinuities of arbitrary shapes and orientations embedded in an infinite, isotropic, homogeneous, and linearly elastic three-dimensional solid. We define the displacement jump along the discontinuities as

$$d_i(\boldsymbol{x}, t) = u_i^+(\boldsymbol{x}, t) - u_i^-(\boldsymbol{x}, t), \quad \boldsymbol{x} \in \Sigma, \quad (i = 1, 2, 3),\tag{2.1}$$

where u_i^+ and u_i^- are the displacement vector fields at the upper Σ^+ and lower Σ^- faces of the discontinuities, respectively, and t is time.

The quasi-static elastic equilibrium (balance of momentum, Hooke's law, and boundary conditions) can be written as the following boundary integral equations relating the traction vector field $\boldsymbol{t}$ acting along the discontinuities to the displacement discontinuity $\boldsymbol{d}$ (see, for example, Hills et al., 1996; Mogilevskaya, 2014):

$$t_i(\boldsymbol{x}, t) = t_i^0(\boldsymbol{x}) + t_i^\infty(\boldsymbol{x}, t) + \int_\Sigma K_{ij}(\boldsymbol{x}, \boldsymbol{\xi}; \mu, \nu) d_j(\boldsymbol{\xi}, t) \mathrm{d}S_{\boldsymbol{\xi}}, \quad \boldsymbol{x} \in \Sigma, \ t > 0, \quad \left(i, j = 1, 2, 3\right). \tag{2.2}$$

In the previous equation, t_i^0 is the initial traction vector at $t = 0$ before any displacement discontinuity has occurred, t_i^∞ is the far-field applied traction vector that can be due to, for instance, tectonic or seasonal stress changes, among others, K_{ij} is the hypersingular (of order $1/r^3$, $r = \|\boldsymbol{x} - \boldsymbol{\xi}\|$) elastostatic traction kernel (e.g., Hills et al., 1996; Mogilevskaya, 2014), and μ and ν are the bulk shear modulus and Poisson's ratio, respectively. We adopt the geomechanics convention of normal stress positive in compression. In equation (2.2) as well as in (2.1), the position vectors are written in the global reference frame, whereas the stress and displacement discontinuity vectors are expressed in a local Cartesian reference system such that the index '3' corresponds to the component that is normal to Σ at $\boldsymbol{x}$, and the indices '1' and '2' represent two tangential (shear) components, orthogonal with each other.

We further introduce the so-called seismic radiation damping term (Rice, 1993) in the quasi-static elastic equilibrium, resulting in the following set of integrodifferential equations,

$$t_i(\boldsymbol{x}, t) = t_i^0(\boldsymbol{x}) + t_i^\infty(\boldsymbol{x}, t) + \int_\Sigma K_{ij}(\boldsymbol{x}, \boldsymbol{\xi}; \mu, \nu) d_j(\boldsymbol{\xi}, t) \mathrm{d}S_{\boldsymbol{\xi}}$$
$$+ \eta_{ij} \frac{\partial d_j(\boldsymbol{x}, t)}{\partial t}, \quad \boldsymbol{x} \in \Sigma, \ t > 0, \quad \left(i, j = 1, 2, 3\right), \tag{2.3}$$

where $\eta_{11} = \eta_{22} = \mu/2 v_s$, $\eta_{33} = (\lambda + 2\mu)/2 v_p$ and $\eta_{ij} = 0$ if $i \neq j$, with $v_s = \sqrt{\mu/\rho}$ the shear wave velocity of the medium, ρ the bulk density, $\lambda = 2\mu\nu/(1 - 2\nu)$ the Lamé's first parameter, and $v_p = \sqrt{(\lambda + 2\mu)/\rho}$ the compressional wave velocity. Equation (2.3) is known in the earthquake modeling community as "quasi-dynamic" approximation of the fully elastodynamic boundary integral equations. The radiation damping term corresponds to the instantaneous drop of stress at a given point $\boldsymbol{x}$ along the fault due to a local change in slip (or opening) rate. For slow ruptures, which are the main topic of our work, the term is negligibly small. It will only become relevant when slip undergoes a frictional instability, notably facilitating the numerical time integration by slowing down the otherwise infinite speed that would emerge in a purely quasi-static model.

Failure of the pre-exisiting discontinuities is governed by Terzaghi's effective stress (Terzaghi, 1923). The effective traction vector t_i' is defined as

$$t_i'(\boldsymbol{x}, t) = t_i(\boldsymbol{x}, t) - \delta_{i3} p(\boldsymbol{x}, t), \quad \boldsymbol{x} \in \Sigma, \ t > 0, \quad (i = 1, 2, 3), \tag{2.4}$$

where δ_{ij} is the Kronecker delta.

The pre-existing discontinuities are assumed to obey a Mohr–Coulomb failure criterion without any cohesion. The yield criterion can be thus written as the following local inequality,

$$F(t_i', \delta) = \sqrt{t_1'^2 + t_2'^2} - f(\delta)\,t_3' \leq 0, \tag{2.5}$$

where f is a local friction coefficient that may generally depend on the slip δ. Note that in principle, any kind of friction law can be considered in (2.5). Here, we formulate the yield function based on slip-dependent friction because it corresponds to the more general friction law we adopt in the following chapters.

We adopt a local elastoplastic-like constitutive relation for the discontinuities' interfaces following traditional modeling approaches of rock joints (see, for example, Fredriksson, 1976; Michalowski and Mroz, 1978; Plesha, 1987; Mroz and Giambanco, 1996; Stupkiewicz and Mróz, 2001). We therefore split the rate of displacement discontinuity $\dot{d}_i$ in an elastic and plastic part,

$$\dot{d}_i(\boldsymbol{x}, t) = \dot{d}_i^e(\boldsymbol{x}, t) + \dot{d}_i^p(\boldsymbol{x}, t), \quad \boldsymbol{x} \in \Sigma, \ t > 0, \quad (i = 1, 2, 3), \tag{2.6}$$

where the superscripts 'e' and 'p' denote the elastic and plastic (frictional or opening) parts, respectively. Note that in equation (2.5), $\delta = \|d_k^p\|$ $(k = 2, 3)$, with d_k^p the shear part of the displacement discontinuity (plastic) vector. We further introduce a linear elastic local relation between the rate of effective tractions and the rate of the elastic part of the displacement discontinuity,

$$\dot{t}_i'(\boldsymbol{x}, t) = -C_{ij}\dot{d}_j^e(\boldsymbol{x}, t), \quad \boldsymbol{x} \in \Sigma, \ t > 0, \quad (i = 1, 2, 3), \tag{2.7}$$

where C_{ij} is a diagonal elastic stiffness matrix containing the shear and normal stiffness components of the local elastic springs modeling the fault elastic response. Note that the minus sign in the previous equation comes from our convention of signs for tractions and displacement discontinuities.

In the rock mechanics literature, the relation (2.7) is generally non-linear (e.g., Bandis et al., 1983). The elastic stiffness matrix depends on the current effective traction vector. Such non-linear relation can be indeed used to account for non-linear changes in permeability when modeling the hydro-mechanical response of fractures and joints (see, for example, Rutqvist and Stephansson, 2003), resulting in similar relations to the ones used in the geophysics literature to model mature faults (Rice, 1992). In this thesis, we are however interested in modeling a rather rigid-plastic interface. Numerically, we thus consider values of the elastic stiffness components that are sufficiently large to obtain $\|\dot{d}_i^p\| \gg \|\dot{d}_i^e\|$ whenever plastic flow occurs. The purpose of the elastic spring (2.7) can be then viewed as a "penalty" parameter, similar to the one used sometimes in computational contact mechanics (Wriggers, 2006).

We use a non-associated Mohr-Coulomb flow rule to describe the evolution of the plastic part of the displacement discontinuity,

$$\dot{d}_i^p = -\dot{\gamma}\frac{\partial G}{\partial t_i'}, \quad G = \sqrt{t_1^2 + t_2^2} - \psi(\delta)\, t_3', \quad \dot{\gamma} \geq 0, \tag{2.8}$$

where γ is the plastic multiplier, G is the so-called plastic flow potential, and $\psi = \tan(\phi)$ is the dilatancy coefficient with ϕ the dilatancy angle, that may generally depend on slip δ. Note that the minus sign in the flow rule (2.8) comes from our convention of signs.

Finally, the inequalities for the yield function (2.5) and plastic multiplier (2.8) can be re-written as the Karush-Kuhn-Tucker conditions of elastoplasticity,

$$\dot{\gamma} \geq 0, \quad F \leq 0, \quad \dot{\gamma}F = 0. \tag{2.9}$$

2.2   Spatial discretization

We discretize the set of pre-existing discontinuities Σ using an unstructured triangulation $\Gamma = \cup_{k=1}^{N_E} \Gamma_k$, where Γ_k is the k-th triangular element and N_E is the total number of elements in the mesh. We use the displacement discontinuity method (Crouch & Starfield, 1983) to solve the boundary integrals in the integrodifferential equations (2.3) and employ triangular boundary elements with piece-wise uniform displacement discontinuity. Our formulation of the method uses the explicit formulae of Nintcheu Fata (2009, 2011), which obtained through analytical integration, closed-form solutions for all the singular integrals appearing in the formulation of the method in 3D using constant-displacement-discontinuity triangular elements (Kuriyama & Mizuta, 1993). Nintcheu Fata's formulae are notably written in a recursive manner that facilitates their computational implementation. For complete details of our formulation and implementation, see Appendix A. In particular, we adopt boundary elements with one collocation point located at the centroid of each triangle. The total number of collocation points in the mesh is therefore $N_C = N_E$, and the total number of degrees of freedom in 3D is $N = 3N_C$.

The spatially discretized form of the elastic equilibrium, prior substitution of equation (2.4) into (2.3), reads as

$$t' = t^0 + t^\infty - p + \mathbf{E}d + \mathbf{Q}\dot{d}, \tag{2.10}$$

where $t' \in \mathbb{R}^N$ is the effective traction vector containing the components of effective tractions at all the collocation points, $t^o \in \mathbb{R}^N$ is the initial total traction vector, $t^\infty \in \mathbb{R}^N$ is the far-field applied traction vector, $d \in \mathbb{R}^N$ is the displacement discontinuity vector containing the displacement discontinuity components of all the elements in the mesh, $\mathbf{E} \in \mathbb{R}^{N \times N}$ is the

collocation boundary element matrix which is dense and non-symmetric, and $\mathbf{Q} \in \mathbb{R}^{N \times N}$ is the so-called radiation damping matrix which is diagonal. In equation (2.10), the explicit dependence on time of all vectors (except by $\boldsymbol{t}^0$ which is constant) has been omitted for simplicity.

Equation (2.10) is arranged in order that $\boldsymbol{t} = t_i^m = (t_1^1, t_2^1, t_3^1, t_1^2, t_2^2 ..., t_3^{N_C})$, where the index $i = 1, 2, 3$ denotes the local components expressed in the local reference system of each boundary element, with '3' corresponding to the normal component, and '1' and '2' the tangential ones (see Appendix A for further details), and the index $m = 1, 2, ..., N_C$ denotes the collocation points. Note that $\boldsymbol{p} = (0, 0, p^1, 0, ..., p^{N_C})$ as the pore-fluid pressure affects only the normal component of the effective traction vector.

Finally, an essential tool that allows us to tackle three-dimensional problems in a computationally efficient manner is the approximation of the dense boundary element matrix $\mathbf{E}$ via a hierarchical matrix representation $\mathbf{E}_H$ (Hackbusch, 2015). We use an in-house implementation of hierarchical matrices which reduces significantly the memory requirements and speed up the most expensive numerical calculations of our solver, namely, the matrix-vector multiplications involving $\mathbf{E}_H$ (see Ciardo et al., 2020, and references therein for further details).

2.3   Time integration

We adopt a backward Euler (fully implicit) time integration scheme. Let $\Delta X = X^{n+1} - X^n$ be the increment of a generic variable X from the time t^n to the time t^{n+1} with $\Delta t = t^{n+1} - t^n$ being the time step. By differentiating equation (2.10) with respect to time, we obtain the following fully discretized incremental form of the elastic equilibrium,

$$\Delta \boldsymbol{t}' (\Delta \boldsymbol{d}) = \Delta \boldsymbol{t}^\infty - \Delta \boldsymbol{p} + [\mathbf{E}_H + \mathbf{Q} / \Delta t] \Delta \boldsymbol{d} - \mathbf{Q} \boldsymbol{v}^n, \tag{2.11}$$

where $\boldsymbol{v}^n \in \mathbb{R}^N$ is the slip rate vector at the previous time step. Equation (2.11) is a non-linear system of N equations for $\Delta \boldsymbol{d}$. The non-linearity comes from the elasto-plastic split, equations (2.5) to (2.8), which results in an implicit dependence of $\Delta \boldsymbol{t}'$ on $\Delta \boldsymbol{d}$, as denoted on the left-hand side of equation (2.11).

We solve (2.11) via a Newton-Raphson (NR) scheme. Let us define the NR's residual

$$\boldsymbol{r} (\Delta \boldsymbol{d}) = \Delta \boldsymbol{t}^\infty - \Delta \boldsymbol{p} + [\mathbf{E}_H + \mathbf{Q} / \Delta t] \Delta \boldsymbol{d} - \mathbf{Q} \boldsymbol{v}^n - \Delta \boldsymbol{t}' (\Delta \boldsymbol{d}). \tag{2.12}$$

The k-th NR iteration, where $\Delta \boldsymbol{d}^{k+1} = \Delta \boldsymbol{d}^k + \delta \Delta \boldsymbol{d}$, is given by the following linearized system,

$$\mathbf{J}(\Delta \boldsymbol{d}^k) \cdot \delta \Delta \boldsymbol{d} = -\boldsymbol{r}(\Delta \boldsymbol{d}^k), \tag{2.13}$$

where $\mathbf{J} = \partial \boldsymbol{r} / \partial \Delta \boldsymbol{d}$ is the Jacobian matrix, readily calculated from (2.12) as

$$\mathbf{J} = \mathbf{E}_H + \mathbf{Q} / \Delta t + \mathbf{C}_t, \tag{2.14}$$

with

$$\mathbf{C}_t = -\frac{\partial \Delta \boldsymbol{t}'}{\partial \Delta \boldsymbol{d}} \tag{2.15}$$

the so-called consistent tangent operator of elastoplasticity (see, for example, de Souza Neto et al., 2008).

For a given increment of the total displacement discontinuity vector at the k-th NR iteration $\Delta \boldsymbol{d}^k$, the solution of the linearized system (2.13) requires evaluating the corresponding increment of effective traction vector $\Delta \boldsymbol{t}'(\Delta \boldsymbol{d}^k)$ as well as the consistent tangent operator $\mathbf{C}_t$. Both evaluations depend on the specific forms of friction and dilatancy laws. We elaborate on this in the next section.

2.4   Integration of the constitutive interface law

The integration of the constitutive interface law is performed locally at the collocation point level, in a similar manner to the integration of elastoplastic constitutive equations in computational plasticity that are performed at the material, Gauss points in the case of finite element schemes (e.g., de Souza Neto et al., 2008). The formulation and implementation of the solver are so far general and agnostic to the constitutive details of the interface. This is beneficial from a modular programming point of view, as every time new physical ingredients at the level of the discontinuities' interfaces are incorporated, the solver needs just to be adapted in little terms, in relation to the module concerning the local elastoplastic integration. Note that by integration of the constitutive interface law, we mean precisely two things: to calculate the effective traction vector $\Delta \boldsymbol{t}'$ and the corresponding consistent tangent operator $\mathbf{C}_t$. Expressions for both quantities were derived throughout this doctoral research at the time they were needed to resolve the particular problem at hand. Below, we summarize the constitutive laws utilized in each chapter. Notably, we consider a special case that we denominate as axisymmetric model. It corresponds to the case of a single planar fault hosting frictional ruptures induced by axisymmetric loading (more details in the following chapters). In the limit of a Poisson's ratio $\nu = 0$, such configuration produces axisymmetric circular shear ruptures. In this case, the numerical formulation becomes essentially a two-dimensional one, with one shear and one normal component of displacement discontinuity and traction per collocation point. Details of the collocation boundary element matrix for such a particular case are given in Appendix A.

We consider the following models:

- In Chapter 3, a fully three-dimensional model with constant friction.

- In Chapter 4, a fully three-dimensional with constant friction and an axisymmetric model with constant friction as well.

- In Chapter 5, an axisymmetric model with slip-weakening friction.

- In Chapter 6, no numerical calculations were required.

- In Chapter 7, a fully three-dimensional model and an axisymmetric model with constant friction.

In all of our models, we consider no dilatant behavior. Moreover, in the following sections, we describe in detail the integration of the constitutive interface laws utilized.

2.4.1 Elastic predictor - plastic corrector algorithm

To calculate the increment of effective traction vector $\Delta t'$ for a given Δd, we use a classical elastic predictor–plastic corrector algorithm which is a two-step procedure in which the two possible modes of contact, elastic and plastic, are solved sequentially and the final solution is chosen as the only one satisfying the yield inequality (2.5) (see, for example, de Souza Neto et al., 2008, for details). In the case of constant friction, an explicit solution for the plastic corrector part of the algorithm, also known as radial return mapping, is known in terms of the plastic multiplier increment as (e.g., equation 10.125 in Wriggers, 2006):

$$\Delta\gamma = \frac{\|\boldsymbol{\tau}_s^{\text{trial}}\| - f \cdot t_n^{\text{trial}}}{k_s}, \tag{2.16}$$

where $\boldsymbol{\tau}_s^{\text{trial}}$ is the shear part of the elastic-trial traction vector $\Delta t_i' = -C_{ij}\Delta d_j$, t_n^{trial} the normal part, and f is the local constant friction coefficient.

For the axisymmetric model with the friction coefficient being an arbitrary function of slip, $f(\delta)$, one can show that the plastic multiplier increment follows the following implicit equation (e.g., equation 10.124 in Wriggers, 2006),

$$\Delta\gamma = \frac{|t_s^{\text{trial}}| - f\left(d_s^{p,n} - \Delta\gamma \cdot \text{sgn}\left(t_s^{\text{trial}}\right)\right) \cdot t_n^{\text{trial}}}{k_s}, \tag{2.17}$$

where t_s denotes the one shear component of the traction vector, and $d_s^{p,n}$ is the plastic (frictional) slip from the previous time step. Equation (2.17) is solved locally via a Newton-Raphson procedure.

Given the plastic multiplier increment $\Delta\gamma$, calculations of other relevant quantities such as frictional slip and traction vector are readily done considering the spatially-discretized form of equations (2.6) to (2.8). Finally, even though we do not examine problems involving fault opening in this work, its calculation in our scheme is straightforward. Once the yield function for fault opening is violated, that is, the elastic-trial normal component of the effective traction

vector is negative, the correction is trivial, $t'_n = 0$. The total increment of the normal component of displacement discontinuity resulting from the global elastic equilibrium, equation (2.11), is the fault opening.

2.4.2   Consistent tangent operator

To calculate the consistent tangent operator, we consider the so-called consistency condition $\dot{\gamma}\dot{F} = 0$, which states that when plastic flow occurs (i.e., $\dot{\gamma} > 0$), the stress state t'_i has to remain on the yield function and thus $\dot{F} = 0$. This additional equation can be written in incremental form as

$$\frac{\partial F}{\partial t'_i}\Delta t'_i + \frac{\partial F}{\partial \delta}\Delta \delta = 0. \tag{2.18}$$

Note that for constant friction, $\partial F / \partial \delta = 0$.

In general, we obtain the consistent tangent operator by direct linearization of equations (2.6) to (2.8), to obtain

$$\Delta t'_i = -C_{ij}\left[\Delta d_j + \Delta \gamma \left(\Delta d_j\right)\frac{\partial G}{\partial t'_j}\right], \tag{2.19}$$

with $\partial G/\partial t_1 = \sin(\theta)$, $\partial G/\partial t_2 = \cos(\theta)$, and $\partial G/\partial t'_3 = 0$ because of zero dilatancy, where $\theta = \arctan(t_2/t_1)$ with t_1 and t_2 the two local components of the shear traction vector. Differentiation of the latter expression with respect to Δd_j leads to the following expression for the squared blocks $\mathbf{C}^m_t$ of size 3×3 that composed the global tangent operator $\mathbf{C}_t$:

$$\mathbf{C}^m_t = \mathbf{C}_e - \mathbf{C}_p, \quad \text{with} \quad \mathbf{C}_p = -\begin{pmatrix} k_1\cos(\theta) \\ k_2\sin(\theta) \\ 0 \end{pmatrix} \otimes \begin{pmatrix} \partial \Delta \gamma / \partial \Delta d_1 \\ \partial \Delta \gamma / \partial \Delta d_2 \\ \partial \Delta \gamma / \partial \Delta d_3 \end{pmatrix}, \tag{2.20}$$

where m denotes the m-th collocation point, $\mathbf{C}_e$ is the diagonal elastic stiffness matrix C_{ij}, and $\mathbf{C}_p$ is the plastic part of the tangent operator with $\otimes$ the tensor product. Note that if $\Delta \gamma = 0$, that is, if the collocation point state is elastic or, in other words, no frictional slip occurs, then $\mathbf{C}_p$ is a null matrix, and $\mathbf{C}^m_t = \mathbf{C}_e$. The partial derivatives of the plastic multiplier $\Delta \gamma$ with respect to Δd_i are obtained from the consistency condition, equation (2.18). In the case of constant friction, calculations are straightforward, leading to the following expression:

$$\mathbf{C}^m_t = \begin{pmatrix} k_1\sin^2(\theta) & -k_1\sin(\theta)\cos(\theta) & fk_3\cos(\theta) \\ -k_2\sin(\theta)\cos(\theta) & k_2\cos^2(\theta) & fk_3\sin(\theta) \\ 0 & 0 & k_3 \end{pmatrix} \tag{2.21}$$

From this general 3D operator, the axisymmetric case is obtained readily by considering the only two possible directions of slip in the pseudo-2D configuration, that is, $\theta = 0$ and $\theta = \pi$. Hence, the squared blocks $\mathbf{C}^m_t$ of size 2×2 that compose the block diagonal matrix $\mathbf{C}_t$ are given

by

$$\mathbf{C}_t^m = \begin{pmatrix} 0 & \text{sgn}\left(t_s^{\text{trial}}\right) f k_n \\ 0 & k_n \end{pmatrix}, \tag{2.22}$$

where t_s is the shear component of the traction vector, and k_n is the normal component of the elastic stiffness matrix.

Finally, for the axisymmetric model with slip-weakening friction, the expression for $\mathbf{C}_t^m$ is more cumbersome yet it can be computed from equation (2.20) with the following partial derivatives:

$$\frac{\partial \Delta \gamma}{\partial \Delta d_s} = \frac{k_s \text{sgn}\left(t_s^{\text{trial}}\right)}{A}, \text{ and } \quad \frac{\partial \Delta \gamma}{\partial \Delta d_n} = -\frac{f\left(d_s^p\right) k_n}{A}, \tag{2.23}$$

where $A = f'\left(d_s^p\right) t_n^{\text{trial}} \text{sgn}\left(t_s^{\text{trial}}\right) - k_s$, with f' the first derivative of the arbitrary function describing the dependence of friction on slip. In the case of fault opening, calculations are again trivial; the tangent operator $\mathbf{C}_t$ is simply a null matrix (no more contact at the interface).

2.5 Implementation details and verification tests

The most expensive calculations in our solver are the matrix-vector multiplications involving the dense collocation boundary element matrix $\mathbf{E}$. We use an in-house multi-threaded C++ implementation of hierarchical matrices. The rest of the code is written in the Wolfram Mathematica language, which is binded to the C++ code via an API interface using the Wolfram Library Link Library.

When solving the global Newton–Raphson scheme employed at every backward Euler time step, we consider that convergence is reached when the relative increment of the L^2 norm of the displacement discontinuity vector increment (our primary unknown) between two consecutive iterations falls below 10^{-4}. On the other hand, the linearized system at each Newton-Raphson iteration is solved using a biconjugate gradient stabilized iterative solver (BiCGSTAB) with a tolerance set to 10^{-4}. In general, we choose the time step using an adaptive scheme based on the current rupture speed. Further details can be found in each chapter, as the time integration details depend on the specific problem under consideration.

We extensively verified our numerical solver against analytical and semi-analytical solutions that are derived in this same work and presented in the following chapters.

3 Three-dimensional fluid-driven stable frictional ruptures

In this chapter, we investigate the quasi-static growth of a fluid-driven frictional shear crack that propagates in mixed mode (II+III) on a planar fault interface that separates two identical half-spaces of a three-dimensional solid. The fault interface is characterized by a shear strength equal to the product of a constant friction coefficient and the local effective normal stress. Fluid is injected into the fault interface and two different injection scenarios are considered: injection at constant volume rate and injection at constant pressure. We derive analytical solutions for circular ruptures which occur in the limit of a Poisson's ratio $v = 0$ and solve numerically for the more general case in which the rupture shape is unknown ($v \neq 0$). For an injection at constant volume rate, the fault slip growth is self-similar. The rupture radius ($v = 0$) expands as $R(t) = \lambda L(t)$, where $L(t)$ is the nominal position of the fluid pressure front and λ is an amplification factor that is a known function of a unique dimensionless parameter T. The latter is defined as the ratio between the distance to failure under ambient conditions and the strength of the injection. Whenever $\lambda > 1$, the rupture front outpaces the fluid pressure front. For $v \neq 0$, the rupture shape is quasi-elliptical. The aspect ratio is upper and lower bounded by $1/(1-v)$ and $(3-v)/(3-2v)$, for the limiting cases of critically stressed faults ($\lambda \gg 1$, $T \ll 1$) and marginally pressurized faults ($\lambda \ll 1$, $T \gg 1$), respectively. Moreover, the evolution of the rupture area is independent of the Poisson's ratio and grows simply as $A_r(t) = 4\pi \alpha \lambda^2 t$, where α is the fault hydraulic diffusivity. For injection at constant pressure, the fault slip growth is not self-similar: the rupture front evolves at large times as $\propto (\alpha t)^{(1-T)/2}$ with T between 0 and 1. The frictional rupture moves at most diffusively ($\propto \sqrt{\alpha t}$) when the fault is critically stressed, but in general propagates slower than the fluid pressure front. Yet in some conditions, the rupture front outpaces the fluid pressure front. The latter will eventually catch the former if injection is sustained for a sufficient time. Our findings provide a basic understanding on how stable (aseismic) ruptures propagate in response to fluid injection in 3-D. Notably, since aseismic ruptures driven by injection at constant rate expands proportionally to the squared root of time, seismicity clouds that are commonly interpreted to be controlled by the direct effect of fluid pressure increase might be controlled by the stress transfer of a propagating aseismic rupture instead. We also demonstrate that the aseismic moment M_0 scales to the injected fluid volume V as $M_0 \propto V^{3/2}$.

This chapter is a modified version of the following scientific article:

Sáez, A., Lecampion, B., Bhattacharya, P. & Viesca, R.C. (2022). Three-dimensional fluid-driven stable frictional ruptures. *Journal of the Mechanics and Physics of Solids*, 132, 103672.

Contributions of Alexis Sáez (CRediT, Contributor Roles Taxonomy)

Conceptualization, Methodology, Software, Validation, Formal analysis, Investigation, Writing - Original Draft, Writing - Review & Editing, Visualization, Funding acquisition.

3.1   Introduction

Fluid-driven frictional ruptures play an important role in earthquake and fault mechanics and can occur either as a natural process or be induced by human activities. Some examples of the natural source are related to fault valving behavior (Sibson, 1992; Zhu et al., 2020) and metamorphic dehydration reactions (Wong et al., 1997; Hacker et al., 2003; Kato et al., 2010) in fault systems, whereas seismic swarms (Parotidis et al., 2005; Chen et al., 2012; Hatch et al., 2020; Z. Ross et al., 2020) and aftershock sequences (Bosl & Nur, 2002; Miller et al., 2004; Hainzl et al., 2016; Z. Ross et al., 2017; Miller, 2020) are other natural phenomena commonly attributed to the migration of fluids in fault zones. On the other hand, anthropogenic fluid injections associated with hydrocarbon and geothermal operations routinely produce microseismicity and have been extensively linked to the reactivation of faults (Healy et al., 1968; Deichmann & Giardini, 2009; Keranen et al., 2013; Ellsworth et al., 2019; Eyre et al., 2019).

Evidence for fluid-driven frictional ruptures is generally inferred from the observation of seismicity spreading away from natural or human-related fluid injections in the Earth's crust (S. Shapiro et al., 1997; Parotidis et al., 2005; Hainzl et al., 2016; Z. Ross et al., 2017; Goebel & Brodsky, 2018; Z. Ross et al., 2020). Observed seismicity is the result of unstable (seismic) frictional sliding that radiates detectable seismic waves. Nevertheless, seismic slip is not the only possible result of fluid injection. In fact, stable (aseismic) slip, which is more difficult to detect due to the virtual absence of elastodynamic waves, is a likely frequent result of the injection of fluids as demonstrated by past large-scale fluid injections in the field (Hamilton & Meehan, 1971; Scotti & Cornet, 1994; Bourouis & Bernard, 2007), recent laboratory and in-situ experiments (Guglielmi et al., 2015; Scuderi & Collettini, 2016; Cappa et al., 2019; Passelègue et al., 2020), and recent cases of injection-induced seismicity (Wei et al., 2015; Chen et al., 2017; Eyre et al., 2019).

As suggested by a number of recent experimental and observational studies (Guglielmi et al., 2015; Wei et al., 2015; Duboeuf et al., 2017; Bhattacharya & Viesca, 2019; Cappa et al., 2019; Eyre et al., 2019), injection-induced aseismic slip may trigger seismicity by the transfer of solid stresses to unstable patches in pre-existing structural discontinuities, such as fractures and faults. Such spatio-temporal perturbation of the stress field is due to a quasi-statically expanding fluid-driven slipping patch that propagates along an initially locked and predom-

inantly frictionally-stable pre-existing discontinuity. In this view and in the framework of this model, seismicity can be conceptually understood as the result of instabilities triggered by perturbing the pre-injection stress state of frictionally-unstable patches present either in the same pre-existing discontinuity (due to heterogeneities in rock frictional properties) or in others nearby the propagating rupture. The potential prominence of this triggering mechanism has increased in recent times since new investigations have suggested that fluid-induced aseismic slip can outpace the diffusion of fluid pressure (Bhattacharya & Viesca, 2019; Eyre et al., 2019) and may be in fact the primary cause of observed seismicity during in-situ experiments (Guglielmi et al., 2015; Duboeuf et al., 2017) and responsible for the triggering of hydraulic fracturing-induced earthquakes (Eyre et al., 2019).

Recent efforts for understanding injection-induced aseismic slip have been motivated mostly by the sudden increase of seismicity due to anthropogenic fluid injection (Keranen et al., 2014; Bao & Eaton, 2016; Goebel & Brodsky, 2018). Nevertheless, understanding the mechanics of fluid-driven aseismic slip is indeed relevant to any phenomenon that is predominantly characterized by stable frictional sliding and the pressurization of interfacial fluids. This might be the case of, for instance, some seismic swarms (Chen et al., 2012; Hatch et al., 2020), aftershock sequences (Z. Ross et al., 2017), and slow slip transients near the base of the seismogenic zone due to fault valving (Zhu et al., 2020) or metamorphic dehydration reactions (Kato et al., 2010).

Despite the apparent relevance of fluid-driven aseismic ruptures in a wide variety of natural and anthropogenic phenomena, the spatio-temporal evolution of aseismic slip in response to fluid injection remains poorly constrained in 3-D. This is, in part, due to the challenge of solving such a moving boundary value problem in which both fault slip and rupture shape are unknown. In this article, we investigate the mechanics of injection-induced fault slip by solving the problem of a fluid-driven frictional shear crack that propagates in mixed mode (II+III) on a planar fault that separates two identical half-spaces of a three-dimensional, linear elastic, and impermeable solid. The fault interface is saturated by pressurized fluid and it is characterized by a constant hydraulic transmissivity and a shear strength that is determined by the product of a constant friction coefficient and the local effective normal stress. We consider that fluid is injected into the fault interface under two injection scenarios: injection at constant volume rate and injection at constant pressure. The model is an extension to 3-D of a previous 2-D model presented by Bhattacharya and Viesca (2019) and more recently by Viesca (2021). In the process, we also investigate the fundamental problem of crack-shape selection of a frictional shear crack under localized (point-force-like) and distributed effective shear loadings, including its dependence on the Poisson's ratio of the bulk.

3.2   Problem formulation

We consider a fault plane located along $z = 0$ that separates two semi-infinite, homogeneous, isotropic and linear elastic solids (see Figure 3.1). The fault interface is governed by Coulomb's
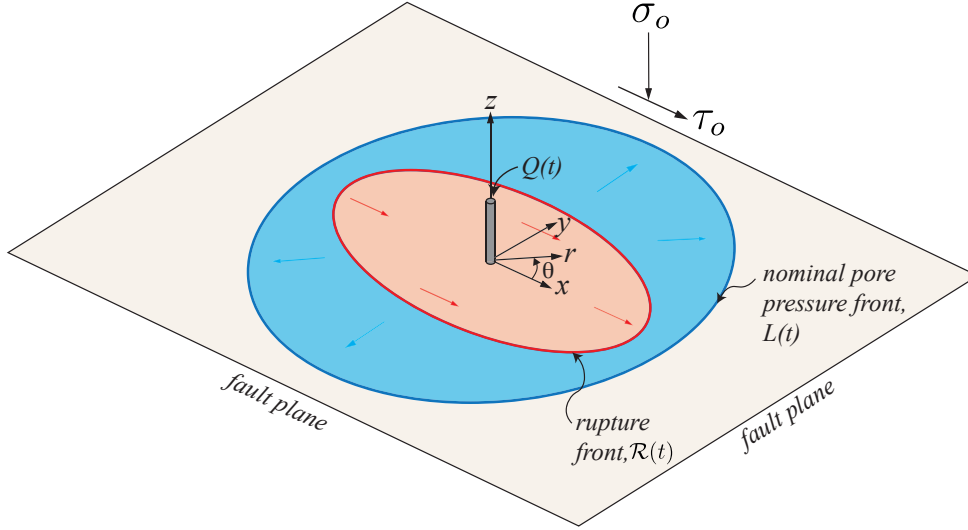
Figure 3.1: Model schematic. A planar fault separates two semi-infinite linear elastic, homogeneous, and isotropic solids. The fault is characterized by a constant friction coefficient and is embedded in uniform initial fluid pressure and stress fields. Fluid is injected right into the fault through a wellbore located along the z axis. Fluid flow is confined within the fault plane and is fault-parallel and axisymmetric with regard to the z-axis. A quasi-static rupture of front $\mathscr{R}(t)$ whose shape is unknown is driven by axisymmetric fluid pressure diffusion that is characterized by a nominal fluid pressure front of radius $L(t)$.

friction with a constant friction coefficient. The initial stress tensor is uniform and is characterized by a shear stress τ_o resolved on the fault plane that acts along the x direction, and a total normal stress σ_o to the fault plane (that acts along the z direction). We assume that fluid is injected into the fault plane through, for instance, a wellbore, that is located along the z axis. We also assume that the solid is impermeable and the fault interface has a uniform and constant hydraulic transmissivity; fluid flow thus occurs only within the fault plane and is fault-parallel and axisymmetric with regard to the z axis. Owing to the planarity of the fault and the uniform direction of the initial shear stress τ_o, fluid flow induces fault slip δ and changes in the shear stress τ resolved on the fault plane that are for all practical purposes (see Chapter **??**, Section 4.8.1 for more details) both characterized by a uniform direction along the x axis. The magnitude of the fault slip δ is maximum at the origin (the injection point) and vanishes along the rupture front $\mathscr{R}(t) = \{(x, y) : \delta(x, y, t) = 0\}$. The rupture front $\mathscr{R}(t)$ is unknown a priori and is to be determined as part of the solution.

The quasi-static elastic equilibrium that relates the fault slip δ to the shear stress τ on the fault plane Γ can be written as the following boundary integral equation (Hills et al., 1996)

$$\tau(x, y, t) = \tau_o + \int_{\Gamma} K(x - \xi, y - \zeta; \mu, \nu)\delta(\xi, \zeta, t)\mathrm{d}\xi\mathrm{d}\zeta, \tag{3.1}$$

where τ_o is the initial shear stress, μ is the shear modulus of the solid, ν is the Poisson's

ratio, and K is the hypersingular (of order $1/r^3$) elastostatic traction kernel (Hills et al., 1996). We adopt the convention of slip positive in clockwise rotation, $\delta(x, y, t) = u_x(x, y, z = 0^+, t) - u_x(x, y, z = 0^-, t)$, where u_x is the displacement component in the x direction. We also adopt the convention of normal stress positive in compression.

The fault is assumed to obey a Mohr-Coulomb shear failure criterion without any cohesion:

$$\left|\tau(x, y, t)\right| \leq f\left(\sigma_o - p(r, t)\right), \tag{3.2}$$

where f is the constant friction coefficient, $\sigma_o - p(r, t)$ denotes Terzaghi's effective normal stress to the fault plane with $p(r, t)$ being the spatiotemporally evolving fluid pressure, which is axisymmetric about the point of injection $\{O; r, \theta, z\}$ (see Figure 3.1). We further assume that fault slip occurs without any normal displacement discontinuity, neither dilatant nor contractant, and that fault slip does not impact fluid flow.

We make the assumption that the surrounding rock can be considered impermeable compared to the fault itself at the scale of the injection duration. Single phase porous media flow (Bear, 2013) in the fault thus reduces (after width averaging across the fault thickness w_h) to the following two-dimensional pressure-diffusion equation on the fault plane

$$S\frac{\partial p}{\partial t} - \frac{k}{\eta}\nabla^2 p = 0, \tag{3.3}$$

where S is a storage coefficient combining the effect of both fluid and pore compressibilities, k is the constant and uniform fault permeability, and η the fluid dynamic viscosity.

The fault is initially fully locked (zero slip rate) and the uniform initial fluid pressure field is equal to p_o. We investigate sustained fluid injection for $t > 0$ under two different scenarios: either at constant volume rate or at constant overpressure. The solutions of both boundary value problems for the two-dimensional diffusion equation are well-known (Carslaw & Jaeger, 1959) and can be written in the following functional form

$$p(r, t) = p_o + \Delta p_* \Pi(r, \alpha t), \tag{3.4}$$

where Δp_* is a characteristic pressure and Π is the dimensionless injection-induced overpressure. These solutions of the diffusion equation (3.3) notably depend on the fault hydraulic diffusivity $\alpha = k/S\eta$ $[L^2/T]$ via the well-known diffusion characteristic length $\sqrt{\alpha t}$.

For a constant volume rate injection from a point source, the two-dimensional flow solution is given in polar coordinates by (section 10.4, eq. 5, Carslaw and Jaeger, 1959):

$$\Delta p_* = \frac{Q_w \eta}{4\pi k w_h}, \quad \Pi(r, t) = E_1\left(\frac{r^2}{4\alpha t}\right), \tag{3.5}$$

where Q_w is the constant injection volume rate $[L^3/T]$, w_h is the fault thickness $[L]$, and E_1 is the exponential integral function. Note that the product $k w_h$ is often denoted as the fault

hydraulic transmissivity $[L^3]$.

For the case of an injection from a finite wellbore at constant overpressure, the solution reads (section 13.5, eq. 6, Carslaw and Jaeger, 1959):

$$\Delta p_* = \Delta p_w, \quad \Pi(r, t) = 1 + \frac{2}{\pi} \int_0^\infty e^{-\xi^2 \alpha t / r_w^2} \frac{J_0(\xi r / r_w) Y_0(\xi) - Y_0(\xi r / r_w) J_0(\xi)}{\xi \left(J_0^2(\xi) + Y_0^2(\xi) \right)} \mathrm{d}\xi, \tag{3.6}$$

where Δp_w is the applied constant overpressure at the wellbore of radius r_w, and J_0 and Y_0 are the zero-order Bessel functions of the first and second kind, respectively.

The uniform initial fluid pressure and stress fields must satisfy the condition $|\tau_o| < f\sigma_o'$ on the fault plane, where $\sigma_o' = \sigma_o - p_o$ is the initial effective normal stress. This condition means no activation of fault slip prior to the start of the injection. Fault slip starts when the fluid pressure increase is sufficient to reach the Mohr-Coulomb shear failure criterion. The ensuing aseismic rupture grows due to the direct effect of the fluid pressure that reduces locally the fault strength in (3.2), and due to the quasi-static nonlocal elastic integral operator (3.1) that operates over the fault slip distribution δ and determines the local shear stress change consistent with the Mohr-Coulomb strength condition.

3.3 Self-similar rupture growth due to injection at constant volume rate

3.3.1 Scaling and similarity

We first investigate the case of a constant volume rate injection, where the fluid pressure evolution driving the rupture is given by equation (3.5). Such a diffusion solution is self-similar: the pressure is only function of the self-similar variable $r/\sqrt{4\alpha t}$, where $L(t) = \sqrt{4\alpha t}$ is the characteristic diffusion lengthscale which corresponds to the evolution of the fluid pressure front disturbance. Because no other time or length scales enter the problem, the quasi-static rupture will also evolve in a self-similar fashion. This result is essential for the problem addressed in this section. We denote the a priori unknown rupture shape as $\mathcal{R}(t) = \{(x, y) : \delta(x, y, t) = 0\}$ and scale it as

$$\mathcal{R}(t) = R(t)\mathcal{S}, \tag{3.7}$$

where $\mathcal{S}$ is the dimensionless rupture front and $R(t)$ the characteristic rupture lengthscale. Moreover, we define the amplification factor λ that relates the instantaneous rupture characteristic scale $R(t)$ to the nominal location of the fluid pressure front $L(t)$, such that $R(t) = \lambda L(t)$. A value of $\lambda > 1$ indicates that the rupture lengthscale is greater than the fluid pressure front radius, whereas a value of $\lambda < 1$ indicates the opposite.

We can scale the spatial variables (x, y) with the diffusion lengthscale $L(t)$ (or alternatively with the characteristic rupture scale $R(t)$) while the characteristic fluid pressure scale is directly

given by Δp_* in equation (3.5). Introducing these characteristic scales in the Mohr-Coulomb and elasticity equations, allows us to close the scaling of the problem as:

$$\frac{\vec{x}}{L(t)} \to \vec{x}, \quad \frac{\tau - f\sigma'_o}{f\Delta p_*} \to \tau, \quad \frac{\delta}{\delta_c(t)} \to \delta, \quad \frac{p - p_0}{\Delta p_*} \to p, \tag{3.8}$$

where the characteristic slip is given by $\delta_c(t) = f\Delta p_* L(t)/\mu$ (or alternatively by $f\Delta p_* R(t)/\mu$ if $R(t)$ is used for the spatial scale). Using this scaling, the dimensionless form of the problem depends on only two dimensionless parameters:

$$T = \frac{1 - \tau_o/f\sigma'_o}{\Delta p_*/\sigma'_o}, \tag{3.9}$$

and the Poisson's ratio ν. The dimensionless rupture shape $\mathscr{S}$ thus depends on both ν and T. The parameter T is similar to the one found by Bhattacharya and Viesca (2019) in their 2D plane-strain model of a frictional shear crack driven by injection at constant pressure, whereas the second dimensionless parameter, the Poisson's ratio, arises from the three-dimensional nature of the problem considered here, in which the rupture propagates in mixed mode (II+III) with an a priori unknown shape.

The *stress-injection parameter T* is crucial in the present study. It encapsulates the information about the initial state of stress acting on the fault and the characteristic injection pressure. More specifically, the numerator of T, $1 - \tau_o/f\sigma'_o$, is a measurement of the "distance" to failure under pre-injection ambient conditions (close to zero for a critically stressed fault, and close to one for a fault initially far away from frictional failure), whereas the denominator $\Delta p_*/\sigma'_o$ is an overpressure ratio which measures the amount of pressurization due to injection with regard to the initial effective normal stress. Both numerator and denominator are indeed independent parameters of a more general model for a shear crack obeying slip-weakening friction in 2-D elastic media investigated by Garagash and Germanovich (2012).

The stress-injection parameter varies between 0 and $+\infty$. The limiting values of T are associated with end-member scenarios that are relatively similar to the ones identified first by Garagash and Germanovich (2012). For small values of T, the condition $1 - \tau_o/f\sigma'_o \ll \Delta p_*/\sigma'_o$ must be satisfied. This means that the fault is 'critically stressed' with regard to the overpressure ratio. For large values of T, the condition $\Delta p_*/\sigma'_o \ll 1 - \tau_o/f\sigma'_o$ must be satisfied, so that the fault is 'marginally pressurized' with regard to the level of stress criticality. Hence, following this prior study, we denominate the corresponding end-member scenarios as a critically stressed fault ($T \ll 1$) and a marginally pressurized fault ($T \gg 1$).

It is worth noting that the characteristic pressure $\Delta p_* = Q_w\eta/4\pi k w_h$ increases (and therefore the stress-injection parameter T decreases) not only when the injection volume rate Q_w grows, but also when the fluid viscosity η increases or the fault hydraulic transmissivity $k w_h$ decreases. On the other hand, large values of Δp_* might be eventually upper bounded if the fluid pressure near the injection point is high enough to make fault opening a significant mechanism driving the propagation of the rupture. Such a problem has been notably addressed in the context of

frictional instabilities in 2-D (Azad et al., 2017).

3.3.2   Analytical solution for circular ruptures

We first consider the particular case where the Poisson's ratio ν is set to zero such that the solution of the problem only depends on the value of T. In this limit ($\nu = 0$), the rupture front $\mathcal{R}(t)$ is circular because the energy release rate for an axisymmetric shear load distributes uniformly along the circular crack front (see Section 3.7.1). The dimensionless rupture shape $\mathcal{S}$ is thus the unit circle and $R(t)$ is simply the rupture radius. For such a frictional shear crack with a constant friction coefficient, there is no fracture energy spent during propagation. The condition for quasi-static crack propagation then reads (see Section 3.7.1)

$$\int_0^{R(t)} \frac{\Delta\tau(r,t)}{\sqrt{R(t)^2 - r^2}} r \, \mathrm{d}r = 0, \tag{3.10}$$

where the axisymmetric shear stress drop is given by

$$\Delta\tau(r,t) = \tau_o - f\left(\sigma_o' - \Delta p_* \Pi(r,t)\right). \tag{3.11}$$

The stress drop can be viewed as the contribution of two terms: a constant, negative term $\tau_o - f\sigma_o'$ which is the difference between the initial shear stress τ_o and the initial fault strength $f\sigma_o'$, and an axisymmetric and positive term $f\Delta p_* \Pi(r,t)$ capturing the local reduction of fault strength due to fluid injection. After a change of variable $s = r/R$ and incorporating the previous definition of the amplification factor $\lambda = R(t)/L(t)$ into equation (3.10), the condition for quasi-static crack propagation can be rewritten in dimensionless form as

$$\int_0^1 \frac{s E_1(s^2\lambda^2)}{\sqrt{1 - s^2}} \mathrm{d}s = T. \tag{3.12}$$

As expected from the scaling analysis, T is the only governing dimensionless parameter and, as a result, there is a unique value of λ for each value of T. The integral in equation (3.12) can be evaluated analytically to obtain the following implicit equation for λ as function of T

$$2 - \gamma + \frac{2}{3}\lambda^2 {}_2F_2\left[\begin{array}{cc} 1 & 1 \\ 2 & 5/2 \end{array}; -\lambda^2\right] - \ln(4\lambda^2) = T, \tag{3.13}$$

where $\gamma = 0.577216...$ is the Euler-Mascheroni's constant and ${}_2F_2[\,]$ is the generalized hypergeometric function. The relation (3.13) is plotted in Figure 3.2. This figure shows that a critically stressed fault ($T \ll 1$) is characterized by a rupture that largely outpaces the fluid pressure front ($\lambda \gg 1$). On the other hand, a marginally pressurized fault ($T \gg 1$) is characterized by a rupture that substantially lags the fluid pressure front ($\lambda \ll 1$).

The limiting behavior of equation (3.13) for small and large λ leads to simple closed-form expressions for the corresponding end-member cases. In the limit of a critically stressed fault ($\lambda \gg 1$), equation (3.13) can be asymptotically expanded as $T \approx 1/(2\lambda^2) + O(1/\lambda^4)$, leading to

the following asymptotic solution for the amplification factor

$$\lambda \approx \frac{1}{\sqrt{2T}}.$$
(3.14)

Likewise in the limit of a marginally pressurized fault ($\lambda \ll 1$), equation (3.13) follows the asymptotic expansion $T \approx 2 - \gamma - \ln(4\lambda^2) + O(\lambda^2)$, that can be inverted to obtain

$$\lambda \approx \frac{1}{2}e^{(2-\gamma-T)/2}.$$
(3.15)

Since in the critically stressed limit, the pressurized fault patch is small compared to the rupture area, the fluid pressure perturbation can be approximated by a monopole distribution. Such approximation is, in terms of local reduction of fault strength, equal to a point force given by

$$f\Delta p_* \Pi(r,t) \approx f\Delta p_* \left(2\pi \int_0^{+\infty} \Pi(r,t)r\mathrm{d}r\right)\delta^{dirac}(r)/2\pi r = 2\alpha f\Delta p_* t\delta^{dirac}(r)/r, \quad (3.16)$$

where δ^{dirac} is the Dirac delta function in polar coordinates. Replacing this approximation in equation (3.11), and then evaluating the crack propagation condition, equation (3.10), leads equivalently to the asymptotic solution for λ in the critically stressed limit, equation (3.14).

On the other hand, in the marginally pressurized limit where the crack size is small compared to the pressurized area, the fluid pressure perturbation within the crack can be approximated by considering the behavior of the exponential integral function in equation (3.5) for small values of its argument. Such approximate injection-induced local reduction of fault strength is

$$f\Delta p_* \Pi(r,t) \approx -f\Delta p_* \left(2\ln\left(r/\sqrt{4\alpha t}\right) + \gamma\right).$$
(3.17)

Again, replacing this approximation in the crack propagation condition, equation (3.10), leads alternatively to the asymptotic solution for λ in the marginally pressurized limit, equation (3.15).

The purpose of the previous analysis is to highlight the asymptotic form of the driving forces related to the two end-member cases. As we will see later, both fault slip and rupture shape will also show well-defined asymptotic behaviors, and thus the results can be directly associated with the type of force that drives the crack growth in both limiting cases.

The asymptotic solutions (3.14) and (3.15) are shown in Figure 3.2 together with the general solution given by equation (3.13). Note that the transition between both propagation regimes (defined as $\lambda = 1$) occurs at $T \approx 0.5915$.

Another interesting analytical result is the rupture speed V_r that decreases with the square
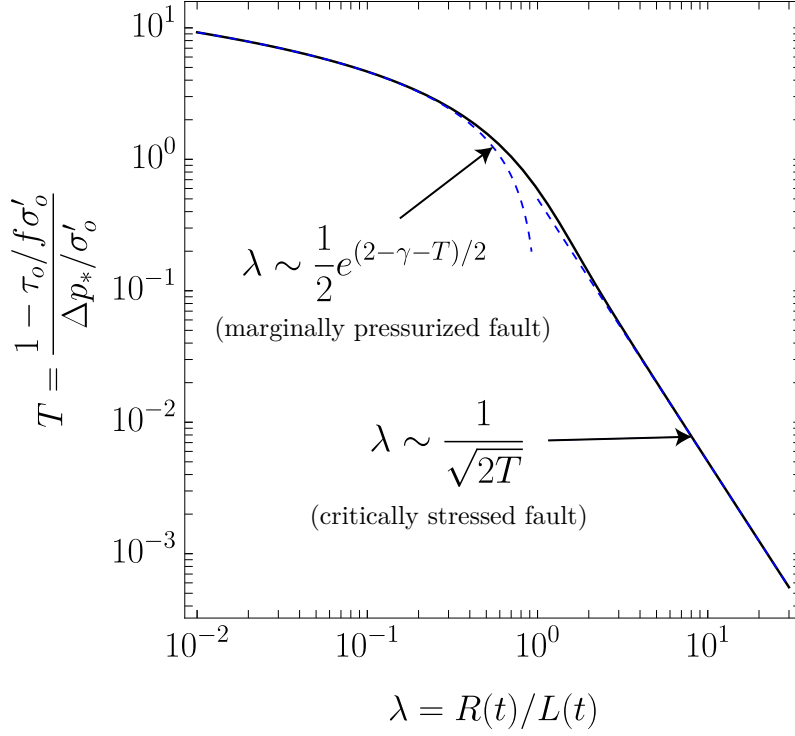
Figure 3.2: Analytical solution for the amplification factor λ for circular ruptures ($\nu = 0$) driven by injection at constant volume rate. λ relates the rupture radius $R(t)$ to the nominal position of the fluid pressure front $L(t) = \sqrt{4\alpha t}$ as $R(t) = \lambda L(t)$. The amplification factor λ is a unique function of the stress-injection parameter $T = (1 - \tau_o/f\sigma_o')/(\Delta p_*/\sigma_o')$. The black curve corresponds to the analytical solution given by equation (3.13), the blue dashed curves represent the asymptotic solutions for a critically stressed fault ($T \ll 1$, $\lambda \gg 1$), equation (3.14), and a marginally pressurized fault ($T \gg 1$, $\lambda \ll 1$), equation (3.15).

root of time and is simply given by

$$V_r = \lambda \sqrt{\frac{\alpha}{t}}. \tag{3.18}$$

The singularity of the rupture speed at $t = 0$ is a consequence of the self-similar diffusion lengthscale $\sqrt{4\alpha t}$ and the absence of inertia. In addition, the acceleration of the rupture front is equal to $-\lambda\sqrt{\alpha}/(2t^{3/2})$. This power-law deceleration is comparable to tensile hydraulic fracture propagation under a constant injection rate albeit at a different power-law of time (Detournay, 2016).

3.3.3 Numerical solution for circular ruptures

The numerical solution for circular ruptures allows us to obtain the axisymmetric self-similar slip profiles and also to verify our numerical solver against the previously derived solution for the amplification factor $\lambda(T)$. We use the boundary-element-based solver described in Chapter 2, and run seven simulations for values of $T = 0.001, 0.01, 0.1, 0.7, 2.0, 4.0$ and 7.0 with $\nu = 0$. We perform 10 fully implicit time steps for each simulation.

Axisymmetric slip profiles and accumulated fault slip at the injection point

Figure 3.3a displays typical slip and pore pressure spatial profiles at different times after the start of injection. The slip profiles correspond to the case $T = 0.1$ where the rupture front outpaces the fluid pressure front ($\lambda \approx 2.3$). Owing to the self-similarity of the problem, the slip profiles at different times collapse into one single curve under the scaling of equation (3.8). As a consequence, there is a unique dimensionless slip profile for a given value of the stress-injection parameter T. The unique self-similar slip profiles for the different values of T are shown in Figs. 3.3b and 3.3d for critically stressed and marginally pressurized cases, respectively.

Furthermore, in Section 3.7.2, we derive closed-form analytical expressions for the self-similar slip profiles in the limiting cases of critically stressed ($\lambda \gg 1$) and marginally pressurized ($\lambda \ll 1$) faults, that are:

$$\frac{\delta(r,t)\mu}{f\Delta p_* R(t)} = \frac{8}{\pi}\left[\sqrt{1-\bar{r}^2} - |\bar{r}|\arccos(|\bar{r}|)\right] \tag{3.19}$$

in the marginally pressurized limit, and

$$\frac{\delta(r,t)\mu}{f\Delta p_* L(t)} = \frac{2\sqrt{2T}}{\pi}\left[\frac{\arccos(|\bar{r}|)}{|\bar{r}|} - \sqrt{1-\bar{r}^2}\right], \tag{3.20}$$

in the critically stressed limit, where $\bar{r} = r/R(t)$ is the self-similar radial coordinate. Equation (3.20) is indeed valid for $r \gg L(t)$ and it corresponds to the "outer" solution in the critically stressed limit. Both analytical expressions are shown in Figures 3.3b and 3.3d together with the numerical results.

The accumulated fault slip at the injection point, $\delta(r=0,t)$, is plotted in Figure 3.3c as a function of the stress-injection parameter T. Note that $\delta(r=0,t)$ is normalized by the position of the fluid pressure front $L(t)$ on the left axis and by the rupture radius $R(t)$ on the right axis. $\delta(r=0,t)$ is easily obtained from equation (3.19) in the marginally pressurized limit as

$$\delta(r=0,t) = \frac{8}{\pi}\frac{f\Delta p_*}{\mu}R(t), \tag{3.21}$$
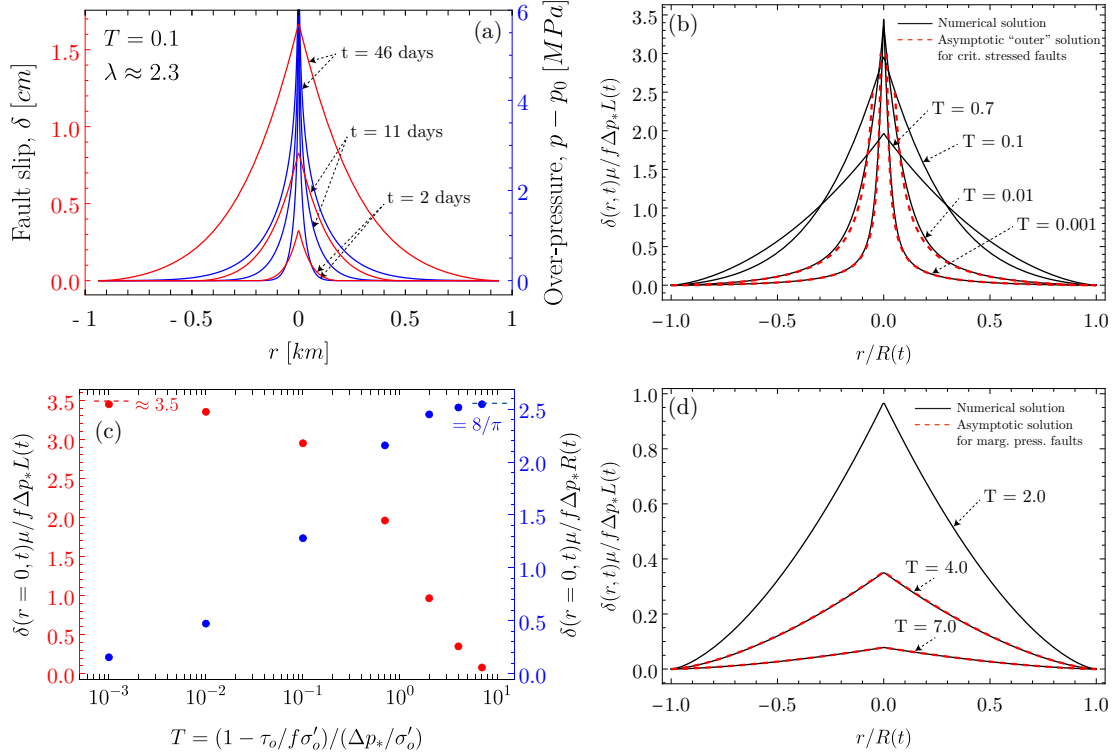
Figure 3.3: (a) Axisymmetric spatial profile of slip (red) and fluid overpressure (blue) at three different times for a circular rupture driven by the injection of fluid at constant volume rate. The stress-injection parameter is $T = 0.1$ for the particular choice of simulation parameters: $\sigma_0 = 120 \ [MPa]$, $\tau_0 = 47.958 \ [MPa]$, $p_0 = 40 \ [MPa]$, $f = 0.6$, $\mu = 30 \ [GPa]$, $\nu = 0$, $\alpha = 0.01 \ [m^2/s]$, $Q_w = 1.8 \ [m^3/min]$, $kw_h = 3 \cdot 10^{-12} \ [m^3]$, $\eta = 8.9 \cdot 10^{-4} \ [Pa \cdot s]$. (b) and (d) Self-similar slip profiles as a function of the self-similar radial coordinate $r/R(t)$ for different values of the stress-injection parameter T considering both numerical and asymptotic analytical solutions. (c) Normalized accumulated fault slip at the center of the rupture (the injection point) as a function of the stress-injection parameter T, including prefactors derived analytically ($8/\pi$) and numerically (3.5).

whereas in the critically stressed limit,

$$\delta(r=0,t) \approx c\frac{f\Delta p_*}{\mu}L(t). \tag{3.22}$$

The prefactor c is obtained numerically and is approximately 3.5 (see Figure 3.3c).

Equations (3.19) to (3.22) confirm that the relevant scale for the shear stress is $f\Delta p_*$, as chosen in the scaling analysis. Also, it becomes now clear that the relevant lengthscale in the problem depends on the limiting case under consideration; for marginally pressurized faults, the relevant lengthscale is the rupture radius $R(t)$, whereas for critically stressed faults, the proper lengthscale is the nominal radius of the pressurized fault patch $L(t)$.

Rupture radius and solver verification

In order to determine numerically the instantaneous rupture radius $R(t)$ at every time step t_n and verify our numerical solver against the analytical solution, equation (3.13), we solve numerically for $R(t_n)$ by searching for the position of zero slip $\delta(R,t_n) = 0$. As the solution for slip is axisymmetric in the limit of $\nu = 0$, we search in fact for the zeros along the entire rupture front by taking 100 equally-spaced values of the angular cylindrical coordinate $\theta \in [0,2\pi)$. In this way, we build the rupture front and compute finally the instantaneous rupture radius by fitting the equation of a circle centered at the origin to the zeros found for all the values of θ considered.

Figure 3.4a shows the results for the rupture radius as a function of the nominal location of the fluid pressure front $L(t) = \sqrt{4\alpha t}$ for different values of the stress-injection parameter T. In such plot, self-similar solutions for the rupture growth in the form $R(t) = \lambda L(t)$ are represented by straight lines that cross the origin and have a slope equal to the amplification factor λ. We estimate numerically the amplification factor λ for each value of the stress-injection parameter T, by simply averaging the ratios $R(t^n)/L(t^n)$ over the different time steps of the simulation.

The numerical results for the amplification factor λ are displayed in Figure 3.4b together with the analytical solution, equation (3.13). The numerical results are in excellent agreement with the theoretical predictions. This plus the previous comparison with the asymptotics of fault slip allows us to verify our numerical solver before exploring the case of non-circular ruptures, which is solved by numerical means only. The relative error between the numerical results and the exact analytical solution for the amplification factor λ is showed in the inset of Figure 3.4b and is approximately below 1%.

3.3.4 Numerical solution for non-circular ruptures

We move now to the more general case where the Poisson's ratio is different than zero. It is important to recall that the rupture shape $\mathcal{R}(t)$ is not known a priori but, of course, remains self-similar. In order to cover the relevant parameter space, we run 21 simulations for the same
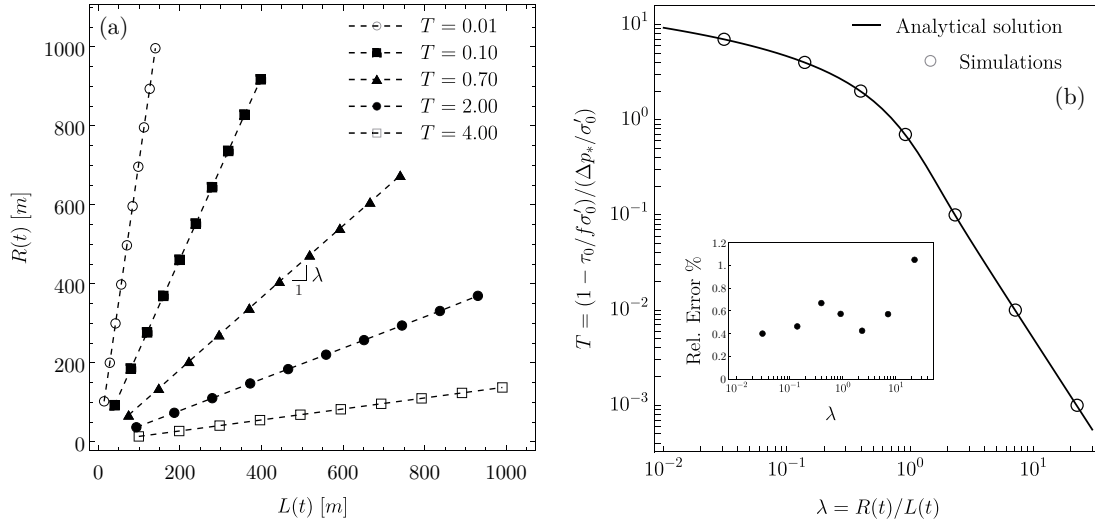
Figure 3.4: (a) Simulation results for the rupture radius $R(t)$ as a function of the fluid pressure front location $L(t) = \sqrt{4\alpha t}$ for different values of the stress-injection parameter T. Self-similar solutions of the rupture growth in the form $R(t) = \lambda L(t)$ are represented by straight lines that cross the origin and have a slope equal to the amplification factor λ. (b) Comparison between the numerical results for the amplification factor λ and the exact value given by the analytical solution, equation (3.13). The relative error for λ as $(\lambda^{num} - \lambda^{exact})/\lambda^{exact}$ is displayed in the inset.

seven values of the stress-injection parameter T considered in the previous section, 0.001, 0.01, 0.1, 0.7, 2.0, 4.0 and 7.0, for three values of the Poisson's ratio $\nu = 0.15$, 0.30, and 0.45.

Rupture shape

We quickly recognize in our simulations that the ruptures evolve systematically in a nearly elliptical shape. We also observe that the aspect ratio of the ruptures depends strongly not only on the Poisson's ratio but also on the stress-injection parameter T, i.e., on the initial stress state and the driving force itself. Snapshots of two rupture simulations having the same Poisson's ratio but different values of the stress-injection parameter are shown in Figures 3.5a-b. It is clear that the aspect ratio for critically stressed faults (Figure 3.5a, $T = 0.001$, $\lambda \gg 1$) is higher than the aspect ratio for marginally pressurized faults (Figure 3.5b, $T = 7.0$, $\lambda \ll 1$).

In order to quantify the rupture shape, we perform a nonlinear regression of the rupture front at every time step assuming an elliptical shape:

$$\mathcal{R}(t) = \left\{ (x, y, z = 0) : \left(\frac{x}{a(t)} \right)^2 + \left(\frac{y}{b(t)} \right)^2 = 1 \right\},\tag{3.23}$$

where a and b are the semi-major and semi-minor axes of the ellipse. We use the same procedure described previously to estimate the rupture front, with the only difference that

now the spatiotemporal evolution of slip is no longer axisymmetric. Typical ellipsoidal fits of the rupture front are displayed in Figures 3.5a-b. Further details of the computation of the rupture fronts can be found in Section 3.7.3, in which an estimate of the misfit between the ellipsoidal fits and the actual numerical front is also provided.

The results for the aspect ratio a/b as a function of the stress-injection parameter T and the Poisson's ratio ν are summarized in Figure 3.5c. Note that the aspect ratio is time-invariant due to the self-similarity of the problem, thus, we average the aspect ratio over the simulations' time steps for better accuracy. Figure 3.5c displays clearly two asymptotic behaviors of the aspect ratio for the two end-member cases of a critically stressed fault and a marginally pressurized fault. Additional simulations were run to better explore the dependence on Poisson's ratio for $T = 0.001$ ($\lambda \approx 22.37$, critically stressed faults) and $T = 7.0$ ($\lambda \approx 0.03$, marginally pressurized faults). The results are shown in Figure 3.5d. We notably found by numerical observation that the aspect ratio grows asymptotically with the Poisson's ratio as

$$
\begin{cases}
a/b \approx 1/(1-\nu) & \text{for critically stressed faults } (T \ll 1,\ \lambda \gg 1) \\
a/b \approx (3-\nu)/(3-2\nu) & \text{for marginally pressurized faults } (T \gg 1,\ \lambda \ll 1)
\end{cases}
\tag{3.24}
$$

It is interesting to note that the aspect ratio for critically stressed faults, $a/b \approx 1/(1-\nu)$, is similar to the results obtained by Gao (1988) and Favier et al. (2006) for three dimensional planar shear-crack under uniform remote loading and a uniform energy release rate along the crack front.

Generalized amplification factor λ

Since the rupture front $\mathscr{R}(t)$ is self-similar and nearly elliptical, we can write $a(t) = \lambda_a L(t)$ and $b(t) = \lambda_b L(t)$, where λ_a and λ_b are the corresponding amplification factors for the semi-major and semi-minor axes of the rupture front, respectively. Note that λ_a and λ_b depend only on the stress-injection parameter T and the Poisson's ratio ν. The evolution of $a(t)$ and $b(t)$ as a function of the fluid pressure front location $L(t) = \sqrt{4\alpha t}$ is shown in Figure 3.6a for different values of the stress-injection parameter T and the Poisson's ratio ν. In this figure, we also include the reference circular case $\nu = 0$, and indicate the meaning of λ_a, λ_b, and λ as the slopes of the straight lines for $a(t)$, $b(t)$, and $R(t)$ (of the reference circular case), respectively. Figure 3.6a shows that the major and minor axes for the elliptic ruptures ($\nu \neq 0$) lie about the radius for the reference circular solution ($\nu = 0$). For a given value of T and any value of ν, we find that the geometric mean of $a(t)$ and $b(t)$, $\sqrt{a(t)b(t)}$, is equal to the radius $R(t)$ of the circular crack solution for the same value of T (and $\nu = 0$). This equality is equivalent to the equality of amplification factors

$$
\lambda = \sqrt{\lambda_a \lambda_b} = \frac{\sqrt{a(t)b(t)}}{L(t)}
\tag{3.25}
$$
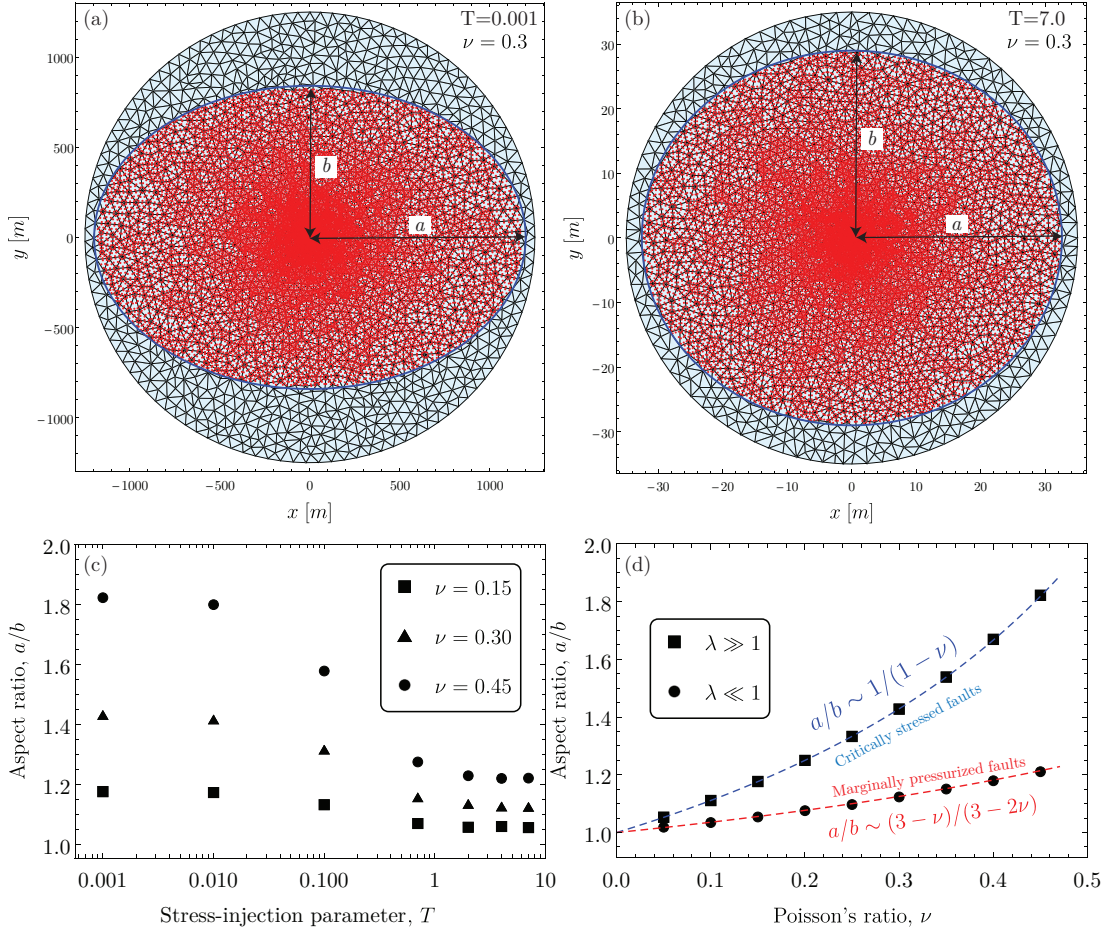
Figure 3.5: Typical simulations' snapshots and ellipsoidal fits (blue curves) of the rupture front for $\nu = 0.3$ and (a) $T = 0.001$ ($\lambda \approx 22.37$, a critically stressed fault) and (b) $T = 7.0$ ($\lambda \approx 0.03$, a marginally pressurized fault). The red points indicate the collocation points that have slipped. In the background, the unstructured mesh made on triangular boundary elements with quadratic shape functions. (c) Aspect ratio a/b as a function of the stress-injection parameter T for different values of the Poisson's ratio ν. (d) Aspect ratio a/b with increased resolution for the Poisson's ratio ν for the two end-member cases, $T = 0.001$ ($\lambda \approx 22.37$, critically stressed faults) and $T = 7.0$ ($\lambda \approx 0.03$, marginally pressurized faults).

This is demonstrated in the inset of Figure 3.6a in which the numerical values of $\lambda^{num} = \sqrt{\lambda_a \lambda_b}$ for all values of T and ν are plotted against the exact solution for circular ruptures λ^{circ}.

The numerical results for equation (3.25) are plotted in Figure 3.6b together with the analytical solution, equation (3.13), for all values of T and ν. In the inset, the relative difference between the numerical results and the analytical solution are also displayed. Figure 3.6b thus demonstrates that equation (3.25) is a generalization of the amplification factor that is now valid for any value of the Poisson's ratio. In the particular case of $\nu = 0$, equation (3.25) reduces simply to $\lambda = R(t)/L(t)$, as originally defined when deriving the analytical solution for the circular rupture case.

Poisson's ratio-independent rupture area

The generalized amplification factor $\lambda = \sqrt{\lambda_a \lambda_b}$ has a clear physical meaning. Indeed, it is equivalent to the squared root of the ratio between the instantaneous elliptic rupture area $A_r(t) = \pi a(t) b(t)$ and the instantaneous pressurized area $\pi L^2(t)$: $\lambda = \sqrt{A_r(t)/(\pi L^2(t))}$ such that the evolution of the rupture area $A_r(t)$ is simply given by

$$A_r(t) = 4\pi \alpha \lambda^2 t \tag{3.26}$$

and is thus independent of the value of the Poisson's ratio ν. The Poisson's ratio (together with the value of T) modifies the shape of the ruptures, which are more or less elongated, but it does not modify the rupture area, which solely depends on T. The rupture area A_r evolves linearly with time and proportionally to the injected volume ($\propto V$) for such a constant injection rate case.

Furthermore, for the two end-member cases of critically stressed and marginally pressurized faults, equations (3.14) and (3.15) lead to simple closed-form expressions for the evolution of the rupture area as function of the stress-injection parameter T:

$$\begin{cases} A_r(t) \approx 2\pi\alpha t/T & \text{for critically stressed faults (T} \ll 1, \lambda \gg 1) \\ A_r(t) \approx \pi\alpha e^{2-\gamma-T} t & \text{for marginally pressurized faults } (T \gg 1, \lambda \ll 1) \end{cases} \tag{3.27}$$

It is worth noting that David and Lazarus (2022) obtained recently a somewhat similar result in their study of tensile crack growth under the Paris' fatigue law (with a uniform energy release rate being a limiting case). They found, also by numerical observation, that a circular crack solution is sufficient to predict the area of a rupture for any non-circular crack.

Rupture front $\mathcal{R}(t)$ for the end-member cases

The asymptotic expressions for the aspect ratio (3.24) plus equation (3.27), lead to the following closed-form expressions for the evolution of the semi-major $a(t)$ and semi-minor $b(t)$ axes of
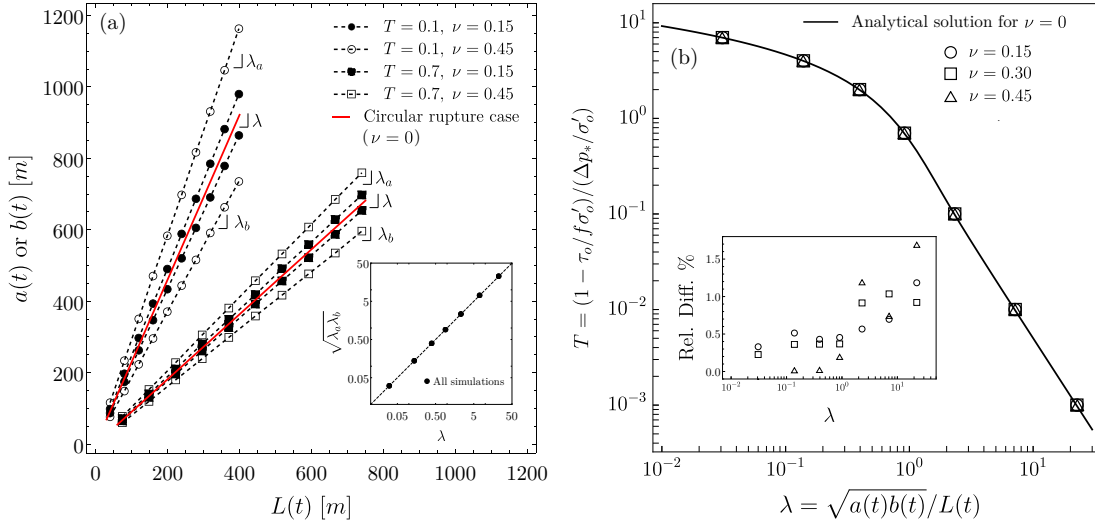
Figure 3.6: (a) Evolution of the semi-major $a(t)$ and semi-minor $b(t)$ axes of quasi-elliptical ruptures as a function of the fluid pressure front location $L(t)$ for different values of the stress-injection parameter T and Poisson's ratio ν. Solid red lines correspond to the analytical solution for $\nu = 0$, equation (3.13). λ_a and λ_b are the slopes of the straight lines for $a(t)$ and $b(t)$, respectively. Inset: comparison between the numerical results for the geometric mean $\sqrt{\lambda_a \lambda_b}$ and the exact analytical solution for circular ruptures λ^{circ}. (b) Comparison between the numerical values of the generalized amplification factor $\lambda^{num} = \sqrt{\lambda_a \lambda_b} = \sqrt{a(t)b(t)}/L(t)$ (symbols) and λ^{circ} (solid line). Inset: the relative difference $(\lambda^{num} - \lambda^{circ})/\lambda^{circ}$ as a function of the amplification factor λ^{circ}.

the rupture front for critically stressed faults ($\lambda \gg 1$):

$$a(t) \approx \sqrt{\frac{2\alpha t}{(1-\nu)T}}, \quad b(t) \approx \sqrt{\frac{(1-\nu)2\alpha t}{T}}, \tag{3.28}$$

and for marginally pressurized faults ($\lambda \ll 1$):

$$a(t) \approx \sqrt{\frac{3-\nu}{3-2\nu}}\sqrt{\alpha t} \cdot e^{(2-\gamma-T)/2}, \quad b(t) \approx \sqrt{\frac{3-2\nu}{3-\nu}}\sqrt{\alpha t} \cdot e^{(2-\gamma-T)/2}. \tag{3.29}$$

Since the rupture front is quasi-elliptical, equations (3.28) and (3.29) fully define the spatiotemporal evolution of the rupture front $\mathscr{R}(t)$ for the end-member cases.

Non-axisymmetric slip profiles and accumulated fault slip at the injection point

The non-axisymmetric self-similar slip profiles are unique for a given combination of T and ν. Some typical slip profiles along the x-axis (normalized by $a(t)$) are shown in Figures 3.7a-b for different values of the stress-injection parameter T and $\nu = 0.3$. The accumulated fault slip at the injection point $\delta(r = 0, t)$ is plotted in Figure 3.7c for all simulations as a function of the stress-injection parameter T and the Poisson's ratio ν. In Figure 3.7c, we include the circular
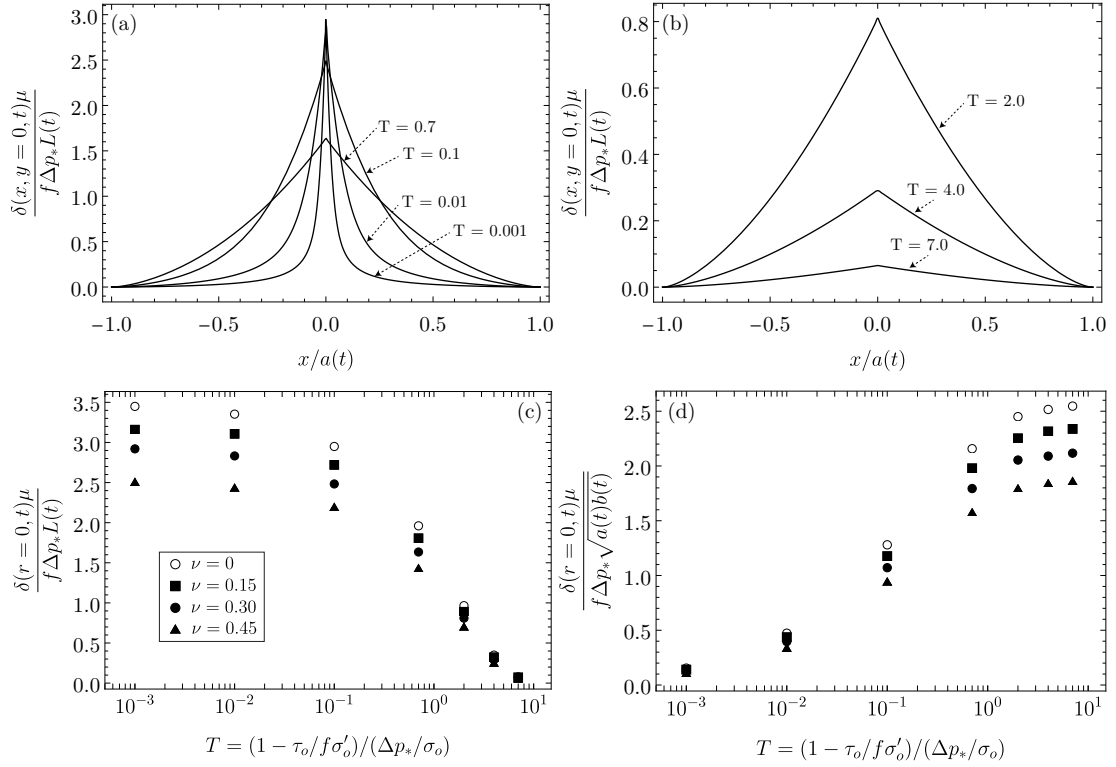
Figure 3.7: (a) and (b) Self-similar slip profiles along the x-axis (normalized by $a(t)$) for different values of the stress-injection parameter T and for $\nu = 0.3$. (c) and (d) Normalized accumulated fault slip at the injection point as a function of the stress-injection parameter T for different values of the Poisson's ratio, scaled by $L(t)$ and $R(t) = \sqrt{a(t)b(t)}$, respectively.

rupture case ($\nu = 0$) and $\delta(r = 0, t)$ is further normalized in Figure 3.7d by the geometric mean $\sqrt{a(t)b(t)}$ which is Poisson's ratio-independent and in the limit of $\nu \to 0$ corresponds to the rupture radius $R(t)$.

Figures 3.7c-d shows that the accumulated fault slip at the injection point decreases for increasing values of the Poisson's ratio. In addition, we recover a similar scaling for $\delta(r = 0, t)$ that in the circular rupture case: $\delta(r = 0, t) \sim f \Delta p_* R(t)/\mu$ in the marginally pressurized limit, with the characteristic rupture scale $R(t)$ taken as $\sqrt{a(t)b(t)}$ in Figure 3.7d; and $\delta(r = 0, t) \sim f \Delta p_* L(t)/\mu$ in the critically stressed limit.

3.3.5 Aseismic moment

The scalar moment release M_0 is a key measurement in seismology to quantify the potency of a rupture (Aki & Richards, 2002). In our planar fault model with a uniform direction of slip δ, the time-dependent aseismic moment (we focus on the case of a circular rupture) is $M_0(t) = 2\pi\mu \int_0^{R(t)} \delta(r, t) r \, dr$, where $R(t)$ is the evolving rupture radius. We can thus compute the aseismic moment numerically for all the seven values of T considered. Furthermore, we

can use the asymptotic solutions of the slip distribution, equations (3.19) and (3.20), to derive closed-form expressions for the limiting behaviors of the aseismic moment. We obtain that

$$M_0(t) \approx \frac{16}{9} f \Delta p_* R^3(t) \tag{3.30}$$

in the marginally pressurized limit, and

$$M_0(t) \approx \frac{8}{3} f \Delta p_* L^2(t) R(t) \tag{3.31}$$

in the critically stressed limit.

Both previous equations provide the proper scaling of the aseismic moment. We use these scalings to normalized the numerical results that are presented in Figure 3.8 as a function of the stress-injection parameter T. In this figure, we include the corresponding prefactors of equations (3.30) and (3.31). Note that the prefactor 8/3 in the critically stressed limit is in good agreement with the numerical solution, despite the slip profile being approximated by the "outer" asymptotic solution of this limit only.

Moreover, equations (3.30) and (3.31) allow us to establish the corresponding scaling relation between the moment release M_0 and the injected volume V that has been extensively sought with the purpose of constraining the magnitude of injection-induced earthquakes (McGarr, 2014; van der Elst et al., 2016; Galis et al., 2017; McGarr & Barbour, 2018). Because $R(t) = \lambda L(t)$, $L(t) = \sqrt{4\alpha t}$ and $V(t) = Q_w t$, the aseismic moment M_0 scales to the injected volume V as

$$M_0 \propto V^{3/2}. \tag{3.32}$$

3.4   Non-self-similar rupture growth due to injection at constant pressure

3.4.1   Scaling and similarity

Under the scenario of constant pressure injection, the evolution of fluid pressure given by equation (3.6) is no longer self-similar. This is due to the presence of a finite wellbore radius r_w where the pressure is set constant which introduces a new characteristic length in the problem. As a result, the frictional rupture will not evolve self-similarly, like for a constant injection rate. We recall that self-similar solutions always correspond to idealized models in which the dimensional parameters of the independent variables (space and time in our case) are equal to zero or infinity (Barenblatt, 1996). The infinitesimal nature of the constant-volume-rate fluid source of the previous section and its subsequent self-similarity, can be seen in fact as an intermediate-asymptotic behavior of a more realistic physical system in which both the fluid source and the domain are finite. In this view, the solution of Section 3.3 is valid for times $t \gg r_*^2/\alpha$, where r_* is the characteristic length of the fluid source, and for $t \ll R_*^2/\alpha$, where R_*
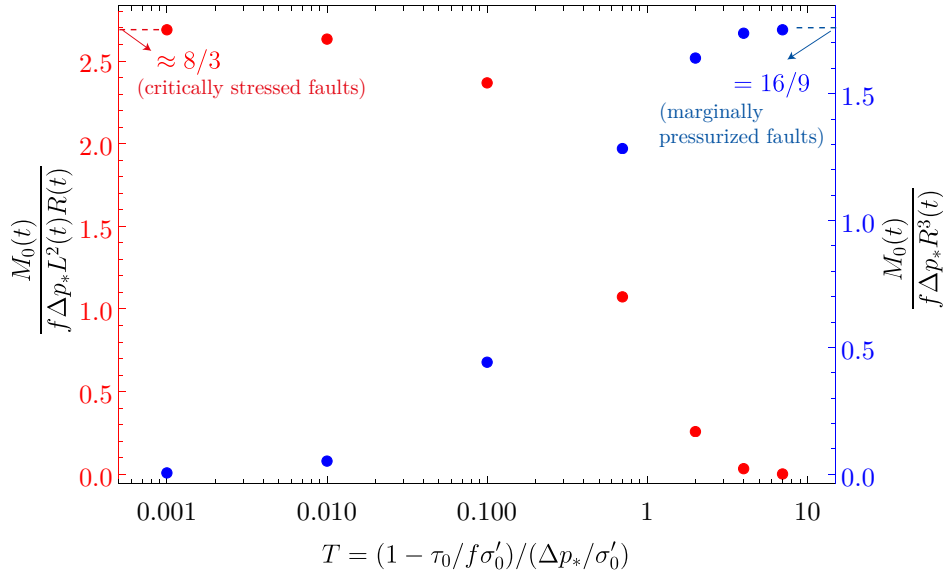
Figure 3.8: Normalized aseismic moment for circular ruptures ($\nu = 0$) as a function of the stress-injection parameter T. Numerical results and asymptotic behaviors for critically stressed ($T \ll 1$, $\lambda \gg 1$) and marginally pressurized ($T \gg 1$, $\lambda \ll 1$) faults.

is the characteristic length of a finite domain. Note that the introduction of, for instance, a frictional lengthscale in the self-similar problem of injection at constant volume rate, would also cause the loss of self-similarity in the model.

The scaling thus differs slightly from the scaling of the previous section. The finite wellbore radius r_w introduces a characteristic diffusion timescale $t_c = r_w^2/\alpha$ with α the fault hydraulic diffusivity, such that we obtain:

$$\frac{t}{t_c} \to t, \ \frac{\vec{x}}{r_w} \to \vec{x}, \ \frac{\tau - f\sigma'_o}{f\Delta p_w} \to \tau, \ \frac{\delta}{\delta_c} \to \delta, \ \frac{p - p_0}{\Delta p_w} \to p, \tag{3.33}$$

where Δp_w is the constant overpressure imposed at the wellbore, and $\delta_c = f\Delta p_w r_w/\mu$ is the characteristic slip.

As already mentioned, the loss of self-similarity is due to the finite size of the wellbore. In fact, radial flow from an infinitesimal fluid source at constant pressure is not physically possible. Injection of a finite volume from an infinitesimal fluid source in such geometrical conditions always leads to infinite pressure.

The dimensionless solution of the problem depends now on three dimensionless parameters, a slightly different stress-injection parameter T that is a function of the constant wellbore overpressure Δp_w

$$T = \frac{1 - \tau_o/f\sigma'_o}{\Delta p_w/\sigma'_o}, \tag{3.34}$$

the Poisson's ratio ν, and the dimensionless time $\alpha t / r_w^2$.

The limiting values of T are determined by the condition for fault slip activation, $f \Delta p_w \geq f \sigma_o' - \tau_o$, and the condition for no slip prior to injection, $f \sigma_o' - \tau_o > 0$. Together, these conditions imply that T varies between 0 and 1, so that the stress-injection parameter is now upper bounded, unlike the case of injection at constant volume rate in which T can theoretically go up to $+\infty$.

The limit of $T \to 1$ is characterized by the condition $f \Delta p_w \to f \sigma_o' - \tau_o$. This condition can be interpreted as a scenario in which the pressure at the fluid source, Δp_w, is just enough to activate fault slip. This is the reason why such end-member case has been named in prior studies as marginally pressurized faults (Garagash & Germanovich, 2012; Bhattacharya & Viesca, 2019; Viesca, 2021). On the other hand, considering that Δp_w is always positive and finite, the limit of $T \to 0$ is associated with the condition $\tau_0 \to f \sigma_0'$. This condition represents the case of faults that are about to fail before injection, and is thus named as critically stressed faults. Unlike the problem of injection at constant volume rate in which the fluid pressure near the injection point is always increasing, here the pressure at the wellbore is fixed and thus the terminology of critically stressed and marginally pressurized faults is unambiguous. Note that $\sigma_0' > \Delta p_w > 0$, with the upper bound being the transition to fault opening that we do not cross in this study.

3.4.2   Approximate analytical solution for circular ruptures

The solution of the diffusion equation for injection at constant pressure from a finite source, equation (3.6), does not allow to treat the problem of a circular rupture analytically. Nevertheless, as we are interested in solutions for times that are in general large compared to the characteristic diffusion time, $t_c = r_w^2 / \alpha$, we can use the following asymptotic expansion for the instantaneous pressure profile that is valid for $t \gg t_c$ (Jaeger, 1955)

$$\Pi(r, t) \approx 1 - 2\ln(\bar{r}) \left\{ \frac{1}{\ln(4\bar{t}) - 2\gamma} - \frac{\gamma}{(\ln(4\bar{t}) - 2\gamma)^2} \right\} \tag{3.35}$$

where $\bar{r} = r / r_w$ and $\bar{t} = \alpha t / r_w^2$ are the dimensionless radial coordinate and the dimensionless time, respectively, and $\gamma = 0.577216...$ is the Euler-Mascheroni's constant.

Figure 3.9a shows the comparison between the 'exact' numerical solution for the fluid pressure profile, equation (3.6) (solved via numerical inversion of the Laplace transform, Stehfest, 1970) and the asymptotic expansion (3.35). In Figure 3.9a, we also include an asymptotic expansion of $\Pi(r, t)$ with higher order corrective terms that are function of $\bar{r}$ and the successive time derivatives of the terms in curly brackets in (3.35) (Jaeger, 1955). The higher order terms have cumbersome expressions but are necessary to capture the "near front" behavior of the fluid pressure profile as shown in Figure 3.9a. However, for the sake of simplicity, we neglect these corrective terms in the following.

Similarly to the case of injection at constant volume rate, we define the instantaneous rupture radius $R(t)$ and use the condition for quasi-static propagation of a circular crack with zero fracture energy under axisymmetric shear load, equation (3.10), with now $\Delta\tau(r,t) = \tau_o - f\left(\sigma'_o - \Delta p_w \Pi(r,t)\right)$. After some algebraic operations, this propagation condition can be rewritten as

$$\frac{1}{R(t)} \int_0^{R(t)} \frac{\Pi(r,t)}{\sqrt{R(t)^2 - r^2}} r\,\mathrm{d}r = T \tag{3.36}$$

where T is the stress-injection parameter defined in equation (3.34) for the constant pressure injection case. We approximate $\Pi(r,t) = \left(p(r,t) - p_0\right)/\Delta p_w$ by the asymptotic expansion (3.35). Note that in equation (3.35), one could consider to drop the term of $O\left(1/\ln(\bar{t})^2\right)$ and use a first order approximation for $\Pi(r,t)$ instead; however, we found that better results are systematically obtained by keeping the second order term in any further mathematical operation and performing first order approximations afterwards.

The integration limits of equation (3.36) have to be considered carefully, since the asymptotic expansion for $\Pi(r,t)$ gives non-physical values that are greater than unity for $r/r_w < 1$ and negative for r/r_w beyond the intersection with the abscissa (see Figure 3.9a). In fact, the intersection with the abscissa defines conveniently a nominal position of the fluid pressure front, $\tilde{L}(t)/r_w = \exp(-(1/2)\left(2\gamma - \ln\left(4\bar{t}\right)\right)^2 / \left(3\gamma - \ln\left(4\bar{t}\right)\right))$, that is given at the first order by

$$\tilde{L}(t) = \sqrt{c_1 \alpha t} \tag{3.37}$$

where $c_1 = e^{\ln(4)-\gamma} = 2.245838... \approx 2.25$. The position of the fluid pressure front $\tilde{L}(t)$ given by equation (3.37) is shown in Figure 3.9a at different dimensionless times. With a change of variable $s = r/R$ and taking care of the integration limits as discussed before, we can rewrite equation (3.36) in dimensionless form as

$$\int_0^{\beta_0} \frac{1}{\sqrt{1-s^2}} s\,ds + \int_{\beta_0}^{\beta} \frac{\Pi(sR,t)}{\sqrt{1-s^2}} s\,ds = T \tag{3.38}$$

where $\beta_0 = r_w/R$, and $\beta = 1$ if $R \le \tilde{L}$, or $\beta = \tilde{L}/R$ otherwise $(R > \tilde{L})$.

Equation (3.38) can be solved to obtain the evolution of the normalized rupture radius $R(t)/r_w$ as a function of the dimensionless time $\alpha t/r_w^2$ and the stress-injection parameter T. The solution is piecewise due to the piecewise definition of β that indeed separates the two possible rupture regimes. One regime is characterized by $R(t) < \tilde{L}(t)$ which represents a rupture front that lags the fluid pressure front, whereas the other regime is characterized by $R(t) > \tilde{L}(t)$ in which the rupture front outpaces the fluid pressure front.

In addition, the first integral of the left-hand side of equation (3.38) can be neglected if we assume that the rupture radius $R(t)$ is much bigger than the wellbore radius r_w, so that $\beta_0 = r_w/R \ll 1$. Hereafter, we consider $\beta_0 = 0$. Let us first consider the case in which $R(t) < \tilde{L}(t)$. After integrating equation (3.38) with $\beta = 1$, we obtain at the first order the following explicit
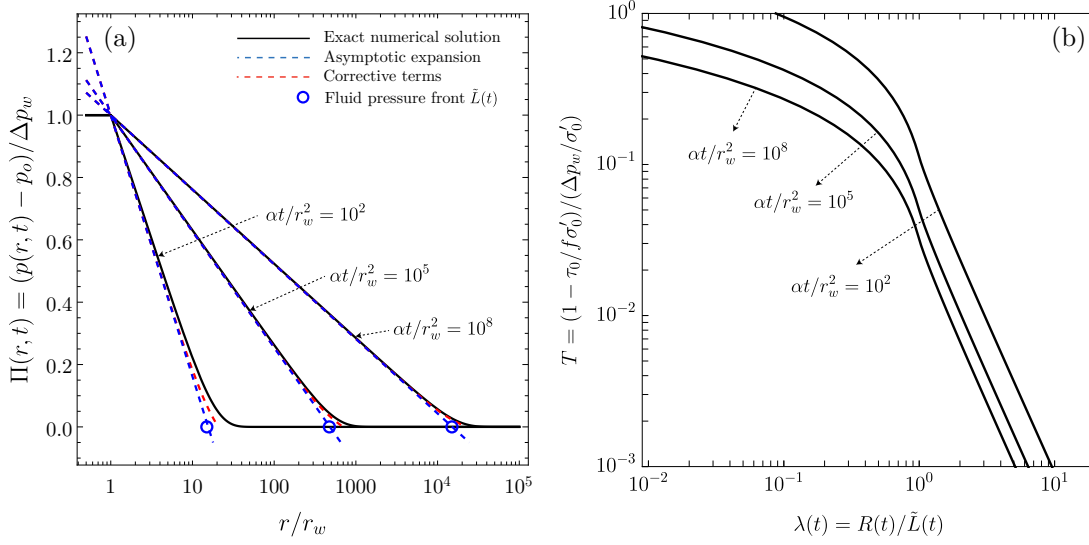
Figure 3.9: (a) Instantaneous spatial profile of fluid pressure for injection at constant pressure, $\Pi(r, t)$, as function of the dimensionless radial coordinate r/r_w at different dimensionless times $\alpha t/r_w^2$. Comparison between the exact solution given by equation (3.6), the asymptotic expansion (3.35) valid for $\alpha t/r_w^2 \gg 1$, and an asymptotic expansion with higher order corrective terms (Jaeger, 1955). (b) Approximate analytical solution for circular ruptures driven by injection at constant pressure, given by the amplification factor $\lambda(t) = R(t)/\tilde{L}(t)$ as a function of the stress-injection parameter T at different dimensionless times $\alpha t/r_w^2$.

expression for the evolution of the normalized rupture radius in the form of a power-law

$$R(t)/r_w = g(T) \left(\frac{\alpha t}{r_w^2} \right)^{(1-T)/2} \tag{3.39}$$

where $g(T) = c_2 e^{-c_3 T}$, with $c_2 = e^{(2-\gamma)/2} = 2.036825...$ and $c_3 = (\ln(4) - \gamma)/2 = 0.404539....$

Note that the transition between the two rupture regimes happens at a certain time t^* when $R(t^*) = \tilde{L}(t^*)$. Using the first-order equations (3.37) and (3.39), we obtain that this transition time is

$$\frac{\alpha t^*}{r_w^2} = \left(\frac{g(T)}{c_1} \right)^{2/T} \tag{3.40}$$

Finally, the solution for the case $R(t) > \tilde{L}(t)$ is obtained by integrating equation (3.38) with $\beta(t) = \tilde{L}(t)/R(t)$. The solution for the rupture radius is now implicit and it is given by

$$f_1(\beta) \ln(R(t)/r_w) + f_2(\beta) = \ln(\tilde{L}(t)/r_w)(f_1(\beta) - T) \tag{3.41}$$

40

where

$$f_1(\beta) = 1 - \sqrt{1 - \beta^2}, \text{ and } \quad f_2(\beta) = \ln\left(\frac{2\beta}{1 + \sqrt{1 - \beta^2}}\right) + \sqrt{1 - \beta^2}\left(1 - \ln(\beta)\right) - 1 \tag{3.42}$$

Equations (3.39) to (3.42) can be used to define a time-dependent amplification factor in the form $\lambda(t) = R(t)/\tilde{L}(t)$. Such approximate analytical solution for $\lambda(t)$ is plotted in Figure 3.9b at different dimensionless times, as a function of the stress-injection parameter T.

3.4.3   Numerical solution for circular ruptures

We now solve numerically for the case of circular ruptures to obtain the evolution of the axisymmetric slip profiles $\delta(r, t)$. In addition, the computation of the slip profiles allows us to calculate numerically the rupture radius $R(t)$ and test the accuracy of the approximate analytical solution derived in the previous section. For this purpose, we run six simulations for values of the stress-injection parameter $T = 0.01, 0.1, 0.3, 0.5, 0.7$, and 0.9 and set $\nu = 0$. We perform 9 fully implicit time steps per simulation for values of the dimensionless time logarithmically spaced between 1 to 10^8.

Axisymmetric slip profiles and accumulated fault slip at the rupture center

Figures 3.10a, 3.10b and 3.10c display the non-self-similar slip profiles for different values of the stress-injection parameter T. Since the solution is not self-similar, the dimensionless slip profiles are not unique for a single value of the stress-injection parameter, but rather time-dependent. Note that the slip profiles near the injection point are now smooth due to the finite size of the fluid source. On the other hand, Figure 3.10d shows the normalized accumulated fault slip at the center of the rupture $\delta(r = 0, t)$ as a function of the dimensionless time $\alpha t/r_w^2$ for different values of the stress-injection parameter T. This figure suggests that at large times $\delta(r = 0, t) \sim (f\Delta p_w/\mu)R(t)$, up to a factor 0.1 to 0.2 approximately, for the values of T considered.

Rupture radius and comparison with approximate analytical solution

Based on the numerical solution of the axisymmetric slip profiles $\delta(r, t)$, we compute the instantaneous rupture radius $R(t)$ at every time step for each simulation. We use the same procedure described in Section 3.3.3 for building the rupture front and computing the rupture radius. The results are plotted in Figure 3.11a together with the approximate analytical solution derived in the previous section.

The approximate analytical solution (valid for large times, $\alpha t/r_w^2 \gg 1$) is in good agreement with the numerical results for values of T ranging from 0.1 to 0.7, with an average relative difference of about 5%. Near the limit of a marginally pressurized fault ($T = 0.9$), the analytical solution is less accurate (average relative difference around 20%) due to the fact that
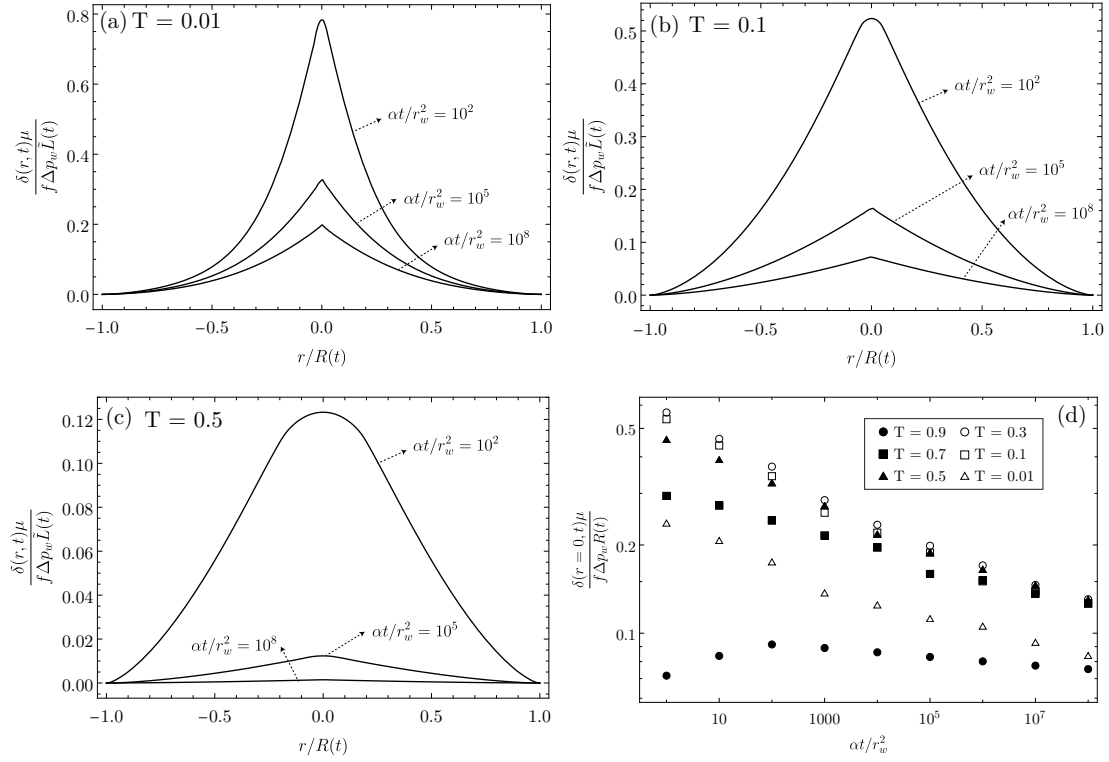
Figure 3.10: Non-self-similar normalized slip profiles for circular ruptures driven by injection at constant pressure as a function of the normalized radial coordinate $r/R(t)$ at different dimensionless times $\alpha t/r_w^2$. (a) Stress-injection parameter $T = 0.01$, (b) $T = 0.1$, (c) $T = 0.5$. (d) Normalized accumulated fault slip at the center of the rupture as a function of dimensionless time $\alpha t/r_w^2$ for different values of the stress-injection parameter T.
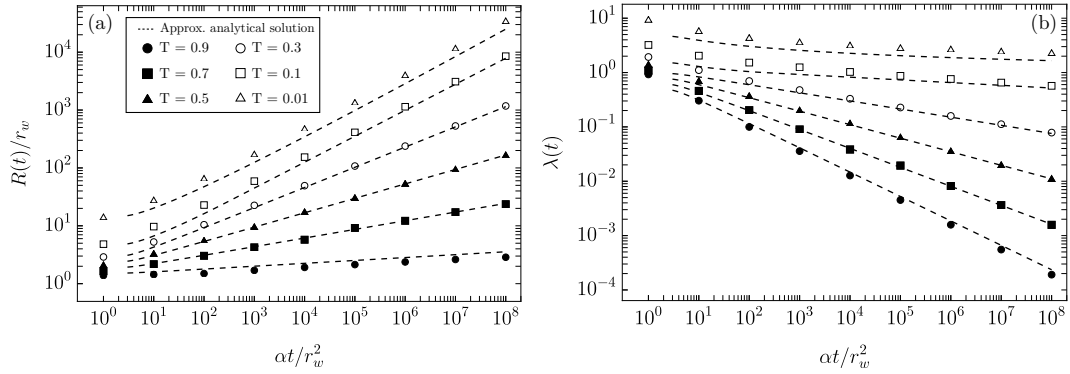
Figure 3.11: Comparison between numerical results and approximate analytical solution for circular ruptures driven by injection at constant pressure. (a) Dimensionless rupture radius $R(t)/r_w$ as a function of dimensionless time $\alpha t/r_w^2$ for different values of the stress-injection parameter T. (b) Same as (a) but for the time-dependent amplification factor $\lambda(t) = R(t)/\tilde{L}(t)$.

the assumption $R(t) \gg r_w$ is not properly satisfied. On the other hand, near the limit of a critically stressed fault ($T = 0.01$), the analytical solution loses accuracy possibly due to the fact that the "near front" behavior of the fluid pressure profile is not well captured by the asymptotic expansion, equation (3.35). The absolute value of the relative difference between the approximate analytical solution and the numerical results is around 30% in average.

Finally, Figure 3.11b displays the numerical results for the time-dependent amplification factor $\lambda(t) = R(t)/\tilde{L}(t)$ and the corresponding approximate analytical solution for it. Note that for values of $T \gtrsim 0.7$, the rupture lags the fluid pressure front at all times, whereas for $T \lesssim 0.01$ the rupture outpaces the fluid pressure front at all times considered here. The case of intermediate values, $0.5 \gtrsim T \gtrsim 0.1$, is interesting because a transition of propagation regime occurs at early times.

3.4.4   Numerical solution for non-circular ruptures

Finally, we solve numerically for the more general case where the Poisson's ratio is different than zero. We run 12 simulations for four values of the stress-injection parameter $T = 0.1$, 0.3, 0.5, and 0.7, plus three values of the Poisson's ratio $\nu = 0.15$, 0.30, and 0.45.

Similarly to the case of injection at constant volume rate, the simulations show that ruptures evolve systematically in a nearly elliptical shape. We thus define the rupture front $\mathscr{R}(t)$ according to the equation of an ellipse (equation (3.23)), and compute the semi-major $a(t)$ and semi-minor $b(t)$ axes of the elliptical front following the same procedure described in Section 3.3.4. Figure 3.12a shows the temporal evolution of the aspect ratio $a(t)/b(t)$ for $\nu = 0.3$ and different values of the stress-injection parameter T. It can be observed that for values of T closer to zero (critically stressed faults), the aspect ratio decreases over time and tends to a constant value at large times, whereas for values of T closer to one (marginally pressurized
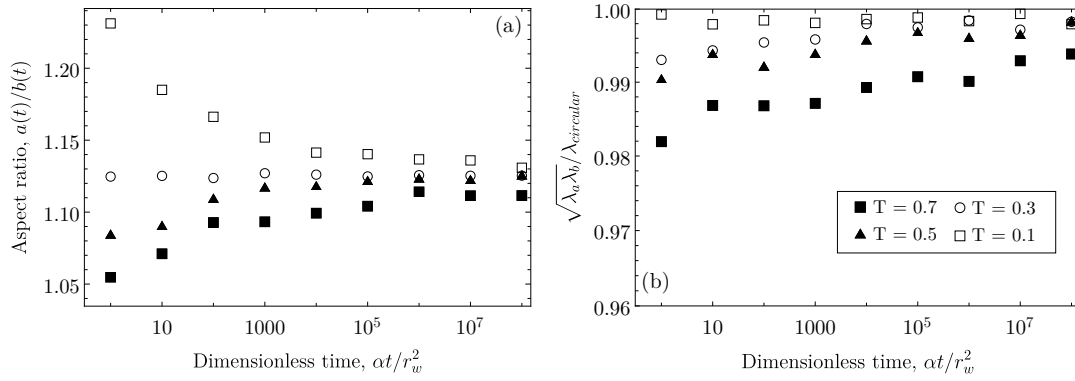
Figure 3.12: (a) Aspect ratio a/b as a function of dimensionless time $\alpha t/r_w^2$ for different values of the stress-injection parameter T. (b) Geometric mean $\sqrt{\lambda_a(t)\lambda_b(t)}$ for $\nu = 0.3$ divided by the amplification factor for circular ruptures ($\nu = 0$), $\lambda_{circular}$, as a function of dimensionless time $\alpha t/r_w^2$ for different values of the stress-injection parameter T.

faults), the aspect ratio increases over time and tends at large times to a constant value as well. Finally, for intermediate values of T, the aspect ratio is nearly constant (see results for $T = 0.3$).

Figure 3.12b displays the ratio between the geometric mean $\sqrt{\lambda_a(t)\lambda_b(t)}$ for $\nu = 0.3$, where λ_a and λ_b are defined as $\lambda_a(t) = a(t)/\tilde{L}(t)$ and $\lambda_b(t) = b(t)/\tilde{L}(t)$, respectively, and the numerical values of the amplification factor $\lambda(t)$ for the circular rupture case ($\nu = 0$). We observe that like the case of injection at constant volume rate, the (now time-dependent) geometric mean $\sqrt{\lambda_a\lambda_b}$ is almost equal to the amplification factor $\lambda(t)$ for circular ruptures, meaning that the rupture areas for the values of $\nu = 0$ and $\nu = 0.3$ are approximately the same for the values of T considered here.

3.5 Discussions

3.5.1 Comparison between 2-D and 3-D models

We examine here the differences between our 3-D model and its counterpart in 2-D. In the two-dimensional case, the diffusion of fluid pressure along the one-dimensional frictional interface is self-similar under both injection scenarios (constant volume rate and constant pressure) when considering a fluid point source (Carslaw & Jaeger, 1959). The solution in 2-D elasticity for the evolution of the crack length under injection at constant pressure was presented by Bhattacharya and Viesca (2019) and Viesca (2021). They showed that the amplification factor $\lambda = \ell(t)/\ell_d(t)$, where $\ell(t)$ is the position of the crack tip (equal to the half-crack length) and $\ell_d(t)$ is a nominal position of the fluid pressure front, is time-invariant and depends only on the stress-injection parameter T (equation (3.34)). Interestingly, we found qualitatively the same response in our 3-D model but for injection at constant volume rate.

On the other hand, the solution of the 2-D model for injection at constant volume rate has not

been presented yet. We derive such solution in Section 3.7.4 and found that the amplification factor λ is time-dependent (and hence, not self-similar) and follows

$$\exp\left(-\lambda^2/2\right)\left[\left(1+\lambda^2\right) I_0\left(\lambda^2/2\right) + \lambda^2 I_1\left(\lambda^2/2\right)\right] - 2\lambda/\sqrt{\pi} = x_c/\ell_d, \tag{3.43}$$

where $\ell_d = \sqrt{4\alpha t}$ and $x_c = \sqrt{4\pi} k \left(f\sigma'_o - \tau_o\right) / f q_w \eta$. I_0 and I_1 are the modified Bessel functions of the first kind of zero and first order, respectively. Equation (3.43) represents a unique relation between the amplification factor λ and the ratio between the position of the fluid pressure front ℓ_d and the characteristic length x_c, which is plotted in Figure 3.13a together with the corresponding asymptotes for small λ (short-run-out rupture regime) and large λ (long-run-out rupture regime, details in Section 3.7.4).

The characteristic length x_c corresponds to the position of the fluid pressure front at the onset of crack growth (activation of slip or crack nucleation). Upon crack initiation, the rupture lags the fluid pressure front and expands faster than the diffusion of fluid pressure. The crack catches the fluid pressure front ($\lambda = 1$) when the normalized fluid pressure front $\bar{\ell}_d \approx 3.1435$ or, in other words, when the fluid pressure front ℓ_d has grown approximately three times the size x_c necessary for the crack to start growing. After that, the rupture outpaces the fluid pressure front and the crack keeps propagating faster than the diffusion of fluid pressure until it reaches a steady propagation regime that is characterized by a constant rupture speed V_R equal to (see Section 3.7.4)

$$V_R = \frac{f\alpha q_w \eta}{\pi k \left(f\sigma'_o - \tau_o\right)}, \tag{3.44}$$

where q_w $[L/T]$ is the constant injection volume rate per unit fault thickness w_h and unit out-of-the-plane length b, such that $q_w = Q_w / w_h b$ with Q_w the injection volume rate $\left[L^3/T\right]$.

The temporal evolution of the crack half length can be seen directly in Figure 3.13b, in which the analytical solution is recast in terms of dimensionless half-crack length and dimensionless time. Here, the short-run-out regime translates into an early-time solution that is valid for t near $x_c^2/4\alpha$, and a late-time solution that is approached asymptotically in the limit $t \gg x_c^2/4\alpha$.

This response of the 2-D model under constant rate of injection has no analog in 3-D. Injection at constant volume rate in the 3-D model leads to a rupture speed that decreases with the squared root of time, $V_R = \lambda\sqrt{\alpha/t}$ (Equation (3.18)). Moreover, the relative position of the rupture front and the fluid pressure front is time-invariant in 3-D.

Our analysis shows that the response of the 2-D and 3-D models under the same injection scenario are different even qualitatively. These differences have to be carefully considered when linking theoretical and numerical predictions to laboratory measurements and field observations in which, generally, 3-D models prevail.
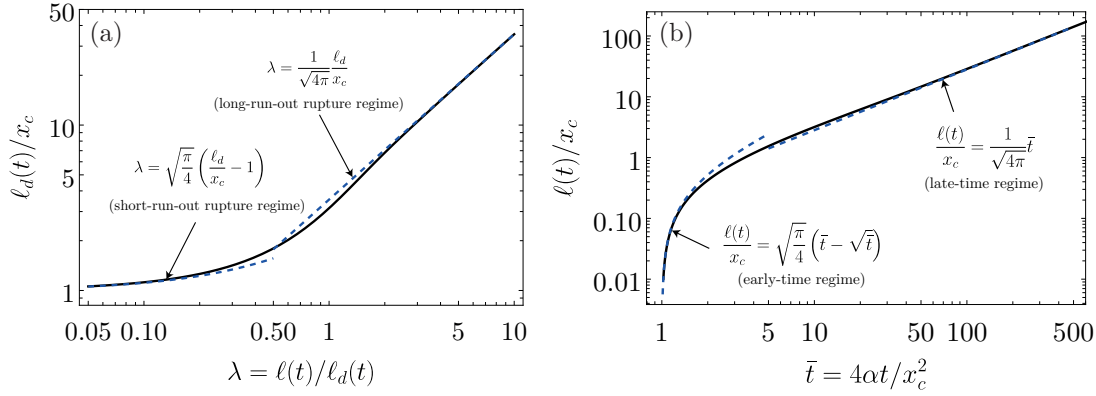
Figure 3.13: Analytical solution for a frictional shear crack in 2-D elasticity driven by injection at constant volume rate from a point source. (a) Ratio between the position of the fluid pressure front ℓ_d and the position of the fluid pressure front at the onset of crack growth x_c, with $\ell_d = \sqrt{4\alpha t}$ and $x_c = \sqrt{4\pi} k \left(f\sigma'_o - \tau_o \right)/f q_w \eta$, versus the amplification factor $\lambda = \ell(t)/\ell_d(t)$ (solid black curve), where $\ell(t)$ is the half-crack length. Dashed blue curves correspond to the asymptotes of the short-run-out ($\lambda \ll 1$) and long-run-out ($\lambda \gg 1$) rupture regimes. (b) Dimensionless half-crack length $\ell(t)/x_c$ versus dimensionless time $\bar{t} = (\ell_d/x_c)^2 = 4\alpha t/x_c^2$ (solid black curve). Dashed blue curves correspond to the same asymptotes of panel (a) but in terms of dimensionless half-crack length and time, which show themselves in this plot as early-time and late-time solutions.

3.5.2 Assumption of constant friction

In the context of rock friction and earthquake mechanics, laboratory-derived friction laws (Dieterich, 1979; Ruina, 1983) have been widely used to describe the entire spectrum of slip rates in natural faults (Scholz, 2019). These empirical friction laws capture the dependence of friction on slip rate and the history of sliding (via a state variable) as observed during velocity-step laboratory experiments on bare rock surfaces and simulated fault gouge (Marone, 1998). It seems then interesting to discuss under what conditions a constant friction coefficient can mimic more complex models of fluid-driven frictional ruptures with rate-and-state friction.

Results in 2-D antiplane elasticity of fluid-driven fault slip propagating on a strengthening (aging) rate-and-state frictional interface have been notably reported by Dublanchet (2019), for the case of injection of fluid at a constant volume rate. Two distinct regimes of crack propagation were observed in Dublanchet's numerical simulations (following a first initial phase of slip rate acceleration): a stable crack growth that tends ultimately to a constant rupture speed, and an unstable crack growth in which the rupture speed blows up in a finite time. He observed that what determines the stable/unstable fault response is the sign of the difference between the residual shear stress left within the crack τ_r and the initial shear stress resolved on the fault plane τ_o. If $\tau_r - \tau_o > 0$ (a condition that is guaranteed in a constant-friction model), crack propagation is always stable, whereas if $\tau_r - \tau_o < 0$, the crack may evolve towards an instability. Such ultimate stability condition can be indeed understood under the

classic Griffith energy-balance and the small scale yielding approximation (Rice, 1968), as performed by Garagash and Germanovich (2012) for a fluid-driven slip-weakening frictional shear crack in 2-D.

The stable regime of crack propagation found by Dublanchet (2019) is indeed the most relevant in the context of aseismic ruptures. Furthermore, during such stable propagation regime, Dublanchet noticed that the crack behaves exactly as if it were governed by a constant friction coefficient within the slipping patch. This is because in that regime, the leading-order terms of the quasi-static elastic equilibrium are the nonlocal stress transfer along the fault and the effect of fluid pressure change on reducing the constant part of the shear strength in the rate-and-state friction law. It is not surprising then that our 2-D model of a constant-friction shear crack derived in the Section 3.7.4 and summarized in Figure 3.13, shows qualitatively the same response (under the same injection scenario), notably the ultimate steady crack propagation regime characterized by a constant rupture speed V_R. In our 2-D model, $V_R \propto f\alpha q_w/(f\sigma'_o-\tau_o)$ (see equation (3.44)), which depends on the constant friction coefficient f, hydraulic diffusivity α, injection rate q_w, and residual τ_r and initial τ_o shear stress, in the same form as in the rate-and-state model (Eq. 23 in Dublanchet, 2019), considering that $f\sigma'_o$ is the residual shear strength in the constant-friction model.

A similar result, also in 2-D elasticity, has been recently obtained by Garagash (2021) using a different approach. He developed a Griffith-energy-balance-like equation of motion for the evolution of crack length on rate-and-state faults that he then applied to the study of slip transients due to point-force-like fluid injections. He notably showed that for injection at constant volume rate on neutrally and under-stress (with regard to the ambient slip rate) strengthening rate-and-state faults (obeying the slip law), the frictional ruptures expand initially within the limits of the pressurized fault patch and move faster than the latter, until they eventually outpace the fluid pressure front and reach also a terminal steady propagation regime characterized by a constant rupture speed. This response is again qualitatively the same of our 2-D model of a constant-friction shear crack, and the same found by Dublanchet (2019) for the stable propagation regime. Moreover, as pointed out by Garagash (2021), the ultimate behavior of the crack under these conditions is due to the diminishing effect of rate-and-state fracture energy in the Griffith energy balance compared to the effect of the fluid injection (in the energy release rate) with increasing rupture size, such that, in the limit of large-run-out rupture, the crack behaves as having zero toughness, which is the case of a friction coefficient that is constant.

Our discussion in 2-D elasticity suggests that the assumption of a constant friction coefficient describes to first order the behavior of rate-and-state friction under conditions that are relevant for the study of fluid-driven aseismic ruptures (rate-strengthening in both aging and slip laws, and approaching the large-run-out rupture regime or late time solution), in which the frictional fracture energy can be neglected. We expect our results in 3-D to provide also first-order descriptions of fluid-driven aseismic ruptures in the context of rate-and-state friction, yet this assumption remains to be confirmed in future studies.

3.5.3 Implications to injection-induced seismicity

As suggested by a number of experimental and observational studies (Hamilton & Meehan, 1971; Scotti & Cornet, 1994; Bourouis & Bernard, 2007; Guglielmi et al., 2015; Wei et al., 2015; Chen et al., 2017; Duboeuf et al., 2017; Cappa et al., 2019; Eyre et al., 2019), aseismic slip seems to be a frequent result of fluid injections into the subsurface and might play a significant role in injection-induced seismicity related to hydrocarbon and geothermal operations. It is thought that fluid motion drives aseismic slip which in turn transmits solid stresses that trigger part of the observed induced seismicity (Guglielmi et al., 2015; Wei et al., 2015; Duboeuf et al., 2017; Bhattacharya & Viesca, 2019; Eyre et al., 2019). Our results open the possibility of quantifying this triggering mechanism in a three-dimensional scenario that is more realistic than previous two-dimensional models for fluid-driven aseismic fault slip (Bhattacharya & Viesca, 2019; Dublanchet, 2019; Eyre et al., 2019; Garagash, 2021; Viesca, 2021).

First, we note that injection protocols generally consist of a series of injections conducted at a constant volume rate. Results of Section 3.3 are thus more relevant for geo-energy applications. In particular, we showed that aseismic slip induced by injection at constant volume rate is self-similar in a diffusive manner. As a consequence, the rupture front expands proportionally to the square root of time in the same way as the fluid pressure front does. Induced seismicity that is commonly considered to be driven by the direct effect of fluid pressure increase due to the square-root-of-time feature of seismicity clouds (S. Shapiro et al., 1997; S. Shapiro et al., 2005), might instead be controlled by the stress transfer of a propagating aseismic rupture (Bhattacharya & Viesca, 2019). This would notably be the case of critically stressed fractures and faults in which the rupture front is predicted to be systematically ahead of the fluid pressure front. Our results suggest that assessing whether seismicity is induced by aseismic-slip stress transfer or fluid pressure increase might not be possible from the observation of square root time dependence of seismicity front alone.

Our model is, of course, idealistic in the sense that it represents a single and isolated fracture or fault in 3-D. Nonetheless, recent two-dimensional simulations of fluid induced aseismic slip in fractured rock masses have shown that the same patterns predicted by a single fracture in 2-D emerge collectively for a set of fractures (Ciardo & Lecampion, 2023). Notably, a collective aseismic slip front outpaces the migration of fluids when the fracture network is in the critically stressed regime in a global sense (Ciardo & Lecampion, 2023). In addition, field observations indicate critically stressed fractures/faults are likely to be preferred, high-permeability, conduits of fluid flow than the fractures and faults that are not optimally oriented with regard to the stress field (Barton et al., 1995). Together, these observations suggest that seismicity triggered by injection-induced aseismic slip might be indeed a general feature of reservoir rocks in response to fluid injections.

Moreover, if aseismic slip is the dominant mechanism for the triggering of seismicity, current estimates of reservoir hydraulic diffusivity α based on spatio-temporal seismicity patterns (S. Shapiro et al., 1997) might be rather related to the quantity $\alpha\lambda^2$ (see equation (3.26)), with λ

being an equivalent amplification factor of the fractured rock mass. Such amplification factor would be intrinsically dependent not only on hydraulic properties of the fracture network, but also on the distribution of fracture orientations with regard to the stress field and the rate of injection. To illustrate this point, let us consider characteristic values for a fracture/fault located at around 3 km depth with $\sigma_o' \sim 50$ [MPa]. Assume the fracture is close to the critically stressed limit, say $1 - \tau_o/f\sigma_o' \sim 0.1$, plus an injection rate $Q_w \sim 30$ [l/s] (typical of deep geothermal projects) and fluid dynamic viscosity $\eta \sim 10^{-3}$ [Pa·s]. The fracture/fault hydraulic transmissivity kw_h can vary over several orders of magnitude (e.g., Wibberley and Shimamoto, 2003). Consider, for instance, a plausible range $kw_h \sim 10^{-13} - 10^{-15}$ [m^3]. The resulting range for the stress-injection parameter is $T \sim 0.002 - 0.2$, which leads to an amplification factor $\lambda \sim 1.6 - 15.8$. If aseismic slip would be the dominant mechanism in this hypothetical case, estimates of α based on the squared root dependence of a purely pore-pressure-driven triggering mechanism would be off (over-predicted) by a factor $\lambda^2 \sim 2.5 - 250$.

Another finding of our study is related to the scaling relation between the aseismic moment release M_0 and the accumulated injected volume of fluid V. This type of relation has been extensively sought with the purpose of constraining the magnitude of injection-induced earthquakes based on operational parameters (McGarr, 2014; van der Elst et al., 2016; Galis et al., 2017; McGarr & Barbour, 2018). We found that the aseismic moment scales to the injected volume of fluid as $M_0 \propto V^{3/2}$, for injection at constant volume rate. Interestingly, the same power-law scaling has been found for self-arrested injection-induced seismic ruptures based on fully-dynamic rupture simulations and fracture mechanics arguments (Galis et al., 2017). We emphasize that our scaling relation is derived for purely aseismic (quasi-static) ruptures, whereas the relation found by Galis et al. (2017) represents seismic (dynamic) events.

3.5.4   Implications to seismic swarms and aftershock sequences

Seismic swarms and aftershock sequences are often characterized by diffusive spatiotemporal patterns that are thought to be caused by naturally injected fluids into fault zones (Bosl & Nur, 2002; Miller et al., 2004; Parotidis et al., 2005; Chen et al., 2012; Hainzl et al., 2016; Z. Ross et al., 2017; Z. Ross et al., 2020). Moreover, natural fluid releases are likely represented by the sudden increase of injection rate at the fluid source origin followed by stabilization towards a constant rate. This might be the case of, for instance, breaking an initially sealed and highly-pressurized reservoir. Of course, after a certain period of injection at approximately constant rate, the rate of injection has to decrease until the pressure at the initially highly-pressurized fluid source equilibrates the fluid pressure of the surroundings; we neglect the rupture growth during that stage and also after injection ceases. Our results for sustained injection at constant volume rate can be thus discussed in the context of natural fluid-driven seismicity in seismic swarms episodes and aftershock sequences.

Indeed, the previous discussion on injection-induced aseismic slip in fractured rock masses is easily extendable to fault zones. Notably, seismicity is expected to be now constrained

into a relatively well-defined fault plane of thickness that equals the size of the damage zone. Observed seismicity would be the result of instabilities that occur either in the main fault plane or in the fracture network of the damage zone. Similarly to the case of a fractured rock mass, the triggering of seismicity by aseismic-slip stress transfer would depend on how critically stressed the main fault plane or the damage zone fracture network is. The square root time migration of seismicity might be insufficient to discriminate whether aseismic slip or elevated fluid pressure is the direct triggering mechanism. Likewise, estimates of fault hydraulic diffusivity α based on seismicity patterns might rather represent the quantity $\alpha \lambda^2$.

3.5.5   Permeability variations

Our model assumes that fluid flow occurs within a frictional interface characterized by a constant hydraulic transmissivity. However, permeability changes due to variations of the effective normal stress or, equivalently, the normal interfacial deformation/closure, are well-documented in the fracture/joint rock mechanics literature (e.g., Bandis et al., 1983) and fault mechanics literature as well (e.g., Rice, 1992). In addition, fracture/fault dilatant-behavior can also induce significant permeability variations (e.g., Ciardo and Lecampion, 2019). The effect of such hydro-mechanical couplings on the propagation of aseismic slip remains to be investigated in 3-D and requires the solution of the fully-coupled hydro-mechanical problem as solved, for instance, by Ciardo and Lecampion (2019) in 2-D.

3.6   Summary and concluding remarks

We have studied the quasi-static propagation of aseismic fault slip driven by fluid pressure diffusion under two different injection scenarios, namely, at constant volume rate and at constant pressure. Our model considers a frictional shear crack that grows in mixed mode (II+III) on a planar fault interface that separates two identical half-spaces of a three-dimensional, isotropic, homogeneous, linear elastic and impermeable solid. The fault interface is characterized by: a shear strength that is equal to the product of a constant friction coefficient and the local effective normal stress, a uniform stress state before injection, and a uniform and constant hydraulic transmissivity. The problem admits analytical treatments for circular ruptures which occur in the limit of a Poisson's ratio $\nu = 0$, and it is solved numerically for the more general case in which the frictionally-constrained crack shape is to be determined as part of the solution ($\nu \neq 0$).

For injection at constant volume rate from a point source, the fault rupture is self-similar. For the limiting case of a circular crack ($\nu = 0$), the rupture radius evolves simply as $R(t) = \lambda L(t)$, where $L(t) = \sqrt{4\alpha t}$ is the nominal position of the fluid pressure front and λ is an amplification factor which is similar to the one presented by Bhattacharya and Viesca (2019) and Viesca (2021) in their 2-D model. We derived an analytical solution for λ as a function of a unique dimensionless parameter T. The stress-injection parameter T varies between 0 and $+\infty$ and contains the information related to the pre-injection fault stress state and the strength of the

injection. Whenever $\lambda > 1$, the rupture front outpaces the fluid pressure front. As in previous studies (Garagash & Germanovich, 2012; Bhattacharya & Viesca, 2019), two end-member cases have been identified, namely, critically stressed faults ($T \to 0$) that largely outpace the fluid pressure front ($\lambda \gg 1$), and marginally pressurized faults ($T \to +\infty$) that significantly lags the fluid pressure front ($\lambda \ll 1$). Simple closed-form asymptotic expressions have been derived for λ and also for the axisymmetric slip distribution $\delta(r, t)$, for the two end-member cases. Other results include the rupture speed that decays with the square root of time as $V_r(t) = \lambda\sqrt{\alpha/t}$, and the accumulated fault slip at the injection point which is $\delta(r = 0, t) \approx 3.5\left(f\Delta p_*/\mu\right)L(t)$ for critically stressed faults, and $\delta(r = 0, t) = (8/\pi)\left(f\Delta p_*/\mu\right)R(t)$ for marginally pressurized faults, where f is the friction coefficient, Δp_* is the characteristic overpressure of the injection, and μ is the shear modulus.

For the more general case in which the Poisson's ratio is different than zero, we solved the problem of determining the equilibrium shape of the frictional shear crack over the entire parameter space. We found that the crack shape is quasi-elliptical and the aspect ratio is upper and lower bounded by $1/(1 - v)$ and $(3 - v)/(3 - 2v)$. The two bounds are associated with the limiting cases of critically stressed faults and marginally pressurized faults, respectively. There is thus a strong dependence of the aspect ratio not only on the Poisson's ratio but also on the initial stress state and the driving force itself. Moreover, we found that the rupture area is Poisson's ratio-independent and grows simply as $A_r(t) = 4\pi\alpha\lambda^2 t$. If $\lambda > 1$, the rupture area is greater than the diffusively pressurized fault patch. Interestingly, λ is the same amplification factor that for the circular rupture case, meaning that knowing the solution of the circular shear crack is sufficient to determine the area of any other resulting crack shape for any value of the Poisson's ratio and the same value of T. In addition, simple closed-form asymptotic expressions are provided for the semi-major $a(t)$ and semi-minor $b(t)$ axes of the quasi-elliptical crack that fully define the rupture front for the corresponding end-member cases.

For injection at constant pressure from a finite source of radius r_w, the fault rupture is not self-similar. The rupture radius grows at large times as $R(t) = \lambda(t)\sqrt{c_1\alpha t}$, where $c_1 \approx 2.25$, $\sqrt{c_1\alpha t}$ is the nominal position of the fluid pressure front and $\lambda(t)$ is an amplification factor known as function of dimensionless time $\alpha t/r_w^2$ and T. The stress-injection parameter T varies in this case between 0 and 1. $\lambda(t)$ decreases monotonically with time and the rupture radius expands as $R(t) \propto (\alpha t)^{(1-T)/2}$. For critically stressed faults ($T \to 0 \implies (1 - T)/2 \to 1/2$), the rupture evolves almost diffusively, whereas for marginally pressurized faults ($T \to 1 \implies (1 - T)/2 \to 0$), the rupture grows extremely slow. Generally speaking, the rupture front propagates slower than the diffusive fluid pressure front. Yet in some cases the rupture front outpaces the fluid pressure front, the latter will eventually catch the former if injection is sustained for a sufficient time.

Among the two injection scenarios considered, injection at constant volume rate is the one with broader implications. This is due to injection protocols in the geo-energy industry normally consist of a series of injections at constant volume rate, whereas naturally injected fluids into the Earth's crust are likely represented by the same kind of source. Since aseismic

ruptures expand diffusively (proportional to the square root of time) for that type of injection, irrespective of the pre-injection stress state and the parameters of the injection, current interpretations of fluid-driven seismicity might need to be revisited.

Indeed, it is commonly assumed that seismicity clouds are driven by the direct effect of fluid pressure increase whenever seismic events are observed to spread away from the injection zone with square root time dependence (S. Shapiro et al., 1997; Bosl & Nur, 2002; Parotidis et al., 2005; Chen et al., 2012; Hainzl et al., 2016; Z. Ross et al., 2017; Z. Ross et al., 2020). Our results challenge that interpretation and open the possibility that those episodes might be controlled by the stress transfer of a propagating aseismic rupture instead (Bhattacharya & Viesca, 2019). This would be notably the case of critically stressed fractures/faults in which the rupture front is predicted to be systematically ahead of the fluid pressure front ($\lambda \gg 1$). Furthermore, current estimates of reservoir and fault zone hydraulic diffusivity α based on seismicity patterns (e.g., S. Shapiro et al., 1997; S. Shapiro et al., 2005; Z. Ross et al., 2017) might be rather related to the quantity $\alpha\lambda^2$, with λ being a representative amplification factor of the fractured rock mass or fault zone.

Another important finding is related to the scalar moment M_0 due to purely aseismic (quasi-static) motion. We found that it scales to the injected volume of fluid V as $M_0 \propto V^{3/2}$. Interestingly, this relation is the same as the one found by Galis et al. (2017) for self-arrested injection-induced seismic (dynamic) ruptures.

We expect our analytical and numerical results to provide a conceptual and quantitative framework to undertand various applied problems in geomechanics and geophysics associated with aseismic fracture/fault slip induced by fluid motion. Moreover, our analytical results provide a simple mean for verifying and benchmarking 3-D numerical solvers as performed here.

3.7 Supplementary material

3.7.1 Propagation condition for a constant-friction circular shear crack under axisymmetric shear load

The stress intensity factors of a circular crack of radius R under an arbitrary shear traction vector of components σ_{xz} and σ_{yz} (with regard to the reference frame showed in Figure 3.1) applied anti-symmetrically on the crack surfaces read as (eq. 4.4.59 in Fabrikant, 1989; eq. 4 in Lai et al., 2002)

$$K_{II}(R,\phi) + iK_{III}(R,\phi) = \frac{1}{\pi\sqrt{\pi R}} \int_0^{2\pi} \int_0^R \left[\frac{\left\{\sigma_{xz}(r,\theta) + i\sigma_{yz}(r,\theta)\right\} \sqrt{R^2 - r^2} e^{-i\phi}}{R^2 + r^2 - 2Rr\cos(\phi - \theta)} \right. $$
$$\left. + \frac{\nu}{2-\nu} \frac{\left\{\sigma_{xz}(r,\theta) - i\sigma_{yz}(r,\theta)\right\} \sqrt{R^2 - r^2} \left\{3R - re^{i(\phi-\theta)}\right\} e^{i\phi}}{R(R - re^{i(\phi-\theta)})^2} \right] r\,\mathrm{d}r\,\mathrm{d}\theta, \quad (3.45)$$

where ϕ is the polar angular coordinate, such that $\tan(\phi) = x/y$.

Consider a shear load of axisymmetric magnitude $\Delta\tau(r)$ along the x direction, such that $\sigma_{xz}(r,\theta) = \Delta\tau(r)$ and $\sigma_{yz}(r,\theta) = 0$. Evaluating the integral of the right-hand side of the previous equation with regard to θ, we obtain:

$$K_{II}(R,\phi) = \frac{2\cos(\phi)}{\sqrt{\pi R}} \int_0^R \Delta\tau(r) \left[\frac{1}{\sqrt{R^2-r^2}} + \frac{3\nu}{2-\nu} \frac{\sqrt{R^2-r^2}}{R^2} \right] r \, \mathrm{d}r, \tag{3.46}$$

$$K_{III}(R,\phi) = \frac{2\sin(\phi)}{\sqrt{\pi R}} \int_0^R \Delta\tau(r) \left[-\frac{1}{\sqrt{R^2-r^2}} + \frac{3\nu}{2-\nu} \frac{\sqrt{R^2-r^2}}{R^2} \right] r \, \mathrm{d}r. \tag{3.47}$$

Let us consider the energy release rate of a pure shear crack in 3-D elasticity, $\mathcal{G} = K_{II}^2/E' + K_{III}^2/2\mu$ (Lawn, 1993), where E' is the plane strain modulus. Using the previous equations for the stress intensity factors in the limiting case of a material with Poisson's ratio $\nu = 0$ ($E' = E = 2\mu$), we obtain the following expression for the energy release rate,

$$\mathcal{G} = \frac{2}{\pi\mu R} \left(\int_0^R \frac{\Delta\tau(r)}{\sqrt{R^2-r^2}} r \, \mathrm{d}r \right)^2. \tag{3.48}$$

The fracture energy $\mathcal{G}_c$ of a constant-friction shear crack is zero, such that Griffith energy balance $\mathcal{G} = \mathcal{G}_c$ reduces simply to

$$\int_0^R \frac{\Delta\tau(r)}{\sqrt{R^2-r^2}} r \, \mathrm{d}r = 0, \tag{3.49}$$

that is the expression used in the main text as the condition for crack propagation. The same expression can be alternatively obtain by enforcing the condition of no singularity for the two fault shear stress components, namely, $K_{II} = 0$ and $K_{III} = 0$, with $\nu = 0$ in equations (3.46) and (3.47), respectively.

3.7.2 Asymptotics of fault slip for circular ruptures driven by injection at constant volume rate

The quasi-static elastic equilibrium that relates the fault slip distribution δ to the shear stress drop $\Delta\tau$ within an axisymmetric circular shear crack ($\nu = 0$) of radius $R(t)$ is (Salamon & Dundurs, 1971, 1977; Bhattacharya & Viesca, 2019)

$$\Delta\tau(r,t) = \frac{\mu}{2\pi} \int_0^{R(t)} \frac{\partial\delta(\xi,t)}{\partial\xi} \left(\frac{K[k(r/\xi)]}{\xi+r} + \frac{E[k(r/\xi)]}{\xi-r} \right) \mathrm{d}\xi, \tag{3.50}$$

where K and E are the complete elliptic integrals of the first and second kind, respectively, and $k(x) = 2\sqrt{x}/(1+x)$.

The inverse relation of the previous equation is given by Sneddon (1951) (Eq. 121, p. 489) as

$$\delta(r,t) = \frac{4R(t)}{\pi\mu} \int_{\bar{r}}^{1} \frac{\xi \mathrm{d}\xi}{\sqrt{\xi^2 - \bar{r}^2}} \int_{0}^{1} \frac{\Delta\tau(s\xi R(t), t) s \mathrm{d}s}{\sqrt{1 - s^2}}, \tag{3.51}$$

where $\bar{r} = r/R(t)$ is the self-similar radial coordinate.

Considering that the shear stress drop $\Delta\tau(r,t) = \tau_0 - f\left[\sigma'_o - \Delta p_* E_1\left(r^2/4\alpha t\right)\right]$ (equation (3.11)), the stress-injection parameter $T = \left(f\sigma'_o - \tau_o\right)/f\Delta p_*$ (equation (3.9)), and the amplification factor is defined as $\lambda = R(t)/L(t)$ with $L(t) = \sqrt{4\alpha t}$, we can recast the above equation in dimensionless form,

$$\bar{\delta}(\bar{r};T) = \frac{\delta(r,t)\mu}{f\Delta p_* R(t)} = \frac{4}{\pi} \int_{\bar{r}}^{1} \frac{\xi \mathrm{d}\xi}{\sqrt{\xi^2 - \bar{r}^2}} \int_{0}^{1} \frac{\left(E_1\left(s^2\xi^2\lambda^2\right) - T\right) s \mathrm{d}s}{\sqrt{1 - s^2}}, \tag{3.52}$$

where $\bar{\delta}(\bar{r};T)$ is the normalized self-similar slip distribution that is unique for a given value of T. We recall that the amplification factor λ is known by equation (3.13) as a function of T as well.

Equation (3.52) admits analytical integration in the limiting cases of critically stressed ($\lambda \gg 1$) and marginally pressurized ($\lambda \ll 1$) faults. One of the inner integrals, $\int_{0}^{1} E_1\left(s^2\xi^2\lambda^2\right) s \mathrm{d}s/\sqrt{1 - s^2}$, has indeed the same limiting behaviors than the crack propagation condition, equation (3.12). For large values of λ, such integral is approximated asymptotically as $\sim 1/\left(2\xi^2\lambda^2\right) + O\left(1/\lambda^4\right)$ (see equation (3.14)), whereas for small values of λ is $\sim 2 - \gamma \ln\left(4\xi^2\lambda^2\right) + O\left(\lambda^2\right)$ (see equation (3.15)). Considering the previous asymptotic expressions, equation (3.52) can be evaluated analytically to obtain the following closed-form expressions for the self-similar slip distribution:

$$\frac{\delta(r,t)\mu}{f\Delta p_* R(t)} = \frac{8}{\pi}\left(\sqrt{1 - \bar{r}^2} - |\bar{r}|\arccos\left(|\bar{r}|\right)\right) \tag{3.53}$$

in the marginally pressurized limit ($T \gg 1$, $\lambda \ll 1$), and

$$\frac{\delta(r,t)\mu}{f\Delta p_* L(t)} = \frac{2\sqrt{2T}}{\pi}\left(\frac{\arccos\left(|\bar{r}|\right)}{|\bar{r}|} - \sqrt{1 - \bar{r}^2}\right) \tag{3.54}$$

in the critically stressed limit ($T \ll 1$, $\lambda \gg 1$).

The latter is indeed valid for $r \gg L(t)$ only. It corresponds to the "outer" solution of the critically stressed limit in which the reduction of frictional strength due to the fluid pressure perturbation can be approximated as a point force. Equations (3.53) and (3.54) can be equivalently derived by using the asymptotic expressions of the fluid pressure perturbation in the limiting cases (see details on those approximations in Section 3.3.2). In addition, the condition for having no singularity at the crack tip, $\partial\delta/\partial r = 0$ at $r = R$, is equivalent to the crack propagation condition, equation (3.10), and will lead to same expressions that relates λ and T, equations (3.14) and (3.15), in the corresponding end-member cases.
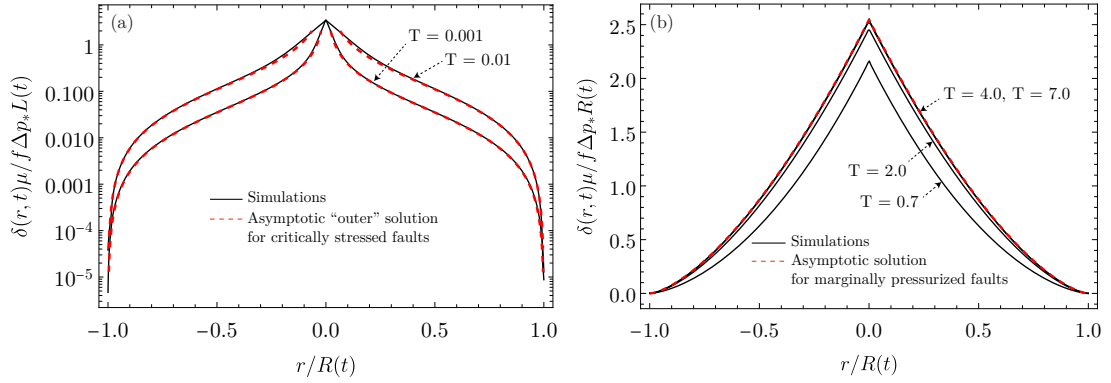
Figure 3.14: Comparison between asymptotics of fault slip and results from the simulations for (a) critically stressed faults ($\lambda \gg 1$), and (b) marginally pressurized faults ($\lambda \ll 1$).

Equations (3.53) and (3.54) are plotted in Figure 3.14 together with the slip profiles obtained from the numerical simulations for values of T that are representative of the limiting cases. We use logarithmic scale in the critically stressed limit in order to facilitate the comparison. Note that the marginally pressurized limit is reached for values of $T \gtrsim 4$ (Figure 3.14b). On the other hand, in the critically stressed limit (Figure 3.14a), the "outer" solution breaks of course for small r (it diverges at $r = 0$ indeed); an "inner" solution should be derived in order to solve the boundary layer at $r \sim O(L(t))$ as done by Garagash and Germanovich (2012) and Viesca (2021).

3.7.3   Numerical computation of rupture fronts

Given the numerical (piece-wise quadratic) solution of fault slip $\delta(x, y, t_n)$ at a given time step t_n, we take 100 equally-spaced values of the angular cylindrical coordinate $\theta_i \in [0, 2\pi)$ (with $i = 1, ..., 100$), and compute for each of them, the root of the system of equations $\delta(x_i, y_i, t_n) = 0$ plus $\tan(\theta_i) = x_i / y_i$, via a Newton-Raphson procedure. We then use the solution, in the form of a data set of 100 coordinate pairs (x_i, y_i), to perform nonlinear regression analysis using the routine *NonlinearModelFit* of Wolfram Mathematica. The nonlinear curve fittings are performed considering the equation of a circle for the case $v = 0$ (with the rupture radius R^m as the model's parameter) and the equation of an ellipse for the case $v \neq 0$ (with the semi-major a^m and semi-minor b^m axes of the ellipse as the model's parameters).

In order to quantify the misfit between the model and the data, we consider the quantity $\beta = (1/N_\theta R_*) \sum_{i=1}^{N_\theta} |r_i^m - r_i^d|$, where r_i^m is the radial distance (from the reference system origin to the rupture front) predicted by the model at θ_i, r_i^d is the same quantity but for the data, N_θ is the total number of data points (100), and R_* is used to scale the distances and is taken as R^m for the circular case ($v = 0$), and $\sqrt{a^m b^m}$ for the elliptical case ($v \neq 0$). Note that $r_i^m = R^m$ for $v = 0$, and $r_i^m = a^m b^m / \sqrt{(a^m \sin(\theta_i))^2 + (b^m \cos(\theta_i))^2}$ for $v \neq 0$. The values of β averaged over the 10 time steps considered in each simulation are shown in Table 3.1.

It is worth mentioning that in the case of $v = 0$, the exact shape of the rupture front is a circle. Hence, the departure of β from zero corresponds uniquely to numerical errors. The average of β over all values of T in the circular rupture case is 0.00644259. Thus, in the case of non-circular ruptures ($v = 0.15$, 0.30 and 0.45), one may consider that values of β that are only larger than the ones for circular ruptures quantify an "actual" departure of the rupture front from an exact ellipse. From Table 3.1, we observe that such difference increases systematically with increasing values of v and decreasing values of T, and is at most of 2% in the worst case ($v = 0.45$, $T = 0.001$).

Two graphical examples of the computation of the elliptical rupture fronts are displayed in Figure 3.15. Figure 3.15a corresponds to the case of the most elongated rupture, which is also the case that departs the most from an ellipse. On the other hand, Figure 3.15b corresponds to the case of the least elongated rupture, in which the β-value is essentially in the other of numerical errors (circular rupture case).

T	Poisson's ratio v			
	0	0.15	0.30	0.45
0.001	0.00574263	0.00724403	0.00969618	0.02028980
0.01	0.00608538	0.00648519	0.01010820	0.01888480
0.1	0.00571406	0.00643673	0.00849989	0.01005640
0.7	0.00689874	0.00630272	0.00653986	0.00754184
2.0	0.00732939	0.00606131	0.00629030	0.00639826
4.0	0.00664432	0.00708104	0.00690700	0.00671446
7.0	0.00668360	0.00644491	0.00681493	0.00691824

Table 3.1: Misfit parameter β of non-linear regression analyses conducted to compute the rupture radius of circular ruptures ($v = 0$) and the semi-major and semi-minor axes of the quasi-elliptical ruptures ($v \neq 0$), for the self-similar case of injection at constant volume rate. Values of β are averaged over the 10 time steps for each combination of T and v.
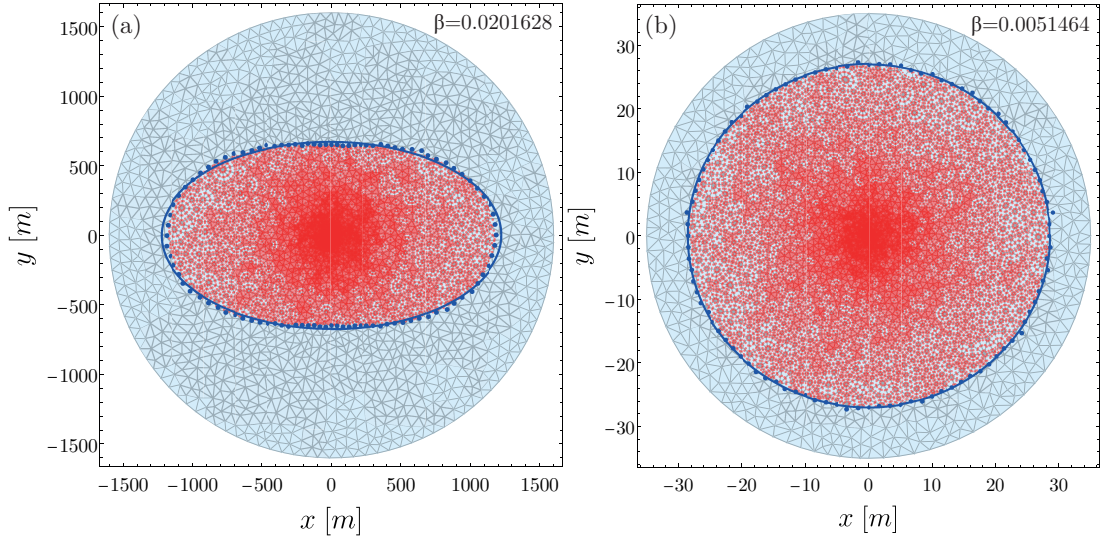
Figure 3.15: Two examples of the computation of the elliptical rupture fronts at given snapshots for (a) the most elongated rupture ($T = 0.001$, $v = 0.45$) and (b) the least elongated rupture ($T = 7.0$, $v = 0.15$). The blue points correspond to the position of the rupture front computed numerically from the solution for fault slip $\delta(x, y, t)$, for each one of the one hundred equally-spaced angular cylindrical directions $\theta_i \in [0, 2\pi)$ considered. The blue solid curves correspond to the ellipsoidal curve fittings to the one hundred coordinate pairs. In the background, the unstructured triangular mesh made on piece-wise quadratic boundary elements used throughout this study.

3.7.4 Analytical solution in 2-D for a frictional shear crack driven by injection at constant volume rate

Consider the same problem formulated in Section 3.2 but in 2-D elasticity. Fluid is injected via a point source at $x = 0$ into a planar 1-D frictional interface located along the x-axis. Injection is sustained for $t > 0$ at a constant volume rate q_w $[L/T]$ per unit fault thickness and unit out-of-the-plane length. The quasi-static crack propagation condition for a 1-D straight constant-friction (zero-toughness) symmetric shear crack (either mode II or III) of half-crack length $\ell(t)$ reduces to (Barenblatt, 1962)

$$\int_{-\ell(t)}^{\ell(t)} \frac{\Delta\tau(x, t)}{\sqrt{\ell^2(t) - x^2}} \, dx = 0, \tag{3.55}$$

where $\Delta\tau(x, t)$ is the shear stress drop given by

$$\Delta\tau(x, t) = \tau_0 - f\left(\sigma'_o - \Delta p(t)\Pi(\xi)\right), \tag{3.56}$$

with $\xi = x/\sqrt{4\alpha t}$ and (section 2.9, eq. 7, Carslaw and Jaeger, 1959)

$$\Delta p(t) = \frac{q_w\eta}{\sqrt{\pi}k}\sqrt{\alpha t}, \quad \Pi(\xi) = \exp\left(-\xi^2\right) - \sqrt{\pi}\,|\xi|\,\mathrm{Erfc}\,(|\xi|). \tag{3.57}$$

As defined in the main text, η is the fluid dynamic viscosity, k is the fault intrinsic permeability, and α is the fault hydraulic diffusivity.

Let us define the nominal position of the fluid pressure front $\ell_d(t) = \sqrt{4\alpha t}$, a time-dependent amplification factor λ in the form $\lambda(t) = \ell(t)/\ell_d(t)$, and the following characteristic length

$$x_c = \sqrt{4\pi}\frac{k\left(f\sigma'_o - \tau_o\right)}{f q_w \eta}, \tag{3.58}$$

The crack propagation condition can be then rewritten in dimensionless form

$$\frac{1}{\pi}\int_{-1}^{1}\frac{\Pi(\lambda s)}{\sqrt{1 - s^2}}ds = \frac{x_c}{\ell_d}, \tag{3.59}$$

that represents a unique relation between the amplification factor λ and the normalized position of the fluid pressure front ℓ_d/x_c.

The left-hand side of the previous integral can be evaluated analytically to obtain the following implicit equation for λ as a function of ℓ_d/x_c,

$$\exp\left(-\lambda^2/2\right)\left[\left(1 + \lambda^2\right) I_0\left(\lambda^2/2\right) + \lambda^2 I_1\left(\lambda^2/2\right)\right] - 2\lambda/\sqrt{\pi} = x_c/\ell_d, \tag{3.60}$$

where I_0 and I_1 are the modified Bessel functions of the first kind of zero and first order, respectively.

The previous equation is the one reproduced in the main text and it is plotted in Figure 3.13a. Asymptotic expansions of the left-hand side of this equation for small and large λ lead to the following closed-form asymptotic solutions for the short-run-out rupture ($\lambda \ll 1$) and long-run-out rupture ($\lambda \gg 1$) regimes:

$$\begin{cases} \lambda = \sqrt{\frac{\pi}{4}}\left(\frac{\ell_d}{x_c} - 1\right) & \text{, for } \lambda \ll 1 \\ \lambda = \frac{1}{\sqrt{4\pi}}\frac{\ell_d}{x_c} & \text{, for } \lambda \gg 1 \end{cases}, \tag{3.61}$$

that are also plotted in Figure 3.13a.

From the asymptotic for the short-run-out rupture regime, we note that solutions are defined only for $\ell_d/x_c \geq 1$. The limit of $\ell_d/x_c = 1$ represents the instant in which activation of slip (or crack nucleation) happens and implies that $\ell_d = x_c$ at that moment. From the latter, it becomes clear that the characteristic length x_c is the size of the pressurized patch necessary for the crack to start growing.

On the other hand, the previous asymptotics can be recast in terms of the dimensionless half-crack length $\ell(t)/x_c$ and the dimensionless time $\bar{t} = (\ell_d/x_c)^2 = 4\alpha t/x_c^2$, to obtain the following

expressions:

$$
\begin{cases}
\frac{\ell(t)}{x_c} = \sqrt{\frac{\pi}{4}} \left(\bar{t} - \sqrt{\bar{t}} \right) & \text{, for } t \text{ near } x_c^2/4\alpha \\
\frac{\ell(t)}{x_c} = \frac{1}{\sqrt{4\pi}} \bar{t} & \text{, for } t \gg x_c^2/4\alpha
\end{cases}
,
\tag{3.62}
$$

which corresponds to early-time and late-time solutions, respectively. From the asymptotic for late times, we can write

$$
\ell(t) = \frac{2\alpha}{\sqrt{\pi} x_c} t.
\tag{3.63}
$$

Hence, the ultimate behavior of the crack is a steady propagation regime at constant rupture speed V_R equal to

$$
V_R = \frac{f \alpha q_w \eta}{\pi k \left(f \sigma_o' - \tau_o \right)},
\tag{3.64}
$$

which is the other equation used in the main text.

4 Post-injection aseismic slip as a mechanism for the delayed triggering of seismicity

In this chapter, we investigate via a hydro-mechanical model the propagation and ultimate arrest of aseismic slip during the so-called post-injection stage. We show that after shut-in, fault slip propagates in pulse-like mode. The conditions that control the propagation as a pulse and notably when and where the ruptures arrest are fully established. In particular, critically-stressed faults can host rupture pulses that propagate for several orders of magnitude the injection duration and reach up to nearly double the size of the ruptures at the moment of shut-in. We consequently argue that the persistent stressing of increasingly larger rock volumes caused by post-injection aseismic slip is a plausible mechanism for the triggering of post-injection seismicity —a critical issue in the geo-energy industry. Our physical model shows quantitative agreement with field observations of documented cases of post-injection-induced seismicity.

This chapter is a modified version of the following scientific article:

Sáez, A. & Lecampion, B. (2023). Post-injection aseismic slip as a mechanism for the delayed triggering of seismicity. *Proceedings of the Royal Society A: Mathematical, Physical and Engineering Sciences*, 479, 20220810.

Contributions of Alexis Sáez (CRediT, Contributor Roles Taxonomy)

Conceptualization, Methodology, Software, Validation, Formal analysis, Investigation, Writing - Original Draft, Writing - Review & Editing, Visualization, Funding acquisition.

4.1   Introduction

It has been long recognized that subsurface fluid injections can induce fast fault slip (Healy et al., 1968) that radiates detectable elastodynamic waves, and also slow, sometimes called aseismic slip (Hamilton & Meehan, 1971), which is generally more difficult to detect by classical

monitoring networks. Evidence for injection-induced aseismic slip dates back to the 1960's, when a slow surface fault rupture was causally linked to fluid injection operations of an oil field in LA, USA (Hamilton & Meehan, 1971). Since then, an increasing number of studies have inferred the occurrence of aseismic slip episodes as a result of anthropogenic subsurface fluid injections (Scotti & Cornet, 1994; Bourouis & Bernard, 2007; Wei et al., 2015; Eyre et al., 2022), with recent in-situ experiments of fluid injection into natural fault systems demonstrating by direct measurements of fault deformation that slow slip was systematically the dominant style of fault motion (Guglielmi et al., 2015; Cappa et al., 2019).

Injection-induced aseismic slip is thought to play an important role in seismicity induced by industrial fluid injections, a phenomenon that has become critical in ensuring the sustainable development of unconventional hydrocarbon reservoirs (Bao & Eaton, 2016) and deep geothermal resources (Deichmann & Giardini, 2009; Ellsworth et al., 2019). It is understood that fluid-driven slow ruptures transmit stresses quasi-statically to unstable fault patches and trigger instabilities at distances that can be far from the region affected by the pressurization of pore-fluid (Bhattacharya & Viesca, 2019; Eyre et al., 2019). Moreover, a similar mechanism might be also operating behind some natural episodes of seismicity such as seismic swarms and aftershock sequences. In fact, both phenomena are commonly interpreted to be driven by either the diffusion of pore pressure (Miller et al., 2004; Parotidis et al., 2005) or the propagation of aseismic slip (Lohman & McGuire, 2007; Perfettini & Avouac, 2007), with recent studies suggesting that both mechanisms might be indeed coupled and responsible for the observed spatio-temporal patterns of seismicity (Z. Ross et al., 2017; Sirorattanakul et al., 2022; Yukutake et al., 2022). Likewise, tectonic tremors and low-frequency earthquakes are often considered to be driven by slow slip events in subduction zones (Rogers & Dragert, 2003; Shelly et al., 2006), at depths where systematic evidence of over-pressurized fluids is found (Shelly et al., 2006; Kato et al., 2010). Metamorphic dehydration reactions (Peacock, 2009) and fault-valving behavior (Sibson, 2020) are the two common candidates to explain not only this inferred over-pressurization, but also the very nature of pore pressure and aseismic slip transients in these zones (Zhu et al., 2020).

The seemingly relevant role of fluid-driven aseismic slip in the previous phenomena have motivated the development of physical models that, in recent years, have contributed to a better understanding of the mechanics of this hydro-mechanical problem. Some recent advances include a better notion of how the initial state of stress, the fluid injection parameters, the fault hydraulic properties, and the possible rate-strengthening dependence of rock friction, may affect the dynamics of fluid-driven aseismic slip transients in 2D (Dublanchet, 2019; Garagash, 2021; Viesca, 2021; Yang & Dunham, 2021) and 3D media (Sáez et al., 2022). The three-dimensional case is the relevant one for field applications and has been shown to be not only quantitatively but also qualitatively very different from two-dimensional configurations (Sáez et al., 2022). One common aspect of all prior studies is that they focus on fluid sources that are continuous (uninterrupted) in time. Yet much less is known about aseismic ruptures after the injection of fluids has stopped. In particular, the conditions that control the further propagation and ultimate arrest of fluid-driven aseismic slip are fairly unknown, despite a

recent investigation for a two-dimensional plane-strain configuration (Jacquey & Viesca, 2023). This is of broad interest since, ultimately, any kind of fluid source and accompanying rupture will have to stop. Understanding the mechanics of post-injection aseismic slip in a realistic three-dimensional scenario is thus of major importance. It corresponds to the first goal of this study.

Our second goal is to understand how and to which extent post-injection aseismic slip can be considered as a possible mechanism for the triggering of seismicity after the end of subsurface fluid injections. It is well-known since the Denver earthquakes in the 1960s (Healy et al., 1968) that upon shutting off the wells, seismicity might continue to occur. Multiple observations suggest that indeed, it is not rare that the largest events of injection-induced seismic sequences happen during the post-injection stage. Examples of those cases are the 2006 $M_L > 3$ Basel earthquakes in Switzerland, and the 2017 M_w 5.5 Pohang earthquake in South Korea, both causally linked to hydraulic stimulation operations of deep geothermal reservoirs (Deichmann & Giardini, 2009; Ellsworth et al., 2019). Also, the 2015 M_w 3.9 earthquake in western Canada, occurred after the end of hydraulic fracturing operations in a hydrocarbon reservoir (Bao & Eaton, 2016). Because the shut-in of the wells does not guarantee the cessation of seismic events, current efforts to manage the seismic risk in the geo-energy industry such as the so-called traffic light systems (Baisch et al., 2019), might be subjected to important limitations in their effectiveness. Understanding the physical mechanisms underpinning post-injection seismicity is thus of paramount importance for the successful development of both hydrocarbon and geothermal reservoirs. We therefore aim in this study at understanding the combined effect of pore pressure diffusion and solid stress changes due to aseismic slip in the triggering of seismicity.

4.2 Governing equations and scaling analysis

4.2.1 Governing equations

We consider a planar fault in an infinite, linearly elastic, isotropic, impermeable, and three-dimensional solid, as depicted in Figure 4.1. The initial stress tensor is assumed to be uniform and is characterized by a shear stress τ_0 resolved on the fault plane that acts along the x direction and a total normal stress σ_0 (acting along the z direction). We assume a uniform initial pore pressure field of magnitude p_0 that is perturbed by the sudden injection of fluids into a poroelastic fault zone of width w. We model such fluid injection via a line-source that is located along the z axis and crosses the entire fault width. The fault zone permeability k and storage coefficient S are assumed to be uniform and constant. As a result, fluid flow is axisymmetric with regard to the z axis and occurs only within the fault zone. We further assume that the shear modulus μ and Poisson's ratio v of the poroelastic fault zone and impermeable elastic host rock are the same. Under such conditions, the displacement field induced by the fluid injection is irrotational and the pore pressure diffusion equation of poroelasticity reduces to its uncoupled version (Marck et al., 2015), $\partial p / \partial t = \alpha \nabla^2 p$, where $\alpha = k / S\eta$ is the

fault hydraulic diffusivity, with η the fluid dynamic viscosity.

By neglecting any poroelastic coupling within the fault zone upon activation of slip, the quasi-static elastic equilibrium that relates fault slip to the shear stress components along the fault, can be written as the following boundary integral equations,

$$\tau_i(x, y, t) = \tau_i^0 + \int_\Gamma K_{ij}(x - \xi, y - \zeta; \mu, \nu)\delta_j(\xi, \zeta, t)\mathrm{d}\xi\mathrm{d}\zeta, \text{ with } i, j = x, y, \tag{4.1}$$

where $\tau_i^0 = (\tau_0, 0)^{\mathrm{T}}$ is initial shear traction vector, K_{ij} is the hypersingular (of order $1/r^3$) elastostatic traction kernel (see for example, Hills et al., 1996), and $\delta_j = u_j^+ - u_j^-$ is the fault slip vector, with $u_j^\pm$ the displacement vector at the upper (+) and lower (−) faces of the slip surface Γ.

The fault interface is assumed to obey a Mohr-Coulomb shear failure criterion with a constant friction coefficient f and no cohesion expressed as the following local inequality,

$$\|\tau_i(x, y, t)\| \le f\left(\sigma_0' - \Delta p(r, t)\right), \tag{4.2}$$

where $\sigma_0' = \sigma_0 - p_0$ is the initial effective normal stress, and $\Delta p(r, t) = p(r, t) - p_0$ is the axisymmetric pore pressure perturbation, with r the radial coordinate.

Owing to the unidirectionality of the initial shear traction vector and the axisymmetry property of the equivalent shear load in terms of magnitude, both fault slip and maximum shear stress are characterized by an approximately uniform direction along the x axis (see Section 4.8.1 for further details). The latter implies that for all practical purposes in this paper, the differences between $\|\delta_i\|$ and $|\delta_x|$, and $\|\tau_i\|$ and $|\tau_x|$, are negligible (an approximation that was implicit in Sáez et al., 2022). We therefore refer interchangeably hereafter to fault slip as $\delta \equiv \delta_x$ and fault shear stress as $\tau \equiv \tau_x$. Moreover, for the particular case in which $\nu = 0$, $K_{xy} = K_{yx} = 0$ (see, for instance, eq. 7.4 in Hills et al., 1996) and thus the direction of slip (or maximum shear) occurs exactly along the x direction.

The injection of fluid starts at $t = 0$ and consists of two subsequent stages: a continuous injection stage characterized by a constant rate of injection Q, and a post-injection stage in which the injection rate drops instantaneously to zero at $t = t_s$ (see Figure 4.1c). Hereafter, we refer to t_s as the shut-in time. The solution of the linear diffusion equation before shut-in (when $0 < t \le t_s$) is known as $\Delta p(r, t) = \Delta p_* E_1\left(r^2/4\alpha t\right)$ (section 10.4, eq. 5, Carslaw and Jaeger, 1959), where

$$\Delta p_* = \frac{\Delta p_c}{4\pi}, \text{ and } \Delta p_c = \frac{Q\eta}{kw}. \tag{4.3}$$

In the previous equations, Δp_* is the intensity of the injection with units of pressure, Δp_c is a characteristic pressure that is in the order of magnitude of the overpressure at the fluid source, and $E_1(x) = \int_x^\infty \left(e^{-x\xi}/\xi\right)\mathrm{d}\xi$ is the exponential integral function. The solution after shut-in
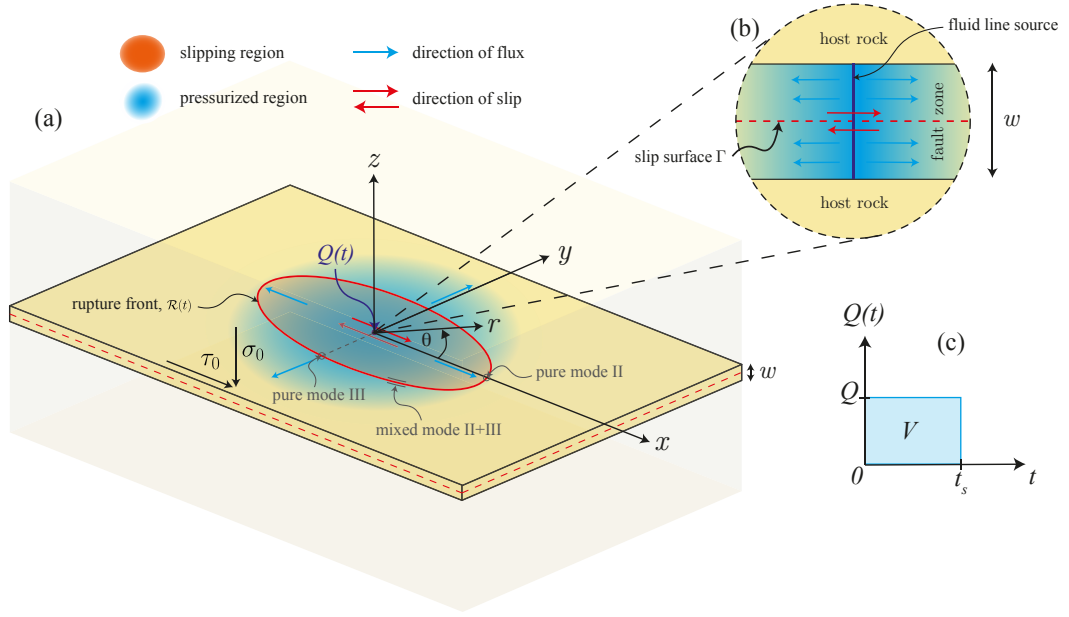
Figure 4.1: Model schematics. (a) and (b), fluid is injected into a permeable fault zone of width w via a line source that crosses the entire fault zone width. The fault is planar and embedded in an unbounded linearly elastic impermeable host rock. The initial stress tensor is uniform. (c) Fluid is injected at a constant rate Q until $t = t_s$ (the shut-in time) at which the injection is instantaneously stopped.

(when $t > t_s$), is obtained simply by superposition as

$$\Delta p(r, t) = \Delta p_* \left\{ E_1 \left(\frac{r^2}{4\alpha t} \right) - E_1 \left(\frac{r^2}{4\alpha (t - t_s)} \right) \right\}. \tag{4.4}$$

Note that the infinitesimal size of the fluid source in our model provides a proper finite volume of injected fluid $V = Q t_s$, but infinite pressure at the injection point. In this regard, our model must be understood as the late-time asymptotic solution of a more general model where the fluid source possess a finite characteristic size, say ℓ_*. Our results will be thus applicable when t_s is much larger than the characteristic diffusion time ℓ_*^2/α over the finite source lengthscale. This is indeed the case of most borehole fluid injections, where the borehole radius is $\ell_* \sim 10$ [cm]. By assuming values of hydraulic diffusivity in the range 10^{-4} to 1 [m²/s], the characteristic time ℓ_*^2/α takes values between 100 down to 0.01 [s] which are much smaller than typical fluid injection duration in geo-energy applications. Moreover, the asymptotic behavior of the exponential integral function for small values of its argument, $E_1(x) \approx -\gamma - \ln(x)$, where γ is the Euler-Mascheroni's constant, allows us to identify Δp_c as the pressure scale that is in the order of magnitude of the overpressure at $r = \ell_*$ when $t \gg \ell_*^2/\alpha$, as previously stated.

Equations (4.1), (4.2) and (4.4) constitute a complete system of equations to solve for the spatio-temporal evolution of fault slip $\delta(x, y, t)$ and, particularly, the moving boundary representing

the slipping region $\mathscr{S}(t)$. The slipping patch $\mathscr{S}(t)$ may be defined mathematically as the region in which the equality of equation (4.2) holds: $\mathscr{S}(t) = \{(x, y) \in \Gamma : |\tau(x, y, t)| = f(\sigma_0' - \Delta p(r, t))\}$. The initial conditions are naturally taken as $\delta(x, y, 0) = 0$ and $\dot{\delta}(x, y, 0) = 0$ (fault initially at rest and fully locked).

4.2.2   Scaling analysis and limiting regimes

The shut-in of the injection provides the natural characteristic timescale of the problem, the shut-in time t_s. This latter introduces, via the solution of the pore-pressure diffusion equation (4.4), a characteristic diffusion lengthscale $\sqrt{4\alpha t_s}$. Alternatively, one may choose (as suggested by Sáez et al., 2022) to scale the spatial coordinates by a characteristic rupture lengthscale at the moment of shut-in, say R_s^*. We normalize the pore pressure perturbation $\Delta p(r, t)$, equation (4.4), by the intensity of the injection Δp_*. Introducing the foregoing characteristic scales in the Mohr-Coulomb shear failure criterion, equation (4.2), gives the normalized shear stress, $(\tau - f\sigma_0')/f\Delta p_*$, which in turn is introduced in the balance of momentum, equation (4.1), allowing us to close the scaling of the problem by normalizing the fault slip by $(f\Delta p_*/\mu)\sqrt{4\alpha t_s}$, or alternatively by $(f\Delta p_*/\mu)R_s^*$ if the characteristic rupture lengthscale is chosen for the spatial scale.

It can be shown by using the previous scales that the model depends, in addition to dimensionless space and time, on one single dimensionless number:

$$\mathscr{T} = \frac{f\sigma_0' - \tau_0}{f\Delta p_*}, \tag{4.5}$$

and the Poisson's ratio ν.

The so-called stress-injection parameter $\mathscr{T}$ is identical to the one presented recently by Sáez et al. (2022) for the problem of continuous injection, and similar to the one introduced first by Bhattacharya and Viesca (2019) in their 2D plane-strain model. $\mathscr{T}$ is defined as the ratio between the amount of stress necessary to activate fault slip $f\sigma_0' - \tau_0$, and $f\Delta p_*$ which quantifies the effect of the fluid injection on the reduction of fault strength near the injection point. The stress-injection parameter can vary theoretically between 0 and $+\infty$ (Sáez et al., 2022). However, for practical purposes, we note here that $\mathscr{T}$ is upper bounded. Since $\Delta p_c = 4\pi\Delta p_*$ is in the order of magnitude of the overpressure at the fluid source, the minimum amount of overpressure that one needs to guarantee the activation fault slip under such a line-source approximation is $f\Delta p_c \sim f\sigma_0' - \tau_0$. Substituting the previous relation into (4.5) leads to an order-of-magnitude upper bound $\mathscr{T} \lesssim 10$ (the factor 4π indeed). Note that the introduction of Δp_c and the resulting upper bound for $\mathscr{T}$ in this work put now the results of the continuous-injection problem (Sáez et al., 2022) in a more practical perspective. The limiting values of $\mathscr{T}$ are associated with two end-member scenarios that were first introduced by Garagash and Germanovich (2012). When $\mathscr{T}$ is close to zero, $\tau_0 \to f\sigma_0'$ and thus the fault is critically stressed (about to fail before the injection starts). On the other hand, when $\mathscr{T} \sim 10$,

the fault is "marginally pressurized" as the injection has provided just the minimum amount of overpressure to activate fault slip, $f \Delta p_c \sim f \sigma'_0 - \tau_0$. We will make extensive use of the terms critically-stressed fault/regime and marginally-pressurized fault/regime to refer to these limiting cases throughout this article.

As shown recently by Sáez et al. (2022), an important aspect of the foregoing two limiting regimes is that they follow different scales during the stage of continuous injection, which is particularly valid in the post-injection problem right at the moment of shut-in t_s. Indeed, the proper slip scale δ_* in the critically-stressed limit comes from choosing $\sqrt{4\alpha t_s}$ as the characteristic lengthscale,

$$\delta \sim \delta_* = \frac{f \Delta p_*}{\mu} \sqrt{4\alpha t_s}. \tag{4.6}$$

The proper scale for the slip rate follows from differentiation of the slip scale with respect to time,

$$v \sim v_* = \frac{f \Delta p_*}{\mu} \sqrt{\frac{\alpha}{t_s}}. \tag{4.7}$$

The slip and slip rate scales of the marginally-pressurized limit can be obtained likewise by choosing the characteristic rupture scale R_s^* as the spatial lengthscale of the problem, i.e., $\delta \sim \left(f \Delta p_* / \mu\right) R_s^*$ and $v \sim \left(f \Delta p_* / \mu\right) R_s^* / t_s$. Nonetheless, the latter scales will be seen later to be somewhat irrelevant in the post-injection stage, because marginally-pressurized faults will host ruptures that after shut-in arrest almost immediately.

Finally, the second dimensionless parameter of the model, the Poisson's ratio v, is expected to have only an effect on the rupture shape. As shown by Sáez et al. (2022) for the continuous-injection stage, the Poisson's ratio modifies the aspect ratio of the resulting rupture fronts which become more elongated for increasing values of v. The position of the elongated rupture fronts is nevertheless determined primarily by the position of circular ruptures, that correspond to a limiting case in which the Poisson's ratio of the solid v is zero. The case of circular ruptures is thus particularly insightful and notably simpler, since in that limit, we can take advantage of the axisymmetry property of the mechanical problem (Bhattacharya & Viesca, 2019; Sáez et al., 2022).

4.3   Pore-pressure diffusion: the pore-pressure back front

The pore-pressure perturbation $\Delta p(r, t)$ is the only external action driving the rupture after shut-in. It is thus essential to examine in detail its spatio-temporal evolution. Various normalized spatial distributions of pore pressure are plotted in Figure 4.2a at different dimensionless times. We first observe that pore pressure decreases quickly after the stop of injection near the fluid source in the sense $r \ll \sqrt{4\alpha(t - t_s)}$, asymptotically as $\Delta p(r, t) / \Delta p_* \approx \ln\left(\bar{t} / (\bar{t} - 1)\right)$ (red dashed curve), with $\bar{t} = t / t_s$ the dimensionless time. Moreover, at large times ($\bar{t} \gg 1$), it
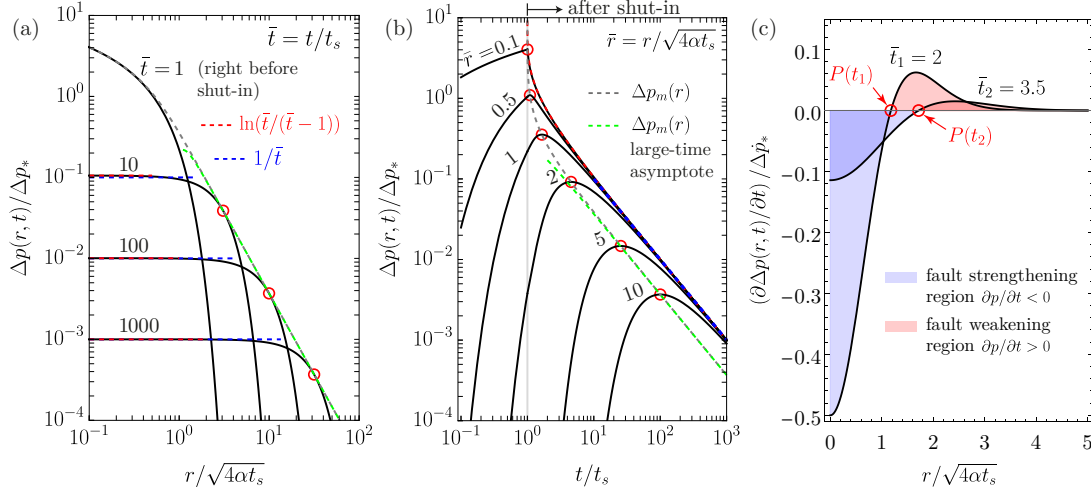
Figure 4.2: (a) Normalized spatial distribution of pore pressure at different dimensionless times. Dashed curves correspond to asymptotic behaviors as explained in the main text. (b) Evolution of normalized pore pressure at some fixed dimensionless radial positions. Red circles indicate the instants at which the maximum pressure Δp_m is reached. (c) Spatial distribution of pore pressure rate normalized by $\Delta \dot{p}_* = \Delta p_* / t_s$, at two dimensionless times after shut-in. Red circles indicate the position of the pore-pressure back front $P(t)$, equation (4.8).

decreases simply as $\Delta p(r,t)/\Delta p_* \approx 1/\bar{t}$ (blue dashed curve) for points that are close to the injection now in the sense $r \ll \sqrt{4\alpha t}$. The latter indicates that the region in which the previous asymptotic behavior is approximately satisfied grows diffusively ($\propto \sqrt{\alpha t}$), and has the shape of a plateau in Figure 4.2a.

Moreover, Figure 4.2a displays that after shut-in the pore pressure keeps increasing away from the injection line. To better understand such process, it may result convenient to look at the temporal evolution of pore pressure at fixed normalized positions over the fault plane. Figure 4.1b displays such a plot. Here, we observe that pore pressure remains increasing for some time after injection stops ($\bar{t} > 1$) and eventually reaches a maximum (red circles). After this instant of maximum pressure, the pore pressure decreases following ultimately the same asymptotes of Figure 4.2a, meaning that the aforementioned diffusely expanding plateau has reached the corresponding fixed radial positions in Figure 4.2b.

The relation between a given position over the fault plane and the time at which the maximum pressure is reached, defines a "back front" of pore pressure, $\mathscr{P}(t) = \left\{ r(t) \in \Gamma : \partial \Delta p(r,t)/\partial t = 0 \right\}$. Owing to the axisymmetry property of pore pressure diffusion in our model, $\mathscr{P}(t)$ is circular and is thus fully defined by its radius $P(t)$. Differentiating equation (4.4) with respect to time and solving for $\partial \Delta p/\partial t = 0$ leads to the following expression for the normalized radius of the pore-pressure back front,

$$\frac{P(t)}{\sqrt{4\alpha t_s}} = \left[\bar{t}\left(\bar{t}-1\right) \ln\left(\frac{\bar{t}}{\bar{t}-1}\right) \right]^{1/2}, \tag{4.8}$$

which further reduces to $P(t)/\sqrt{4\alpha t_s} \approx \sqrt{\bar{t}}$, or simply $P(t) \approx \sqrt{4\alpha t}$, at large times. Note that the large-time asymptote of $P(t)$ is the same expression than that of the radius of the pore-pressure perturbation front $L(t) = \sqrt{4\alpha t}$ for the continuous-injection stage, albeit each expression describes different processes.

On the other hand, the maximum pore pressure increase undergone historically at a given position r, say $\Delta p_m(r)$, is obtained by simply evaluating the pore pressure perturbation $\Delta p(r, t)$ at the time t_m in which the maximum occurs, i.e., $\Delta p(r, t_m(r))$. t_m comes from solving for time in (4.8) with $P(t) = r$. $\Delta p_m(r)$ is displayed in Figure 4.2a (gray dashed curve) representing the pore pressure back front $\mathscr{P}(t)$ in this plot, which corresponds to the envelope of all curves (for all times) associated with instantaneous spatial distributions of pore pressure. Note that $\Delta p_m(r)$ cannot be obtained in closed form since equation (4.8) is not invertible for time, nevertheless, in the large-time limit, $t_m(r)/t_s \approx \bar{r}^2$, such that $\Delta p_m(r)/\Delta p_* \approx E_1(1) - E_1(\bar{r}^2/(\bar{r}^2 - 1))$. The previous asymptotic approximation is also plotted in Figure 4.2a (green dashed curve). Similarly, an expression for Δp_m as a function of time t may be derived, which is indeed obtainable in closed form as $\Delta p_m(t) = \Delta p(P(t), t)$ (gray and green dashed curves in Figure 4.2b).

4.4　Pulse-like circular ruptures

Circular ruptures occur in the limit of a Poisson's ratio $\nu = 0$. As discussed in previous sections, a Poisson's ratio different than zero is expected to affect mainly the shape of the resulting ruptures, and less significantly other relevant quantities of the fault response (Sáez et al., 2022). Circular ruptures are thus a particularly insightful case, in which the axisymmetry property of the mechanical problem (Bhattacharya & Viesca, 2019; Sáez et al., 2022) simplifies the analysis of results. The effect of Poisson's ratio on the rupture shape will be quantified in Section 4.5.

4.4.1　Recall on the self-similar solution before shut-in

The solution for the continuous-injection stage ($t \le t_s$) of the same problem was presented recently by Sáez et al. (2022). We briefly summarize some of their results as they provide the starting point for the understanding of the post-injection phase. Sáez *et al.* showed that fault slip induced by injection at constant volume rate (from an infinitesimal source) is self-similar in a diffusive manner. The rupture radius $R(t)$ evolves simply as $R(t) = \lambda L(t)$, where $L(t) = \sqrt{4\alpha t}$ is the nominal position of the pore-pressure perturbation front, and λ is the so-called amplification factor for which an analytical solution as function of the stress-injection parameter $\mathscr{T}$ exists (eq. (21) in Sáez et al., 2022). The asymptotic behavior of λ for the limiting values of $\mathscr{T}$ is particularly insightful. For critically-stressed faults ($\mathscr{T} \ll 1$), the amplification factor turns out to be large ($\lambda \gg 1$) and thus the rupture front outpaces largely the fluid pressure front ($R(t) \gg L(t)$), with λ obeying the simple asymptotic relation $\lambda \approx 1/\sqrt{2\mathscr{T}}$. On the other hand, for marginally-pressurized faults ($\mathscr{T} \gg 1$), the amplification factor is small ($\lambda \ll 1$), such that the rupture front lags significantly the fluid pressure front ($R(t) \ll L(t)$),

with $\lambda \approx (1/2) \exp\left[\left(2 - \gamma - \mathscr{T}\right)/2\right]$, where $\gamma = 0.577216...$ is the Euler-Mascheroni's constant. These simple closed-form expressions provide important insights into the response of faults during continuous fluid injections. They allow us to to estimate the slip front position in a compact and convenient way that also determine whether aseismic-slip stress transfer ($\lambda > 1$) or pore pressure increase ($\lambda < 1$) is the dominant mechanism in the possible triggering of seismicity associated with coupled fluid flow and fault slip processes.

4.4.2   Transition from crack-like to pulse-like rupture: the locking front

In Section 4.3, we showed that the shut-in of the injection is characterized by the emergence of the so-called pore-pressure back front, which corresponds to the instantaneous position at which the pressure has reached its maximum historically. With reference to Figure 4.2c, we consequently see that pore pressure is instantaneously increasing at every point on the fault plane located beyond the position of this front: $\partial \Delta p(r, t)/\partial t > 0$ for all $r > P(t)$. This results in a moving region where the fault shear strength $\tau_s(r, t) = f\left(\sigma_0' - \Delta p(r, t)\right)$ is decreasing. Such reduction of fault strength is indeed what uniquely drives the propagation of the rupture after shut-in. On the other hand, in the complementary inner region $r < P(t)$, the opposite holds, and $\partial \Delta p(r, t)/\partial t < 0$ (see Figure 4.2c). The pore pressure is thus diminishing and the effective normal stress and thus fault shear strength is rising as a result. Furthermore, the enhanced fault shear strength may eventually become locally greater than the resolved shear stress τ, consequently re-locking the slip surface. We observe the development of this re-locking process systematically in all our numerical solutions, starting virtually right after shut-in. Such re-locking process is characterized by a locking front $\mathscr{B}(t)$ propagating outwardly from the injection location. The emergence of this locking front marks the transition from crack-like (before shut-in) to pulse-like (after shut-in) propagation mode, a prominent feature of post-injection aseismic slip.

Similarly to the rupture front $\mathscr{R}(t)$, the locking front $\mathscr{B}(t)$ must be circular when $\nu = 0$, and is thus fully defined by its radius $B(t)$. Figure 4.3 shows the transition from crack-like to pulse-like propagation as seen in the normalized slip δ, slip rate ν, and shear stress τ and strength τ_s spatial distributions, at times right before shut-in and at some time after shut-in. The aseismic pulses can be seen clearly in Figure 4.3b for the slip rate distribution, where the positions of the locking and rupture fronts are highlighted. Note that both the magnitude (peak slip rate) and width of the pulses decrease monotonically with time. On the other hand, the Mohr-Coulomb inequality given by equation (4.2) establishes that, within the slipping patch ($B(t) < r < R(t)$), the shear stress must be equal to the fault shear strength, whereas in the re-locked region ($r < B(t)$), the shear stress must be lower than the fault shear strength. Both cases can be clearly seen in Figure 4.3c, where the positions of the rupture and locking fronts are also highlighted. Note that the normalized shear strength in Figure 4.3c is equal to $(\tau_s - f\sigma_0')/f\Delta p_* = -\Delta p/\Delta p_*$, which is minus the normalized pore pressure perturbation. In addition, we observe that at some distance away from the locking front and towards the injection point, the shear stress after shut-in is slightly greater than the shear stress right
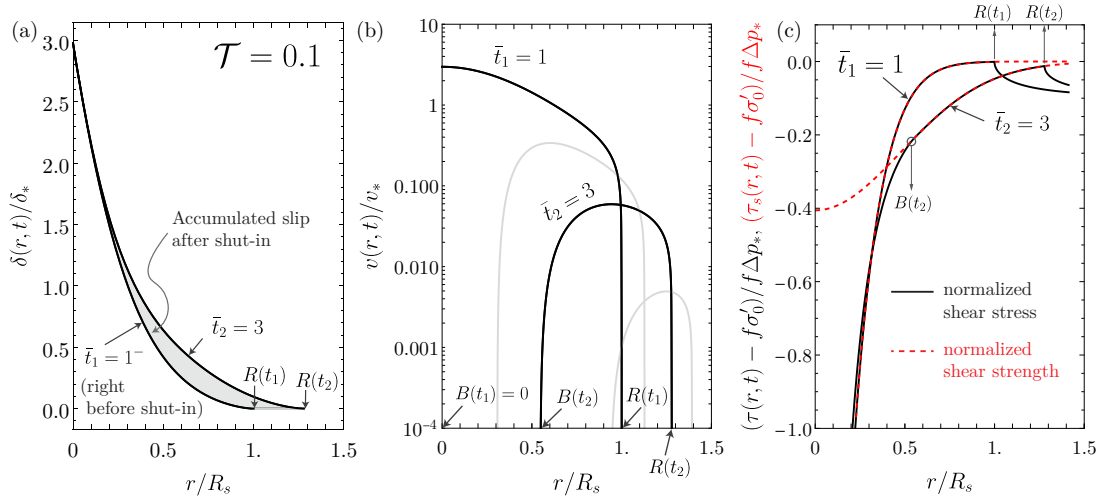
Figure 4.3: Normalized spatial profiles of (a) slip δ, (b) slip rate v, and (c) shear stress τ and shear strength τ_s, for a mildly critically-stressed fault with $\mathcal{T} = 0.1$, at two dimensionless times, one right before shut-in ($\bar{t}_1 = 1$) and the other one at some moment after shut-in ($\bar{t}_2 = 3$). The positions of the locking $B(t)$ and rupture $R(t)$ fronts are highlighted throughout panels (a) to (c). In panel (b), gray curves correspond to aseismic pulses at times $\bar{t} = 1.54$ and 6.25.

before shut-in. This amplification of fault shear stress after shut-in is due to the amount of slip accumulated through the passage of the slip pulse (shown in Figure 4.3a) and the non-local redistribution of stresses associated with it via the quasi-static non-local integral operator of equation (4.1). We further elaborate on the amplification of shear stress behind the locking front when analyzing the characteristics of slip rate and shear stress rate along the fault in Section 4.4.5.

4.4.3   Evolution of the rupture, locking, and pore-pressure back fronts: conditions for pulse-like propagation and arrest

We have identified three relevant fronts that propagate simultaneously upon the stop of the injection: the rupture front of radius $R(t)$, the pore-pressure back front of radius $P(t)$, and the locking front of radius $B(t)$. The temporal evolution of these three fronts is shown in Figure 4.4a for an exemplifying case with $\mathcal{T} = 0.15$. Since the only external action that drives the rupture pulses is the further increase of pore pressure after shut-in at distances $r > P(t)$, the pore-pressure back front must be located behind the rupture front in order to guarantee the sustained propagation of the rupture: $P(t) < R(t)$. Similarly, the propagation of the locking front is driven by the existence of a region within the pulse where the pore pressure decreases (and thus the shear strength increases to effectively re-lock the fault), such that $P(t) > B(t)$. Hence, the following inequalities must be satisfied during pulse-like propagation in the post-injection stage, $B(t) < P(t) < R(t)$, which are verified in all our numerical solutions, such as the one displayed in Figure 4.4a.
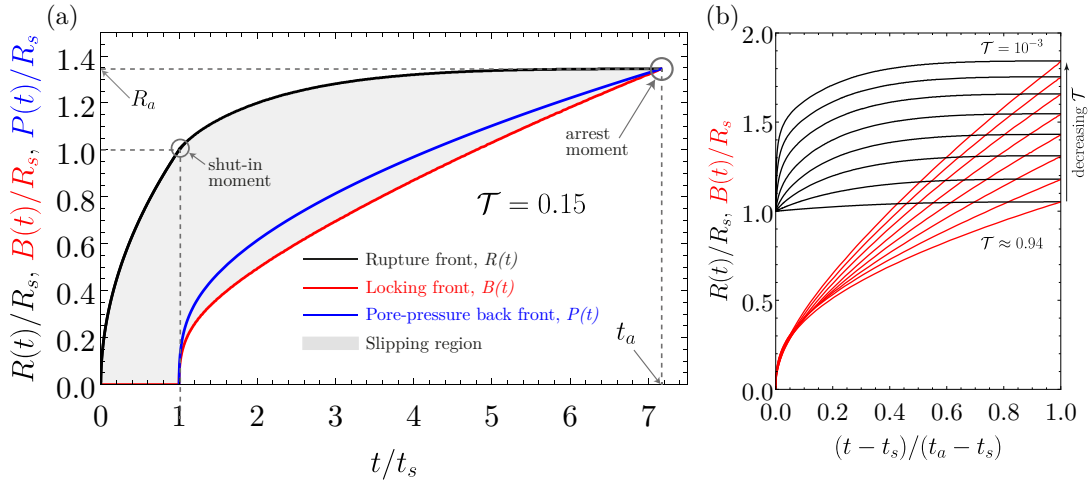
Figure 4.4: (a) Evolution of the rupture front radius, locking front radius, and pore-pressure back front radius, for an exemplifying case with $\mathcal{T} = 0.15$. The front radii are normalized by the rupture radius at the moment of shut-in R_s. Instants of shut-in of the injection t_s and arrest of the rupture t_a are highlighted, as well as the maximum run-out distance R_a. (b) Evolution of the rupture front radius and locking front radius for many values of $\mathcal{T}$ ranging from ≈ 0.94 to 10^{-3}.

On the other hand, since the Coulomb's shear strength on the fault plane is always bounded, the shear stress developed at the front of the rupture pulse must be bounded as well, to effectively allow both quantities to be equal. In other words, the slipping patch must propagate with no stress singularity at the "fracture" front of such a cohesive-like crack (Barenblatt, 1962). Hence, both stress intensity factors in mode II and mode III must be equal to zero at $r = R(t)$. This fracture-mechanics-like propagation condition was derived in appendix B of Sáez et al. (2022) for any axisymmetric circular shear rupture, and is still valid for pulse-like (annular) ruptures as long as the "fracture" is understood not as the current slipping patch, but rather as the region that has ever experienced any amount of slip since the start of the injection (i.e., for all $r < R(t)$). The condition reads as (Sáez et al., 2022)

$$\int_0^{R(t)} \frac{\Delta\tau\,(r,t)}{\sqrt{R(t)^2 - r^2}} r\,\mathrm{d}r = 0 \iff \int_0^{B(t)} \frac{\tau_0 - \tau^*\,(r,t)}{\sqrt{R(t)^2 - r^2}} r\,\mathrm{d}r + \int_{B(t)}^{R(t)} \frac{\tau_0 - f\left(\sigma_0' - \Delta p(r,t)\right)}{\sqrt{R(t)^2 - r^2}} r\,\mathrm{d}r = 0.$$

(4.9)

Note that $\Delta\tau\,(r,t) = \tau_0 - \tau\,(r,t)$, with τ_0 the initial shear stress and $\tau\,(r,t)$ the instantaneous shear stress distribution. In the right-hand side of equation (4.9), we have split the integral into two parts recognizing that within the slipping patch, the shear stress must be equal to the fault shear strength: $\tau\,(r,t) = f\left(\sigma_0' - \Delta p(r,t)\right)$, whereas in the re-locked region, $\tau^*\,(r,t)$ corresponds to the instantaneous shear stress distribution which depends on the current slip distribution through the quasi-static non-local integral operator of equation (4.1).

The second propagation condition for the post-injection aseismic pulses comes from the

analysis of Garagash (2012) for seismic and aseismic pulses driven by thermal pressurization. As we discuss in detail in Section 4.4.5, our aseismic pulses are akin to an annular "crack" of inner radius $B(t)$ and outer radius $R(t)$, as long as the dislocation density is replaced by the slip rate gradient $\partial v/\partial r$, and the change of shear stress by the shear stress rate $\partial \tau/\partial t$. The near-tip asymptotic behavior of classical cracks (Rice, 1968) is thus valid but in terms of $\partial \tau/\partial t$ and v. Having this result in mind, we can now invoke Garagash's healing condition, which states that the shear stress rate $\partial \tau/\partial t$ must be non-singular at the locking front to effectively allow the fault to re-lock. This is because within the slipping patch and, particularly, at the locking front, the shear stress rate must equal the shear strength rate (the plastic consistency condition, see for example, appendix A in Sáez et al., 2022), in our case, $\partial \tau/\partial t = -f\partial \Delta p/\partial t$. Since $\partial \Delta p/\partial t$ is bounded all over the fault plane, it follows that $\partial \tau/\partial t$ cannot be singular at the locking front.

Garagash obtained an integral equation similar to (4.9) based on the non-singularity of shear stress rate at the locking front (equation (19) in Garagash, 2012). Such integral equation is valid under the assumptions of his study in 2D elasticity for a solitary steady pulse traveling in anti-plane (III) or in-plane (II) mode of sliding. Indeed, if our pulse that is non-steady would be solved in 2D elasticity, a similar expression can be derived for the two symmetric pulses (traveling in opposite directions) that would emerge in that case, from known stress intensity factors (SIF) formulae (Tada et al., 2000). To the best of our knowledge, the SIF formulae for an annular crack under axisymmetric loading are unknown (numerical procedures have been proposed to calculate them in mode I, e.g., Clements and Ang, 1988). Nevertheless, one can still formalize this second propagation condition based on the near-tip asymptotic behavior of classical cracks as (Barenblatt, 1962; Rice, 1968)

$$K_{\dot{\tau}} = 0, \text{ with } \frac{\partial \tau(r,t)}{\partial t} \simeq \frac{K_{\dot{\tau}}}{\sqrt{2\pi\,[B(t)-r]}} \text{ when } r \to B(t)^-. \tag{4.10}$$

$K_{\dot{\tau}}$ is the so-called "stress-rate intensity factor" (Garagash, 2012) with units of $(\text{pressure/time}) \cdot \text{length}^{1/2}$. It quantifies the intensity of the leading-order (singular) term of $\partial \tau/\partial t$ near the locking front. Note that $K_{\dot{\tau}}$ may be also written in terms of the mode II, $K_{2,\dot{\tau}}$, and mode III, $K_{3,\dot{\tau}}$, stress-rate intensity factors, as $K_{\dot{\tau}}^2 = K_{2,\dot{\tau}}^2 + K_{3,\dot{\tau}}^2$. Indeed, since the two components of the shear stress rate on the fault plane must be non-singular along the locking front, equation (4.10) can be stated in the stronger form, $K_{2,\dot{\tau}} = K_{3,\dot{\tau}} = 0$. Note also that the stress-rate intensity factor is not the same than the stress intensity factor rate, at least along the locking front. For the latter, there is no stress intensity factor whatsoever, since there is no fracture tip and thus no potential singular term for τ when $r \to B(t)^-$. Hence, although it could have been tempting to write the healing condition (4.10) as $\mathrm{d}\mathcal{G}/\mathrm{d}t = 0$, where $\mathcal{G}$ is the energy release rate, such statement is not true.

Equations (4.9) and (4.10) are, therefore, the necessary conditions for the propagation of post-injection aseismic slip as an annular pulse. Together, these two equations describe the motion of the rupture front $R(t)$ and locking front $B(t)$ that are at quasi-static equilibrium with a given $\Delta\tau(r,t)$. Yet as already mentioned, we cannot solve these two equations without solving the

entire moving boundary value problem. However, they provide additional insights into the mechanics of the problem and, as shown in Section 4.4.5, define important characteristics of the slip rate and shear stress rate distributions along the fault plane.

We now seek for the conditions that characterize the final arrest of the rupture pulses. Figure 4.4a shows that as expected at the moment of arrest, the locking front $B(t)$ catches up the rupture front $R(t)$. Since in that instant the rupture pulse effectively vanishes, equation (4.10) has no relevance. However, the "fracture" (slipped surface) is still present and, to be at mechanical equilibrium, equation (4.9) must be satisfied. Since the second term of the right-hand side of (4.9) approaches zero at the time of arrest, equation (4.9) takes now the simpler form

$$\int_0^{R_a} \frac{\tau_0 - \tau^*(r, t_a)}{\sqrt{R_a^2 - r^2}} r \, \mathrm{d}r = 0, \tag{4.11}$$

where t_a is the time of arrest and $R_a = R(t_a)$ is the corresponding rupture radius at the arrest time (the maximum run-out distance). In the previous equation, R_a may be equivalently replaced by $B_a = B(t_a)$. Furthermore, since the rupture after shut-in is driven uniquely by the further increase of pore pressure that occurs in the region $r > P(t)$, the rupture arrest will be also characterized by the moment at which the pore-pressure back front catches up the rupture front (see Figure 4.4a). Therefore, the following conditions must be also met exactly at the time of arrest,

$$R(t_a) = B(t_a) = P(t_a), \tag{4.12}$$

and more importantly, by combining the previous equation with equation (4.8), we obtain an analytic relation between the radius R_a and time t_a of arrest,

$$R_a = \sqrt{4\alpha t_a} \left((t_a/t_s - 1) \ln\left(\frac{t_a}{t_a - t_s} \right) \right)^{1/2}, \tag{4.13}$$

which in the large-time limit ($t_a \gg t_s$) becomes simply $R_a \approx \sqrt{4\alpha t_a}$. Equations (4.11) and (4.13) provide a complete system of equations to solve for the time at arrest t_a and the maximum run-out distance R_a. However, the shear stress profile left by the arrested rupture $\tau^*(r, t_a)$ in equation (4.11) is unknown analytically. Hence, we must determine at least one of these two quantities numerically.

4.4.4   Arrest time and maximum run-out distance

We now determine numerically the normalized arrest time t_a/t_s and normalized maximum run-out distance R_a/R_s by spanning the relevant parameter space with 40 values of $\mathcal{T}$ ranging from 10^{-3} to 10, equally spaced in logarithmic scale. The results are presented in Figure 4.5. Marginally-pressurized faults ($\mathcal{T} \sim 10$) produce slip pulses that arrest almost immediately after the stop of the injection and practically do not grow further than the size of the ruptures
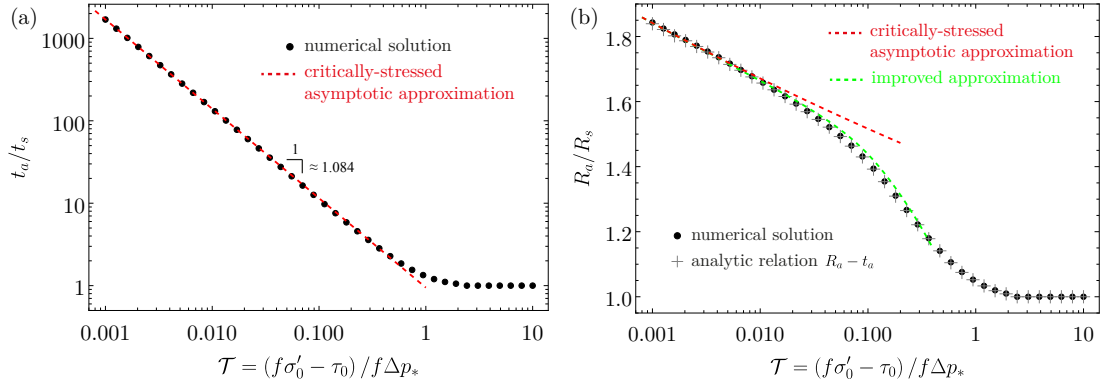
Figure 4.5: (a) Normalized arrest time and (b) normalized maximum run-out distance as a function of the stress-injection parameter $\mathcal{T}$. In (a) and (b), the red dashed line represents the asymptotic behavior in the critically-stressed regime ($\mathcal{T} \ll 1$), equations (4.14) and (4.15), respectively. In (b), the green dashed curve is an improved approximation obtained by substituting equation (4.14) directly into (4.13). The gray crosses correspond to the evaluation of R_a via the analytic relation, equation (4.13), using the numerical solution of t_a.

at the moment of shut-in (R_s), whereas critically-stressed faults ($\mathcal{T} \ll 1$) host events that can last up to $\approx 10^3$ times the injection time t_s and grow approximately up to 1.8 times the rupture radius at the shut-in time (for the smallest value of $\mathcal{T}$ considered). Critically-stressed faults are, therefore, the asymptotic regime of more practical interest. We thus focus on determining its behavior precisely.

For the normalized arrest time, Figure 4.5a shows a clear power law between t_a/t_s and $\mathcal{T}$. Using a linear least square regression, we obtain

$$\frac{t_a}{t_s} \approx a\mathcal{T}^{-b}, \tag{4.14}$$

with $a = 0.946876$ and $b = 1.084361$. In solving the least-squares problem, we have considered data points satisfying $\mathcal{T} \lesssim 0.01$ ($\ll 1$) and obtained an R^2 equal to 0.999993.

We can now use the analytic relation between R_a and t_a, equation (4.13), to construct a critically-stressed asymptotic approximation for the normalized maximum run-out distance using the power-law relation (4.14). In particular, at large arrest times ($t_a \gg t_s$), (4.13) is approximately equal to $R_a/R_s \approx (1/\lambda)\sqrt{t_a/t_s}$. Substituting $\lambda \approx 1/\sqrt{2\mathcal{T}}$ (see Section 4.4.1) and (4.14) into the previous expression, leads to the sought critically-stressed approximation,

$$\frac{R_a}{R_s} \approx \left(\frac{2a}{\mathcal{T}^{b-1}}\right)^{1/2}, \text{ or } R_a \approx \left(\frac{4a\alpha t_s}{\mathcal{T}^b}\right)^{1/2}. \tag{4.15}$$

In addition, we can substitute equation (4.14) directly into (4.13) to provide an improved asymptotic approximation for the critically-stressed regime that is approximately valid over a broader range of values of $\mathcal{T}$ (green curve in Figure 4.5b). Note that in Figure 4.5b, we have also plotted the values of R_a not from the numerical solution, but rather by evaluating the

75
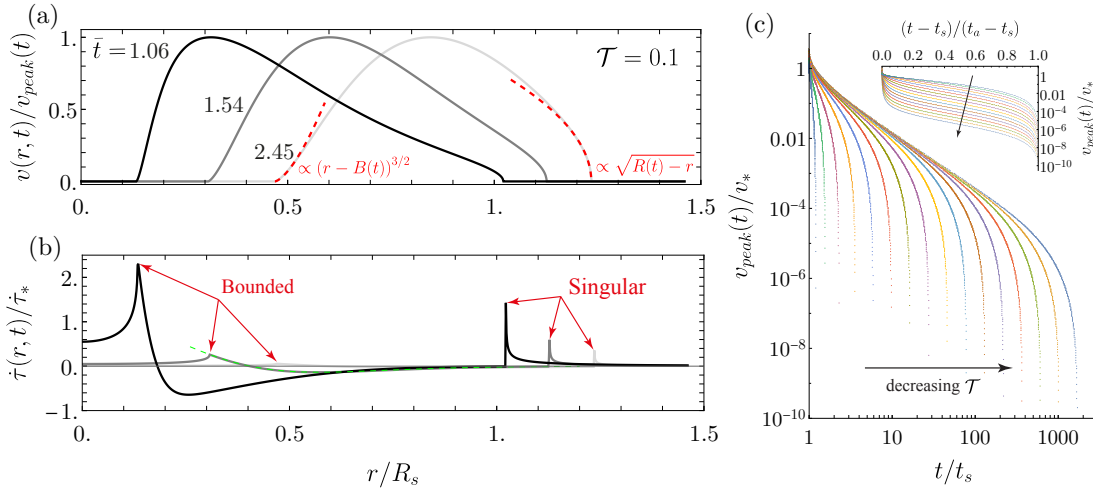
Figure 4.6: (a) Slip rate distribution normalized by the instantaneous peak slip rate $v_{peak}(t)$ at three dimensionless times for a mildly critically-stressed fault with $\mathcal{T} = 0.1$. Red dashed curves represent the tip asymptotic behavior, equation (4.17). (b) Shear stress rate distributions normalized by the stress-rate scale $\dot{\tau}_* = f \Delta p_* / t_s$, for the same times than in (a). The singular and non-singular stress rate fields near the rupture and locking fronts, respectively, are highlighted in red. The green dashed curve corresponds to the normalized rate of shear strength at $\bar{t} = 1.54$. (c) Evolution of the normalized peak slip rate in time for many values of $\mathcal{T}$ ranging from ≈ 0.75 to 10^{-3} (from left to right). In the inset, same results but time is scaled to be between 0 at shut-in and 1 at arrest.

analytic relation (4.13) (gray crosses) given the numerical solution of t_a. The latter is just to illustrate the exactness of the relation between the radius of arrest and the time of arrest (4.13).

4.4.5   Characteristics of slip rate and shear stress rate

We now examine in detail the slip-rate characteristics of the aseismic pulses (Figure 4.6). Let us consider the quasi-static elastic equilibrium that relates the fault shear stress τ and slip distribution δ for an axisymmetric circular shear rupture, in the compact form given by Bhattacharya and Viesca (2019). We differentiate that integral equation with respect to time (using Leibniz's integral rule, applying the condition of no shear stress singularity at the rupture front $\partial \delta (R(t), t)/\partial r = 0$, and the fact that $\partial v/\partial r = 0$ within the re-locked region $0 < r < B(t)$) to arrive to the following relation[1],

$$\frac{\partial \tau (r, t)}{\partial t} = \frac{\mu}{2\pi} \int_{B(t)}^{R(t)} \frac{\partial v(\xi, t)}{\partial \xi} \left(\frac{K[k(r/\xi)]}{\xi + r} + \frac{E[k(r/\xi)]}{\xi - r} \right) d\xi, \tag{4.16}$$

where $K[\cdot]$ and $E[\cdot]$ are the complete elliptic integrals of the first and second kind, respectively, and $k(x) = 2\sqrt{x}/(1 + x)$. Equation (4.16) is akin to the elastic equilibrium of an annular crack

---

[1]albeit with a minus one factor due to the difference between the geomechanics convention of positive stresses in compression and the classical solid mechanics convention of positive stresses in tension.

of inner radius $B(t)$ and outer radius $R(t)$, but in terms of shear stress rate $\partial\tau/\partial t$ and slip rate gradient $\partial v/\partial r$, instead of shear stress τ and slip gradient $\partial\delta/\partial r$. The asymptotic behavior of the slip rate distribution near the rupture and locking fronts thus follows the tip asymptotics for displacement discontinuity of classical cracks (Rice, 1968):

$$v(r,t) \propto \sqrt{R(t)-r} \ \text{ when } \ r \to R(t)^-\ , \text{ and } \ v(r,t) \propto (r-B(t))^{3/2} \ \text{ when } \ r \to B(t)^+. \quad (4.17)$$

Note that the rupture front features a stress-rate singularity in the classical form

$$\frac{\partial\tau(r,t)}{\partial t} \simeq \frac{K_{\dot\tau,R}}{\sqrt{2\pi\,(r-R(t))}} \ \text{ when } \ r \to R(t)^+, \qquad\qquad (4.18)$$

where $K_{\dot\tau,R}$ is the "stress-rate intensity factor". The subscript R is introduced to distinguish $K_{\dot\tau,R}$ from the stress-rate intensity factor of the locking front $K_{\dot\tau}$ already introduced in equation (4.10). Note that the singularity may be written in a stronger form for the two components of shear stress rate on the fault plane (the mode II and mode III directions), as already discussed for the locking front in Section 4.4.3. On the other hand, the healing condition (4.10) has been already taken into account in equation (4.17) for the locking front, such that the leading-order term of the slip rate is now the next term of the near-tip asymptotic expansion of classical cracks $v \propto s^{3/2}$ (Rice, 1968), where s is the distance from the tip towards the slipping patch. In this way, the shear stress rate is bounded at the locking front, whereas nothing prevents the shear stress rate to be infinite at the rupture front. It is indeed the shear stress τ the one quantity that must be bounded at the rupture front, according to the condition (4.9).

The foregoing tip asymptotics are highlighted in red in Figures 4.6a-b, which show typical slip pulses and their corresponding shear stress rate distributions along the fault plane at three times. In Figure 4.6b, the green dashed curve corresponds to the normalized rate of shear strength at $\bar t = 1.54$ that must be equal to the normalized shear stress rate within the slipping patch according to the consistency condition mentioned in Section 4.4.3. Such equality can be clearly visualized in this figure. Note that the slip rate in Figure 4.6a is normalized by the instantaneous maximum slip rate $v_{peak}(t)$, that decays fast in time. The evolution of the maximum slip rate is indeed displayed in Figure 4.6c for relevant values of $\mathcal{T}$ ranging from 10^{-3} to ≈ 0.75 (greater values than 0.75 correspond to ruptures that arrest almost immediately after shut-in). Owing to the relatively fast decay of the maximum slip rate after shut-in, the peak shear stress rate at both the locking and rupture fronts is also observed to decay fast, as depicted in Figure 4.6b.

4.5   Pulse-like non-circular ruptures

In this section, we examine the effect of a Poisson's ratio different than zero on the propagation and ultimate arrest of the post-injection aseismic pulses. For this purpose, we consider a fixed value of $\nu = 1/4$ (Poisson's solid).

4.5.1   Recall on the self-similar solution before shut-in

Sáez et al. (2022) also solved the continuous-injection problem for the case of $v \neq 0$. They showed that the rupture front is well-approximated by an elliptical shape that becomes more elongated for increasing values of v and decreasing values of $\mathcal{T}$: the more critically stressed the fault is, the more elongated the rupture becomes. The aspect ratio of the quasi-elliptical rupture fronts is upper bounded by $1/(1-v)$ in the critically-stressed limit ($\mathcal{T} \ll 1$), and lower bounded by $(3-v)/(3-2v)$ in the marginally-pressurized limit ($\mathcal{T} \sim 10$). Furthermore, the rupture area $A_r(t)$ evolves simply as $A_r(t) = 4\pi\alpha\lambda^2 t$ (linear with time), and interestingly it does not depend on the Poisson's ratio v (see figure 6 in Sáez et al., 2022). The previous numerical observations led to closed-form approximate expressions for the entire evolution of the quasi-elliptical rupture fronts in terms of the semi-major $a(t)$ and semi-minor $b(t)$ axes of an ellipse, as $a(t) = R(t)/\sqrt{1-v}$ and $b(t) = R(t)\sqrt{1-v}$ in the critically-stressed regime, and $a(t) = R(t)\sqrt{3-v}/\sqrt{3-2v}$ and $b(t) = R(t)\sqrt{3-2v}/\sqrt{3-v}$ in the marginally-pressurized regime, with $R(t)$ the rupture radius of a circular rupture for the same value of $\mathcal{T}$, which is known analytically (see Section 4.4.1).

4.5.2   Effect of v on the propagation of the aseismic pulses

We summarize the main characteristics of the propagation of pulse-like non-circular ruptures in Figure 4.7. This figure is composed by four snapshots of the normalized slip rate distribution for a mildly critically-stressed fault with $\mathcal{T} = 0.1$. Each snapshot represents a remarkably different propagation phase. The first one, Figure 4.7a, corresponds to a moment right before stopping the injection, specifically at $\bar{t} = 0.99$, where $\bar{t} = t/t_s$. At this time, the rupture is still propagating in crack-like mode. For this value of $\mathcal{T}$, the quasi-elliptical rupture front outpaces the pore-pressure perturbation front. Note that the spatial coordinates in Figure 4.7 are normalized by the rupture lengthscale $R_s = \lambda\sqrt{4\alpha t_s}$ (radius of a circular rupture with the same value of $\mathcal{T}$, see Section 4.4.1). The second snapshot, Figure 4.7b, displays the rupture after shut-in at approximately 4.75 times the injection duration. In this figure, we can already observe the locking front and thus the propagation of the rupture as an annular pulse. Interestingly, although the rupture front is clearly elongated along the mode II direction of sliding (same as it is before shut-in), the locking front seems to be slightly elongated along the mode III direction instead.

Figures 4.7c and 4.7d show the most remarkable effects of considering a Poisson's ratio different than zero. Figure 4.7c corresponds to the instant at which the locking front is about to coalesce with the rupture front along the mode III direction of sliding. Note that at this time of coalescence t_c, approximately equal to 9.44 times the injection duration in this case, the pore-pressure back front is also intersecting both the rupture and locking fronts. Let us denote the maximum run-out distance of the rupture in the mode III direction as ℓ_c (see Figure 4.7c for its definition). The previous observation, that was somewhat expected from the analysis of circular ruptures (see equation (4.12)), means that there is a unique relation between ℓ_c and t_c,
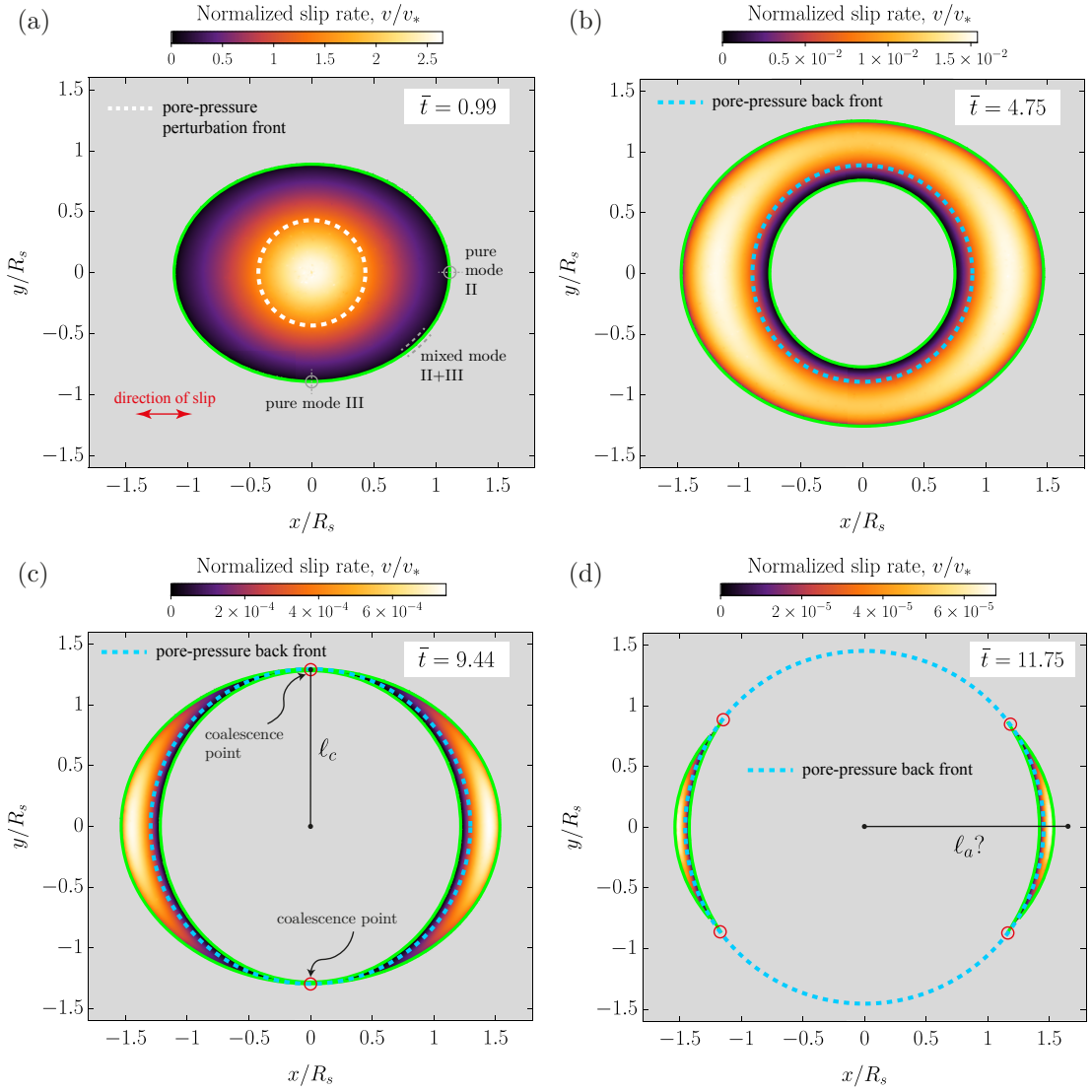
Figure 4.7: Snapshots of normalized slip rate distribution for a non-circular rupture with $\mathcal{T} = 0.1$ and $\nu = 0.25$. The spatial coordinates x and y are scaled by the rupture radius at the shut-in time R_s for the same $\mathcal{T}$ but $\nu = 0$, whereas dimensionless time $\bar{t} = t/t_s$ as usual. (a) Crack-like propagation right before shut-in ($\bar{t} = 0.99$). (b) Propagation as an annular pulse after shut-in ($\bar{t} = 4.75$). (c) Moment in which the locking and rupture fronts are about to coalesce ($\bar{t} \approx 9.44$). (d) Propagation after coalescence of the fronts as two "moon-shaped" pulses traveling in opposite directions ($\bar{t} = 11.75$). The maximum run-out distance of the rupture ℓ_a that will be eventually reached at some later time is depicted. The positions at which the locking, rupture, and pore-pressure back fronts intersect each other are indicated with red circles.

in the form $\ell_c = P(t_c)$, where $P(t)$ is the instantaneous radius of the pore-pressure back front known analytically from equation (4.8). Moreover, after the coalescence of the fronts, Figure 4.7d displays that the original annular pulse is split into two symmetric "moon-shaped" pulses that travel in opposite directions. The moving positions at which the locking and rupture fronts are intersecting each other are shown with red circles in Figure 4.7d. These positions are again such that the pore-pressure back front is located exactly at the same place. The condition (4.12) for circular ruptures at the time of arrest is thus still valid for non-circular ruptures but now at any time $t_c \le t \le t_a$. Finally, the instantaneous rupture area of each moon-shaped pulse decreases continuously with time and will eventually collapse into a point located along the x axis at some distance ℓ_a as depicted in Figure 4.7d. ℓ_a corresponds to the maximum run-out distance of the entire rupture and, similarly to the case of circular ruptures, equation (4.13) will now take the form $\ell_a = P(t_a)$, where t_a is the time of arrest.

4.5.3   Effect of ν on the arrest time and maximum run-out distance

We calculate the time of arrest t_a and maximum run-out distance of the rupture ℓ_a, as well as the time of coalescence t_c and maximum run-out distance in the mode III direction ℓ_c, for ten values of the stress-injection parameter $\mathcal{T}$ ranging from 10^{-3} to ≈ 0.59. This range allows us to span the most relevant part of the parameter space associated with critically-stressed faults. Figure 4.8a summarizes the results for the normalized arrest time t_a/t_s and normalized time of coalescence t_c/t_s, including the results for the arrest time of circular ruptures $t_a^{\nu=0}$. We observe that the coalescence of the fronts occurs at earlier times than the arrest of circular ruptures. Moreover, a Poisson's ratio $\nu \ne 0$ has the clear effect of delaying the arrest of the aseismic pulses with regard to the circular case. To better quantify this delayed arrest, we plot the same results in the inset but normalize the arrest and coalescence times by the arrest time of circular ruptures. It can be seen that the more critically-stressed the fault is, the longer it takes for non-circular ruptures to arrest compared to circular ones. Furthermore, the ratio $t_a/t_a^{\nu=0}$ seems to approach an asymptotic value of ≈ 1.21 in the critically-stressed limit (when $\mathcal{T} \to 0$).

Figure 4.8b shows the results for the normalized maximum run-out distance of the rupture ℓ_a/R_s and normalized maximum run-out distance in the mode III direction ℓ_c/R_s. In accordance with the results for t_c and t_a, the distance ℓ_c is lower than the arrest radius of circular ruptures R_a for the same value of $\mathcal{T}$, whereas the maximum run-out distance of non-circular ruptures ℓ_a is greater than the maximum run-out distance of its circular counterpart R_a. In addition, the relations $\ell_c = P(t_c)$ and $\ell_a = P(t_a)$ discussed in the previous section are shown to be in good agreement (gray crosses in Figure 4.8b) with the numerical results up to numerical discretization errors. Moreover, the inset shows the run-out distances ℓ_a and ℓ_c but normalized by the arrested radius of circular ruptures R_a. The maximum run-out distance ℓ_a seems to approach an asymptotic value in this case of $\approx 1.1 R_a$ in the limit of critically-stressed faults.
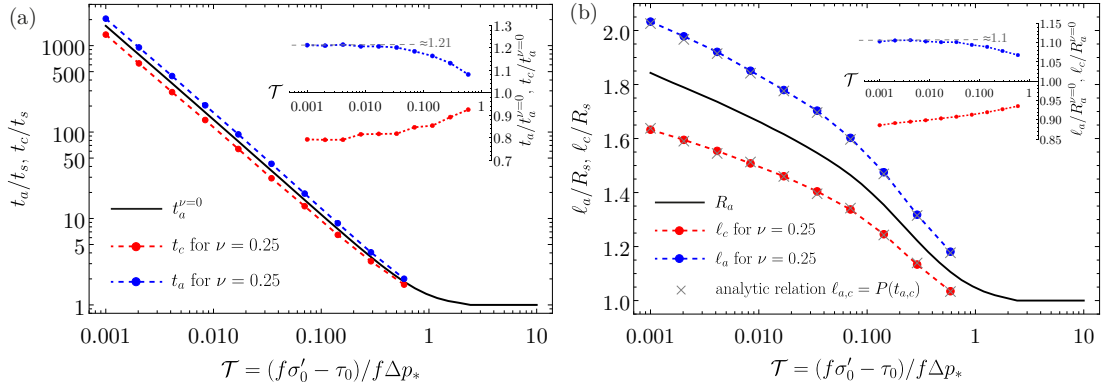
Figure 4.8: (a) Normalized arrest time t_a and coalescence time t_c for $\nu = 0.25$ as a function of the stress-injection parameter $\mathcal{T}$ for values ranging from 10^{-3} to ≈ 0.59. The inset shows the same results but normalized by the arrest time of circular ruptures $t_a^{\nu=0}$. (b) Same as (a) but for the maximum run-out distance of the rupture in the mode II ℓ_a and mode III ℓ_c directions of sliding. In the inset, same results but normalized by the arrest radius of circular ruptures R_a. Gray crosses in (b) come from evaluating t_a and t_c of panel (a) in equation (4.8) for the pore-pressure back front.

4.6 Discussion

4.6.1 Critically-stressed regime versus marginally-pressurized regime

Figures 4.5 and 4.8 summarize one of the most important results of this article. Marginally-pressurized faults ($\mathcal{T} \sim 10$) produce aseismic pulses that arrest almost immediately after shut-in, whereas critically-stressed faults ($\mathcal{T} \ll 1$) are predicted to host ruptures that propagate for several orders of magnitude the injection duration and grow up to approximately twice the size of the ruptures at the moment of shut-in (for the smallest value of $\mathcal{T}$ considered). Critically-stressed faults are therefore the relevant propagation regime that is able to sustain seismicity after shut-in. Under this regime, the long-lived aseismic pulses provide a longer exposure of the surrounding rock mass to continuous stressing due to aseismic slip and, at the same time, their longer run-out distances perturb a larger volume of rock mass up to $\approx 2^3 = 8$ times larger than the volume affected at the moment of shut-in, therefore increasing the likelihood of triggering earthquakes during the post-injection stage compared to the marginally-pressurized case.

To illustrate under what conditions these two regimes can occur, let us consider some characteristic values of a fault undergoing fluid injection. Consider that water is injected into a fault zone at a constant volume rate $Q \sim 30$ [l/s], which is typical of hydro-shearing treatments of deep geothermal reservoirs at around 3 to 4 km depth (Ellsworth et al., 2019). Assume also a fluid dynamic viscosity $\eta \sim 10^{-3}$ [Pa·s]. The fault hydraulic transmissivity can vary over several orders of magnitude. Consider, for instance, a plausible value of $kw \sim 10^{-12}$ [m^3] (Evans, Genter, et al., 2005). This yields a characteristic pressure at the fluid source of $\Delta p_c = 30$ [MPa] and an intensity of the injection $\Delta p_* \approx 2.4$ [MPa] (equation (4.3)). Let us

consider for the initial effective normal stress a characteristic value of $\sigma'_0 \sim 60$ [MPa], that is somewhat consistent with a depth of 3-4 km under gravitational loading and hydrostatic conditions. Assuming a friction coefficient $f = 0.6$, the initial fault shear strength is $f\sigma'_0 = 36$ [MPa], while the intensity of the strength reduction due to fluid injection is $f\Delta p_* \approx 1.4$ [MPa]. The amount of initial shear stress τ_0 acting on the fault will finally determine the regime of the fault response in this example. Consider first a fault that is close to failure, say $\tau_0 = 35.9$ [MPa] (0.1 [MPa] to failure). This leads to a small value of the stress-injection parameter $\mathcal{T} \approx 0.07$ (equation (4.5)), and therefore to a fault responding in the so-called critically-stressed regime ($\mathcal{T} \ll 1$). Before shut-in, the fluid-induced aseismic slip front in this example is predicted to outpace the pore pressure perturbation front by a constant factor $\lambda \approx 1/\sqrt{2\mathcal{T}} \approx 2.7$ (Section 4.4.1), for the case of circular ruptures. Consider that the injection was conducted during a period of $t_s = 1$ [day]. Then, after shut-in, the post-injection aseismic pulse is expected to propagate for $t_a - t_s \approx 16$ [days] (equation (4.14)) and reach a maximum run-out distance of ≈ 1.54 times the run-out distance at the moment of shut-in (equation (4.15)). To close this dimensional example, let us assume that the fault has a hydraulic diffusivity of, say, $\alpha = 0.01$ [m^2/s]. The radius of the rupture at the moment of shut-in is $R_s = \lambda\sqrt{4\alpha t_s} \approx 159$ [m] (see again Section 4.4.1), and the maximum run-out distance of post-injection aseismic slip will be $R_a \approx 1.54 \cdot 159$ [m] ≈ 245 [m]. If the hydraulic diffusivity were ten times lower, R_s and R_a would decrease by approximately 30%.

Consider the same example of the previous paragraph, but now with a fault that is further away from failure. Assume, for instance, a lower value of the initial shear stress $\tau_0 = 25$ [MPa] (11 [MPa] to failure). The stress-injection parameter for this case becomes $\mathcal{T} \approx 7.9$, well within the marginally-pressurized regime ($\mathcal{T} \sim 10$). Prior shut-in, the slip front is predicted to lag the pore pressure perturbation front by a factor $\lambda \approx (1/2)\exp[(2 - \gamma - \mathcal{T})/2] \approx 0.02$ (Section 4.4.1). Moreover, upon the stop of the injection, the rupture is expected to arrest almost immediately (see Figure 4.5), such that $t_a \approx t_s \approx 1$ [day] and $R_a \approx R_s = \lambda\sqrt{4\alpha t_s} \approx 1.2$ [m]. In the two previous examples, the end-member regimes were achieved by changing only the initial shear stress acting on the fault or, equivalently, the distance to failure. This highlights the importance of the pre-injection stress state on determining the response of the fault. However, there is another relevant quantity that may equally change the fault response regime, namely, the intensity of the injection Δp_*. So far, we have assumed hydraulic parameters resulting in $\Delta p_* \approx 2.4$ [MPa] (and $\Delta p_c = 30$ [MPa]). Imagine now that the fault is still relatively close to failure as in the first example ($\tau_0 = 35.9$ [MPa]) but a much smaller amount of fluid is being injected, say $Q = 1$ [l/s]. This is unlikely the case of a hydraulic stimulation but could instead occur in the case of a natural source of fluids occurring at the same depth. The intensity of the injection (equation (4.3)) is now $\Delta p_* \approx 0.08$ [MPa] (with $\Delta p_c = 1$ [MPa]), and the corresponding stress-injection parameter $\mathcal{T} \approx 2.1$. This will lead equivalently to a rupture that lags the fluid pressure front during continuous injection ($\lambda \approx 0.37$) and that arrest almost immediately after shut-in. The latter, despite the fact that the fault was "just" 0.1 [MPa] away from failure under ambient conditions. On the other hand, a more intense injection than the one with $Q = 30$ [l/s] will act in the direction of moving the fault response towards the critically-stressed regime (decreasing

values of $\mathcal{T}$). Those injections might however sometimes open the fault (if $\Delta p_c \gtrsim \sigma_0'$), a mechanism that is not accounted in this work.

4.6.2 Conceptual model of post-injection seismicity

In the next sections, we use our model to investigate to which extent post-injection aseismic slip can be considered as a mechanism for the delayed triggering of seismicity. However, before going into the details of the discussion, it seems convenient to establish first a few general concepts. First, we note that any model that aims at explaining observations of post-injection seismicity must produce spatio-temporal changes of pore pressure or solid stresses after shut-in. Our model produces both of them. In fact, the pore pressure changes alone are essentially equal to the ones already considered by Parotidis et al. (2004) to explain the so-called back front of seismicity that is sometimes observed after the termination of fluid injections. Note that Parotidis et al.'s model assumes the increase of pore pressure as the only triggering mechanism of seismicity. We, instead, elaborate on a mechanism based on the combined effect of transient changes in solid stresses due to aseismic slip and pore pressure after shut-in. For the sake of simplicity, we carry out all discussions in terms of circular ruptures only. Rupture non-circularity does not modify the order of magnitude of the results.

Let us define now conceptually what seismicity means in the context of our model. We consider that a single fault plane undergoes some transient fluid injection that may be approximated as a pulse of injection rate (see Figure 4.1c). It is assumed that as a result of the injection, the fault slides predominantly aseismically. Seismic events are thought to be triggered on unstable patches of the same fault plane (due to, for instance, heterogeneities in rock frictional properties) or other pre-existing discontinuities in the surroundings of the slowly propagating rupture. The former and latter events are commonly denominated as on-fault and off-fault seismicity, respectively, a terminology that we use later on. Note that an important underlying assumption of this conceptual model is that the unstable patches of the *aseismic* fault do not represent a sufficiently large area to change its predominantly stable mode of sliding to a large dynamic rupture.

We define a Mohr-Coulomb failure function in the form,

$$F(\boldsymbol{x}, t; \boldsymbol{n}) = |\tau(\boldsymbol{x}, t; \boldsymbol{n})| - f\left(\sigma(\boldsymbol{x}, t; \boldsymbol{n}) - p(\boldsymbol{x}, t)\right), \tag{4.19}$$

where τ and σ are the shear and total normal stresses acting on a certain unstable patch with unit normal vector $\boldsymbol{n}$ at a given position $\boldsymbol{x}$ and time t, p is the pore-fluid pressure, and f is a constant (static) friction coefficient. The failure function is such that $F \leq 0$ always. The inequality $F < 0$ holds when no frictional failure occurs, whereas the equality $F = 0$ is valid whenever frictional sliding is activated. The initial stress state is assumed such that $F(\boldsymbol{x}, t < 0; \boldsymbol{n}) < 0$ at all pre-existing discontinuities before injection starts. Once injection begins, the failure function may approach zero by changes in the solid stresses τ and σ and the pore pressure p. Upon failure of a certain patch, slip may evolve seismically only if the

friction coefficient is allowed to weaken. The time-dependent nucleation of instabilities and, moreover, the explicit modeling of seismicity, are out of the scope of our study. Instead, we consider a conceptual model in which any positive change of the failure function at a certain position and time may lead to frictional sliding and, subsequently, to the *possibility* of triggering an instability.

We introduce two types of changes of the failure function that will prove to be useful for our analysis. The first one, a static change ΔF between two times,

$$\Delta F(\boldsymbol{x}; \boldsymbol{n}) = \Delta \tau(\boldsymbol{x}; \boldsymbol{n}) - f\left(\Delta \sigma(\boldsymbol{x}; \boldsymbol{n}) - \Delta p(\boldsymbol{x})\right). \tag{4.20}$$

The second one, an instantaneous change $\dot{F}$,

$$\dot{F}(\boldsymbol{x}, t; \boldsymbol{n}) = \dot{\tau}(\boldsymbol{x}, t; \boldsymbol{n}) \operatorname{sgn}(\tau(\boldsymbol{x}, t; \boldsymbol{n})) - f\left(\dot{\sigma}(\boldsymbol{x}, t; \boldsymbol{n}) - \dot{p}(\boldsymbol{x}, t)\right). \tag{4.21}$$

ΔF is widely known in seismology as the Coulomb stress change (King et al., 1994), a terminology we adopt hereafter. Note that in equation (4.20), we assume that the change of shear stress $\Delta \tau$ is positive if it occurs in the same direction as the shear stress at the selected initial time. On the other hand, in equation (4.21), $\operatorname{sgn}(\cdot)$ is the sign function and the dot over the scalar fields represents a partial derivative in time. $\dot{F}$ is commonly denominated as the Coulomb stressing rate, a quantity that is sometimes correlated to seismicity rates (Dieterich, 1994). Finally, we highlight that positive contributions to failure $\Delta F > 0$ ($\dot{F} > 0$) are given by both positive changes of pore pressure $\Delta p > 0$ ($\dot{p} > 0$) and negative changes of total normal stress $\Delta \sigma < 0$ ($\dot{\sigma} < 0$). The effect of the shear stress is however less straightforward and knowledge about the direction of τ and thus about the absolute state of stress is required to evaluate its relative contribution to ΔF ($\dot{F}$).

4.6.3   On-fault seismicity

Theoretical considerations

On fault, both aseismic-slip stress transfer and pore pressure changes are active during the post-injection stage. We use the Coulomb stressing rate $\dot{F}$ as an indicator of the regions where seismicity is expected. Let us first note that due to the planarity of the fault, the total normal stress rate $\dot{\sigma}$ is zero. Hence, the only component of stress rate that is active along the fault plane is the shear one $\dot{\tau}$. Moreover, since the absolute state of stress of the fault is known, we can assume by convention that $\tau > 0$ and consequently that positive rates of shear stress are the ones that contribute to frictional failure. Along the fault plane, equation (4.21) thus further simplifies to

$$\dot{F}(\boldsymbol{x}, t) = \dot{\tau}(\boldsymbol{x}, t) + f \Delta \dot{p}(\boldsymbol{x}, t). \tag{4.22}$$

We first analyze the stress-transfer effect, $\dot{\tau}$ in equation (4.22). With reference to the characteristics of slip rate and shear stress rate that we describe in detail in Section 4.4.5, it can

be readily shown that the shear stress rate acting on possible unstable patches is positive everywhere along the fault plane. For the region outside of the pulse, this can be derived after differentiating equation (4.1) with respect to time and noting that seismicity should be triggered predominantly in the proximity of both the locking and rupture fronts, as a consequence of the amplification of shear stress rate concentrated near the tips of the aseismic pulses (see Figure 4.6b). Regarding the inside of the pulse, the value of $\dot{\tau}$ in our model, which is simply equal to the fault shear strength rate, is somewhat irrelevant. The actual stress-transfer effect comes rather from considering that unstable patches may be effectively locked and surrounded by aseismic slip. The latter would increasingly load the locked patches in shear until eventually a dynamic event could be triggered.

With regard to the pore-pressure effect, $f\Delta\dot{p}$ in equation (4.22), its contribution to seismicity can be understood readily from the mere definition of the pore-pressure back front. At distances $r > P(t)$, where $P(t)$ is the radius of the front, the pore pressure rate is positive. Therefore, the region ahead of the pore-pressure back front is where fluid-induced instabilities are expected, a result that was already introduced by Parotidis et al. (2004). Conversely, at distances $r < P(t)$, the opposite holds $\Delta\dot{p} < 0$, and thus the triggering of instabilities is here inhibited.

We are now ready to superimpose the effects of $\dot{\tau}$ and $f\Delta\dot{p}$ to notably determine the sign of $\dot{F}$. This is schematized in Figure 4.9a, where four different regions in which the results of the superposition operate differently, are delineated by the three relevant fronts of the problem, namely, the rupture front $R(t)$, the pore-pressure back front $P(t)$, and the locking front $B(t)$. In region R1 for distances ahead of the pulse $r > R(t)$, the Coulomb stressing rate $\dot{F}$ is always positive. In this region, seismicity is expected to be triggered by the contribution of both a positive shear stress rate $\dot{\tau} > 0$ and a positive pore pressure rate $\Delta\dot{p} > 0$. Let us further analyze the magnitude and distribution of $\dot{F}$ here. This is shown in Figure 4.9b, where the spatial profile of normalized Coulomb stressing rate is plotted at various dimensionless times for an exemplifying case with $\mathscr{T} = 0.1$. The solitary contribution of the pore pressure rate, which is independent of the value of $\mathscr{T}$, is also included in this figure. Note that the scale of the Coulomb stressing rate $\dot{F}_*$ comes from equation (4.22) and is equal to $\dot{F}_* = f\Delta p_*/t_s$. We observe from Figure 4.9b that ahead of the rupture pulse and at early times after shut-in, $\dot{F}$ is dominated by the amplification of shear stress rate ($\dot{\tau} \gg \Delta\dot{p}$), whereas at intermediate times and notably at large times, the pore pressure rate becomes the most dominant quantity ($\Delta\dot{p} \gg \dot{\tau}$) from some distance ahead of the rupture front that gets increasingly closer to the slip front with time. However, at the rupture front itself and very close to it, the shear stress rate will always dominate the magnitude of $\dot{F}$ due to the square-root singularity of $\dot{\tau}$ discussed in Section 4.4.5.

Let us now consider the regions R2 and R3 that compose the slipping patch. Here, seismic events are promoted by the increase of shear stress $\dot{\tau} > 0$ acting on locked unstable patches that are loaded by surrounding aseismic slip, a mechanism that is denoted by $\dot{\delta} > 0$ in Figure 4.9a. Moreover, in region R2 ahead of the pore pressure back front $r > P(t)$, the pore pressure

rate is also positive, meaning that the Coulomb stressing rate $\dot{F}$ is strictly positive too. The triggering of instabilities in region R2 is thus expected. Conversely, in the region R3 behind the pore pressure back front $r < P(t)$, the pore pressure rate is negative. As such, its effect counterbalances the positive contribution due to aseismic slip ($\dot{\delta} > 0$). Whether $\dot{F}$ is positive or negative in this region is not possible to know from our calculations, because we do not explicitly model the effect of any potential locked patch on the shear loading. Nevertheless, by assuming that the shear loading $\dot{\tau}$ is some unknown but positive quantity, the solitary effect of the pore pressure changes provides a lower bound for $\dot{F}$ within the slipping patch. Even more, the pore-pressure effect $f\Delta\dot{p}$ is a lower bound of $\dot{F}$ over the entire fault plane since as already discussed, the stress-transfer effect $\dot{\tau}$ is positive everywhere. This can be clearly observed in Figure 4.9b when looking at the regions behind (R4) and ahead (R1) of the rupture pulse.

Finally, in the region R4 behind the slip pulse $r < B(t)$, seismicity is promoted by the amplification of the shear stress rate near the locking front, albeit such amplification is going to be neutralized to some extent by the negative pore pressure rate operating in this region. In fact, Figure 4.9b shows that the negative pore pressure rate appears to completely neutralize the stress rate amplification behind the locking front for the particular case shown in this figure. Furthermore, a general proof of this numerical observation can be developed as follows. First, we recall that $\dot{F} = 0$ within the slipping patch and, particularly, when $r \to B(t)^+$. Note that we have just referred to $\dot{F}$ with the same notation than the Coulomb stressing rate acting on unstable locked patches (equation (4.22)). However, we are rather referring by $\dot{F}$ in this particular case to the rate of the failure function on the portion of the slipping patch that is aseismically sliding. Since $\dot{\tau}$ and $\Delta\dot{p}$ are both continuous at the locking front (the former due to the healing condition discussed in Section 4.4.3), the previous limit is also valid when approaching $B(t)$ from the outside of the pulse: $\dot{F} = 0$ when $r \to B(t)^-$. Because both $\dot{\tau}$ and $\Delta\dot{p}$ decrease monotonically with increasing distances measured from the locking front and towards the injection point $r = 0$, we conclude that $\dot{F} < 0$ for all points located behind the locking front, $r < B(t)$. We highlight that this statement is valid at any time after shut-in and for any value of $\mathcal{T}$. More importantly, it allows us to establish unequivocally that seismicity is not expected to occur behind the locking front, despite the positive increase of shear stress operating behind the rupture pulse.

The final region along the slip plane where seismicity is theoretically expected after shut-in ($\dot{F} > 0$) is highlighted in Figure 4.9a by the white points that represent the location and time of possible seismic events. Note that in this figure, we intentionally draw increasingly less events as time goes. This is due to the Coulomb stressing rate decreases many orders of magnitude at intermediate and large times comparing to early times (see Figure 4.9b) and as such, the seismicity rate is expected to decrease in a similar manner. Moreover, the lower limit of the seismically active region resembles the back front of seismicity proposed by Parotidis et al. (2004). Indeed, Parotidis et al.'s back front is equal to the pore-pressure back front $P(t)$ of this work (eq. 5 in Parotidis et al., 2004, equation (4.8) here). Whether some instabilities can be triggered or not in region R3 seems quite irrelevant from an observational point of view, since such small spatial differences between the locking front and the pore pressure back front are
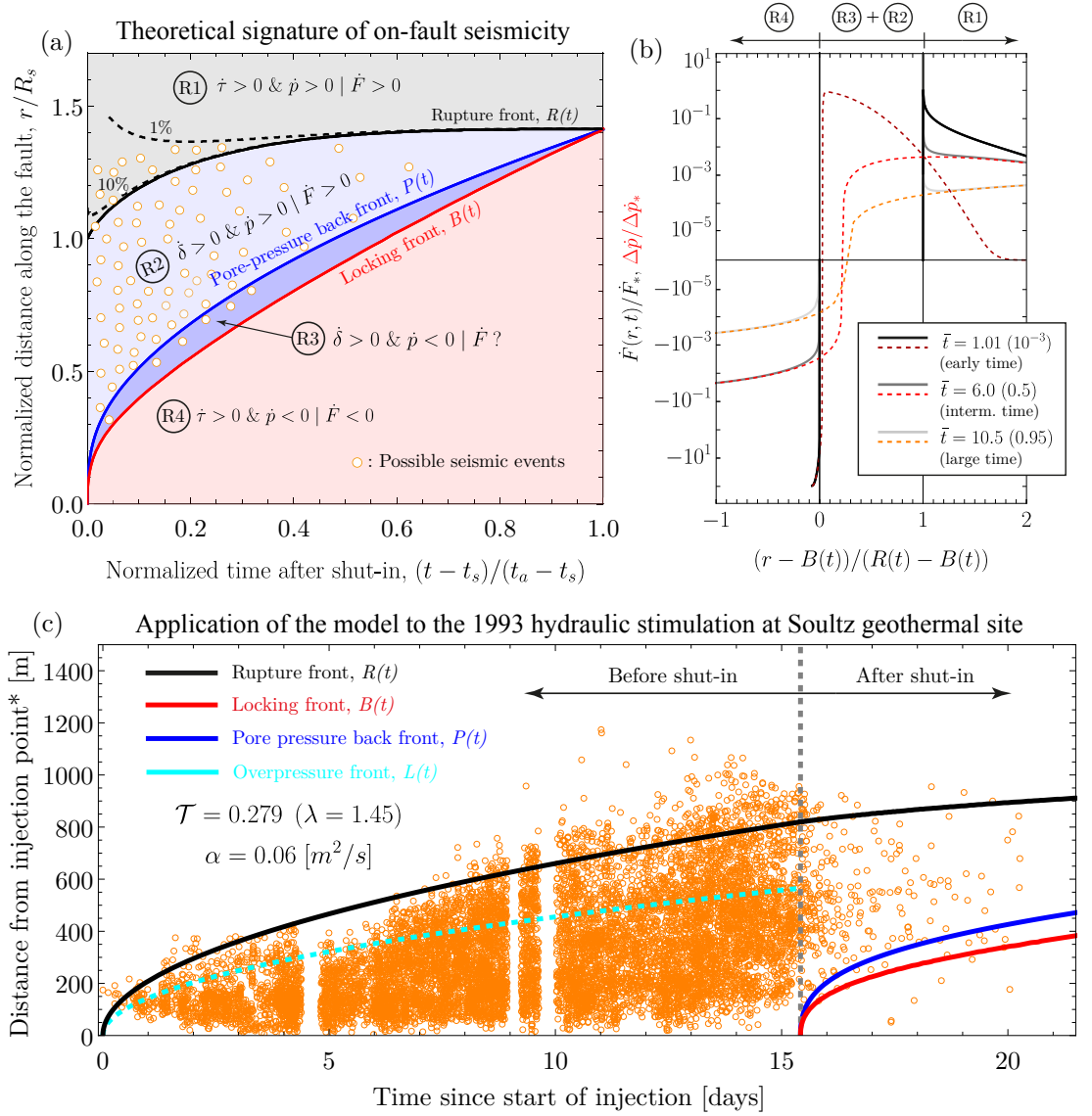
Figure 4.9: (a) Theoretical signature of on-fault seismicity after shut-in. Distance versus time plot showing regions over the fault plane (R1 to R4) where the combined effect of aseismic-slip stress transfer ($\dot{\tau}$ or $\dot{\delta}$) and pore pressure changes ($\dot{p}$) operates in different manners. White points represent the location/time of possible seismic events where the Coulomb stressing rate $\dot{F}$ is predicted to be positive. Dashed curves correspond to the position where $\dot{F}$ is 1% and 10% of the characteristic Coulomb stressing rate $\dot{F}_* = f\Delta p_*/t_s$. (b) Normalized Coulomb stressing rate $\dot{F}$ (solid lines in gray scale) and pore pressure rate $\Delta\dot{p}$ (dashed lines in red scale) along the fault plane at three dimensionless times for the same rupture than in (a), $\mathcal{T} = 0.1$. Dimensionless times in the legend box are in the format $\bar{t} = t/t_s$, $((t - t_a)/(t_a - t_s))$. (c) Application of our model to the 1993 hydraulic stimulation of the GPK1 well at the Soultz-sous-Forêts geothermal site in France (Baria et al., 1996). The migration of seismicity from the injection point is well-represented by our model based on realistic field parameters as described in the main text. *The injection point has been taken at 2,925-m depth as in Parotidis et al. (2004).

very likely indistinguishable in seismic catalogs and, in many cases, possibly even smaller than their location errors. Therefore, the back front of on-fault seismicity of post-injection aseismic slip is for practical purposes equal to the one of Parotidis et al. (2004).

Finally, unlike the back front of seismicity that corresponds to a sharp front ($\Delta \dot{p} = 0$), the upper limit of the seismically active region or seismicity front is not sharply defined. This is because the Coulomb stressing rate $\dot{F}$ vanishes theoretically only at infinity. The definition of a seismicity front thus requires some degree of arbitrariness likely associated with a chosen threshold to trigger instabilities. In our case, to be somehow consistent with the definition of the back front in terms of rates, one possible choice is to define the front of seismicity as a small percentage of the Coulomb stressing rate undergone in the proximity of the rupture front. Since the scale $\dot{F}_* = f \Delta p_* / t_s$ represents such a quantity at least at early times, we calculate and display curves associated with 1% and 10% of $\dot{F}_*$ in Figure 4.9a. We recognize that other choices are possible, notably in terms of Coulomb stress rather than in terms of rates.

The 1993 hydraulic stimulation at the Soultz geothermal site, France

With the previous theoretical considerations in mind, we aim now at testing our model against field observations of post-injection seismicity. We choose the well-documented case of the 1993 hydraulic stimulation at the Soultz geothermal site in France, where direct evidence of significant aseismic slip induced by the fluid injection exists (Cornet et al., 1997). Our focus is the first injection test of the GPK1 well, where 25,000 [m^3] of water were injected into granite over a period of about 15 days. The injection was conducted with a step incremental flow rate that reached a maximum of 36 [l/s] through a 550-m open-hole section located at depths between 2,850 m and 3,400 m (Cornet et al., 1997). Figure 4.9c shows the spatio-temporal evolution of seismicity of the more than 10,000 events recorded during the injection test, before and after shut-in (Baria et al., 1996).

Previous studies have suggested that this injection test stimulated a network of fractures (Evans, Moriya, et al., 2005), whereas our model considers the stimulation of only one single planar fault in 3D. Nevertheless, recent simulations of injection-induced aseismic slip in a 2D Discrete Fracture Network (DFN) have shown that the same patterns predicted by a single fracture in 2D emerge collectively for the DFN (Ciardo & Lecampion, 2023). This is notably the case of a set of fractures operating under critically stressed conditions (Ciardo & Lecampion, 2023). Since the fractures intersecting the open-hole section of the borehole in this test are known to be critically stressed (Evans, 2005), we make the seemingly reasonable assumption that the response of the fracture network can be approximated by an equivalent single planar fault in 3D.

To compute the evolution of the relevant fronts associated with the signature of seismicity predicted by our model, we must estimate two quantities independently: the fault hydraulic diffusivity α and the stress-injection parameter $\mathscr{T}$. Thanks to the estimates of aseismic

slip based on borehole-wall deformation by Cornet et al. (1997), we may estimate the fault hydraulic diffusivity based on the formula of accrued slip at the injection point in the critically-stressed regime, $\delta(r = 0, t = t_s) \approx 3.5\left(f\Delta p_*/\mu\right)\sqrt{4\alpha t_s}$ (equation (4.6) here, with the pre-factor in eq. 28 of Sáez et al., 2022), where $t_s = 370$ [hr] is the shut-in time. Considering a shear modulus $\mu = 20$ [GPa] (Cornet et al., 1997) and a constant friction coefficient $f = 0.6$, we just need to estimate Δp_* (equation (4.3)). For the latter, we approximate the injection history as a pulse of injection characterized by the same duration of 370 [hr] and a constant injection rate that equals the actual volume of injected fluid, which yields $Q \approx 19$ [l/s]. The hydraulic transmissivity kw has been estimated by others at the highest pressures of the test in approximately 1.7×10^{-12} [m^3] (Evans, Genter, et al., 2005). Assuming a water dynamic viscosity of $\eta = 8.9 \times 10^{-4}$ [Pa·s], we can finally calculate the pressure intensity $\Delta p_* \approx 0.8$ [MPa] and the characteristic overpressure at the fluid source $\Delta p_c \approx 10$ [MPa]. The latter is indeed very close to the actual downhole overpressure measured at 2,850 m depth, equal to 9.1 [MPa] (Cornet et al., 1997). Finally, based on the estimates by Cornet et al. (1997) who reported fracture slip along the open-hole section up to 4.7 [cm], we estimate a fault hydraulic diffusivity of $\alpha \approx 0.06$ [m^2/s]. This value of α is in the same order of magnitude than the one estimated through a different method by Parotidis et al. (2004).

With this estimate of diffusivity, we compute the evolution of the pore pressure back front after shut-in (equation (4.8)), and the evolution of the overpressure front $L(t) = \sqrt{4\alpha t}$ before shut-in, both displayed in Figure 4.9c. The next step is to compute the evolution of the rupture and locking fronts for which we must estimate the stress-injection parameter $\mathcal{T}$ (equation (4.5)). From the previous analysis of determining α, we already know that $f\Delta p_* \approx 0.48$ [MPa], so that we just need to estimate the initial distance to failure, $f\sigma_0' - \tau_0$. This is perhaps the most difficult quantity to estimate in our model. Although in this case, we do know that the fault is critically stressed (Evans, 2005), the value of $\mathcal{T}$ in the critically-stressed regime is very sensitive to changes in the order of tenths or hundredths of one megapascal, which is quite challenging to constrain confidently. It seems then more reasonable to assume a priori that the amplification of shear stress near the slip front contributes to some significant extent to drive the seismicity front before shut-in —since the fault is critically stressed and the overpressure front slightly lags the seismicity front— and consequently determine the amplification factor λ that explains well the evolution of seismicity. We find $\lambda = 1.45$ to explain well the data before shut-in (see Figure 4.9c). In the previous estimate, we considered the fact that some seismicity is expected to be triggered ahead of the slip front and thus the rupture front must lag the seismicity front to some extent. Finally, this value of λ yields a value of $\mathcal{T} \approx 0.279$ (Section 4.4.1), which in turn gives a distance to failure of approximately 0.1 [MPa]. The latter is within the range of initial distances to failure of fractures intersecting the open-hole section as estimated by Evans (2005).

The corresponding rupture and locking fronts resulting from $\mathcal{T} \approx 0.279$ are shown in Figure 4.9c. We observe that our model seems capable of explaining relatively well the migration of seismicity during this episode of combined fluid flow and aseismic slip, both before and after shut-in. Our hydro-mechanical model enriches previous analyses of the migration of
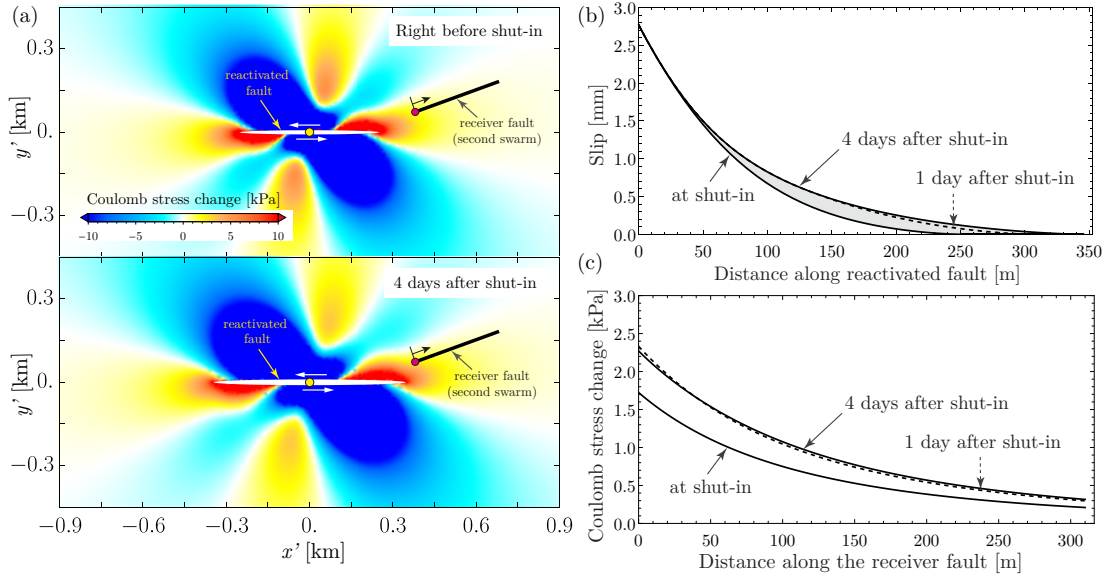
Figure 4.10: Application example of our model to the 2013 hydraulic stimulation of the GRT-1 well at the Rittershoffen geothermal site in France. (a) Coulomb stress change ΔF due to injection-induced aseismic slip on the reactivated fault for discontinuities oriented as the receiver fault. The plane x'-y' is perpendicular to the reactivated fault and crosses at its origin the injection point at a depth of about 2,370 m. Yellow and red circles correspond to the injection point and the nearest point of the receiver fault to the injection, respectively. (b) Slip distributions over the reactivated fault at different times after shut-in. (c) Coulomb stress change along the receiver fault after shut-in. The distance along the receiver fault is measured from the red circle indicated in (a) and in the direction of the black arrow.

seismicity (Parotidis et al., 2004) by considering the previously overlooked effect of stress transfer due to aseismic slip, which was previously suggested to be important in this field case (Cornet, 2016) but never tested likely due to the lack of physical models. Notably, the theoretical signature of post-injection seismicity (Figure 4.9a) seems to be present in the seismicity cloud. Moreover, the arrest time of the aseismic pulse for this value of $\mathcal{T}$ is predicted as $t_a \approx 3.78 \times t_s \approx 58$ days (equation (4.14)), which is ≈ 43 days after shut-in. Seismicity was however recorded only within the first 5 days upon the stop of the injection, which is $\bar{t} \approx 0.12$ of normalized time as defined in Figure 4.9a. This seems again consistent with our theoretical reasoning that most of the seismicity should be expected at early times after shut-in, when the Coulomb stressing rate is the highest in the post-injection problem (Figure 4.9b).

4.6.4   Off-fault seismicity

Seismicity can be triggered not only on unstable patches laying along the *aseismically* sliding fault, but also on unstable patches present in other pre-existing discontinuities nearby the propagating slow rupture. Because fluid flow is assumed to occur only within the permeable fault zone that hosts the reactivated slip plane, off-fault seismicity can be triggered

uniquely by the mechanism of stress transfer due to aseismic slip in our model. Equations (4.20) and (4.21) thus take the following forms that exclude the null pore pressure changes, $\Delta F(\boldsymbol{x};\boldsymbol{n}) = \Delta\tau(\boldsymbol{x};\boldsymbol{n}) - f\Delta\sigma(\boldsymbol{x};\boldsymbol{n})$ and $\dot{F}(\boldsymbol{x},t;\boldsymbol{n}) = \dot{\tau}(\boldsymbol{x},t;\boldsymbol{n})\,\mathrm{sgn}(\tau(\boldsymbol{x},t;\boldsymbol{n})) - f\dot{\sigma}(\boldsymbol{x},t;\boldsymbol{n})$, respectively. Evaluating the previous expressions requires knowledge of the normal vectors $\boldsymbol{n}$ of pre-existing discontinuities and the absolute state of stress, both of which are obviously site-specific and always partially uncertain. Given the site-specific nature of the required information, we address the challenge of exploring the off-fault triggering mechanism by analyzing a specific field example. Moreover, in Section 4.8.2, we discuss some further implications of our model such as the Coulomb stressing rate in the vicinity of the reactivated fault and the off-fault counterpart of the seismicity signature shown in Figure 4.9a.

The 2013 hydraulic stimulation at the Rittershoffen geothermal site, France

We focus on the 2013 hydraulic stimulation of the GRT-1 well in the crystalline basement of the Rittershoffen geothermal field in France, at a depth of about 2 [km] (Baujard et al., 2017; Lengliné et al., 2017). This stimulation lasted for about 1 day and was accompanied by swarm-like seismicity that illuminated a single planar structure that was reactivated in shear due to the fluid injection (Lengliné et al., 2017). Our model of a single planar fault in 3D seems therefore a good approximation for this field case. Upon shut-in, seismicity stopped immediately. However, after 4 days in which no seismic activity was detected, a short-lived second swarm began and developed along a nearby sub-parallel structure likely part of an en-echelon fault system (Lengliné et al., 2017). Several hypotheses were discussed by Lengliné et al. (2017) to explain what possibly led the second fault to failure as well as the 4-days delay of this second swarm. The favoured hypothesis for the failure of the second fault was in fact the stress transfer due to injection-induced aseismic slip associated with the first fault. However, the authors discarded post-injection aseismic slip as a mechanism for explaining the delayed triggering of the second swarm. They argued that slip on the first fault would be difficult to promote after shut-in due to fault pressure drops quickly to zero, thus moving the fault interface away from failure (Lengliné et al., 2017). In light of our results, this statement is valid only locally at the injection point, where the fault interface re-locks immediately upon the stop of the injection. However, as we have seen, pore pressure keeps increasing away from the injector after shut-in, which drives the propagation of a pulse-like frictional rupture that further accumulates slip on the fault. Hence, injection-induced aseismic slip can potentially explain as a unique mechanism both the failure of the second fault and the delayed triggering of the swarm of this particular case for which the reactivated fault is indeed thought to be critically stressed (Lengliné et al., 2017).

Again, as in the 1993 Soultz case, we want to estimate the fault hydraulic diffusivity α and the stress-injection parameter $\mathcal{T}$. In the absence of reliable estimates of both aseismic slip and hydraulic diffusivity, we assume for the purpose of this illustration a characteristic value of $\alpha = 0.05$ [m^2/s] for the reactivated fault. This is in the order of magnitude of diffusivities estimated from other fluid injections in nearby reservoirs (Parotidis et al., 2004), as well as

in this same geothermal field via pressure transient analysis (Baujard et al., 2017). Yet the latter must be considered with care since the estimates are based on production tests that are strongly influenced by near-well processes (Baujard et al., 2017). To estimate the stress-injection parameter $\mathscr{T}$, we follow a similar approach than the one used in the previous section for the 1993 Soultz case. We assume the aseismic slip front to play an important role in explaining the migration of seismicity which consist in this case of more than 1,300 events (Lengliné et al., 2017). Considering a rupture radius at the moment of shut-in $R_s = 250$ [m] (see figure 9 in Lengliné et al., 2017), we obtain from $R_s = \lambda\sqrt{4\alpha t_s}$ (Section 4.4.1) with $t_s = 19$ [hr] in this case, an amplification factor $\lambda \approx 2.14$, which yields a stress-injection parameter $\mathscr{T} \approx 0.117$.

This value of $\mathscr{T}$ gives an arrest time of aseismic slip $t_a \approx 9.70 \times t_s \approx 184$ [hrs] (equation (4.14)), which is equivalent to approximately 7 days after the stop of the injection. The latter is indeed longer than the 4-days delay of the second swarm. Yet the relatively short time between the estimated arrest time and the occurrence of the second swarm suggests that most of the post-injection stress transfer from the first to the second fault must have occurred shortly after stopping the injection. To better quantify this, we calculate the Coulomb stress change associated with the reactivation of the main fault in our model. The Coulomb stress calculations are based on the following combination of parameters: $Q = 38$ [l/s], $\eta = 8.9 \times 10^{-4}$ [Pa·s], $kw = 10^{-11}$ [m³], $\mu = 20$ [GPa], $f = 0.6$, $\sigma'_0 = 10$ [MPa] and $\tau_0 = 5.981$ [MPa]. The constant injection rate Q is obtained by equating the injected volume of fluid of the actual injection history considering the same injection duration. The fault hydraulic transmissivity kw is calculated such that the characteristic overpressure at the fluid source Δp_c (equation 4.3) approximately matches the maximum downhole overpressure measured at a depth of 1,920 m during the injection, approximately equal to 3 [MPa] (Baujard et al., 2017). Finally, the initial stress state (σ'_0 and τ_0) is chosen to be consistent with the value of $\mathscr{T}$, the injection intensity Δp_*, and the partially constrained stress state in the zone (Lengliné et al., 2017).

Following Lengliné et al. (2017), we further consider that the fluid injection induced pure left-lateral aseismic slip on a strike-slip feature oriented N25^{o}E and dipping 70°W. As the second swarm occurred over a fault with variable strike, we focus for the purpose of our illustrative example on the northern branch of the second fault only. We thus consider a receiver fault oriented N5^{o}E with the same dip angle than the main fault (Lengliné et al., 2017) (see Figure 4.12a). We calculate the slip distribution over the reactivated fault at three times: right at the moment of shut-in, 1 day after shut-in, and 4 days after shut-in, as displayed in Figure 4.12b. In this figure, we can observe that 1 day after stopping the injection most of the post-injection aseismic slip accumulated at the time the second swarm began, has already taken place. The Coulomb stress change associated with the foregoing slip distributions are shown in the top and bottom panels of Figure 4.12a, at the shut-in time and 4 days after shut-in (when the second swarm started), respectively. Our Coulomb stress analysis indicates that the location of the second swarm is in a region of positive Coulomb stress change, which is consistent with the calculations in Lengliné et al. (2017). Note that our distribution of Coulomb stress change is different than the one in Lengliné et al. (2017) since the slip distribution of our model is

peaked around the injection point and not uniform.

Finally, Figure 4.12c displays the spatio-temporal evolution of the Coulomb stress change along the receiver fault at the same three times than before, with the origin at the red circle indicated in Figure 4.12a. Note that the magnitude of the Coulomb stress change is about 2 [kPa]. This value is quite low and suggests that if aseismic-slip stress transfer is responsible for the delayed triggering of the second swarm, such a fault must be very critically stressed under the assumptions of our example. Given that pore pressure diffusion can sometimes weaken unstable areas even off fault, we can postulate a hydraulic connection between the two faults, possibly created by a wing crack in a step-like en-echelon fault system, and estimate the resulting overpressure 4 days after shut-in. By assuming $\alpha = 0.05$ [m^2/s] still as a representative value of diffusivity, the overpressure at the nearest point (red circle in Figure 4.12a) of the receiver fault with regard to the injection point (yellow circle in Figure 4.12) is approximately 6 [kPa] (equation 4.4). The latter is in the same order of magnitude than the Coulomb stress change due to aseismic slip, suggesting that both mechanisms may be equally important in our example. Note that 4 days after the stop of the injection, the increment of Coulomb stress with regard to the moment of shut-in, is just about 0.5 [kPa] (Figure 4.12c). Hence, most of the post-injection increment has already happened within the first day.

Although our analysis has oversimplified many aspects of this field case, our physical model seems to have the potential to reproduce field observations of post-injection off-fault seismicity, as illustrated by this application example. However, an in-depth analysis would be needed to fully clarify the role of post-injection aseismic slip in this particular field case.

4.6.5   Possible evidence for post-injection aseismic slip and other relevant field cases

In addition to the foregoing field cases, there are apparently a few other cases of geo-energy projects where observations of seismicity after shut-in suggest the occurrence of post-injection aseismic slip. One of these cases is the 2016 long-lived seismic swarm that persisted for more than 10 months after completion of hydraulic fracturing operations of a hydrocarbon reservoir in western Canada (Eyre et al., 2020). In this case study, the authors attributed indeed the delayed swarm activity to post-injection aseismic slip. Unlike the off-fault setting of the Rittershoffen case in France, the configuration here is a clear case of on-fault seismicity. Specifically, aseismic slip is thought to be induced by hydraulic fractures that intersect (and pressurize) frictionally-stable segments of a nearby fault at the reservoir level (shales), which in turn transmits solid stresses to distal segments of the same fault but in carbonate units that are thought to slide unstably (Eyre et al., 2019). One key aspect of the proposed conceptual model for post-injection seismicity in this case, is the assumption of heterogeneities in fault permeability to explain a remarkable characteristic of the swarm, namely, a nearly constant rate of post-injection seismicity (Eyre et al., 2020). The proposed model assumes that elevated pore pressure remains trapped within the fault after shut-in at the reservoir level, due to the

extremely low permeability of the shale formations. These trapped fluids are therefore thought to be responsible for a nearly steady propagation of aseismic slip that could explain the constant rate of seismicity (Eyre et al., 2020). Although their proposed model slightly differs from our model (in which the fault permeability is homogeneous), this case study seems to provide relevant evidence for the mechanisms discussed here. Moreover, as suggested by Cornet (2016), another case in which aseismic slip might have triggered post-injection seismicity is the Basel earthquakes in 2006 in Switzerland; a hypothesis that has been recently considered in combination with other triggering mechanisms via plane-strain geomechanical modelling (Boyet et al., 2023).

Further and possibly more conclusive evidence for post-injection aseismic slip may come from carefully-designed laboratory and/or in-situ experiments of fluid injection. Laboratory experiments where a finite rupture grows along a pre-existing interface (Passelègue et al., 2020; Gori et al., 2021; Cebry et al., 2022) are particularly promising to explore the post-injection stage. On the other hand, in-situ experiments where the fault deformation is monitored simultaneously at the injection point and at another point away from it (Cappa et al., 2022), may also provide the opportunity to investigate this mechanism when combined with hydro-mechanical modelling that includes the depressurization stage (Larochelle et al., 2021).

4.6.6   Model limitations: solution as an upper bound

Our model contains the minimal physical ingredients to reproduce post-injection aseismic slip in 3D media. As such, the effects of a number of additional effects remain to be investigated. In particular, we have assumed that fluid flow induces mechanical deformation but not vice versa. It has been however suggested for long time that variations of effective normal stress may induce permeability changes in fractures (Witherspoon et al., 1980) and faults (Rice, 1992). Also, it is known that frictional slip may be accompanied by dilatant (or contracting) fracture/fault-gouge behavior that would inevitably induce changes in fluid flow and thus in the propagation of fault slip (see Ciardo and Lecampion, 2019, for example). Poroelastic effects in the surrounding medium around the fault may be of first order in some cases (see, for instance, Heimisson et al., 2022). Accounting for a permeable host rock may notably speed up the depressurization of pore-fluid within a fault zone after shut-in due to the leak-off of fluid. Consequently, the arrest time and maximum run-out distance of the rupture pulses would likely decrease. In this regard, our model in which the leak-off of fluid into the surrounding medium is neglected would represent an upper bound for the arrest time and maximum run-out distance similarly to the case of the arrest of mode I hydraulic fractures (Möri & Lecampion, 2021).

In relation to friction, we consider the simplest description that allows us to produce unconditionally stable fault slip, namely, a constant friction coefficient. However, laboratory-derived friction laws (Dieterich, 1979; Ruina, 1983) are widely used in the geophysics community to reproduce the entire spectrum of slip velocities of natural earthquakes (Scholz, 2019).

Unconditionally stable fault slip may be obtained notably in some regimes of so-called rate-strengthening faults when subjected to continuous fluid sources (Dublanchet, 2019; Garagash, 2021). For the post-injection problem, a more complex constitutive friction law would add a finite amount of fracture energy as well as frictional healing. In this regard, our model represents a situation in which the fracture energy spent during propagation is zero and there is no possibility for the friction coefficient to heal with time. The dissipation of a finite amount of fracture energy at the rupture front would resist propagation of the aseismic pulses. Similarly the healing of the friction coefficient would further contribute to the re-locking process of the fault thus accelerating the propagation of the locking front. Both ingredients are therefore expected to shorten the arrest time and maximum run-out distance of the rupture pulses. Our model thus represents also an upper bound with regard to these two mechanisms. Finally, it is worth mentioning that injection-induced aseismic slip also occurs during the quasi-static phase preceding the nucleation of dynamic ruptures (Garagash & Germanovich, 2012; Dublanchet, 2019).

4.7   Concluding remarks

We have provided an in-depth investigation of how post-injection aseismic slip propagates and ultimately arrests in 3D media. Our results provide for the first time a conceptual and quantitative framework that may help to understand various observations and applied problems in geomechanics and geophysics associated with slow ruptures driven by the motion of fluids. Among them, a particularly relevant problem for geo-energy applications is the phenomenon of post-injection seismicity. It has been long recognized that aseismic slip may alter the stress state of large rock volumes during borehole fluid injections (Scotti & Cornet, 1994). Based on our findings, we suggest that aseismic slip may continue stressing even larger and more distant regions after shut-in, during timescales that could span even months for fluid injections of only a few days, if the reactivated discontinuity is critically stressed as quantified by the value of the stress-injection parameter $\mathcal{T}$. Our physical model shows quantitative agreement with field observations of documented cases of post-injection induced seismicity (Cornet et al., 1997; Lengliné et al., 2017), thus providing support for the mechanisms presented here. Further and possibly more conclusive evidence may potentially come from revisiting more case studies via geomechanical modeling, notably from laboratory and/or in-situ experiments that can either monitor or infer the propagation of slow ruptures.

Current efforts to manage the seismic risk associated with subsurface fluid injections such as the so-called traffic light systems might be subjected to important limitations in their effectiveness in light of our results. Traffic light systems work under the tacit assumption that operational measures will become shortly effective in preventing the occurrence of events of larger magnitude than some pre-defined threshold (Baisch et al., 2019). Our results suggest that instead, the stressing of increasingly larger rock volumes perturbed by aseismic slip may be persistent if the chosen operational measure is shutting in the well. Future works should therefore focus on developing physics-based strategies to mitigate the seismic risk associated

with post-injection aseismic slip.

4.8   Supplementary material

4.8.1   Rake angle

In the main text, we mention that the direction of slip (or maximum shear) can be well-approximated as being entirely along the x axis, which is the direction of the initial maximum shear stress in our model (see Figure 4.1 in the main text). Here, we consider the case of $\nu = 1/4$ (a Poisson's solid) and quantify the accuracy of this approximation, to numerical precision.

We solve for our model in the continuous-injection stage, for two cases: $\mathcal{T} = 0.001$ and $\mathcal{T} = 0.5878$. The former corresponds to a fault that is very critically stressed ($\mathcal{T} \ll 1$) in which the equivalent shear load driving the rupture tends to be a point force superimposed on a uniform load of opposite sign (Sáez et al., 2022), whereas the latter represents a case in which the slip front is always located near the overpressure front ($\lambda \approx 1$), and the equivalent shear load is more evenly distributed. Since the continuous-injection problem is self-similar (Sáez et al., 2022), we examine the numerical results at a single instant, and the conclusions remain valid at any time.

Figures 4.11a-d show the results for $\mathcal{T} = 0.001$. The rake angle is measured counterclockwise from the x axis: $\phi = \arctan\left(\delta_y/\delta_x\right)$. If the rake angle is zero, the direction of slip aligns exactly with the x axis. We observe that ϕ increases when approaching the injection point at $r = 0$, where the fluid-injection equivalent point force is located (Sáez et al., 2022). However, the rake angle is at most about 0.5 degrees, corresponding to a y-component of slip magnitude of 1% or less of the x-component δ_x.

On the other hand, Figures 4.11e-h show the results for $\mathcal{T} = 0.5878$. In this case, where the equivalent shear load is more evenly distributed, the rake angle is also more widely distributed and around 0.1 degrees. Note that larger values than this correspond to numerical noise. This maximum magnitude of the rake angle corresponds to a y-component of slip magnitude of 0.2% or less of the x-component δ_x.

Furthermore, a theoretical explanation for the small rake angle observed in our numerical solutions can be devised (M. Lebihain, private communication, May 2023) from the first-order perturbative theory for shear cracks of Gao (1988). Gao calculated variations of the slip components for a shear crack whose shape differs slightly from a circular reference configuration. The variations of slip with respect to the circular configuration are written in
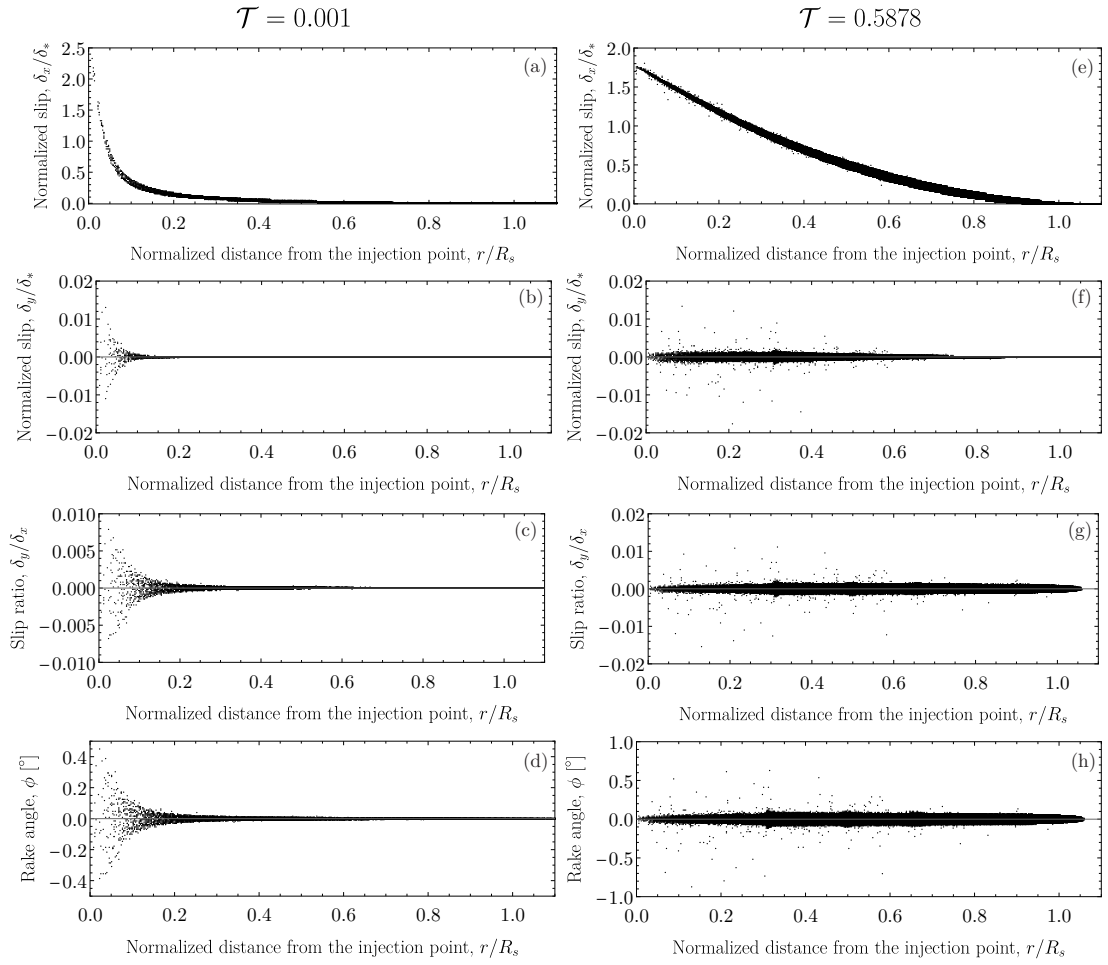
Figure 4.11: Rake angle approximation. (a) to (d) Results for $\mathcal{T} = 0.001$. (e) to (h) Results for $\mathcal{T} = 0.5878$

polar coordinates as (equation 10 in Gao, 1988):

$$
\delta \Delta u_j(r,\theta) = 2\frac{(1-\nu^2)}{E} \int_0^{2\pi} K_2^0(\theta';a)\,k_{2j}(\theta';r,\theta,a)\left(a(\theta')-a(\theta)\right)a(\theta)\mathrm{d}\theta'
$$
$$
+ 2\frac{(1+\nu)}{E} \int_0^{2\pi} K_3^0(\theta';a)\,k_{3j}(\theta';r,\theta,a)\left(a(\theta')-a(\theta)\right)a(\theta)\mathrm{d}\theta', \quad \text{with} \quad j=r,\theta,
$$

where K_2^0 and K_3^0 are the mode-II and mode-III stress intensity factors (for $\nu \neq 0$) along the rupture front of the circular crack configuration that are generated by the equivalent shear loading driving the rupture (see Sáez et al., 2022, appendix B), k_{2j} and k_{3j} are the crack face weight functions for the circular reference crack (see, for instance, equation 12 in Gao, 1988, for their expressions in polar coordinates), and $a(\theta)$ is the perturbed rupture front that differs slightly from the circular one. Note that for the sake of clarity in the notation, we wrote the slip components as $\delta_r = \Delta u_r$ and $\delta_\theta = \Delta u_\theta$.

Since the circular configuration is exact when $\nu = 0$, and the greater the value of ν the more elongated (less circular) the rupture shape becomes (Sáez et al., 2022), it seems convenient to consider ν as the perturbation variable (Favier et al., 2006). By expanding to first order in ν the rupture front a, stress intensity factors K_2^0 and K_3^0, and crack face weight functions k_{2j} and k_{2j}, one can show that the first-order variations of both slip components $\delta \Delta u_r$ and $\delta \Delta u_\theta$ are expressed in terms of convolutions that operate over the mode-II and mode-III stress intensity factors of the circular rupture case with $\nu = 0$. Since those stress intensity factors must be zero due to the no-singularity condition of shear stress along the front (the condition for rupture propagation in Sáez et al., 2022), the first-order corrections of both slip components are zero. As the zero-order ($\nu = 0$) contribution of slip in the y-direction is also zero (null rake angle ϕ when $\nu = 0$), we conclude that possible non-zero contributions to δ_y (or ϕ) will come only from terms that involve ν^2 or higher order, possibly resulting in the small variation of the rake angle we obtained in our numerical solutions.

4.8.2   Off-fault seismicity

In the main text, we discuss the triggering mechanism of off-fault post-injection seismicity by considering an illustrative field example: the 2013 hydraulic stimulation of the GRT-1 well at the Rittershoffen geothermal field in France (Lengliné et al., 2017). Here, we discuss some further implications of our model by analyzing an hypothetical case of hydraulic stimulation into a deep geothermal reservoir.

We recall that because fluid flow is assumed to occur only within the permeable fault zone that hosts the reactivated slip plane, off-fault seismicity can be triggered uniquely by the mechanism of stress transfer due to aseismic slip in our model. Hence, equations (4.20) and (4.21) in the main text, take the following forms that exclude the pore pressure changes,

$$
\Delta F(\boldsymbol{x};\boldsymbol{n}) = \Delta \tau(\boldsymbol{x};\boldsymbol{n}) - f\Delta\sigma(\boldsymbol{x};\boldsymbol{n}), \tag{4.23}
$$
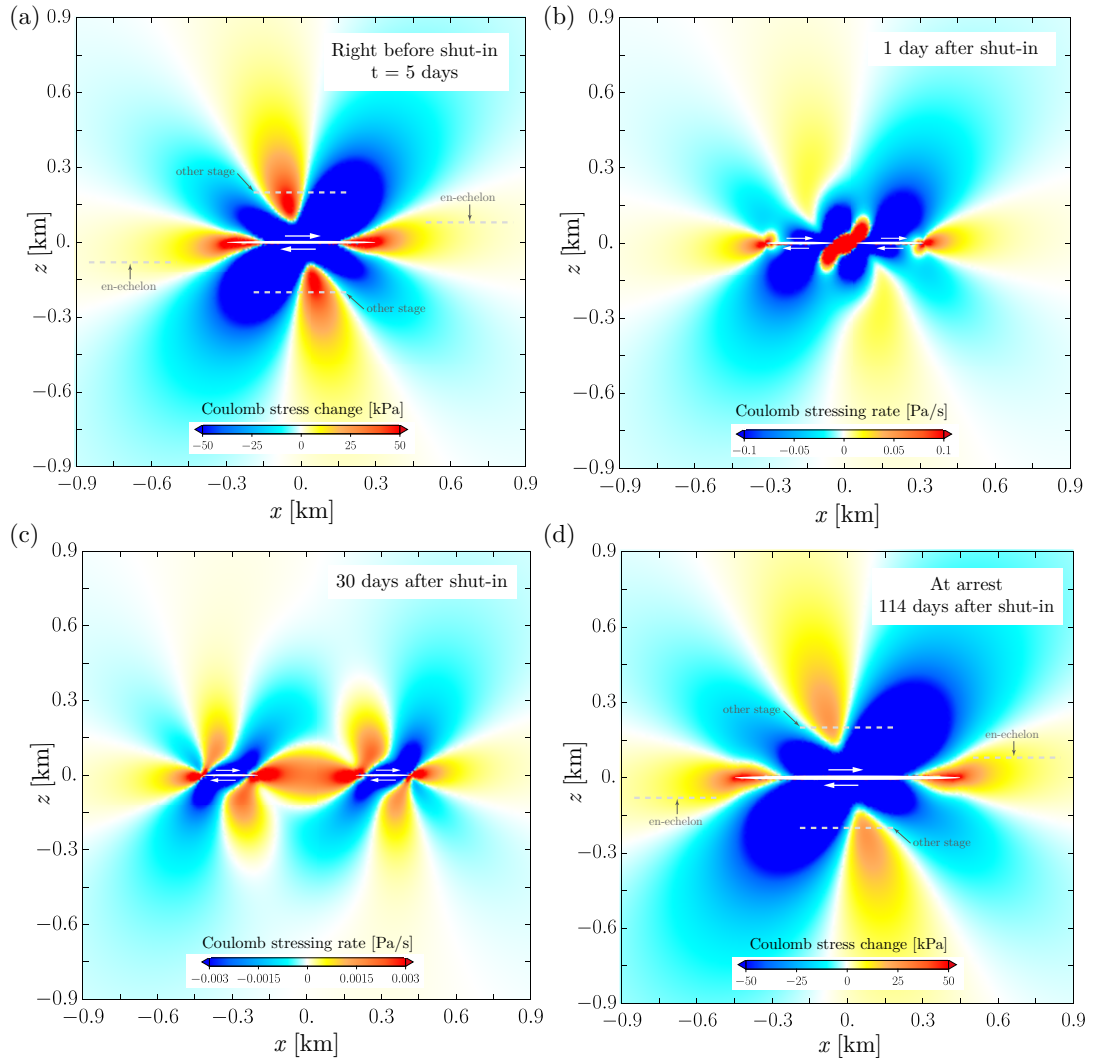
Figure 4.12: (a) and (d) Coulomb stress change ΔF and (b) and (c) Coulomb stressing rate $\dot{F}$ on pre-existing discontinuities that are sub-parallel to a reactivated fault lying on the plane $z = 0$. This example corresponds to the hydraulic stimulation of a single planar fault in a deep geothermal reservoir, where the stress-injection parameter $\mathcal{T} = 0.05$ and $\nu = 0$. ΔF is from the initial stress state at $t = 0$ to the (a) moment right before shut-in, and (d) to the moment in which the rupture arrests. Dashed lines schematize sub-parallel fractures associated with either other stimulation stages or en-echelon fracture systems. $\dot{F}$ is after (b) 1 day and (c) 30 days since the start of the injection.

and

$$\dot{F}(\boldsymbol{x}, t; \boldsymbol{n}) = \dot{\tau}(\boldsymbol{x}, t; \boldsymbol{n}) \operatorname{sgn}(\tau(\boldsymbol{x}, t; \boldsymbol{n})) - f \dot{\sigma}(\boldsymbol{x}, t; \boldsymbol{n}), \qquad (4.24)$$

respectively. To evaluate the previous expressions, knowledge about the normal vectors $\boldsymbol{n}$ of the pre-existing discontinuities is required. To keep the analysis general to some extent, there are at least two natural choices for the orientation of discontinuities that seem worth to consider. The first one is the case of discontinuities optimally oriented with regard to stress field: at angles $\theta_* = \pm (\pi/4 - \arctan(f)/2)$ measured from the local direction of the maximum principal stress. The calculation of the latter direction requires the full initial stress tensor plus computations of its variation in time due to the redistribution of stresses caused by the propagation of the aseismic pulses. Positive changes of the Coulomb stress function would highlight the regions where seismicity is most likely expected in a context in which the orientations of the discontinuities nearby the rupture are fairly unknown. The second option is to consider discontinuities that are sub-parallel to the reactivated fault. For example, in the context of hydraulic stimulation of deep geothermal reservoirs, multi-stage stimulation techniques aim at reactivating isolated sub-parallel fractures that intersect the open-hole section of the stimulation well at different depths/stages. Positive changes of the Coulomb stress function in this case would highlight the effect of one stage on the others. In addition, it is not rare that the reactivated fractures are part of en-echelon fracture systems such that other sub-parallel discontinuities either overlap or form a step-like feature with the reactivated one. Because of its simplicity and relevance for geo-energy applications, we only consider hereafter sub-parallel discontinuities.

Figure 4.12 displays some static (ΔF) and instantaneous ($\dot{F}$) changes of the Coulomb stress function for a circular rupture that propagates on a critically-stressed fault with $\mathscr{T} = 0.05$. The results are plotted on the x-z plane of our global reference system (see Figure 4.1 in the main text) corresponding to the plane where the direction of slip is contained entirely. All calculations in this figure are for a particular choice of parameters representing the hydro-shearing treatment of a deep geothermal reservoir at approximately 4 km depth: injection rate $Q = 20$ [l/s], injection duration $t_s = 5$ [days], hydraulic diffusivity $\alpha = 5 \times 10^{-3}$ [m^2/s], hydraulic transmissivity $kw = 10^{-13}$ [m^2], fluid dynamic viscosity $\eta = 2 \times 10^{-4}$ [Pa·s], rock shear modulus $\mu = 30$ [GPa], constant friction coefficient $f = 0.6$, initial total normal stress $\sigma_0 = 120$ [MPa], initial pore pressure $p_0 = 40$ [MPa], and initial shear stress $\tau_0 = 47.9045$ [MPa]. For this particular choice of parameters, the accumulated amount of slip at the injection point at the shut-in time is $\delta \approx 1.9$ [cm]. Note that δ can be approximated analytically from the slip scale δ_* in the critically-stressed regime, equation (4.6) in the main text, with the pre-factor 3.5 derived in equation (28) in Sáez et al. (2022).

Figure 4.12a shows the static change of Coulomb stress ΔF from the initial conditions to the moment right before the end of the injection. At this time, the rupture is still propagating in crack-like mode, with a radius equal to $R_s = \lambda \sqrt{4\alpha t_s} \approx 297$ [m] ($\lambda \approx 1/\sqrt{2\mathscr{T}} \approx 3.2$). The spatial pattern of ΔF is remarkably different to the classic pattern of sub-parallel faults having a more

homogeneously distributed slip (see figure 2a in King et al., 1994, for example) compared to our slip distribution which is more peaked near the injection point (see Figure 4.3a in the main text). Particularly, we obtain positive changes of Coulomb stress near the center of the rupture, which may affect sub-parallel discontinuities of other stimulation stages. Such sub-parallel fractures are schematized in Figure 4.12a by dashed lines. In addition, the positive changes of Coulomb stress in the proximity of the rupture front may induce seismicity on nearby discontinuities composing, for instance, an en-echelon arrangement of fractures, a situation that is also schematized in Figure 4.12a.

On the other hand, Figures 4.12b and 4.12c display the Coulomb stressing rate $\dot{F}$ caused by the aseismic pulse propagation respectively 1 day and 30 days after the end of the injection. We can observe here the off-fault counterpart of the along-fault amplification of shear stress rate near the locking and rupture fronts shown in Figure 4.6b. Note that the positive rate of Coulomb stress near the locking front affects a region where, before shut-in, the Coulomb stress has dropped $\Delta F < 0$ (see Figure 4.12a). Furthermore, the final change of Coulomb stress ΔF from the beginning of the injection until the moment in which the rupture ultimately arrest (Figure 4.12d), shows that overall there is a drop of Coulomb stress in the off-fault region affected by the stress-rate amplification associated with the passage of the locking front. The latter suggests that off-fault seismicity is not expected to be seen behind or around the locking front, similarly to the case of on-fault seismicity that is analyzed in Section 4.6.3 in the main text. This observation is of course based on the particular case of pre-existing discontinuities that are parallel to the reactivated fault. In this configuration, the main role of post-injection aseismic slip seems to be the one of continuing inducing seismicity in nearly the same regions of positive Coulomb stress change at the time of shut-in (Figure 4.12a) but at increasingly further distances. Note that for this example, the rupture radius at arrest is $R_a \approx 449$ [m], which is $R_a/R_s \approx 1.51$ times greater than the rupture radius at shut-in, whereas the time of arrest is $t_a \approx 119$ [days], that is $t_a/t_s \approx 23.8$ times longer than the injection duration. Finally and more generally speaking, depending on the orientation of the surrounding pre-existing discontinuities and the pre-injection stress field, seismicity can continue to be triggered in regions of positive Coulomb stress change after shut-in with significant time delays and at increasingly further distances, perturbing the stress state of large rock volumes with characteristic sizes that are in the order of the spatial extent of the arrested rupture. For instance, for the example considered here, $R_a/R_s \approx 1.51$ and thus the rock volume altered by aseismic slip is in the order of $(1.51)^3 = 3.4$ times larger at arrest than at shut-in.

4.8.3 Numerical time integration

Adaptive time-stepping scheme

One of the most challenging quantities to be solved accurately in our problem is the position of the locking front, notably, at early times after shut-in when it moves at very high speeds. It seems thus natural to adjust the time step based on the speed of the locking front, such that

the time increment Δt during the post-injection stage is chosen smaller at early times than at large times. On the other hand, before shut-in, the relevant front speed is the one of the rupture front, such that a general adjustable time step Δt to be used in both stages (during and after fluid injection), may be constructed as

$$\Delta t = \beta \frac{\Delta x}{\max\{v_r, v_b\}}, \tag{4.25}$$

where v_r is the rupture front speed, v_b is the locking front speed, Δx is the boundary element size (uniform in this work), and β is a constant parameter that controls the number of elements that the fronts advance during one time step. The front speeds v_r and v_b are estimated via finite differences based on the solution of the previous time step. Most of the time, we consider a value of $\beta = 1.5$ which results in a front advancement of 1 to 2 elements per time step. Moreover, we further impose for robustness that at a given time step neither the rupture front nor the locking front can advance more than n_{max} and less than n_{min} elements. If any of the two fronts advance more than n_{max} elements, the trial time step estimated via equation (4.25) is divided by two, whereas if any of the two fronts advances less than n_{min} elements, the trial time step Δt is multiplied by two. We select $n_{min} = 1$, such that at least one of the two fronts must always advance during one time step, while n_{max} is generally set to be equal to 3, except by the most marginally-pressurized cases (the greatest values of $\mathcal{T}$), in which n_{max} must be increased not to be so stringent in these cases that are the stiffest numerically.

Some remarks on the 3D numerical solution

With regard to the time integration, since one time step in the 3D solver is much more expensive computationally than in the axisymmetric solver, we consider a different time-stepping strategy in order to keep the problem numerically tractable. Taking advantage of the exact analytical solution for circular ruptures before shut-in and the accurate numerical solution calculated via the axisymmetric solver in the post-injection stage, we control the numerical error in the fully 3D solution as follows. With $v = 0$ in the 3D solver, we solve for 5 time steps between the start of the injection and the shut-in time, and 55 time steps between the shut-in time and the arrest time of such already-known circular rupture solution. The time steps before shut-in are selected such that the rupture front advances the same distance with each time increment, whereas the time steps after shut-in are chosen considering that the locking front is the one that advances the same distance with each time step. The relative error in the 3D solver is estimated based on the position of the rupture and locking fronts, before and after shut-in, respectively. Before shut-in, we calculate the relative error as $(R^{num} - R^{an})/R^{an}$, where R^{num} is the rupture front radius estimated numerically from the 3D solver, and R^{an} is the exact analytical solution. After shut-in, we estimate the relative error as $(B^{num} - B^{axi})/B^{axi}$, where B^{num} is the locking front radius computed numerically from the 3D solver, and B^{axi} is the same quantity but calculated accurately via the axisymmetric solver. Not surprisingly, the largest error occurs at early times after shut-in. Moreover, the error decreases monotonically with time during the post-injection stage while the time step is always increasing. The relative

error reaches its minimum value near the time of arrest. We find that the use of 100,000 elements (equal to 300,000 degrees of freedom) produces results that are sufficiently accurate for the purpose of our work. For the most unfavorable case which is the least critically-stressed case ($\mathcal{T} = 0.59$), the relative error is below 2%.

With the previous error estimate for the circular rupture case ($\nu = 0$), we then switch to the non-circular problem for which $\nu = 0.25$. For a given value of $\mathcal{T}$, we use the same 60 time steps as for the circular rupture case. Because the final time of arrest and maximum run-out distance for non-circular ruptures are always greater than the corresponding circular counterparts for the same value of $\mathcal{T}$, additional time steps are always required. The subsequent time increments are chosen always to be smaller than the last of the sixty time steps to make sure the minimum error estimated previously is approximately an upper bound for the error of the remaining part of the problem. In this way, we manage to estimate with sufficient accuracy the arrest time and maximum run-out distance of non-circular ruptures, by systematically reducing the time increment until eventually the rupture arrests. It is worth mentioning that we use the same convergence tolerances in the 3D solver as in the axisymmetric solver.

5 Fluid-driven slow slip and earthquake nucleation on a slip-weakening circular fault

In this chapter, we extend the constant-friction fault model of Chapter 3 to account for a friction coefficient that weakens with slip. This enables the model to develop a proper cohesive zone besides incorporating a finite amount of fracture energy, both ingredients absent in the former model. To do so, we consider two friction laws characterized by a linear and an exponential weakening of friction respectively. We focus on the particular case of axisymmetric circular shear ruptures as they capture the most essential aspects of the dynamics of unbounded ruptures in three dimensions. It is shown that fluid-driven slow slip can occur in two distinct modes in this model: as an interfacial rupture that is unconditionally stable, or as the quasi-static nucleation phase of an otherwise dynamic rupture. Whether the interface slides in one way or the other depends primarily on the sign of the difference between the initial shear stress (τ_0) and the in-situ residual strength (τ_r^0) of the fault. For ruptures that are unconditionally stable ($\tau_0 < \tau_r^0$), fault slip undergoes four distinct stages in time. Initially, ruptures are self-similar in a diffusive manner and the fault interface behaves as if it were governed by a constant friction coefficient equal to the peak (static) friction value. Slip then accelerates due to frictional weakening while the cohesive zone develops. Once the latter gets properly localized, a finite amount of fracture energy emerges along the interface and the rupture dynamics is governed by an energy balance of the Griffith's type. We show that in this stage, fault slip always transitions from a large-toughness to a small-toughness regime due to the diminishing effect of the fracture energy in the near-front energy budget as the rupture grows. Moreover, while slip grows likely confined within the pressurized region in prior stages, here the rupture front can largely outpace the pressurization front if the fault is close to the stability limit ($\tau_0 \approx \tau_r^0$). Ultimately, self-similarity is recovered and the fault behaves again as possessing a constant friction coefficient, but this time equal to the residual (dynamic) friction value. It is shown that in this ultimate regime, the fault interface operates to leading order with zero fracture energy. On the other hand, when slow slip propagates as the nucleation phase of a dynamic rupture ($\tau_0 > \tau_r^0$), fault slip also initiates in a self-similar manner and the interface operates at a constant peak friction coefficient. The maximum size that aseismic

ruptures can reach before becoming unstable (inertially dominated) can be as small as a critical nucleation radius equal to the shear modulus divided by the slip-weakening rate, and as large as infinity when faults are close to the stability limit ($\tau_0 \approx \tau_r^0$). The former case corresponds to faults that are critically stressed before the injection starts, in which case ruptures always expand much further away than the pressurized region. The larger the critical nucleation radius is with regard to the cohesive zone size, the longer ruptures can accelerate aseismically before becoming unstable. When the nucleation radius is smaller than the cohesive zone size, aseismic ruptures accelerate upon departing from the self-similar response due to continuous frictional weakening over the entire slipping region, undergoing nucleation unaffected by the residual fault strength. Conversely, when the nucleation radius is (much) larger than the cohesive zone size, aseismic ruptures transition towards a stage controlled by a front-localized energy balance and undergo nucleation in a 'crack-like' manner. Our results include analytical and numerical solutions for the problem solved over its full dimensionless parameter space, as well as expressions for relevant length and time scales characterizing the transition between different stages and regimes. Due to its three-dimensional nature, the model enables quantitative comparisons with field observations as well as preliminary engineering design of hydraulic stimulation operations. Existing laboratory and in-situ experiments of fluid injection are briefly discussed in light of our results.

This chapter is a modified version of the following scientific article:

Sáez, A. & Lecampion, B. (2023). Fluid-driven slow slip and earthquake nucleation on a slip-weakening circular fault. Under review in *Journal of the Mechanics and Physics of Solids*.

Contributions of Alexis Sáez (CRediT, Contributor Roles Taxonomy)

Conceptualization, Methodology, Software, Validation, Formal analysis, Investigation, Writing - Original Draft, Writing - Review & Editing, Visualization, Funding acquisition.

5.1 Introduction

Sudden pressurization of pore fluids in the Earth's crust has been widely acknowledged as a trigger for inducing slow slip on pre-existing fractures and faults (Hamilton & Meehan, 1971; Scotti & Cornet, 1994; Guglielmi et al., 2015; Wei et al., 2015). Sometimes referred to as injection-induced aseismic slip, this phenomenon is thought to play a significant role in various subsurface engineering technologies and natural earthquake-related phenomena. Notable examples of the natural source include seismic swarms and aftershock sequences, often attributed to be driven by the diffusion of pore pressure (Miller et al., 2004; Parotidis et al., 2005) or the propagation of slow slip (Lohman & McGuire, 2007; Perfettini & Avouac, 2007), with recent studies suggesting that the interplay between both mechanisms may be indeed responsible for the occurrence of some seismic sequences (Z. Ross et al., 2017; Sirorattanakul et al., 2022; Yukutake et al., 2022). Similarly, low-frequency earthquakes and tectonic tremors are commonly considered to be driven by slow slip events occurring downdip the seismogenic

zone in subduction zones (Rogers & Dragert, 2003; Shelly et al., 2006), where systematic evidence of overpressurized fluids has been found (Shelly et al., 2006; Kato et al., 2010; Behr & Bürgmann, 2021), with recent works suggesting that the episodicity and some characteristics of slow slip events may be explained by fluid-driven processes (Warren-Smith et al., 2019; Zhu et al., 2020; Perez-Silva et al., 2023).

Anthropogenic fluid injections are, on the other hand, known to induce both seismic and aseismic slip (Scotti & Cornet, 1994; Guglielmi et al., 2015; Wei et al., 2015). For instance, hydraulic stimulation techniques employed to engineer deep geothermal reservoirs aim to reactivate fractures through shear slip, thereby enhancing reservoir permeability by either dilating pre-existing fractures or creating new ones. The occurrence of predominantly aseismic rather than seismic slip, is considered a highly favorable outcome, as earthquakes of relatively large magnitudes can pose a significant risk to the success of these projects (Deichmann & Giardini, 2009; Ellsworth et al., 2019). Injection-induced aseismic slip can, however, play a rather detrimental role in some cases, as slow slip is accompanied by quasi-static changes of stress in the surrounding rock mass which, in turn, may induce failure of unstable fault patches that could sometimes lead to earthquakes of undesirably large magnitude (Eyre et al., 2019). Moreover, since injection-induced aseismic slip may propagate faster than pore pressure diffusion, this mechanism can potentially trigger seismic events in regions that are far from the zone affected by the pressurization of pore fluids (Guglielmi et al., 2015; Bhattacharya & Viesca, 2019; Eyre et al., 2019). Fluid-driven aseismic slip may play a similar role in other subsurface engineering technologies than deep geothermal energy, such as hydraulic fracturing of unconventional oil and gas reservoirs (Eyre et al., 2019), oil wastewater disposal (Chen et al., 2017), and carbon dioxide sequestration (Zoback & Gorelick, 2012).

The apparent relevance of injection-induced aseismic slip in the aforementioned phenomena has motivated the development of physical models that are contributing to a better comprehension of this hydro-mechanical problem. The first rigorous investigations on the mechanics of injection-induced aseismic slip focused, for the sake of simplicity, on idealized two-dimensional configurations. Specifically, on the propagation of fault slip under plane-strain conditions considering either in-plane shear (mode II) or anti-plane shear (mode III) ruptures, with a fluid source of infinite extent along the out-of-the-plane direction. Yet these studies have significantly contributed to establishing a fundamental qualitative understanding of how the initial state of stress, the fluid injection parameters, the fault hydraulic properties, and the fault frictional rheology affect the dynamics of fluid-driven aseismic slip transients (Dublanchet, 2019; Garagash, 2021; Viesca, 2021; Yang & Dunham, 2021), the applicability of such models remains limited as three-dimensional configurations are expected to prevail in nature. Recently, Sáez et al. (2022) examined the propagation of injection-induced aseismic slip under mixed-mode (II+III) conditions, on a fault embedded in a fully three-dimensional domain. An important finding of this study is that for the same type of fluid source (either constant injection rate or constant pressure in Sáez et al., 2022), the spatiotemporal patterns of fault slip differ even qualitatively between the three-dimensional model and its two-dimensional counterpart, highlighting the importance of resolving more realistic rupture

configurations.

In the three-dimensional model of Sáez et al. (2022), the perhaps strongest assumption is the consideration of a constant friction coefficient at the fault interface. This friction model, known as Coulomb's friction, corresponds to the minimal physical ingredient that can produce unconditionally stable shear ruptures. As discussed by Sáez et al. (2022), a model with Coulomb's friction represents a case in which the frictional fracture energy spent during rupture propagation is effectively zero, without the possibility of developing a process zone in the proximities of the rupture front. In this paper, we eliminate this assumption and therefore extend the model of Sáez et al. (2022) to account for a friction coefficient that weakens upon the onset of fault slip. This incorporates into the model the proper growth and localization of a process zone, with the resulting finite amount of fracture energy. We do so by considering the simplest model of friction that can provide the sought physical ingredients, namely, a slip-weakening friction coefficient (Ida, 1972). We consider the two most common types of slip-weakening friction: a linear and an exponential decay of friction with slip, from some peak (static) value towards a constant residual (dynamic) one.

On the other hand, as shown by Sáez et al. (2022) for the Coulomb's friction case, a Poisson's ratio different than zero has mainly an effect on the aspect ratio of the resulting quasi-elliptical ruptures which become more elongated for increasing values of v. The characteristic size of mixed-mode, quasi-elliptical ruptures is nevertheless determined primarily by the rupture radius of circular ruptures, which occur in the limit of $v = 0$ for such an axisymmetric problem. The case of a null Poisson's ratio is therefore particularly insightful and notably simpler since in that limit, we can leverage the axisymmetry property of the problem to compute more efficient numerical solutions (Bhattacharya & Viesca, 2019; Sáez et al., 2022; Sáez & Lecampion, 2023b) besides allowing the problem to be tractable analytically to some extent. We therefore focus in this paper on the case of mixed-mode circular ruptures alone. We also note that our model can be considered as an extension of the two-dimensional model of Garagash and Germanovich (2012). While Garagash and Germanovich focused their investigation on the problem of nucleation and arrest of dynamic slip, our work here is concerned primarily with a different phenomenon, namely, the propagation of aseismic slip. Nonetheless, since aseismic slip could correspond indeed to the nucleation phase of an ensuing dynamic rupture, we also examine the problem of nucleation of a dynamic instability under mixed-mode conditions. In fact, by pursuing this route, we provide an extension of the nucleation length of Uenishi and Rice (2002) to the three-dimensional, axisymmetric case, for both tensile and shear ruptures. Similarly, we extend some other relevant nucleation lengths identified by Garagash and Germanovich (2012).
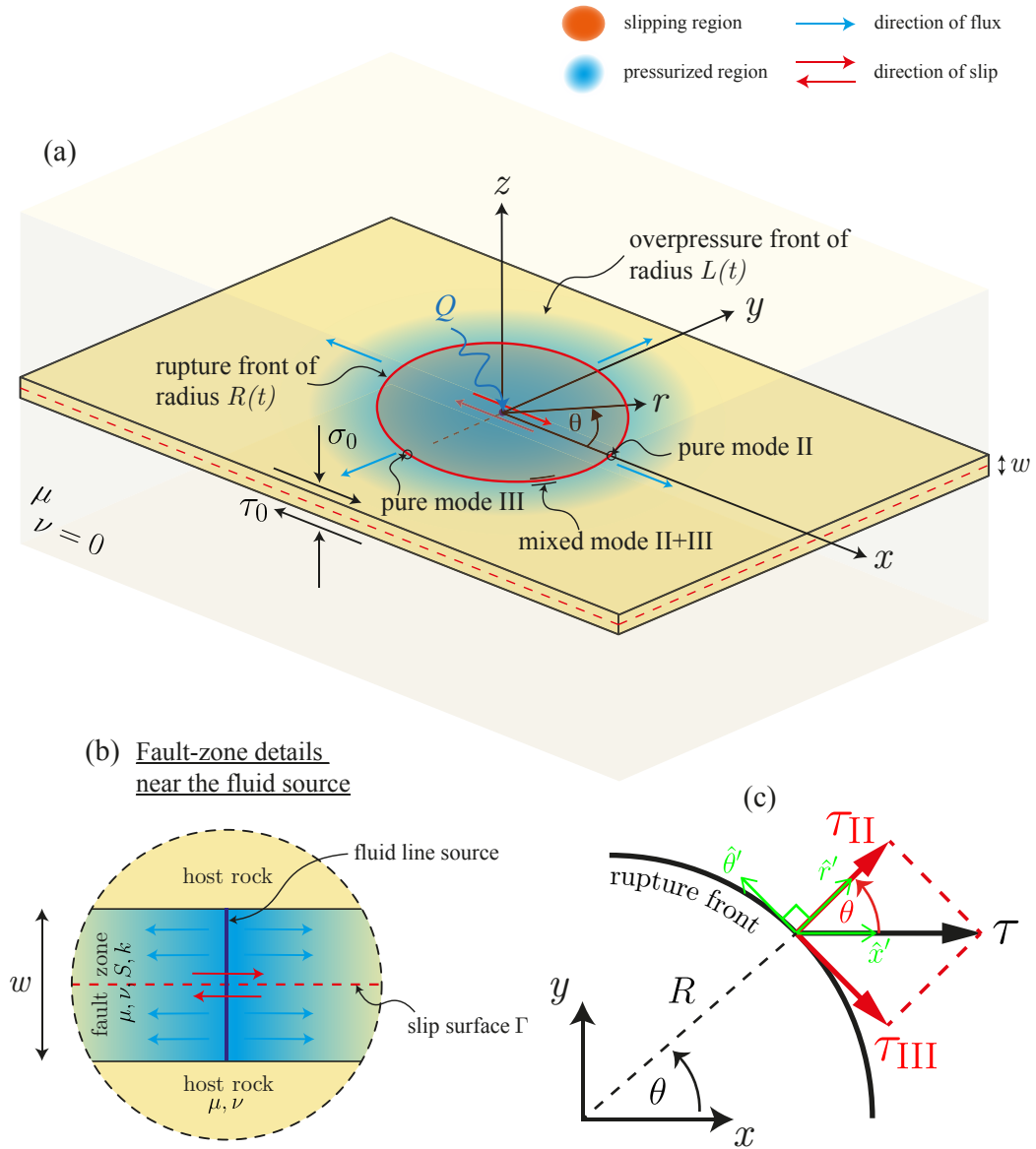
Figure 5.1: Model schematics. (a, b) Fluid is injected into a permeable fault zone of width w via a line-source that crosses the entire fault zone width. The fault is planar and embedded in an unbounded linearly elastic impermeable host rock of same elastic constants. The initial stress tensor is uniform. The resulting mixed-mode (II+III) shear rupture is circular when Poisson's ratio $\nu = 0$. (c) Direction of shear stress τ along the rupture front and the corresponding mode-II and mode-III components with regard to both the Cartesian and cylindrical coordinate systems.

5.2 Problem formulation

5.2.1 Governing equations

Fluid is injected into a poroelastic fault zone of width w that is characterized by an intrinsic permeability k and a storage coefficient S, assumed to be constant and uniform (see Figure 5.1b). The fault zone is confined within two linearly elastic half-spaces of same elastic constants, namely, a shear modulus μ and Poisson's ratio ν. The initial stress tensor is assumed to be uniform and is characterized by a resolved shear stress τ_0 and total normal stress σ_0 acting along the x and z directions of the Cartesian reference system of Figure 5.1a, respectively. We consider the injection of fluids via a line source that is located along the z axis and crosses the entire fault zone width. Under such conditions, fluid flow is axisymmetric with regard to the z axis and occurs only within the porous fault zone. Moreover, the displacement field induced by the fluid injection is irrotational and the pore pressure diffusion equation of poroelasticity reduces to its uncoupled version (Marck et al., 2015), $\partial p / \partial t = \alpha \nabla^2 p$, where $\alpha = k/S\eta$ is the fault hydraulic diffusivity, with η the fluid dynamic viscosity. Solutions of the previous linear diffusion equation are known extensively for a broad range of boundary and initial conditions (Carslaw & Jaeger, 1959). Here, we focus on the perhaps most practical case in which the fluid injection is conducted at a constant volumetric rate Q. For the following boundary conditions: $2\pi r w(k/\eta)\partial p/\partial r = -Q$ when $r \to 0$ and $p = p_0$ when $r \to \infty$, with p_0 the initial pore pressure field assumed to be uniform, the solution of the diffusion equation in terms of the overpressure $\Delta p(r, t) = p(r, t) - p_0$ reads as (section 10.4, eq. 5, Carslaw and Jaeger, 1959)

$$\Delta p(r, t) = \Delta p_* E_1\left(\frac{r^2}{4\alpha t}\right), \text{ with } \Delta p_* = \frac{Q\eta}{4\pi k w}, \tag{5.1}$$

where Δp_* is the intensity of the injection with units of pressure, and $E_1(x) = \int_x^\infty \left(e^{-x\xi}/\xi\right) d\xi$ is the exponential integral function.

Let us define the following characteristic overpressure,

$$\Delta p_c = \frac{Q\eta}{kw}, \tag{5.2}$$

which relates to the injection intensity as $\Delta p_c = 4\pi \Delta p_*$. A close examination of equation (5.1) for the large times in which the line-source approximation is valid, $t \gg r_s^2/\alpha$ with r_s the characteristic size of the actual fluid source, shows that Δp_c is in the order of magnitude of the overpressure at the fluid source. Moreover, as discussed in Section 5.10, the fluid-source overpressure, say Δp_s, increases slowly (logarithmically) with time, such that for practical applications, one could think in considering Δp_s to be rather constant and approximately equal to the characteristic overpressure Δp_c. Because of its simplicity, we adopt such approximation $\Delta p_s \approx \Delta p_c$ throughout this work, with the implications further discussed in Section 5.10. Having established that, we note that in this work we consider exclusively injection scenarios in which the characteristic fluid-source overpressure satisfies $\Delta p_c \lessapprox \sigma_0'$, where $\sigma_0' = \sigma_0 - p_0$ is

the initial effective normal stress. In this way, we make sure that the walls of the fault remain always in contact, thus avoiding hydraulic fracturing. This latter scenario has been notably addressed in the context of slip instabilities by others (Azad et al., 2017).

Suppose now that the fault zone possesses a slip surface located at $z = 0$ where the totality of fault slip is accommodated (see Figure 5.1b). The slip surface is assumed to obey a Mohr-Coulomb shear failure criterion without any cohesion such that the maximum shear stress τ and fault strength τ_s satisfy at any position along the slip surface and any time, the following local relation

$$|\tau| \le \tau_s = f \times \left(\sigma'_0 - \Delta p \right), \tag{5.3}$$

where Δp is the overpressure given by equation (5.1) and f is a local friction coefficient that depends on fault slip δ (Ida, 1972). There are two common choices for the slip-weakening friction model, namely, a friction coefficient that decays linearly with slip,

$$f(\delta) = \begin{cases} f_p - \left(f_p - f_r \right) |\delta|/\delta_c & \text{if } |\delta| \le \delta_c \\ f_r & \text{if } |\delta| > \delta_c, \end{cases} \tag{5.4}$$

and a friction coefficient that decays exponentially with it,

$$f(\delta) = f_r + \left(f_p - f_r \right) e^{-|\delta|/\delta_c}. \tag{5.5}$$

In the previous equations, f_p is the peak (or static) friction coefficient, f_r is the residual (or kinetic) friction coefficient, and δ_c is the characteristic 'distance' over which the friction coefficient decays from f_p to f_r, as displayed in Figure 5.2. Moreover, we assume that the slip surface is fully locked before the injection starts and, as such, the initial shear stress τ_0 must be lower than the in-situ static strength of the fault, $\tau_p^0 = f_p \sigma'_0$.

According to equation (5.3), the injection of fluid has the effect of reducing the fault strength owing to the increase of pore-fluid pressure which decreases the effective normal stress locally. Such pore pressure increase will be eventually sufficient to activate fault slip when the fault strength equates the pre-injection shear stress τ_0, which marks the onset of the interfacial frictional rupture. Indeed, owing to the line-source approximation of the fluid source, the activation of slip in our model occurs immediately upon the start of the injection as a consequence of the weak logarithmic singularity that the exponential integral function features near the origin (see Section 5.10). In the three-dimensional axisymmetric configuration under consideration, the resulting shear rupture will propagate under mixed-mode II+III conditions, where II and III represent the in-plane shear and anti-plane shear deformation modes, respectively. The modes of deformation are schematized in Figure 5.1c in terms of the near-front shear stress components. Moreover, as stated in the introduction, we restrict ourselves to the case of circular ruptures alone. Such an idealized case is exact for radial fluid flow when the Poisson's ratio $\nu = 0$ (Bhattacharya & Viesca, 2019; Sáez et al., 2022). Moreover, in some limiting regimes of the fault response, numerically-derived asymptotic expressions for the
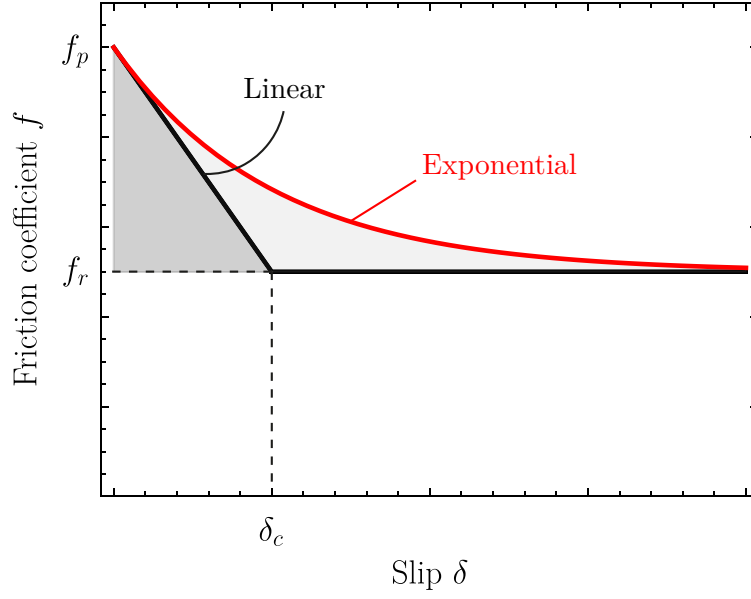
Figure 5.2: Slip weakening friction law for (black) linear weakening and (red) exponential decay with slip. If the friction coefficient f is multiplied by some constant effective normal stress that is approximately uniform and representative of the one acting along the process zone, then the gray areas times such effective normal stress represent fracture energy G_c. Note that $G_c^{\text{exp}} = 2 \cdot G_c^{\text{lin}}$ when δ_c is the same in both models.

aspect ratio of elongated ruptures ($v \neq 0$) (Sáez et al., 2022) may result useful to construct approximate solutions for the evolution of non-circular rupture fronts using the solution for circular ruptures, at least in the case of Coulomb's friction (Sáez et al., 2022).

By neglecting any fault-zone poroelastic coupling upon the onset of the rupture, the quasi-static elastic equilibrium that relates fault slip δ to the shear stress τ acting along the fault can be written as the following boundary integral equation along the x axis (Salamon & Dundurs, 1977; Bhattacharya & Viesca, 2019),

$$\tau(r,t) = \tau_0 + \frac{\mu}{2\pi} \int_0^{R(t)} F(r,\xi) \frac{\partial \delta(\xi,t)}{\partial \xi} d\xi, \tag{5.6}$$

where the kernel $F(r,\xi)$ is given by

$$F(r,\xi) = \frac{K(k(r/\xi))}{\xi+r} + \frac{E(k(r/\xi))}{\xi-r}, \text{ with } k(x) = \frac{2\sqrt{x}}{1+x}, \tag{5.7}$$

and $K(\cdot)$ and $E(\cdot)$ are the complete elliptic integrals of the first and second kind, respectively. Note that in equation (5.6), the shear stress τ can be written as a function in space of the radial coordinate only due to the aforementioned axisymmetry property when $v = 0$. Equations (5.1), (5.3), and (5.6), plus the corresponding constitutive friction law, either (5.4) or (5.5), provide a complete system of equations to solve for the spatio-temporal evolution of fault slip $\delta(r,t)$

and the position of the rupture front $R(t)$: our primary unknowns in the problem.

5.2.2   Front-localized energy balance

Under certain conditions and over a certain spatial range, the previous problem may be formulated equivalently through an energy balance of the Griffith type, that is, as a classical shear crack in the theory of Linear Elastic Fracture Mechanics (LEFM) (Broberg, 1999). The idea that frictional ruptures could be approximated by classical shear cracks is relatively old (Ida, 1972; Palmer & Rice, 1973). Yet it has been just recently validated by modern experiments concerned with the problem of frictional motion on both dry and lubricated interfaces (Svetlizky et al., 2019).

Let us assume that there exists a localization length ℓ_* near the rupture front such that the shear stress evolves from some peak value τ_p at the rupture front $r = R$ to some residual and approximately constant amount τ_r at distances $r < R - \ell_*$. The localization length ℓ_* is sometimes called the process zone size or cohesive zone size for the similarity of the shear rupture problem to the case of tensile fractures (Barenblatt, 1962). Let us further assume that ℓ_* is small in comparison to the rupture radius R. Under such conditions, we can invoke the 'small-scale yielding' approximation of LEFM to shear ruptures (Palmer & Rice, 1973). In particular, during rupture propagation, the influx of elastic energy into the edge region G, also known as energy release rate, must equal the frictional fracture energy G_c. The energy release rate for an axisymmetric, circular shear rupture is (Appendix B of Sáez et al., 2022)

$$G = \frac{2}{\pi \mu R(t)} \left[\int_0^{R(t)} \frac{\tau_0 - \tau_r(r, t)}{\sqrt{R(t)^2 - r^2}} r \, dr \right]^2 . \tag{5.8}$$

In the previous equation, it is assumed that the current shear stress acting on the 'crack' faces is the residual strength τ_r. This is consistent with the small-scale yielding approach where the details of the process zone are neglected for the calculation of G (Rice, 1968; Palmer & Rice, 1973). On the other hand, the fracture energy G_c corresponds to the energy dissipated within the process zone per unit area of rupture growth, which in the case of a frictional shear crack is equal to the work done by the fault strength τ_s against its residual part τ_r (Palmer & Rice, 1973),

$$G_c = \int_0^{\delta_*} [\tau_s(\delta) - \tau_r(\delta_*)] \, d\delta, \tag{5.9}$$

where δ_* is the accrued slip throughout the process zone assuming, again, that there exists a proper localization length ℓ_*.

Let us now recast the Griffith's energy balance, $G = G_c$, in a way that will be more convenient for analytic derivations. For a mixed-mode shear rupture, the energy release rate can be expressed as $G = K_{II}^2(1 - \nu)/2\mu + K_{III}^2/2\mu$ (Irwin, 1958), where K_{II} and K_{III} are the mode-II and mode-III stress intensity factors. Here, K_{II} and K_{III} are understood as the intensities of the singular fields

of LEFM that emerge as intermediate asymptotics at distances $\ell_* \ll r \ll R$. Moreover, since $v = 0$, we can conveniently define

$$K^2 = K_{II}^2 + K_{III}^2 = 2\mu G, \quad \text{and} \quad K_c = \sqrt{2\mu G_c}, \tag{5.10}$$

where K is an 'axisymmetric stress-intensity factor' and K_c an 'axisymmetric fracture toughness'. Note that if one considers the singular terms of the mode-II and mode-III shear stress components acting nearby and ahead of the rupture front, say τ_{II} and τ_{III} respectively (see Figure 5.1c), then K represents the intensity of the square-root singularity associated with the absolute (maximum) shear stress τ (acting along the x-direction of our Cartesian reference system) which relates to the in-plane shear and anti-plane shear stress components as $\tau^2 = \tau_{II}^2 + \tau_{III}^2$.

By combining equations (5.8) and (5.10), we can rewrite the Griffith's energy balance in the sought Irwin's form, $K = K_c$, which yields

$$\frac{2}{\sqrt{\pi R(t)}} \int_0^{R(t)} \frac{\tau_0 - \tau_r(r, t)}{\sqrt{R(t)^2 - r^2}} r \, \mathrm{d}r = K_c. \tag{5.11}$$

Let us now consider some details about the calculation of G_c in equation (5.9). Upon the arrival of the rupture front at a certain location over the fault plane, the fault strength τ_s weakens according to equation (5.3) due to both the decrease of the friction coefficient f and the increase of overpressure Δp. However, the near-front processes associated with energy dissipation for rupture growth in equation (5.9) are for the most part related to the frictional process only. This can be readily seen after closely examining equation (5.1) for the spatio-temporal evolution of Δp. Equation (5.1) introduces the well-known diffusion length scale $L(t) = \sqrt{4\alpha t}$ in the problem, which is itself a proxy for the radius of the nominal area affected by the pressurization of pore fluid (see Figure 5.1a). We note that if the overpressure front L is either in the order of or much greater than the rupture radius R, then Δp varies smoothly over the process zone —whose length ℓ_* is at this point by definition much smaller than R. On the other hand, if L is much smaller than R, then Δp varies abruptly over the slipping region but is highly localized near the rupture center over a small zone that is far away from the process zone, such that the overpressure within the process zone is negligibly small. Hence, the overpressure has the simple role of approximately setting the current amount of effective normal stress within the process zone, which can be reasonably taken as uniform at a given time and evaluated at the rupture front, $\Delta p(R, t)$. The fracture energy G_c can be thus approximated as

$$G_c \approx \left[\sigma_0' - \Delta p(R, t)\right] \int_0^{\delta_*} \left[f(\delta) - f_r\right] \mathrm{d}\delta. \tag{5.12}$$

Note that in addition to the separation of scales between the diffusion of pore pressure and the frictional weakening process just discussed, the previous equation assumes that the friction coefficient itself must effectively evolve throughout ℓ_* (or equivalently over δ_*) towards an

approximately constant residual value $f_r(\delta_*) = f_r$. This latter is guaranteed in the linear-weakening model (5.4) as $\delta_* = \delta_c$, and it seems a good approximation for the exponential-weakening case (5.5) at some $\delta_* > \delta_c$. Assuming this latter separation of scales too, the residual strength of the fault can be then written as

$$\tau_r(r, t) = f_r \times \left[\sigma_0' - \Delta p(r, t) \right].$$ (5.13)

Substituting the previous equation into (5.11) leads after some manipulations to an energy-based equation for the rupture front $R(t)$,

$$\underbrace{\frac{2}{\sqrt{\pi}} \frac{f_r \Delta p_*}{\sqrt{R}} \int_0^R \frac{E_1\left(r^2/L^2\right)}{\sqrt{R^2 - r^2}} r\,\mathrm{d}r}_{K_p} + \overbrace{\frac{2}{\sqrt{\pi}} \left[\tau_0 - f_r \sigma_0'\right] \sqrt{R}}^{K_\tau} = K_c(R, t),$$ (5.14)

where the explicit dependence of the rupture front R and overpressure front L on time t has been omitted for simplicity.

Equation (5.14) is an insightful form of the near-front energy balance, equivalent to the one obtained by Garagash and Germanovich (2012) in two dimensions. It shows that the instantaneous position of the rupture front is determined by the competition between three distinct 'crack' processes that are active during the propagation of the rupture. The first term on the left-hand side K_p is an axisymmetric stress intensity factor (SIF) associated with the equivalent shear load induced by the fluid injection alone, which continuously unclamps the fault. The second term on the left-hand side K_τ is an axisymmetric SIF due to a uniform shear load that is equal to the difference between the initial shear stress τ_0 and the residual strength of the fault without any overpressure, $f_r \sigma_0'$, commonly known as stress drop. Note that this term may be either positive or negative, whereas the first term is always positive. Finally, the right-hand side of the near-front energy balance is associated with the fracture energy G_c that is dissipated within the process zone or, in the Irwin's form, the fracture toughness K_c. Note that in our model, the fracture energy may generally depend on the rupture radius R and time t due to variations in overpressure (see equation (5.12)).

5.3   Two simplified models

5.3.1   The constant friction model

The constant friction model is the simplest idealization of friction that produces fluid-driven stable frictional ruptures. It has been extensively studied in two-dimensional configurations for different injection scenarios (Viesca, 2021; Sáez et al., 2022) and more recently in the fully three-dimensional case (Sáez et al., 2022). Here, we briefly summarize the main characteristics of the circular rupture model (Sáez et al., 2022), whose results will be later put in a broader perspective in relation to the slip-weakening model.

Sáez et al. (2022) showed that fault slip induced by injection at a constant volumetric rate is self-similar in a diffusive manner. The rupture radius $R(t)$ thus evolves simply as

$$R(t) = \lambda L(t), \tag{5.15}$$

where $L(t) = \sqrt{4\alpha t}$ is the diffusion length scale and nominal position of the overpressure front, and λ is the so-called amplification factor for which an analytical solution was derived from the condition that the rupture grows with no stress singularity at its front,

$$\int_0^1 \frac{E_1(\lambda\eta)}{\sqrt{1-\eta^2}}\eta\,\mathrm{d}\eta = \mathcal{T}, \tag{5.16}$$

which leads after evaluating analytically the corresponding integral to

$$2 - \gamma + \frac{2}{3}\lambda^2 {}_2F_2 \left[\begin{array}{cc} 1 & 1 \\ 2 & 5/2 \end{array} ; -\lambda^2 \right] - \ln(4\lambda^2) = \mathcal{T}, \tag{5.17}$$

where $\gamma = 0.577216...$ is the Euler-Mascheroni's constant and ${}_2F_2[\,]$ is the generalized hypergeometric function. Note that λ is a function of a sole dimensionless number, the so-called stress-injection parameter

$$\mathcal{T} = \frac{f_{\mathrm{cons}}\sigma_0' - \tau_0}{f_{\mathrm{cons}}\Delta p_*}, \tag{5.18}$$

where f_{cons} is the constant friction coefficient.

The parameter $\mathcal{T}$ is defined as the ratio between the amount of shear stress that is necessary to activate fault slip $f_{\mathrm{cons}}\sigma_0' - \tau_0$, and $f_{\mathrm{cons}}\Delta p_*$ which quantifies the intensity of the fluid injection. $\mathcal{T}$ can vary in principle between 0 and $+\infty$ (Sáez et al., 2022). However, for practical purposes $\mathcal{T}$ is upper bounded. Indeed, as described previously, $\Delta p_* = \Delta p_c/4\pi$ with Δp_c taken as approximately equal to the overpressure at the fluid source. Hence, one can estimate the minimum amount of overpressure that is required to activate fault slip as $f_{\mathrm{cons}}\Delta p_c \approx f_{\mathrm{cons}}\sigma_0' - \tau_0$. Substituting the previous relation into equation (5.18) leads to an approximate upper bound for $\mathcal{T} \lesssim 10$, where we have approximated the factor 4π by 10. The lower and upper bounds of $\mathcal{T}$ are associated with two end-member regimes that were first introduced by Garagash and Germanovich (2012). When $\mathcal{T}$ is close to zero, $\tau_0 \to f_{\mathrm{cons}}\sigma_0'$ and thus the fault is critically stressed or about to fail before the injection starts. On the other hand, when $\mathcal{T} \approx 10$, the fault is 'marginally pressurized' as the injection has provided just the minimum amount of overpressure to activate fault slip.

The asymptotic behavior of λ for the limiting values of $\mathcal{T}$ is particularly insightful. For critically stressed faults ($\mathcal{T} \ll 1$), the amplification factor turns out to be large ($\lambda \gg 1$), and thus the rupture front outpaces largely the fluid pressure front ($R(t) \gg L(t)$), whereas for marginally pressurized faults ($\mathcal{T} \sim 10$), the amplification factor is small ($\lambda \ll 1$) and thus the rupture front lags significantly the overpressure front ($R(t) \ll L(t)$). In the critically stressed limit, since

$\lambda \gg 1$, the equivalent shear load due to fluid injection can be approximated as a point force,

$$f_{\text{cons}}\Delta p(r,t) \approx f_{\text{cons}}\Delta P(t)\delta^{dirac}(r)/2\pi r, \text{ with } \Delta P(t) = \Delta p_* \int_0^\infty E_1\left(\frac{r^2}{4\alpha t}\right)2\pi r\,\mathrm{d}r = 4\pi\alpha t\Delta p_*,$$

(5.19)

whereas in the marginally pressurized limit, its asymptotic form comes simply from expanding the exponential integral function for small values of its argument as $\lambda \ll 1$: $f_{\text{cons}}\Delta p(r,t) \approx -f_{\text{cons}}\Delta p_*\left[\ln\left(r^2/4\alpha t\right) + \gamma\right]$. Substituting the previous asymptotic forms for the fluid-injection 'forces' into the rupture propagation condition (5.16) leads to the following asymptotes for the amplification factor (Sáez et al., 2022):

$$\lambda \approx \begin{cases} 1/\sqrt{2\mathcal{T}} & \text{for critically stressed faults, } \mathcal{T} \ll 1, \\ \frac{1}{2}\exp\left(\left[2 - \gamma - \mathcal{T}\right]/2\right) & \text{for marginally pressurized faults, } \mathcal{T} \sim 10. \end{cases}$$

(5.20)

Comparing the previous asymptotes with the exact solution (5.17) suggests that the asymptotic approximation (5.20) is accurate up to 5% in the critically stressed and marginally pressurized regimes, for $\mathcal{T} \lesssim 0.16$ and $\mathcal{T} \gtrsim 2$, respectively.

5.3.2   The constant fracture energy model

Consider the simple case in which the fracture energy G_c is constant (and so the fracture toughness K_c). Although this is an idealized scenario, it accounts already for one of the main ingredients of the slip-weakening friction model, that is, a finite fracture energy. At the same time, the constant fracture energy model allows us to examine quickly the different regimes of propagation that emerge from the competition between the three distinct terms that compose the front-localized energy balance (5.14). Furthermore, a constant fracture energy model will result to be an excellent approximation of some important rupture regimes in the slip-weakening model.

Scaling and structure of the solution

Similarly to the case of Coulomb's friction, let us define an amplification factor in the form

$$\lambda(t) = \frac{R(t)}{L(t)}.$$

(5.21)

Unlike the solution of the previous section that is self-similar, here the introduction of a finite fracture energy breaks the self-similarity of the problem and makes the solution for λ be now time-dependent.

Non-dimensionalization of the front-localized energy balance shows that the solution for the

amplification factor λ can be written as

$$\lambda\left(\mathscr{T}_r, \mathscr{K}(t)\right), \tag{5.22}$$

where $\mathscr{T}_r$ and $\mathscr{K}$ are two dimensionless parameters with the physical meanings that we explain below. Interestingly, the dependence of λ on time is only in the second parameter $\mathscr{K}$.

The first parameter $\mathscr{T}_r$ is a dimensionless number in the form

$$\mathscr{T}_r = \frac{f_r \sigma'_0 - \tau_0}{f_r \Delta p_*}, \tag{5.23}$$

which turns out to be identical to the stress-injection parameter of the constant friction model (equation (5.18)) except that the constant friction coefficient f_{cons} is now the residual friction coefficient f_r. For this reason, we name it as the 'residual' stress-injection parameter.

$\mathscr{T}_r$ quantifies the combined effect of the two equivalent shear loads that drive the propagation of the 'fractured' slipping patch, namely, the uniform stress $f_r \sigma'_0 - \tau_0$ and the distributed load associated with fluid injection $f_r \Delta p(r, t)$ whose intensity is $f_r \Delta p_*$. The uniform stress is equal to the difference between the residual fault strength under ambient conditions $f_r \sigma'_0$ and the initial shear stress τ_0. Note that depending on the sign of $f_r \sigma'_0 - \tau_0$, $\mathscr{T}_r$ can be either positive or negative. Moreover, as noted by first Garagash and Germanovich (2012) in their two-dimensional model, the sign of $f_r \sigma'_0 - \tau_0$ is expected to strongly affect the overall stability of the fault response. According to Garagash and Germanovich, if the condition $f_r \sigma'_0 < \tau_0$ is satisfied ($\mathscr{T}_r$ negative), ruptures may ultimately run away dynamically and never stop within the limits of such a homogeneous and infinite fault model. Conversely, when $f_r \sigma'_0 > \tau_0$ ($\mathscr{T}_r$ positive), ruptures would propagate ultimately in a quasi-static, stable manner. Assuming for now that the ultimate stability condition of Garagash and Germanovich (2012) holds in the circular rupture configuration, we consider only ultimately quasi-static cases in this section and, therefore, values for $\mathscr{T}_r$ that are strictly positive. We will soon show that this assumption is indeed satisfied.

Let us now find the limiting values of $\mathscr{T}_r$. As lower bound, $\mathscr{T}_r$ can be as small as possible ($\mathscr{T}_r \to 0$) when $f_r \sigma'_0 \to \tau_0$. Since in this limit, the fault is approaching the ultimate unstable condition of Garagash and Germanovich (2012), we refer to it as the 'nearly unstable' limit. As an upper bound, similarly to the case of constant friction, the maximum value of $\mathscr{T}_r$ is set by the minimum possible magnitude of Δp_*, which in turn relates to the minimum amount of overpressure that is required to activate fault slip. This is given by the approximate relation $f_p \Delta p_c \approx f_p \sigma'_0 - \tau_0$, where f_p is the peak friction coefficient and Δp_c is the characteristic overpressure of the fluid source (equation (5.2)). By substituting this previous relation into (5.23), we find the sought upper bound to be $\mathscr{T}_r \lesssim 4\pi(\sigma'_0 - \tau_0/f_r)/(\sigma'_0 - \tau_0/f_p)$. Since the ratio f_r/f_p is always between 0 and 1 and the maximum value of the upper bound is obtained when $f_r/f_p \to 1$, we obtain such a maximum upper bound as $\mathscr{T}_r \lesssim 10$ (again, the factor 4π). Given that in this limit the upper bound is still related to the minimum amount of overpressure that is

required to activate a frictional rupture, we still denominate it as marginally pressurized limit. Note that the upper bound limit has a quite similar meaning to the one of $\mathscr{T}$ in the constant friction model. Conversely, the lower bound limit of $\mathscr{T}_r$ has no longer the interpretation of a critically stressed fault as for $\mathscr{T}$.

The second parameter of the constant fracture energy model, $\mathscr{K}$, corresponds to a time-dependent dimensionless toughness. It can be either defined using the stress scales of the nearly unstable or marginally pressurized limits depending on the proper regime characterizing the fault response. These two choices are:

$$\mathscr{K}_{nu}(t) = \frac{K_c}{\left(f_r \sigma_0' - \tau_0\right)\sqrt{R(t)}}, \text{ and } \quad \mathscr{K}_{mp}(t) = \frac{K_c}{f_r \Delta p_* \sqrt{R(t)}}, \tag{5.24}$$

for the nearly unstable ($\mathscr{T}_r \ll 1$) and marginally pressurized ($\mathscr{T}_r \sim 10$) regimes, respectively. Note that in (5.24), the explicit dependence of R on time has been emphasized as it provides the time dependence of $\mathscr{K}$.

The dimensionless toughness $\mathscr{K}$ quantifies the relevance of the fracture energy in the near-front energy balance at a given time t. Since for any physically admissible solution in which the injection is continuous, the rupture radius must increase monotonically with time, the solution will always evolve from a large-toughness regime ($\mathscr{K} \gg 1$) to a small-toughness regime ($\mathscr{K} \ll 1$). Moreover, the effect of the fracture energy in the energy balance can be ultimately neglected as the dimensionless toughness effectively vanishes ($\mathscr{K} \to 0$) in the limit $R \to \infty$ (or $t \to \infty$). We denominate this ultimate solution as the zero-toughness or zero-fracture-energy solution. Since the effect of the fracture energy becomes irrelevant in this limit, such asymptotic solution is self-similar (λ in (5.22) becomes time-independent).

Finally, the transition between the large- and small-toughness regimes is characterized by the following rupture length scales (obtained by setting $\mathscr{K}_{nu} = 1$ and $\mathscr{K}_{mp} = 1$, respectively),

$$R_{nu}^* = \left(\frac{K_c}{f_r \sigma_0' - \tau_0}\right)^2 \text{ and } \quad R_{mp}^* = \left(\frac{K_c}{f_r \Delta p_*}\right)^2. \tag{5.25}$$

Note that the two dimensionless toughnesses in (5.24) are of course not independent as they are two choices of one same parameter. They are indeed related through the residual stress-injection parameter $\mathscr{T}_r$ as

$$\mathscr{K}_{mp} = \mathscr{T}_r \mathscr{K}_{nu}. \tag{5.26}$$
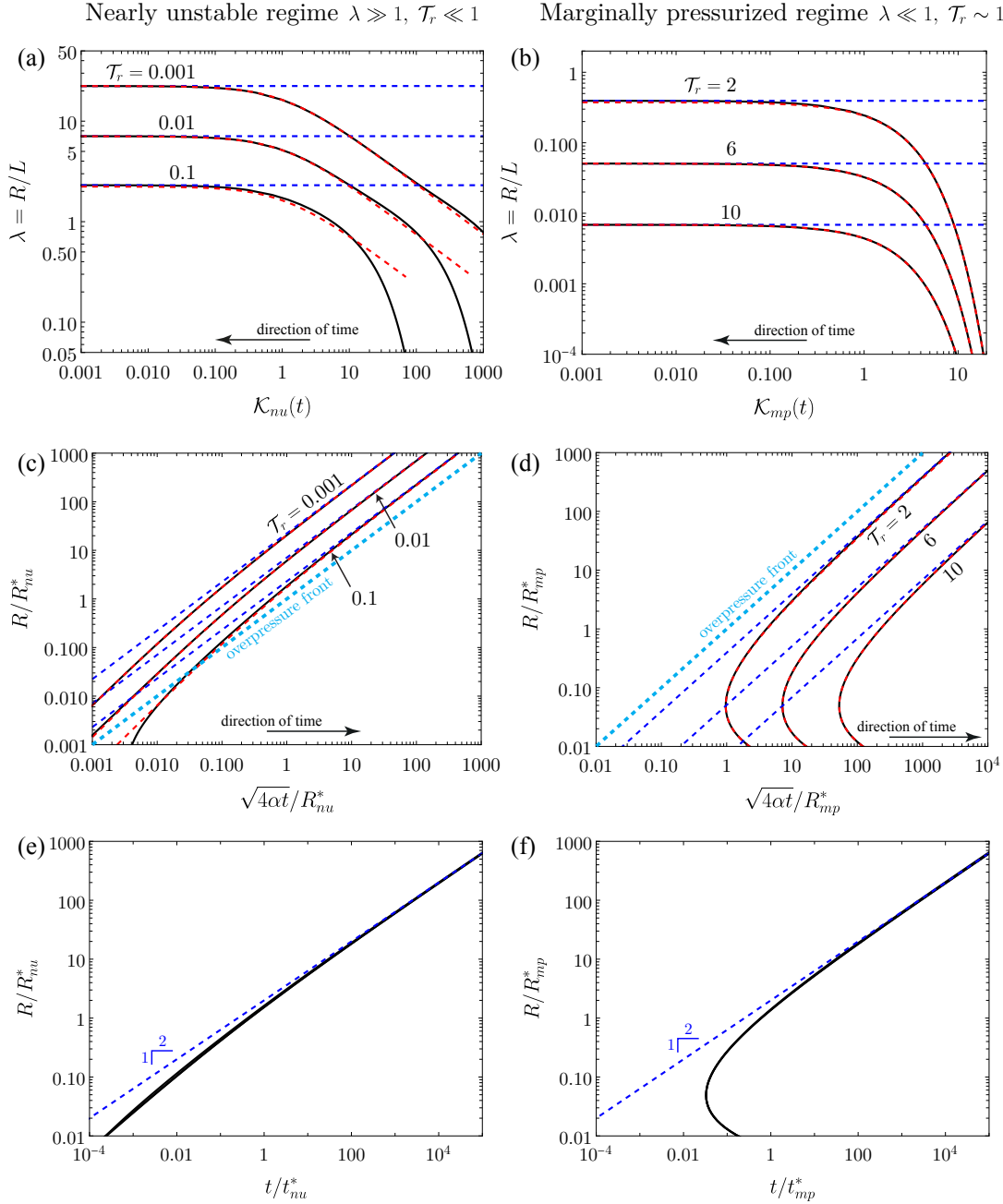
Figure 5.3: The constant fracture energy model. (Left) Nearly unstable regime ($\lambda \gg 1$, $\mathcal{T}_r \ll 1$) and (right) marginally pressurized regime ($\lambda \ll 1$, $\mathcal{T}_r \sim 10$). (a, b) Amplification factor λ as a function of dimensionless toughness $\mathcal{K}(t)$ for different values of $\mathcal{T}_r$. (c, d) Normalized rupture radius R as a function of the normalized squared root of time or position of the overpressure front $L(t) = \sqrt{4\alpha t}$. (e, f) Normalized rupture radius R as a function of dimensionless time t. All curves tend to collapse when using the latter scaling. Legends: black solid lines are the general solution of the constant fracture energy model; red dashed lines correspond to the asymptotes for λ (5.29) in (a, b), and the asymptotes for the normalized rupture radius (5.32) and (5.33) in (c) and (d), respectively; blue dashed lines represent the constant residual friction, ultimate zero-fracture-energy solution.

General and ultimate zero-fracture-energy solutions

Considering the scaling of the previous section plus the definition of the following non-dimensional integral:

$$\Psi(\lambda) = \int_0^1 \frac{E_1(\lambda\eta)}{\sqrt{1-\eta^2}} \eta \, d\eta, \tag{5.27}$$

the front-localized energy balance (5.14) can be written in dimensionless form as

$$\frac{\Psi(\lambda)}{\mathscr{T}_r} - 1 = \frac{\sqrt{\pi}}{2} \mathscr{K}_{nu}, \text{ and } \quad \Psi(\lambda) - \mathscr{T}_r = \frac{\sqrt{\pi}}{2} \mathscr{K}_{mp}, \tag{5.28}$$

in the nearly unstable ($\mathscr{T}_r \ll 1$) and marginally pressurized ($\mathscr{T}_r \sim 10$) regimes, respectively. Note that the non-dimensional integral Ψ is identical to the one in equation (5.16) and can be thus evaluated analytically to obtain the left-hand side of equation (5.17). Moreover, the limiting behaviors of such integral are: $\Psi(\lambda) \approx 1/2\lambda^2 + O(\lambda^{-4})$ when $\lambda \gg 1$, and $\Psi(\lambda) \approx 2 - \gamma - \ln(4\lambda^2) + O(\lambda^2)$ when $\lambda \ll 1$. Using the previous asymptotic expansions and assuming similarly to the constant friction model that $\lambda \gg 1$ when $\mathscr{T}_r \ll 1$, and $\lambda \ll 1$ when $\mathscr{T}_r \sim 10$, we derive from equations (5.28), the following closed-form asymptotic expressions for the amplification factor:

$$\lambda \approx \begin{cases} 1/\sqrt{\left(2 + \sqrt{\pi}\mathscr{K}_{nu}\right)\mathscr{T}_r} & \text{for nearly unstable faults, } \mathscr{T}_r \ll 1, \\ \frac{1}{2} \exp\left[\left(2 - \gamma - \mathscr{T}_r - \mathscr{K}_{mp}\sqrt{\pi}/2\right)/2\right] & \text{for marginally pressurized faults, } \mathscr{T}_r \sim 10, \end{cases} \tag{5.29}$$

where the dependence of both $\mathscr{K}$ and λ on time has been omitted for simplicity.

The full solution of the model given by equations (5.28) together with the asymptotics (5.29) are shown in Figures 5.3a and 5.3b. The direction of time in these plots goes from right to left as the dimensionless toughness $\mathscr{K}(t)$ decreases with time. Moreover, since ultimately ($t \to \infty$, $R \to \infty$) the dimensionless toughness is negligibly small ($\mathscr{K} \to 0$), equations (5.28)a and (5.28)b become both identical to the rupture propagation condition of the constant friction model, equation (5.16), as long as the constant friction coefficient f_{cons} is now understood as the residual one f_r. The solution of the constant friction model (5.17) with $f_{\text{cons}} = f_r$ is also displayed in Figures 5.3a and 5.3b. It is now clear how the constant fracture energy solution approaches asymptotically the constant residual friction solution as $\mathscr{K} \to 0$. This can also be seen in the asymptotics (5.29) that become identical to (5.20) when $\mathscr{K} = 0$.

The previous result has an important implication: the constant friction model analyzed in Sáez et al. (2022) can be now interpreted in two distinct manners: as a scenario in which the friction coefficient does not significantly weaken ($f_{\text{cons}} \approx f_p$), or as the ultimate asymptotic solution of a model with constant fracture energy provided that $f_{\text{cons}} = f_r$. In the former, the fracture energy $G_c = 0$ by definition. In the latter, the effect of the non-zero fracture energy in the rupture-front energy balance is to leading order negligible compared to the other two terms that drive the propagation of the rupture. In addition, because the integral $\Psi(\lambda)$ is

strictly positive and in the ultimate asymptotic regime $\mathcal{K} \to 0$, the near-front energy balance (5.28) admits ultimate quasi-static solutions only if $\mathcal{T}_r > 0$. Negative values of $\mathcal{T}_r$ which are equivalent to the condition $f_r \sigma_0' < \tau_0$ may be thus related to ultimately unstable solutions, not accounted for the quasi-static energy balance. This result supports our assumption that the ultimate stability condition of Garagash and Germanovich (2012) holds in the circular rupture configuration.

We now recast the solution of the constant fracture energy model in a perhaps more intuitive way, as the evolution of the rupture radius with time:

$$R(t) = \lambda(\mathcal{T}_r, \mathcal{K}(t)) \cdot L(t). \tag{5.30}$$

Recalling that $L(t) = \sqrt{4\alpha t}$ and noting that

$$\mathcal{K}_{nu} = (R/R_{nu}^*)^{-1/2}, \text{ and } \quad \mathcal{K}_{mp} = (R/R_{mp}^*)^{-1/2}, \tag{5.31}$$

we solve equations (5.28)a and (5.28)b for R/R^* as a function of the normalized squared root of time $\sqrt{4\alpha t}/R^*$ and $\mathcal{T}_r$, where R^* represents the characteristic rupture length scale of either the nearly unstable or marginally pressurized regime (equation (5.25)).

This version of the solution is displayed in Figures 5.3c and 5.3d. In these plots, the normalized square root of time can be also interpreted as the normalized position of the overpressure front $L(t)$. Indeed, the thicker dashed line corresponds to the current position of the overpressure front. Slip fronts propagating above this line represent cases in which the rupture front outpaces the overpressure front. We observe that such a situation is a common feature of nearly unstable faults ($\mathcal{T}_r \ll 1$), being the analog regime of critically stressed faults in the constant friction model. Moreover, taking into account (5.30) and (5.31), the asymptotics (5.29) can be recast as the following implicit equations for the normalized rupture radius R/R^* as a function of time:

$$\sqrt{4\alpha t}/R_{nu}^* = \frac{R}{R_{nu}^*} \left[\left(2 + \frac{\sqrt{\pi}}{\sqrt{R/R_{nu}^*}} \right) \mathcal{T}_r \right]^{1/2} \tag{5.32}$$

for nearly unstable faults, and

$$\sqrt{4\alpha t}/R_{mp}^* = \frac{2\left(R/R_{mp}^*\right)}{\exp\left[\left(2 - \gamma - \mathcal{T}_r - (\sqrt{\pi}/2)\left(R/R_{mp}^*\right)^{-1/2} \right)/2 \right]} \tag{5.33}$$

for marginally pressurized faults.

Note that the transition from the large-toughness ($\mathcal{K} \gg 1$) to small-toughness ($\mathcal{K} \ll 1$) regime in Figures 5.3c and 5.3d occurs along the vertical axis when $R/R_{nu}^* \sim 1$ and $R/R_{mp}^* \sim 1$, respectively. The characteristic time at which this transition occurs can be approximated by using the constant residual friction solution or, what is the same, the ultimate zero-fracture-

energy solution, $\lambda_r = \lambda(\mathcal{T}_r, \mathcal{K} = 0)$, which yields

$$t_{nu}^* \approx \frac{1}{\alpha \lambda_r^2} \left(\frac{K_c}{f_r \sigma_0' - \tau_0} \right)^4, \text{ and } \quad t_{mp}^* \approx \frac{1}{\alpha \lambda_r^2} \left(\frac{K_c}{f_r \Delta p_*} \right)^4. \tag{5.34}$$

λ_r can be estimated from the asymptotes presented in equation (5.20) for both nearly unstable ($\mathcal{T}_r \ll 1$) and marginally pressurized ($\mathcal{T}_r \sim 10$) faults, provided that $\mathcal{T}$ is replaced by $\mathcal{T}_r$. Normalizing time by the previous characteristic times naturally tends to collapse all solutions for every value of $\mathcal{T}_r$ as displayed in Figures 5.3e and 5.3f, where the power law 1/2 reflects the diffusively self-similar property of the ultimate zero-fracture-energy solution.

Finally, it seems worth mentioning that the solution for marginally pressurized faults is non-physical at times in which the rupture is small, $R/R_{mp}^* \lesssim 0.05$ (see Figures 5.3d and 5.3f). This could be related either to the occurrence of a dynamic instability or to a rupture size that is too small compared to realistic process zone sizes. Indeed, the solution constructed here for the case of constant fracture energy has the inherent limitations of LEFM theory. First, it does not account for the initial stage in which the process zone is under development ($R < \ell_*$) and, second, it is an approximate solution that relies on the small-scale yielding assumption ($R \gg \ell_*$). Both limitations are overcome in the next section by solving numerically the governing equations of the coupled initial boundary value problem for slip-weakening friction.

5.4　Scaling analysis, map of rupture regimes and ultimate stability condition

5.4.1　Scaling analysis

The scaling of the slip-weakening problem comes directly from the two-dimensional linear-weakening model of Garagash and Germanovich (2012), which is also valid for the exponential-weakening version of the friction law. We summarize the scaling as follows:

$$\bar{t} = \frac{t}{R_w^2/\alpha}, \quad \bar{r} = \frac{r}{R}, \quad \bar{\tau} = \frac{\tau}{f_p \sigma_0'}, \quad \bar{\delta} = \frac{\delta}{\delta_w}, \quad \Delta \bar{p} = \frac{\Delta p}{\Delta p_*}, \tag{5.35}$$

where the bar symbol represents dimensionless quantities, δ_w is the slip weakening scale, and R_w is an elasto-frictional rupture length scale, given respectively by (see also Uenishi and Rice, 2002)

$$\delta_w = \frac{f_p}{f_p - f_r} \delta_c, \text{ and } \quad R_w = \frac{\mu}{(f_p - f_r)\sigma_0'} \delta_c. \tag{5.36}$$

In the previous equation, $(f_p - f_r)\sigma_0'/\delta_c$ is the so-called slip-weakening rate (Uenishi & Rice, 2002).

Nondimensionalization of the governing equations of the model using the previous scaling shows that the normalized fault slip $\bar{\delta}$ depends in addition to dimensionless space $\bar{r}$ and time $\bar{t}$, on the following three dimensionless parameters:

$$\mathscr{S} = \frac{\tau_0}{f_p \sigma_0'}, \quad \mathscr{P} = \frac{\Delta p_*}{\sigma_0'}, \quad \mathscr{F} = \frac{f_r}{f_p}. \tag{5.37}$$

The first parameter $\mathscr{S}$ is the pre-stress ratio or sometimes called, stress criticality. It is the quotient between the initial shear stress τ_0 and the initial static fault strength $f_p \sigma_0'$. The pre-stress ratio $\mathscr{S}$ quantifies how close to frictional failure the fault is under ambient (pre-injection) conditions. The range of values for $\mathscr{S}$ is naturally

$$0 \leq \mathscr{S} < 1, \tag{5.38}$$

being zero when the fault has no initial shear stress whatsoever, and close to one when the fault is critically stressed or about to fail under ambient conditions, $\tau_0 \to f_p \sigma_0'$.

The second parameter $\mathscr{P}$ is the overpressure ratio, which quantifies the intensity of the injection Δp_* with regard to the initial effective normal stress σ_0'. The range of possible values for $\mathscr{P}$ is determined as follows. Its upper bound comes from the maximum possible amount of overpressure that in our model corresponds to a scenario in which the fault interface is about to open: $\Delta p_c \approx \sigma_0'$, where $\Delta p_c = 4\pi \Delta p_*$ (equation (5.2)). On the other hand, the lower bound of $\mathscr{P}$ comes from the minimum amount of overpressure that is required to activate fault slip: $f_p \Delta p_c \approx f_p \sigma_0' - \tau_0$. By replacing the previous approximate relations into $\mathscr{P} = \Delta p_*/\sigma_0'$, we obtain the sought range of values for $\mathscr{P}$ in an approximate sense as

$$10^{-1}(1 - \mathscr{S}) \lesssim \mathscr{P} \lesssim 10^{-1}, \tag{5.39}$$

where $\approx 10^{-1}$ comes from the factor $1/4\pi$. Finally, the third parameter, the residual-to-peak friction ratio $\mathscr{F}$ is such that

$$0 \leq \mathscr{F} \leq 1. \tag{5.40}$$

$\mathscr{F}$ is zero when there is a total loss of frictional resistance upon the passage of the rupture front, a situation that is unlikely to occur for stable, slow slip, as opposed to fast slip in which thermally-activated dynamic weakening mechanisms could make the fault reach quite low values for $\mathscr{F}$ (Rice, 2006). On the other hand, $\mathscr{F}$ is equal to one when the friction coefficient does not weaken at all, which corresponds indeed to the particular case of Coulomb's friction $f_{\text{cons}} = f_p$.

Finally, it will result useful to define the residual stress-injection parameter $\mathscr{T}_r$ of the constant fracture energy model, equation (5.23), as a combination of the three dimensionless

parameters of the slip-weakening model,

$$\mathscr{T}_r = \frac{1 - \mathscr{S}/\mathscr{F}}{\mathscr{P}}.$$

(5.41)

In addition, one can also define a stress-injection parameter based on the peak value of friction f_p instead of the residual one. Such a parameter reads as

$$\mathscr{T}_p = \frac{f_p \sigma_0' - \tau_0}{f_p \Delta p_*} = \frac{1 - \mathscr{S}}{\mathscr{P}}.$$

(5.42)

We denominate $\mathscr{T}_p$ as the 'peak' stress-injection parameter. The latter is indeed the maximum possible value of the residual stress-injection parameter $\mathscr{T}_r$ (when $\mathscr{F} = 1$), so that

$$\mathscr{T}_r \leq \mathscr{T}_p.$$

(5.43)

As a final comment on the scaling, when comparing the fault response for each version of the friction law, the results that we present in the next sections are particularly valid under the assumption that both friction laws are characterized by the same slip-weakening scale δ_c (see Figure 5.2). Alternatively, one could compare the effect of both friction laws under a different condition such as, for instance, an equal fracture energy G_c, or any other criterion. In the case of equal G_c, the characteristic slip weakening scales would be related as $\delta_{c,\text{lin}} = 2\delta_{c,\text{exp}}$. Our results can be then easily re-scaled using the previous relation as the dimensionless solution remains unchanged, and the same could be done with any other criterion.

5.4.2   Map of rupture regimes and ultimate stability condition

Given the similarity of the scaling between our three-dimensional axisymmetric rupture model and the two-dimensional plane-strain model of Garagash and Germanovich (2012), we find, not surprisingly, that the map of regimes of fault behavior in our model is essentially the same as in the two-dimensional problem (Garagash & Germanovich, 2012). Figure 5.4 summarizes the map of regimes in the parameter space composed by $\mathscr{S}$, $\mathscr{P}$ and $\mathscr{F}$. Moreover, as anticipated when examining the constant fracture energy model, the ultimate stability condition of Garagash and Germanovich (2012) holds in the circular rupture case. Therefore, mixed-mode circular ruptures will propagate ultimately ($t \to \infty$, $R \to \infty$) in a quasi-static, stable manner, if any of the following three equivalent conditions is satisfied:

$$f_r \sigma_0' > \tau_0 \iff \mathscr{S} < \mathscr{F} \iff \mathscr{T}_r > 0.$$

(5.44)

Notably, the residual stress-injection parameter $\mathscr{T}_r$ must be strictly positive. Otherwise, ruptures will propagate ultimately in an unstable, dynamic manner. In the latter case, dynamic ruptures will run away and never stop within the limits of such a homogeneous and infinite fault model. Since in this work, we are mainly interested in the propagation of quasi-static slip, the regimes of major interest are the ones corresponding to ultimately stable ruptures and

the quasi-static nucleation phase preceding dynamic ruptures. We examine both scenarios in what follows.

5.5   Ultimately stable ruptures

Figure 5.5 displays the propagation of the slip front in the case of ultimately stable ruptures: $f_r \sigma_0' > \tau_0$. Without loss of generality, we fix the residual-to-peak friction ratio $\mathscr{F} = 0.7$ and examine for both the linear- and exponential-weakening friction laws the parameter space for $\mathscr{P}$ and $\mathscr{S} < 0.7$. The case of an overpressure ratio $\mathscr{P} = 0.05$ is shown in Figures 5.5a and 5.5b. For all values of $\mathscr{S}$ in these figures, we obtain ruptures that propagate in a purely quasi-static manner without any dynamic excursion, that is, the regime R1 in Figure 5.4. Figures 5.5c and 5.5d show, on the other hand, the case of a lower overpressure ratio $\mathscr{P} = 0.035$. For this value of $\mathscr{P}$, we observe the occurrence of the regime R2 for the linear-weakening case and both regimes R1 and R2 for the exponential-weakening case. The regime R2 corresponds to a situation in which a dynamic rupture nucleates, arrests, and is then followed by purely quasi-static slip.

5.5.1   Early-time Coulomb's friction stage and localization of the process zone

It is clear from Figure 5.5 that at early times and for both regimes (R1 and R2), the propagation of the slip front is well approximated by the Coulomb's friction model, $f_{\text{cons}} = f_p$. The rupture radius thus evolves in this stage as

$$R(t) \approx \lambda_p L(t), \tag{5.45}$$

where λ_p is the amplification factor given by equation (5.17) considering the peak stress-injection parameter $\mathscr{T}_p$, and $L(t) = \sqrt{4\alpha t}$ is the position of the overpressure front as usual. This early-time Coulomb's friction similarity solution is meant to be valid while the friction coefficient does not decrease significantly throughout the slipping region, as shown for a few cases in the examples of Figures 5.8d and 5.8e, when looking at the spatial distribution of the friction coefficient for the earliest times (t_1 and t_2). Note that in Figure 5.5, we also include the evolution of the overpressure front with time (light blue dashed line). In the spatial range covered by this figure, the slip front of ultimately stable ruptures always lags the overpressure front ($R(t) \ll L(t)$) as the corresponding values of $\mathscr{T}_p$ are well into the marginally pressurized regime ($\mathscr{T}_p \sim 10$).

Now, beyond this early stage, the propagation of the slip front starts departing from the Coulomb's friction similarity solution while the slipping region experiences further weakening of friction. At this point, a dynamic instability could nucleate, arrest, and be followed by aseismic slip (examples in Figures 5.5c and 5.5d), within a relatively narrow region of the parameter space (R2 in Figure 5.4). More generally, ruptures will propagate in a purely quasi-static manner (examples in Figures 5.5a and 5.5b, regime R1 in Figure 5.4). Either way, when
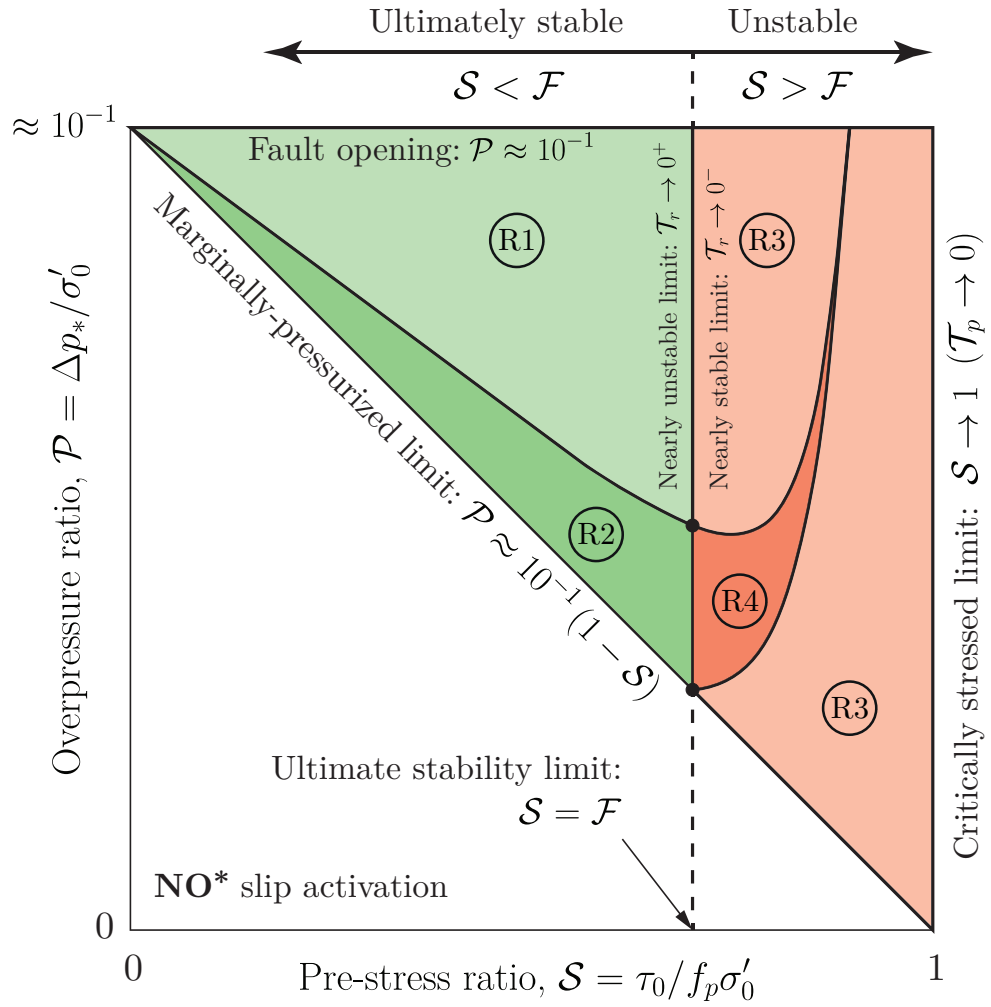
Figure 5.4: Map of rupture regimes for linear slip-weakening model (adapted from figure 11 in Garagash and Germanovich, 2012). (R1) Unconditionally stable fault slip. (R2) Quasi-static slip up to the nucleation of a dynamic rupture, followed by arrest and then purely quasi-static slip. (R3) Quasi-static slip until the nucleation of a run-away dynamic rupture. (R4) Quasi-static slip up to the nucleation of a dynamic rupture, followed by arrest and then re-nucleation of a run-away dynamic rupture. *The condition of no slip is established in the approximate sense discussed in Section 5.10.
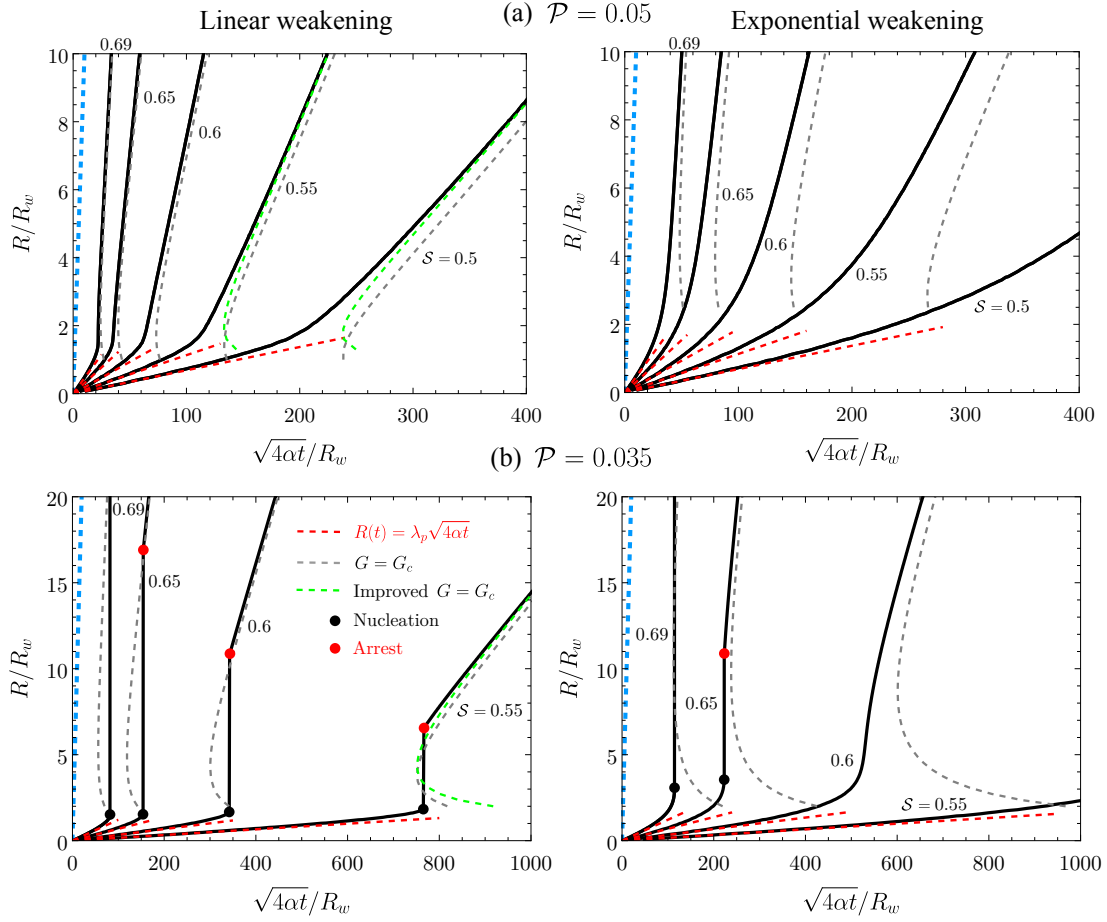
Figure 5.5: Ultimately stable faults, $\mathscr{S} < \mathscr{F} = 0.7$, at distances $R/R_w < 20$. Normalized rupture radius versus square root of dimensionless time for (left) linear and (right) exponential weakening versions of the friction law. (a) $\mathscr{P} = 0.05$ and (b) $\mathscr{P} = 0.035$. Red dashed lines correspond to the analytical constant friction solution considering the peak friction coefficient. Gray dashed lines correspond to the solution of the front-localized energy balance, $G = G_c$. Green dashed lines correspond to an improved version of the front-localized energy balance as explained in the main text, shown here for only a few cases. Light blue lines represent the position of the overpressure front $L(t) = \sqrt{4\alpha t}$. Note that for all cases, $R(t) \ll L(t)$.

this transition happens, the rupture radius becomes greater than the rupture length scale R_w, which is around the same order than the process zone size ℓ_* for the linear weakening law (see, for an example, Figure 5.8f). In the case of the exponential weakening law, Figure 5.5 shows that the transition is smoother and occurs later than for the linear weakening case, whereas the localization of the process zone occurs also at a later time and for rupture lengths that seem to be many times or even an order of magnitude greater than the elasto-frictional length scale R_w (see, also, an example in Figure 5.8f). Furthermore, starting from this point, the process zone has fully developed and thus a proper fracture energy G_c can be calculated. In this way, we can now examine the evolution of the rupture front through the near-front energy balance (5.14), to an accuracy set by the small-scale yielding approximation.

5.5.2   Front-localized energy balance, large- and small-toughness regimes

Using equation (5.12) in combination with (5.1), (5.4) and (5.5), we obtain an expression for the fracture energy of the slip-weakening model as

$$G_c \approx \kappa \left(f_p - f_r\right) \delta_c \left[\sigma_0' - \Delta p_* E_1\left(\lambda^2\right)\right] \tag{5.46}$$

with $\lambda(t) = R(t)/L(t)$ as usual, and κ is a coefficient equal to $1/2$ for the linear weakening case, and 1 for the exponential law, reflecting that the fracture energy of the latter is twice the fracture energy of the former at equal δ_c.

Introducing the scaling of the slip weakening model (5.35) into equation (5.14), one can nondimensionalize the front-localized energy balance in the following form,

$$\mathscr{F}\mathscr{P}\Psi(\lambda) + (\mathscr{S} - \mathscr{F}) = \frac{\sqrt{\pi}}{2}\sqrt{2\kappa}\left(1 - \mathscr{F}\right)\frac{\sqrt{1 - \mathscr{P}E_1\left(\lambda^2\right)}}{\sqrt{R/R_w}}, \tag{5.47}$$

where $\Psi(\lambda)$ is the non-dimensional integral (5.27) whose evaluation is know analytically in (5.17). As expected from the scaling of the problem, equation (5.47) shows that the normalized rupture radius R/R_w depends in addition to dimensionless time $L(t)/R_w$ (which is implicit in λ) on the three dimensionless parameters of the model: $\mathscr{S}$, $\mathscr{P}$ and $\mathscr{F}$.

Considering that for any physically admissible quasi-static solution, the rupture radius must increase monotonically with time, we solve equation (5.47) by imposing R/R_w and then calculating $L(t)/R_w$ for a given combination of dimensionless parameters. The solution of the front-localized energy balance (5.47) is shown in Figure 5.5 together with the full numerical solutions. We observe that in the linear weakening case, the near-front energy balance yields a good approximation of the full numerical solution already for $R \gtrsim 2R_w$. On the other hand, in the exponential decay case, a good approximation is reached only after $R \gtrsim 10R_w$. The difference is due to the fact that the localization of the process zone is less sharp and takes longer for the exponential decay in comparison to the linear weakening case, as exemplified in Figure 5.8f. Moreover, the approximate nature of the energy-balance solution is of course

due to the finite size of the process zone as opposed to the infinitesimal size required by LEFM. Indeed, in the two-dimensional problem, a correction due to the finiteness of the process zone for the linear weakening case was considered by Garagash and Germanovich (2012) based on the work on cohesive tensile crack propagation due to uniform far-field load by Dempsey et al. (2010), providing a solution with improved accuracy. Figure 5.5 shows the results of this correction for a few cases in our model. The solution gets slightly better despite our frictional shear crack is circular and as such, the pre-factors in the scaling relations of the two-dimensional problem should differ from ours.

The front-localized energy balance allows us notably to examine the evolution of the rupture radius beyond the spatial range covered in Figure 5.5, without the need to calculate the full numerical solutions. Note that the energy-balance solution is not only a good approximation over this spatial range but will also become an exact asymptotic solution in the LEFM limit $\ell_*/R \to 0$. Solutions for $10 \leq R/R_w \leq 10^3$ are displayed in Figure 5.6. In particular, Figure 5.6a shows that the higher the pre-stress ratio is, the faster the rupture propagates. Similarly, Figure 5.6b displays that the more intense the injection is (higher overpressure ratio), the faster the rupture propagates too. Both effects are intuitively expected and consistent with the definition and effect of the stress-injection parameter in the constant friction model (Section 5.3.1). Moreover, initially ($R/R_w \leq 10$), we observe in Figure 5.5 that the rupture front lags the overpressure front ($\lambda < 1$) as faults are governed at early times by Coulomb's friction with a peak stress-injection parameter $\mathcal{T}_p$ well into the marginally pressurized regime ($\mathcal{T}_p \sim 10$). Nonetheless, as the rupture accelerates due to the further weakening of friction, Figure 5.6 shows that at later times, the slip front may end up outpacing the overpressure front ($\lambda > 1$). We examine the conditions leading to such behavior in what follows.

Nearly unstable faults, $\lambda(t) \gg 1$

When $\lambda(t) \gg 1$, the term $\Delta p_* E_1\left(\lambda^2\right)$ in (5.46) can be neglected as the overpressure within the process zone is vanishingly small. Hence, the fracture energy G_c becomes approximately constant and simply equal to

$$G_c \approx \kappa\left(f_p - f_r\right)\delta_c\sigma_0'. \tag{5.48}$$

At these length scales and in this regime, the problem becomes now identical to the constant fracture energy model that we extensively analyzed in Section 5.3.2. All the results and insights obtained for nearly unstable faults in that model are therefore inherited here. In fact, the rupture front will always outpace the overpressure front provided that the fault responds in the nearly unstable regime as quantified by the residual stress-injection parameter $\mathcal{T}_r \ll 1$, which is indeed intentionally the case of all the examples shown in Figure 5.6.

Introducing (5.48) into (5.24)a via (5.10), and then (5.24)a into (5.28)a, leads to the dimension-
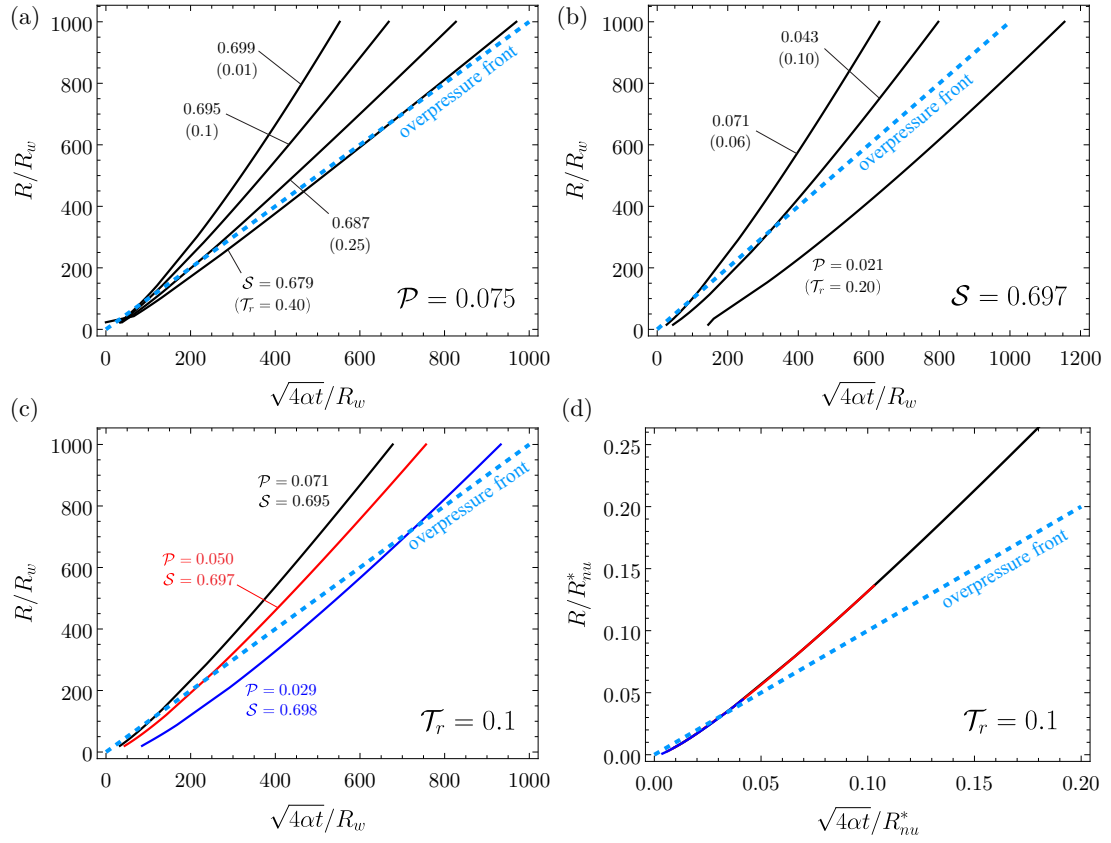
Figure 5.6: Ultimately stable ruptures, $\mathscr{S} < \mathscr{F} = 0.7$, at distances $10 \leq R/R_w \leq 10^3$ for the linear-weakening friction law. Normalized rupture radius R/R_w versus square root of dimensionless time $\sqrt{4\alpha t}/R_w$ for: (a) $\mathscr{P} = 0.075$ and different values of $\mathscr{S}$ (values of $\mathscr{T}_r$ indicated between brackets); (b) $\mathscr{S} = 0.697$ and different values of $\mathscr{P}$; (c) different combinations of $\mathscr{P}$ and $\mathscr{S}$ for the same $\mathscr{T}_r = 0.1$; and (d) same as (c) but re-scaling both axes using R_{nu}^*. Note that all curves collapse under the new scaling in the latter plot.

less form of the front-localized energy balance in the nearly unstable regime,

$$\frac{1}{\mathcal{T}_r}\Psi(\lambda) - 1 = \frac{\sqrt{\pi}}{2}\sqrt{2\kappa}\frac{1}{\sqrt{R/R_{nu}^*}}, \tag{5.49}$$

with

$$\frac{R_{nu}^*}{R_w} = \left(\frac{f_p\sigma_0' - f_r\sigma_0'}{f_r\sigma_0' - \tau_0}\right)^2 = \left(\frac{1-\mathcal{F}}{\mathcal{F}-\mathcal{S}}\right)^2. \tag{5.50}$$

Equations (5.49) and (5.50) can be also obtained by neglecting the term $\mathcal{P}E_1\left(\lambda^2\right)$ in (5.47) and then dividing the latter by $\mathcal{F}-\mathcal{S}$. What is interesting to highlight, is that when the overpressure across the process zone becomes approximately constant (and so the fracture energy G_c), the mathematical structure of the solution for the rupture front in the slip weakening model changes and it is no longer dependent on three but only one single dimensionless number, the residual stress-injection parameter $\mathcal{T}_r$.

The new scaling is exemplified in Figures 5.6c and 5.6d. The former figure shows the evolution of the rupture front as given by equation (5.47) for different combinations of $\mathcal{S}$ and $\mathcal{P}$ that are all characterized by the same value of the residual stress-injection parameter, $\mathcal{T}_r = 0.1$. After re-scaling the solution using the characteristic rupture length scale R_{nu}^* (5.50), Figure 5.6d displays how all curves in Figure 5.6c collapse under the new, constant-fracture-energy scaling. Moreover, by using the asymptotic behavior of $\Psi(\lambda)$ for large λ, equation (5.32) provides an implicit equation for the normalized rupture radius R/R_{nu}^* as a function of the normalized square root of time $\sqrt{4\alpha t}/R_{nu}^*$ and the residual stress-injection parameter $\mathcal{T}_r$, provided that R_{nu}^* is replaced by (5.50).

Marginally pressurized faults, $\lambda(t) \ll 1$

A similar reasoning can be considered now for the case in which $\lambda(t) \ll 1$. Here, the overpressure within the process zone can be taken as approximately constant and equal to the overpressure at the fluid source, Δp_c (5.2), as the rupture radius is much smaller than the pressurized zone, $R(t) \ll L(t)$. Therefore, we can approximate the fracture energy (5.46) as

$$G_c \approx \kappa\left(f_p - f_r\right)\delta_c\left(\sigma_0' - \Delta p_c\right), \tag{5.51}$$

which is constant as well. We recall that Δp_c is a rough approximation of the fluid-source overpressure as discussed in Section 5.10. Again, all the results and insights from the constant fracture energy model are inherited now in this regime. Particularly, the so-called marginally pressurized regime as quantified by the residual stress-injection parameter ($\mathcal{T}_r \sim 10$) is the one related to $\lambda(t) \ll 1$. We recall that this marginally pressurized regime is not defined exactly as the one emerging during the early-time Coulomb's friction stage. The latter is defined by the condition $f_p\Delta p_c \approx f_p\sigma_0' - \tau_0$, whereas the former relates to the residual friction coefficient instead, $f_r\Delta p_c \approx f_r\sigma_0' - \tau_0$. We use the same name for these two regimes, yet there is this

subtle difference between them.

By introducing (5.51) into (5.24)b via (5.11), and then (5.24)b into (5.28)b, we obtain the dimensionless form of the front-localized energy balance in the marginally-pressurized regime,

$$
\Psi(\lambda) - \mathscr{T}_r = \frac{\sqrt{\pi}}{2}\sqrt{2\kappa}\frac{1}{\sqrt{R/R^*_{mp}}},
\tag{5.52}
$$

with

$$
\frac{R^*_{mp}}{R_w} = \frac{\left(f_p - f_r\right)^2 \sigma'_0\left(\sigma'_0 - \Delta p_c\right)}{\left(f_r \Delta p_*\right)^2} \approx \left(\frac{1-\mathscr{F}}{\mathscr{F}\mathscr{P}}\right)^2 (1-10\mathscr{P}).
\tag{5.53}
$$

In the latter equation, we have approximated the factor 4π by 10 as usual in the marginally pressurized limit. Alternatively, equations (5.52) and (5.53) can be derived by approximating the term $\mathscr{P}E_1\left(\lambda^2\right) \approx 4\pi\mathscr{P}$ in (5.47) and then dividing the latter by $\mathscr{F}\mathscr{P}$. Moreover, by using the asymptotic behavior of $\Psi(\lambda)$ for small λ, equation (5.33) provides an implicit equation for the normalized rupture radius R/R^*_{mp} as a function of the normalized square root of time $\sqrt{4\alpha t}/R^*_{mp}$ and the residual stress-injection parameter $\mathscr{T}_r$, provided that R^*_{mp} is replaced by (5.53).

The meaning of the rupture length scales R^*_{nu} and R^*_{mp} are the same as in the constant fracture energy model. Essentially, when $R \ll R^*$, the fracture energy plays a dominant role in the near-front energy balance. This is the large-toughness regime. On the other hand, when $R \gg R^*$, the fracture energy becomes increasingly less relevant in the rupture-front energy budget, corresponding to the small-toughness regime. Hence, likewise in the constant fracture energy model, unconditionally stable ruptures in the slip-weakening model will always transition from a large-toughness to a small-toughness regime. This transition is shown in Figures 5.3c and 5.3d for both nearly unstable and marginally pressurized faults, respectively, with R^*_{nu} and R^*_{mp} as in equations (5.50) and (5.53).

5.5.3   Ultimate zero-fracture-energy similarity solution

By taking the ultimate limit $R/R^* \to \infty$ in equations (5.49) and (5.52), it is evident that the fracture-energy term in the energy balance (the right-hand side) vanishes for both the nearly unstable ($\mathscr{T}_r \ll 1$) and marginally pressurized regimes ($\mathscr{T}_r \sim 10$). Hence, in this limit, equations (5.49) and (5.52) become simply

$$
\Psi(\lambda) = \mathscr{T}_r,
\tag{5.54}
$$

which is exactly the rupture propagation condition of the constant friction model (equation (5.16)) but with a constant friction coefficient f_{cons} equal to the residual one f_r. The self-similar constant friction model is therefore the ultimate asymptotic solution of the slip-

weakening model, provided that $f_{\text{cons}} = f_r$. The transition from the small-toughness regime to the constant residual friction solution, also denominated as ultimate zero-fracture-energy solution, is shown in Figures 5.3c and 5.3d for both nearly unstable and marginally pressurized faults, respectively. Note that one could alternatively define a dimensionless toughness $\mathcal{K}$ for both regimes ($\lambda(t) \gg 1$ and $\lambda(t) \ll 1$) as in Section 5.3.2 (equation (5.24)) to show the same type of transition than in Figures 5.3a-b, since the solution for the amplification factor can be written as $\lambda(\mathcal{T}_r, \mathcal{K}(t))$. Such a dimensionless toughness will always decrease with time and ultimately tend to zero, $\mathcal{K} \rightarrow 0$.

Finally, using the constant residual friction solution λ_r, one can estimate as done in Section 5.3.2 (equation (5.34)) the transition timescales between the large-toughness and small-toughness regimes, which results in

$$t_{nu}^* \approx \frac{\left(R_{nu}^*\right)^2}{\alpha \lambda_r^2}, \text{ and } \quad t_{mp}^* \approx \frac{\left(R_{mp}^*\right)^2}{\alpha \lambda_r^2}. \tag{5.55}$$

5.6   The nucleation phase preceding a dynamic rupture

Figure 5.7 displays the case of ultimately unstable ruptures: $f_r \sigma_0' < \tau_0$. Again, without loss of generality, we fix the residual-to-peak friction ratio as $\mathcal{F} = 0.7$, and examine the parameter space for $\mathcal{P}$ and now $\mathcal{S} > 0.7$, for both versions of the slip-weakening friction law. The case of an overpressure ratio $\mathcal{P} = 0.1$ which corresponds to an injection that is about to open the fault, is shown in Figures 5.7a and 5.7b. For all values of $\mathcal{S}$ in these figures, we observe the nucleation of a dynamic rupture that runs away and never stop within the limits of our model, this is, the regime R3 in Figure 5.4. On the other hand, the case of a lower overpressure ratio $\mathcal{P} = 0.05$ is shown in Figures 5.7c and 5.7d. For the linear weakening model, we observe the occurrence of both regimes R3 and R4 of Figure 5.4. The latter corresponds to cases in which a dynamic rupture nucleates, propagates, and arrests, with a new rupture instability nucleating afterward on the same fault, which is ultimately unstable (run-away). Moreover, in Figure 5.7d for the exponential weakening version of the friction law, we do not observe the regime R4, at least for the numerical solutions we include in this figure.

5.6.1   Early-time Coulomb's friction stage and acceleration towards rupture instability

Similarly to the case of ultimately stable ruptures, here, unstable ruptures are also well-described by the Coulomb's friction model at early times (see Figure 5.7). Therefore, the rupture radius evolves approximately as equation (5.45), with λ_p given by equation (5.17) considering the peak stress-injection parameter $\mathcal{T}_p$. Moreover, Figure 5.7 also shows that during the nucleation phase, the slip front may largely outpace the overpressure front ($\lambda_p \gg 1$) when faults are critically stressed as quantified by the peak stress-injection parameter ($\mathcal{T}_p \ll 1$), or significantly lag the overpressure front ($\lambda_p \ll 1$) when faults are marginally pressurized
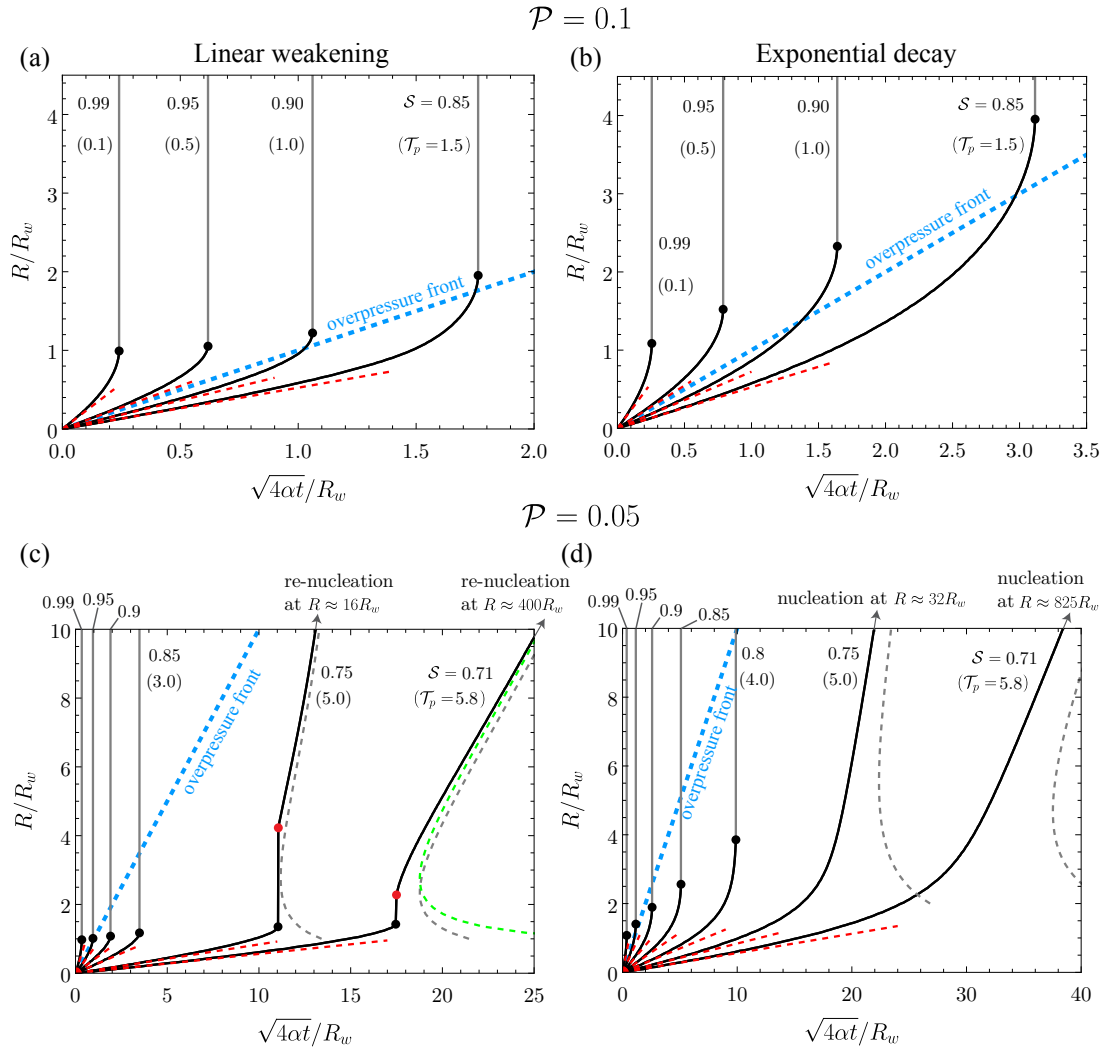
Figure 5.7: Ultimately unstable faults, $\mathscr{S} > \mathscr{F} = 0.7$. Normalized rupture radius versus square root of dimensionless time for (left) linear weakening and (right) exponential decay versions of the slip weakening friction law. (a, b) $\mathscr{P} = 0.1$ and (c, d) $\mathscr{P} = 0.05$. Black and red circles indicate the nucleation and arrest of a dynamic rupture, respectively. Red dashed lines correspond to the analytical Coulomb's friction model considering the peak friction coefficient. In (c) and (d), gray dashed lines represent the near-front energy balance solution. In (c), the green dashed line corresponds to an improved energy-balance solution as explained in the main text.
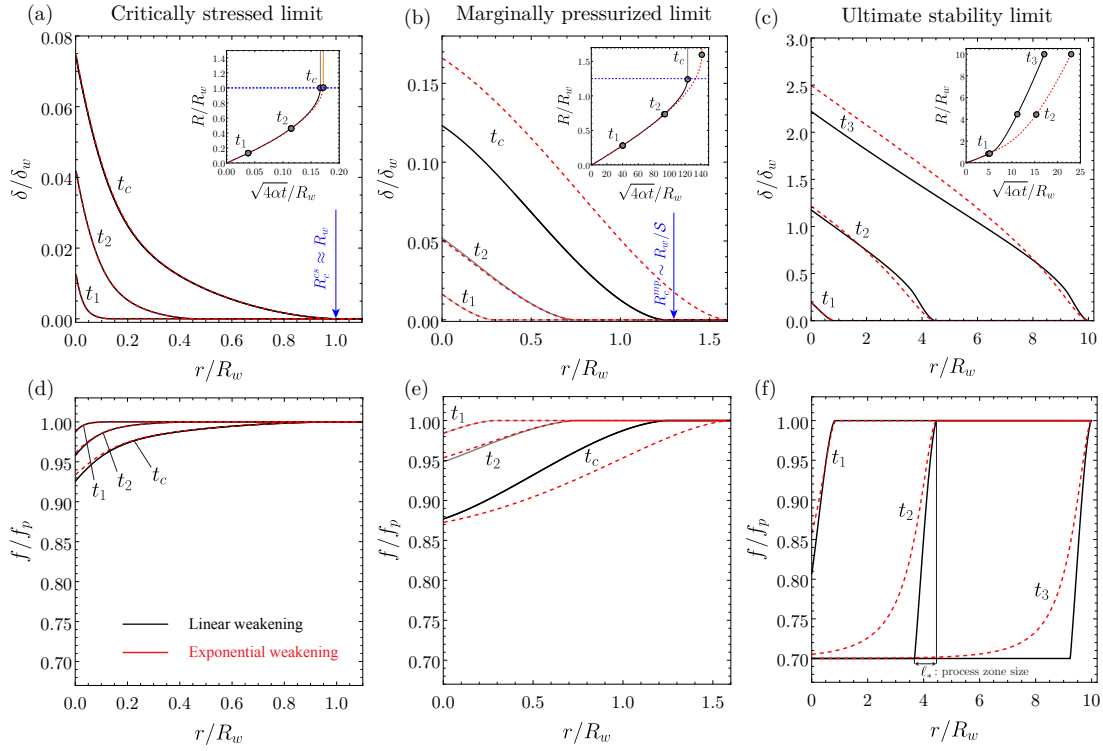
Figure 5.8: (a, b, c) Normalized spatial distribution of slip at the times indicated in the insets and commented in the main text. Insets: normalized rupture radius as a function of the normalized squared root of time. Blue arrows in (a) and (b) represent the theoretical prediction for the nucleation radius in the critically stressed and marginally pressurized limits. (d, e, f) Spatial profile of the normalized friction coefficient at the same times indicated previously. (Left) Critically stressed limit, $\mathscr{S} = 0.995$, $\mathscr{P} = 0.1$, $\mathscr{F} = 0.7$, and associated $\mathscr{T}_p = 0.05$. (Center) Marginally pressurized limit, $\mathscr{S} = 0.8$, $\mathscr{P} = 0.02$, $\mathscr{F} = 0.7$, and associated $\mathscr{T}_p = 10$. (c, f) Ultimate stability limit, $\mathscr{S} = 0.71$, $\mathscr{P} = 0.075$, and $\mathscr{F} = 0.7$.

($\mathcal{T}_p \sim 10$). Figures 5.8d and 5.8e display, on the other hand, the spatial distribution of the friction coefficient for critically stressed and marginally pressurized cases, respectively. We can clearly observe that at the Coulomb's friction stage, $f/f_p \approx 1$ throughout most of the slipping region. Note that in this stage, we could also approximate the spatio-temporal evolution of fault slip in the critically stressed and marginally pressurized regimes, using the analytical asymptotic expressions derived by Sáez et al. (2022) (equation 25 and 26 in Sáez et al., 2022), provided that $f_{\text{cons}} = f_p$. The same can be done for the ultimate zero-fracture-energy solution of ultimately stable ruptures, with $f_{\text{cons}} = f_r$.

Now, beyond this early-time stage, the propagation of the slip front starts departing from the Coulomb's friction similarity solution due to the further weakening of friction. The latter can be seen in Figures 5.8d and 5.8e for intermediate times (t_2) and times close to nucleation (t_c). The slip front accelerates indeed towards the nucleation of a dynamic rupture. Figure 5.7 shows that the rupture radius at the instability time increases with decreasing pre-stress ratio $\mathcal{S}$ and increasing overpressure ratio $\mathcal{P}$, for both versions of the friction law. This is consistent with the extensive analysis of earthquake nucleation provided by Garagash and Germanovich (2012) for the two-dimensional, linear weakening model. Moreover, Figure 5.7 also displays that one of the main effects of the exponential weakening version of the friction law is to smooth the transition of the rupture towards the dynamic instability with regard to the linear law. Furthermore, the exponential law retards the instability time and generally increases the critical radius for the rupture to become unstable. Such effect of the exponential law becomes stronger when the pre-stress ratio $\mathcal{S}$ decreases towards its minimum value in the ultimately unstable case, this is, the ultimate stability limit $\mathcal{S} = \mathcal{F}$.

Given the importance of the nucleation radius to characterize the maximum size that quasi-static ruptures can afford in the ultimately unstable case, we calculate in the next sections theoretical bounds for it, following the procedure of Uenishi and Rice (2002) and Garagash and Germanovich (2012). This corresponds to an extension of their results from the two-dimensional (mode II or III) fault model to the three-dimensional circular (modes II+III) configuration.

5.6.2   Theoretical bounds for the nucleation radius

Critically stressed and marginally pressurized limits

As shown in Sections 5.9.1 and 5.9.2, at the time of instability t_c, the time derivative of the quasi-static elastic equilibrium throughout the slipping region takes the form of the following eigenvalue problem for both the critically stressed ($\mathcal{T}_p \ll 1$) and marginally pressurized ($\mathcal{T}_p \sim 10$) regimes:

$$\frac{1}{2\pi} \int_0^1 F\left(\bar{r}, \bar{\xi}\right) \frac{\partial \bar{v}(\bar{\xi})}{\partial \bar{\xi}} \mathrm{d}\bar{\xi} = \beta \bar{v}(\bar{r}), \tag{5.56}$$

where $\bar{v} = v/v_{\text{rms}}$ is the normalized slip rate distribution (with v_{rms} given by equation (5.67)), and β is the eigenvalue

$$\beta = \frac{R}{R_w} \cdot \begin{cases} 1 & \text{for critically stressed faults } \mathcal{T}_p \ll 1 \\ \tau_0/f_p\sigma'_0 & \text{for marginally pressurized faults } \mathcal{T}_p \sim 10. \end{cases} \tag{5.57}$$

In the previous equations, the dependence of $\bar{v}$ and R on the instability time t_c has been omitted for simplicity. Moreover, equations (5.56) and (5.57) are valid not only for the linear weakening friction law (5.4), but also for the exponential one (5.5). This is due to both the critically stressed and marginally pressurized limits are characterized by small slip at the nucleation time, $\delta(r=0,t_c) \ll \delta_c$ (see, for example, Figure 5.8). It takes just a simple Taylor expansion to show that in this range of slip, the exponential weakening version of the friction law is, to first order in δ/δ_c, asymptotically equal to the linear weakening case. This also means that the residual branch of the linear weakening law does not need to be considered in such stability analysis.

The solution of (5.56) for the eigenvalues and eigenfunctions is calculated in Section 5.9.3. This is done by discretizing the linear integral operator on the left-hand side of (5.56) via a collocation boundary element method using piece-wise ring 'dislocations' of constant slip rate. The most important result is the smallest eigenvalue β_1, which was shown by Uenishi and Rice (2002) for the two-dimensional problem to give the critical nucleation radius. We find (see Table 5.1)

$$\beta_1 \approx 1.003, \tag{5.58}$$

which is interestingly, for all practical purposes, approximately equal to one. Taking hereafter $\beta_1 \approx 1$, the nucleation radius is recovered from equation (5.57) as

$$R_c^{cs} \approx R_w \tag{5.59}$$

for critically stressed faults ($\mathcal{T}_p \ll 1$, vertical line $\mathcal{S} = 1$ on the right side of Figure 5.4), and

$$R_c^{mp} \approx \frac{f_p\sigma'_0}{\tau_0} R_w = \frac{R_w}{\mathcal{S}}, \tag{5.60}$$

for marginally pressurized faults ($\mathcal{T}_p \sim 10$, inclined line $\mathcal{P} \approx 10^{-1}(1-\mathcal{S})$ in Figure 5.4).

The theoretical estimates (5.59) and (5.60) are compared to numerical solutions that are representative of each limiting regime in Figures 5.8a and 5.8b, respectively. In these figures, the blue arrows indicate the theoretical radii at the instability time t_c. We highlight that the critically stressed nucleation radius (5.59) is a proper asymptote that is always reached in the limit $\tau_0 \to f_p\sigma'_0$, up to the numerical approximation made for the eigenvalue (5.58). On the other hand, the marginally pressurized nucleation radius (5.60) can be defined only in an approximate sense due to the reasons explained in Section 5.10. Although this approximation

seems to be quite accurate for the linear weakening law (see Figure 5.8b), the exponential decay version does not seem to follow this trend. This is likely due to the additional assumption of small slip that the exponential weakening law requires in order to be well approximated by a linear relation. In the example of Figure 5.8b, slip does not seem to be small enough. Because of the approximate nature of the marginally pressurized limit, it is challenging to find the model parameters that will result in a sufficiently small slip at the nucleation time for the linear approximation of the exponential weakening law to be valid. Furthermore, equations (5.59) and (5.60) suggest that the minimum possible nucleation radius is the one associated with critically stressed faults (5.59), whereas the greatest possible nucleation radius can be as large as infinity for marginally pressurized faults (5.60), in the limit of zero pre-stress $\tau_0 \to 0$. Yet such a limit corresponds indeed to an ultimately stable rupture, specifically, a case in which the fault is about to open (top left corner of Figure 5.4), so that the dynamic rupture will eventually arrest and then propagate ultimately in a quasi-static manner.

Finally, as shown in Section 5.9, the nucleation radius in the critically stressed limit (5.59) is independent of the specific form of the spatio-temporal evolution of pore pressure, that is, equation (5.59) is also valid for other types of fluid injections than the constant volumetric rate considered in this study. On the other hand, the nucleation radius in the marginally pressurized limit (5.60) is, under certain conditions (see details in Section 5.9.2), also independent of the injection scenario. Moreover, the critically stressed nucleation radius (5.59) is itself an extension of the nucleation length of Uenishi and Rice (2002) (found also previously by Campillo and Ionescu, 1997, under different assumptions) from their two-dimensional fault model to the three-dimensional axisymmetric configuration. Since for the shear mixed-mode (II+III) rupture, the circular front shape is strictly valid only when $v = 0$, our results could be used in combination with perturbation techniques such as the work of Gao (1988) to characterize the corresponding non-circular slipping region at the nucleation time of a shear rupture for $v \neq 0$. Indeed, since the work of Gao (1988) is based on linear elastic fracture mechanics (valid in the small-scale yielding limit) and the nucleation radius (5.59) (and (5.60)) is smaller than the process zone size, one should rather consider a variational approach as the one proposed recently by Lebihain et al. (2022) for cohesive cracks based on the perturbation of crack face weight functions. The approach of Gao (1988) would be still useful to characterize non-circularity in the nearly stable limit of the next section. This would provide an alternative to the work of Uenishi (2018) who considered an energy approach and fixed the rupture shape to an ellipse. An elliptical rupture shape may be a very good approximation for a shear rupture (Sáez et al., 2022), yet not necessarily the actual equilibrium shape. Finally, for a tensile (mode I) rupture, the nucleation radius (5.59) is valid for any value of v, as long as the load driving the rupture growth is peaked around the crack center and axisymmetric in magnitude. Further details about this generalization of our results can be found in Section 5.9.

Nearly stable limit

Figures 5.7c and 5.7d show that the nucleation radius of ultimately unstable ruptures becomes very large, $R(t_c) \gg R_w$, when approaching the ultimate stability condition $f_r \sigma'_0 \to \tau_0$ (vertical line $\mathscr{S} = \mathscr{F}$ in Figure 5.4). Specifically, Figure 5.7c displays a case of large re-nucleation radius (regime R4) in the linear weakening model for $\mathscr{S} = 0.71$ ($\mathscr{F} = 0.7$), whereas Figure 5.7d shows an example of large nucleation radius for the exponential weakening model and the same parameters than before. In the two-dimensional model, Garagash and Germanovich (2012) not only found this same behavior but provided also an asymptote for the nucleation length in this limit, which we also derive here for the circular rupture model.

First, let us note that the condition $R(t_c) \gg R_w$ implies also that $R(t_c) \gg \ell_*$, since the process zone size ℓ_* for the linear weakening model is roughly around the same order than the elasto-frictional lengthscale R_w, and about an order of magnitude larger in the case of the exponential weakening law. Hence, we can invoke the front-localized energy balance, equation (5.14). Indeed, Figures 5.7c and 5.7d display such energy-balance solution for some ruptures that are on their way to becoming unstable. On the other hand, near the ultimate stability limit, $R(t_c)$ is also much bigger than the radius of the overpressure front $L(t_c)$, such that $\lambda(t_c) \gg 1$. Therefore, we can approximate the equivalent shear load associated with the fluid source as a point force via equation (5.19). The corresponding axisymmetric stress intensity factor for such a point force comes from resolving the integral of the left-hand side of equation (5.14) considering (5.19) and $f_{\mathrm{cons}} = f_r$, which gives

$$K_p = \frac{f_r \Delta P(t)}{(\pi R)^{3/2}} \tag{5.61}$$

with $\Delta P(t) = 4\pi \alpha t \Delta p_*$. Substituting the previous equation into (5.14) leads to the following form of the front-localized energy balance,

$$\underbrace{\frac{f_r \Delta P(t)}{(\pi R)^{3/2}}}_{K_p} + \underbrace{\frac{2}{\sqrt{\pi}} \left[\tau_0 - f_r \sigma'_0 \right] \sqrt{R}}_{K_\tau} = K_c, \tag{5.62}$$

where the fracture toughness $K_c = \sqrt{2\mu G_c}$ is, after combining equations (5.36) and (5.48), equal to

$$K_c = (f_p - f_r) \sigma'_0 \sqrt{2\kappa R_w}. \tag{5.63}$$

We recall that the coefficient κ is equal to $1/2$ for the linear weakening friction law and 1 for the exponential weakening case. Moreover, the fracture toughness K_c is constant due to the negligible overpressure within the process zone when $\lambda \gg 1$.

By differentiating equation (5.62) with respect to time and then dividing by $\dot{R}$ on both sides, one can show upon taking the limit at the nucleation time: $R \to R_c$ and $\dot{R} \to \infty$, that $K_p = K_\tau/3$. Substituting this previous relation into (5.62) allows us to eliminate $\Delta P(t_c)$ and so the

instability time t_c in the equation, leading to the sought critical nucleation radius:

$$\frac{R_c^\infty}{R_w} \simeq \frac{9\pi\kappa}{32}\left(\frac{f_p\sigma_0' - f_r\sigma_0'}{\tau_0 - f_r\sigma_0'}\right)^2 = \frac{9\pi\kappa}{32}\left(\frac{1-\mathscr{F}}{\mathscr{S}-\mathscr{F}}\right)^2, \text{ when } f_r\sigma_0' \to \tau_0. \tag{5.64}$$

Note that the previous equation is a proper asymptote due to the small-scale yielding approximation. In addition, the relation $K_p = K_\tau/3$ plus the previous expression for R_c^∞ can provide together an expression for the nucleation time t_c. Indeed, expressions for the instability time t_c in the critically stressed and marginally pressurized limits might be also obtainable analytically, via asymptotic analysis as conducted by Garagash and Germanovich (2012), yet we do not attempt to pursue this route in this paper.

5.7   Discussion

5.7.1   Frustrated dynamic ruptures and unconditionally stable slip: the two propagation modes of injection-induced aseismic slip

In our model, injection-induced aseismic slip can be the result of either a frustrated dynamic rupture that did not reach the required size to become unstable, or the propagation of slip that is unconditionally stable. Whether injection-induced aseismic ruptures occur in one regime or the other, depends primarily on the ultimate stability condition of Garagash and Germanovich (2012), that we demonstrated here to be applicable to the circular rupture configuration as well (equation (5.44)).

Unconditionally stable ruptures

When the initial shear stress τ_0 is lower than the in-situ residual fault strength, $\tau_0 < f_r\sigma_0'$, faults tend to produce mostly unconditionally stable ruptures (regime R1 in Figure 5.4), except for a relatively narrow range of parameters where the nucleation of a dynamic rupture occurs, followed by arrest and purely quasi-static slip (regime R2 in Figure 5.4). We found that unconditionally stable ruptures evolve always between two similarity solutions (see Figure 5.9). At early times (stage I), they behave as being governed by Coulomb's friction, that is, a constant friction coefficient equal to the peak value f_p. During this initial stage, fault slip is self-similar in a diffusive manner and is governed by one single dimensionless number: the peak stress-injection parameter $\mathscr{T}_p$. After, the response of the fault gets more complex in stages II and III yet ultimately, slip recovers the same type of similarity at very large times (stage IV). In this ultimate regime, the rupture behaves as if it were governed by a constant friction coefficient equal to the residual one f_r, and depends also on one single dimensionless number: the residual stress-injection parameter $\mathscr{T}_r$. An interesting characteristic in both limiting regimes is that the rupture propagates as having zero fracture energy G_c. While at early times $G_c = 0$ in an absolute sense as the process zone has not developed yet, at large times the contribution of the finite fracture energy to the rupture-front energy balance is to leading order negligible
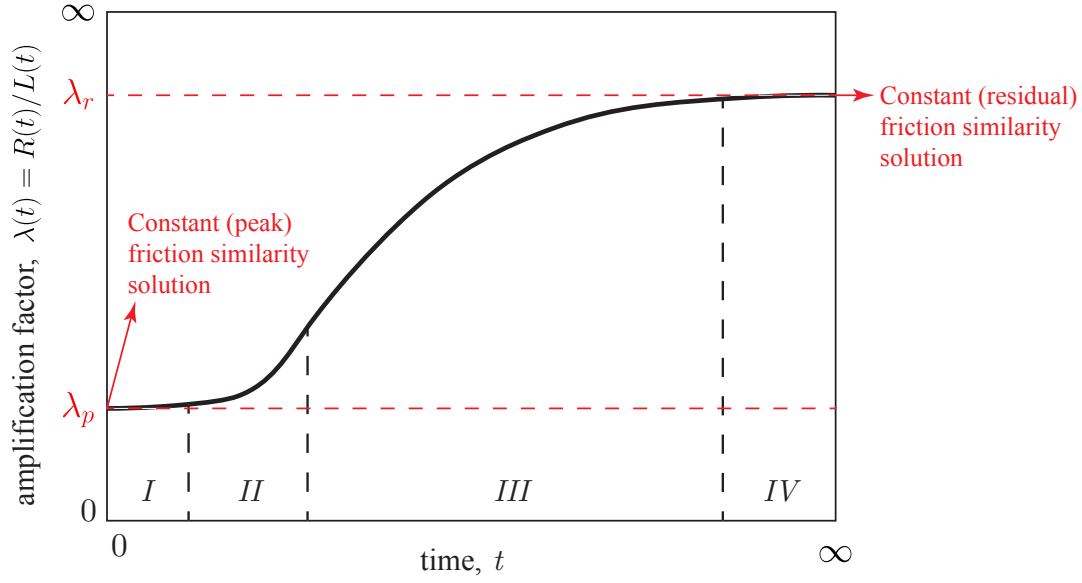
Figure 5.9: Schematic solution for unconditionally stable ruptures undergoing four distinct stages in time. Stage (I), Coulomb's friction similarity solution, $f_{\text{cons}} = f_p$. Stage (II), acceleration due to frictional weakening and localization of the process zone. Stage (III), rupture is governed by an energy balance of the Griffith's type, $G = G_c$, transitioning from a large-toughness to a small-toughness regime. Stage (IV), ultimate constant residual friction similarity solution, $f_{\text{cons}} = f_r$, also denominated ultimate zero-fracture-energy solution. Note that in the case of aseismic slip as a frustrated dynamic instability, stage I is always present, while stages II and III might be experienced to different extents depending on how large the nucleation radius is compared to the process zone size.

compared to the other terms that drive the propagation of the rupture. Furthermore, the two similarity solutions are equivalent to the analytical solution for a constant friction coefficient derived by Sáez et al. (2022), as long as the so-called stress-injection parameter $\mathcal{T}$ (see Section 5.3.1) is replaced by $\mathcal{T}_p$ at early times and $\mathcal{T}_r$ at large times, which are then associated with constant amplification factors λ_p and λ_r, respectively, as shown in Figure 5.9. This is a key finding of our work as it puts the results of the former constant-friction model of Sáez et al. (2022) in a more complete picture of the problem of injection-induced aseismic slip.

In between the two similarity solutions, fault slip undergoes two subsequent stages. First, after departing from the Coulomb's friction solution, the rupture accelerates due to frictional weakening (stage II). The details of the friction law matter here as the rupture radius is of the same order as the process zone size. The exponential weakening law tends to slow down the propagation of slip and smooth the acceleration phase with regard to the linear weakening case when considering the same δ_c in both laws. Fault slip depends in addition to dimensionless space and time, on three non-dimensional parameters: the pre-stress ratio $\mathcal{S}$, the overpressure ratio $\mathcal{P}$, and the residual-to-peak friction ratio $\mathcal{F}$. The higher the initial shear stress on the fault is (higher $\mathcal{S}$) or the more intense the injection is (higher $\mathcal{P}$), the faster the rupture propagates. Note that this dependence of the rupture speed on $\mathcal{S}$ and $\mathcal{P}$ is embedded in both the peak stress-injection parameter $\mathcal{T}_p$ and residual stress-injection parameter $\mathcal{T}_r$. Therefore, it is a general feature present in all stages of injection-induced aseismic slip.

In a subsequent stage, once the process zone has adequately localized, the evolution of the slip front is well approximated by the rupture-front energy balance (stage III). The details of how the friction coefficient weakens from its peak value towards its residual value no longer matter in relation to the position of the slip front or the rupture speed. The only two important quantities here associated with the friction law are: the amount of fracture energy that is dissipated near the rupture front, and the residual friction coefficient f_r. Moreover, the fracture energy is approximately constant (albeit of different magnitude) in the two end-member cases of nearly unstable ($\lambda(t) \gg 1$) and marginally pressurized faults ($\lambda(t) \ll 1$), with the amplification factor λ depending on only two dimensionless numbers: a time-dependent dimensionless toughness $\mathcal{K}(t)$ and the residual stress-injection parameter $\mathcal{T}_r$. A constant fracture energy model as the one introduced in Section 5.3.2 is thus sufficient to capture the dynamics of the slip front for the two end-members. The dimensionless toughness $\mathcal{K}(t)$ quantifies the relevance of the dissipation of fracture energy in the rupture-front energy balance, which decreases monotonically with time. The rupture speed thus increases with time as the diminishing effect of the fracture energy offers less 'opposition' for the rupture to advance. Eventually, $\mathcal{K}(t) \to 0$ when $t \to \infty$ and the rupture reaches asymptotically the large-time similarity solution (stage IV), where the only information about the friction law that matters is f_r.

Finally, the residual stress-injection parameter $\mathcal{T}_r$ plays a crucial role in stages III and IV. When faults are near the ultimate stability limit ($\mathcal{T}_r \to 0$) thus responding in the so-called nearly unstable regime ($\mathcal{T}_r \ll 1$), the slip front always outpaces the overpressure front $\lambda(t) \gg 1$, even

though at early times (stage I) the rupture front would likely lag the overpressure front $\lambda(t) \ll 1$. Conversely, when faults operate in the so-called marginally pressurized regime ($\mathscr{T}_r \sim 10$), the slip front will always move much slower than the overpressure front, $\lambda(t) \ll 1$, over the entire lifetime of the rupture: the slip front will never outpace the overpressure front.

Aseismic slip as a frustrated dynamic instability

When the initial shear stress τ_0 is greater than the in-situ residual fault strength, $\tau_0 > f_r\sigma'_0$, faults will always host a dynamic event, sometimes even more than one (regime R4 in Figure 5.4) if the injection is sustained for sufficient time. The maximum size that aseismic ruptures can reach before becoming unstable is as small as the elasto-frictional length scale R_w for faults that are critically stressed, and as large as infinity for faults that are either marginally pressurized and about to open, or near the ultimate stability limit (so-called nearly stable faults). The spatial range for a fault to exhibit aseismic slip as a frustrated dynamic instability is therefore extremely broad. Moreover, similarly to the case of unconditionally stable ruptures, the quasi-static nucleation phase is governed at early times by the Coulomb's friction similarity solution with $f_{\text{cons}} = f_p$ (stage I in Figure 5.9). Aseismic ruptures can therefore move much faster than the diffusion of pore pressure right after the start of fluid injection when faults are critically stressed according to the peak stress-injection parameter ($\mathscr{T}_p \ll 1$, $\lambda_p \gg 1$), or propagate much slower than that when faults operate in the so-called marginally pressurized regime ($\mathscr{T}_p \sim 10$, $\lambda_p \ll 1$).

After, depending on how large the nucleation radius is with regard to the process zone size, aseismic ruptures may be able to either partially or fully explore stages II and III on their way to reach their critical unstable size. In stage II, the rupture behavior is the same as described in the previous section for unconditionally stable ruptures. Moreover, if the critical nucleation radius is sufficiently large compared to the process zone size, the rupture could transit stage III where the propagation of the slip front is well approximated by an energy balance of the Griffith's type, similar to stage III of unconditionally stable ruptures.

Finally, it is worth noting that critically stressed faults and marginally pressurized faults nucleate dynamic ruptures with very little decrease in the friction coefficient, far from reaching the residual friction value over the entire slipping region at the instability time. Conversely, nearly stable ruptures undergo dynamic nucleation in a 'crack-like' manner, that is, with a small process zone where the fracture energy is dissipated and the remaining much larger part of the 'fracture' (slipping area) is at the residual friction level. In between these two limiting behaviors of dynamic rupture nucleation, a continuum of instabilities is spanned in our model; a result already found by Garagash and Germanovich (2012) and also present in heterogeneous, mechanically-loaded slip-weakening frictional interfaces (Castellano et al., 2023).

5.7.2   Laboratory experiments

Laboratory experiments of injection-induced fault slip on rock samples where a finite rupture grows along a pre-existing interface (Passelègue et al., 2020; Cebry et al., 2022) have recently confirmed some insights predicted by theory. For instance, the meter-scale experiments of Cebry et al. (2022) showed that the closer to frictional failure the fault is before the injection starts, the faster aseismic slip propagates. A somewhat similar observation was made previously by Passelègue et al. (2020) through a set of centimeter-scale experiments and using a rupture-tip energy balance argument. This general feature of injection-induced aseismic slip can be particularly seen in the closed-form expression for the rupture speed of critically stressed faults responding in the Coulomb's friction stage: $V_r = \left[\left(f_p \Delta p_* / \left(f_p \sigma_0' - \tau_0\right)\right)(\alpha/2t)\right]^{1/2}$ (Sáez et al., 2022). This formula displays, in addition to the previous stress state dependence, some other general and quite intuitive features of injection-induced aseismic slip: the more intense the injection is, or the higher the fault hydraulic diffusivity is; the faster the rupture propagates. The latter dependencies remain to be seen in the laboratory, as well as many other aspects of injection-induced fault slip. We discuss a few of them in the context of published experiments in what follows. Notably, our results provide a means for characterizing the conditions under which distinct regimes and stages of injection-induced aseismic slip are expected to emerge under well-controlled conditions in the laboratory, where the validation of the relevant physics incorporated in our model can be potentially realized.

For example, the type of experiments conducted by Passelègue et al. (2020) could provide important insights into the aseismic slip phase preceding dynamic ruptures. Indeed, the nucleation radius of critically stressed faults, equation (5.59), which is itself the circular analog of Uenishi and Rice's nucleation length, has been estimated under somewhat similar laboratory conditions (confining pressures ~ 100 MPa) in R_c^{cs} ~ 1 m (Uenishi & Rice, 2002). Variations of this nucleation radius could be reasonably expected due to uncertainties mostly in the critical slip-weakening scale δ_c. Moreover, a nucleation length of about 1 m has been recently measured by Cebry et al. (2022) during meter-scale experiments of fluid injection with fault normal stresses of about 4 MPa. Since the experiments of Passelègue *et al.* were carried out in a similar rock, if ones corrects the nucleation length of Cebry et al. (2022) by the effective normal stresses that are representative of Passelègue *et al.*'s experiments, we obtain roughly R_c^{cs} ~ 10 cm. Since the critically stressed nucleation radius (5.59) is the minimum possible nucleation size of injection-induced dynamic ruptures in our model, and given that Passelègue et al.'s cylindrical rock samples have a diameter of 4 cm, we expect that their aseismic ruptures might have likely been operating in the Coulomb's friction phase (stage I) and perhaps some excursion in the acceleration phase towards a dynamic instability (stage II), yet never reached the onset of a macroscopic dynamic rupture in the sample. Moreover, as the initial shear stress was set to be 90 percent of the 'in-situ' static fault strength, it is likely that the initial shear stress was greater than the residual strength of the fault thus further supporting the ultimately unstable condition assumed for these experiments.

Another interesting set of fluid injection experiments are the ones reported by Cebry et al.

(2022). Their 3-meters long, quasi-one-dimensional fault, allowed them to observe not only the nucleation of injection-induced dynamic ruptures but also some details of the quasi-static phase preceding such instabilities. Due to the elasticity and fluid flow boundary conditions in their experimental setup, it is not possible to make direct quantitative comparisons with our three-dimensional model, nor with two-dimensional plane-strain models (Garagash & Germanovich, 2012). An unbounded rupture may have certainly propagated before the fault slip reached the shortest side of the sample, yet most of the measurements were conducted starting from this moment. In spite of these differences, it is interesting to note at least two experimental observations that are qualitatively consistent with our model: i) the aseismic slip front continuously decelerates during fluid injection except for the moment right before instabilities occur, and ii) the transition from self-arrested to run-away dynamic ruptures seems to have occurred in relation to the ultimate stability condition (5.44). This type of experiment is well suited to be analyzed via dynamic numerical modeling to provide the possibility for direct quantitative comparisons.

Finally, using rock analog materials with reduced shear modulus such as PMMA (Cebry & McLaskey, 2021; Gori et al., 2021) could provide important insights into injection-induced aseismic slip by reducing the elasto-frictional length scale R_w in approximately one order of magnitude. This "widens" the observable spatial range of the problem thus providing the chance to explore larger-scale processes and regimes that would be otherwise difficult to observe in the laboratory using rock samples. For instance, stage III, where injection-induced aseismic slip is governed by an energy balance of the Griffith's type, or perhaps even stage IV, where ultimately stable ruptures behave as having nearly zero fracture energy, could be potentially investigated in this type of experimental setting. The front-localized energy balance of dynamic ruptures has been extensively studied on both dry (Svetlizky & Fineberg, 2014; Paglialunga et al., 2022) and fluid-lubricated frictional interfaces (Bayart et al., 2016; Paglialunga et al., 2023). Yet the same kind of energy balance for injection-induced slow slip, which is determined by the competition of three distinct factors (equation (5.14)), remains to be investigated experimentally. Indeed, stages III and IV might be the relevant regimes for subsurface processes such as the reactivation in shear of fractures by fluid injection for geo-energy applications, and natural earthquake-related phenomena where coupled fluid flow and aseismic slip processes are thought to play an important role (e.g., seismic swarms, aftershock sequences and slow earthquakes).

5.7.3   In-situ experiments

Fluid injection experiments in shallow natural faults have recently provided important insights into the mechanics of injection-induced fault slip (Guglielmi et al., 2015; Cappa et al., 2022). Yet laboratory experiments under well-controlled conditions are likely better positioned than in-situ experiments to validate the physics of injection-induced fault slip due to the further uncertainties naturally present in the field (e.g., heterogeneities of stress, strength, fracture/fault geometrical complexities, among others), in-situ experiments do have various benefits such

as, for instance, covering a larger decameter scale and providing more realistic field conditions, particularly those ones allowing the growth of fully three-dimensional unbounded ruptures initiated from a localized fluid source, as the one considered in this study. Our results thus provide the opportunity to make quantitative comparisons in these cases.

Among them, the experiments of Guglielmi et al. (2015) have been particularly impactful as they were able to measure for the first time not only micro-seismicity and injection-well fluid pressure and volume rate history (as done previously in large-scale field experiments (Scotti & Cornet, 1994; Cornet et al., 1997), but also the history of induced fracture slip and opening at the injection point/interval. This unique dataset has been analyzed via dynamic numerical modeling by various researchers (Guglielmi et al., 2015; Bhattacharya & Viesca, 2019; Cappa et al., 2019; Larochelle et al., 2021). The multiplicity of proposed models that have fitted the data suggests indeed that more spatially distributed measurements, as done more recently (Cappa et al., 2022), could further help to constrain the underlying physical processes operating behind these experiments. For the purpose of illustrating the application of our model, hereafter we focus on the modeling work of Bhattacharya and Viesca (2019) for the unique reason that they assumed a slip-weakening fault model which makes the application of our results more straightforward.

Let us first estimate the three dimensionless parameters of our model: $\mathscr{S}$, $\mathscr{P}$, and $\mathscr{F}$ (5.37). Considering the best-fit model parameters of Bhattacharya and Viesca (2019): $\mu = 11.84$ GPa, $\delta_c = 0.37$ mm, $f_p = 0.6$, $f_r = 0.42$, $\sigma_0' = 5.08$ MPa, and $\tau_0 = 2.41$ MPa; we can directly compute $\mathscr{S} \approx 0.79$ and $\mathscr{F} = 0.7$. Note that the estimated initial shear stress of 2.41 MPa is greater than the in-situ residual fault strength $f_r \sigma_0' \approx 2.1$ MPa (or alternatively $\mathscr{S} > \mathscr{F}$ (5.44)), so that the injection-induced rupture is inferred to be ultimately unstable. Because no macroscopic dynamic rupture occurred during the experiment, the propagation mode of aseismic slip must be the one of a frustrated dynamic instability. Let us now estimate the remaining dimensionless parameter $\mathscr{P}$. To do so, we need to estimate first the injection intensity Δp_*, equation (5.1). We approximate the injection history via a constant-volume-rate injection characterized by the same total volume of fluid injected during the experiment. This gives roughly $Q \sim 40$ l/min. The fault intrinsic permeability k is widely recognized to have increased during this test (Guglielmi et al., 2015; Bhattacharya & Viesca, 2019; Cappa et al., 2019). It was estimated by Bhattacharya and Viesca (2019) between $k_{\min} = 0.8 \times 10^{-12}$ m^2 and $k_{\max} = 1.3 \times 10^{-12}$ m^2. Consider, for instance, the average $\tilde{k} = 1.05 \times 10^{-12}$ m^2. By assuming a fluid dynamic viscosity of $\eta \sim 10^{-3}$ Pa·s and fault-zone width $w = 0.2$ m (Bhattacharya & Viesca, 2019), the characteristic wellbore overpressure, equation (5.2), is $\Delta p_c \approx 3.17$ MPa, which is very close to the actual, nearly constant wellbore overpressure measured at the latest part of the injection, ~ 3 MPa (see figure 2a in Bhattacharya and Viesca, 2019). Following this approximation for the fluid injection, we obtain an injection intensity $\Delta p_* \approx 0.25$ MPa, which in turn yields $\mathscr{P} \approx 0.05$. By considering either the minimum or maximum fault permeability, we would obtain $\mathscr{P} \approx 0.065$ and $\mathscr{P} \approx 0.04$, respectively; the higher the permeability, the lower the injection intensity.

To understand under what regime aseismic slip may have developed during the initial Coulomb's

friction stage (either critically stressed or marginally pressurized regime), let us calculate the peak stress-injection parameter $\mathscr{T}_p$. Given the known values for $\mathscr{S}$ and $\mathscr{P}$, we obtain via (5.42) $\mathscr{T}_p \approx 4.22$, which is well into the marginally pressurized regime, with an associated amplification factor $\lambda_p \approx 0.12$ (equation (5.20)). By considering $k_{\min}$ and $k_{\max}$ instead, we would obtain just a modest change in $\mathscr{T}_p$ approximately equal to 3.20 and 5.22, respectively. Furthermore, we can estimate the critical nucleation radius in the marginally pressurized regime via equation (5.60). For that, we must calculate first the elasto-frictional lengthscale R_w, equation (5.36). Given the best-fit model parameters, $R_w \approx 4.79$ m, and the nucleation radius is then $R_c^{mp} \approx 6.06$ m. Considering the size of the aseismic rupture estimated by Bhattacharya and Viesca at the final time analyzed in their work, $t_f = 1378$ s (see inset of figure 3a in Bhattacharya and Viesca, 2019), one could expect that the aseismic rupture was quite close to become unstable. Note that in Bhattacharya and Viesca (2019), their original circular rupture solutions were modified to appear elliptical considering the perturbative approach for circular shear cracks of Gao (1988), who gives an aspect ratio $a/b = 1/(1-\nu)$ (to first order in ν), where a and b are the semi-major and semi-minor axes of the elliptical rupture front. The calculations of Gao (1988) involve a planar circular crack whose shape is perturbed under uniform shear load and constant energy release rate along the front. Perhaps, a better correction could be done by considering the asymptotic behavior in the marginally pressurized regime obtained by Sáez et al. (2022), $a/b = (3-\nu))/(3-2\nu)$, at least in the Coulomb's friction stage where the previous equation is valid. This would lead to ruptures that are less elongated than the ones considered by Bhattacharya and Viesca (2019). For example, considering a Poisson's ratio $\nu = 0.25$, the marginally-pressurized aspect ratio is $a/b = 1.1$, whereas Gao's aspect ratio is $a/b \approx 1.33$. The latter was indeed found to be the asymptotic behavior in the critically stressed regime ($\mathscr{T}_p \ll 1$) of the Coulomb's friction stage (Sáez et al., 2022).

Let us assume as a first estimate, that the rupture propagates with Coulomb's friction until the final time $t_f = 1378$ s. In this scenario, the rupture radius would be at this time simply $R_f = \lambda_p \sqrt{4\alpha t_f}$, and the corresponding accumulated slip at the injection point, $\delta_f = (8/\pi)(f_p \Delta p_* / \mu) R_f$ (equation 27 in Sáez et al., 2022). To perform the previous calculations, we need to estimate the fault hydraulic diffusivity $\alpha = k/\eta S$. Considering the storage coefficient S estimated in 2.2×10^{-8} Pa^{-1} (Bhattacharya & Viesca, 2019), we obtain a hydraulic diffusivity $\alpha \approx 0.048$ m^2/s. The final rupture radius and accrued slip are then $R_f \approx 2.01$ m and $\delta_f \approx 0.07$ mm, respectively. Variations in fault permeability considering $k_{\min}$ and $k_{\max}$ would result in $R_f \approx 2.91$ m and 1.35 m, and $\delta_f \approx 0.12$ mm and 0.04 mm, respectively. In any case, the previous quantities do not account for the total slip measured at the injection point which is an order of magnitude higher (~ 1 mm) and estimated rupture radius ~ 5 m. Moreover, there is a clear acceleration of slip in the final part of the injection (see figure 3a in Bhattacharya and Viesca, 2019) which in our model could only come from frictional weakening (stage II). We therefore calculate the evolution of the rupture front and slip at the injection point numerically.

Our numerical solution shows that the nucleation of a dynamic rupture occurs at $R_c \approx 6.08$ m, which is in excellent agreement with the theoretical nucleation radius for marginally pressurized faults calculated previously. The calculated accrued slip at the center of the rupture at the

instability time is 0.35 mm, which is about a third part of the actual measurement. On the other hand, the nucleation time is $t_c = 5885$ s, which is several times longer than t_f. Indeed, at the time t_f the rupture radius is just 2.17 m in our numerical solution, not much larger than the Coulomb's friction approximation (2.01 m). The latter indicates that our model is indeed operating in stage I at t_f. The differences between our calculations and the ones of Bhattacharya and Viesca (2019) are due to time-history variations in permeability not accounted for in our model, and the approximation of the fluid injection via an equivalent constant volume rate. Nevertheless, the theoretical nucleation radius is expected to hold as this quantity is relatively independent of the injection scenario. Finally, we note that a rupture propagating in the marginally pressurized regime is expected to be confined within the pressurized area even at the instability time. In this regard, the main difference with Bhattacharya and Viesca (2019) who suggested that the slip front outpaced the migration of fluids is merely a matter of definitions. In our case, the overpressure front $L(t) = \sqrt{4\alpha t}$ represents the radial distance from the injection point at which the overpressure is approximately 2 percent of the fluid-source overpressure, the latter being approximately 3 MPa at the final time. In Bhattacharya and Viesca (2019), various overpressure isobars are drawn. The one with the lowest overpressure is at 0.5 MPa, which is around 17 percent of the fluid-source overpressure.

5.7.4 A note on rate-and-state fault models: similarities and differences

Laboratory-derived friction laws (Dieterich, 1979; Ruina, 1983) are widely used in the earthquake modeling community to reproduce the entire spectrum of slip velocities on natural faults (Scholz, 2019). These empirical friction laws capture the dependence of friction on slip rate and the history of sliding (via a state variable) as observed during velocity-step laboratory experiments on bare rock surfaces and simulated fault gouge (Marone, 1998). In its simplest form, the rate-and-state friction coefficient is expressed as

$$f(v,\theta) = f_0 + a\ln\left(\frac{v}{v_0}\right) + b\ln\left(\frac{v_0\theta}{d_c}\right), \tag{5.65}$$

where f_0 is the friction coefficient at a reference slip rate v_0 and state variable $\theta_0 = d_c/v_0$ with units of time, d_c is a characteristic slip 'distance' for the evolution of θ, which is usually thought to be an order of magnitude smaller than δ_c of the slip weakening model (Cocco & Bizzarri, 2002; Uenishi & Rice, 2002), and a and b are the rate-and-state friction parameters, both positive and of order 10^{-2}. An additional dynamical equation describing the evolution of the state variable θ is required. For the purpose of this discussion, we consider hereafter a widely used state-evolution equation known as aging law: $\dot{\theta} = 1 - v\theta/d_c$.

The similarities between frictional ruptures obeying slip-weakening and rate-and-state friction have been long recognized (see Cocco and Bizzarri, 2002; Uenishi and Rice, 2002; Ampuero and Rubin, 2008; Garagash and Germanovich, 2012, for example). Furthermore, in the context of injection-induced fault slip, some similarities were already recognized by Garagash and Germanovich (2012), particularly in relation to the nucleation of dynamic slip. Specifically,

they noted that the nucleation length of critically stressed faults for linear slip-weakening friction or, what is the same, the one of Uenishi and Rice (2002), is identical to the nucleation length of rate-and-state faults for $a/b \ll 1$ (Rubin & Ampuero, 2005). On the other hand, the large nucleation length near the ultimate stability limit which is equal (except by a pre-factor of order one) to the one of Andrews (1976), is identical to the nucleation length of rate-and-state faults when approaching the velocity-neutral limit $a/b \to 1$ (Rubin & Ampuero, 2005). The equivalence between the previous nucleation lengths is obtained by recasting the slip-weakening friction law in terms of the rate-and-state parameters, this is, replacing the peak to residual strength drop $(f_p - f_r)\sigma_0'$ by $b\sigma_0'$, and the stress drop $\tau_0 - f_r\sigma_0'$ by $(b-a)\sigma_0'$ (Rubin & Ampuero, 2005; Ampuero & Rubin, 2008).

In addition to the previous similarities, we discuss some additional ones now. For instance, the ultimate stability condition (5.44) has been observed to determine in rate-and-state models whether velocity-weakening faults ($a/b < 1$) produce either self-arrested or run-away ruptures (Norbeck & Horne, 2018). Also, the same stability condition has been observed to determine whether velocity-strengthening faults ($a/b > 1$) host either purely quasi-static slip or a dynamic instability (Dublanchet, 2019). Both results are essentially the same as predicted by slip-weakening fault models. Indeed, the ultimate stability condition is somehow expected to occur in rate-and-state models (both velocity weakening and velocity strengthening) in the vicinity of the velocity-neutral limit ($a/b \to 1$), as the condition (5.44) that the residual fault strength drops at nearly the same level of the shear stress present further ahead of the rupture is reminiscent of the case $a \approx b$ when analyzing the steady-state ($\dot{\theta} = 0$) response of equation (5.65) to an incremental velocity step approximating crudely the passage of a rupture front.

Another similarity between slip-weakening and rate-and-state fault models relates to our constant-residual-friction similarity solution or ultimate zero-fracture-energy regime. As already noted by Sáez et al. (2022) for the particular case of injection at constant volumetric rate in a one-dimensional fault (see section 5.2 in Sáez et al., 2022), the ultimate regime of rate-and-state faults (Dublanchet, 2019) coincides with the solution for a constant friction coefficient (Sáez et al., 2022). It is clear now albeit in a three-dimensional model, that this friction coefficient corresponds to the residual value in a slip-weakening model and that this regime is characterized by negligible fracture energy. The latter is additionally consistent with the work of Garagash (2021) who found that slip transients driven by a point-force-like injection approach a zero-toughness condition as an ultimate regime in a one-dimensional fault. Note that the limit of a point-force-like injection is reached in our three-dimensional model in the nearly unstable limit, but not in the marginally pressurized one. Moreover, the features that give rise to this ultimate asymptotic behavior seem rather general and we think are likely expected to hold under other types of fluid injection. As already shown in Sáez et al. (2022), the spatio-temporal patterns of injection-induced aseismic slip are strongly influenced by the type of fluid injection (or injection rate history). Quantifying this effect is important and we will address it soon in a future study.

We would also like to highlight some differences between slip-weakening and rate-and-state

fault models. Indeed, one of the main physical ingredients that rate-and-state friction would incorporate in our model is frictional healing. The recovery of the friction coefficient with the logarithm of time is a well-established phenomenon (Dieterich, 1979; Ruina, 1983; Marone, 1998) that is essential in physics-based models that attempt to reproduce earthquake cycles (Tse & Rice, 1986; Lapusta et al., 2000). Frictional healing would provide, for instance, the possibility of nucleating multiple dynamic events on the same fault segment. Yet we highlight that this is not a unique characteristic of rate-and-state friction in the sense that two events can also nucleate on the same slip-weakening fault segment (regime R4 in Figure 5.4). Another case in which the rate-and-state framework could be particularly useful is to model the reactivation of faults that are thought to be steadily creeping. In fact, from a Coulomb's friction perspective, rate-and-state faults are always at failure: the shear stress is at any time and over the entire fault extent equal to the fault strength. The initial stress state is a result of the history of sliding. At an initial time $t = 0$, it will be defined by the initial distribution of slip rate v_i and initial state variable θ_i.

To illustrate this latter point and get some further insights into a rate-and-state fault model, consider our same hydro-mechanical model but with a rate-and-state friction coefficient. Due to the 'always-failing' condition, $R(t) \to \infty$ in equation (5.6) and the inequality (5.3) becomes an equality. One possible way of considering the initial stress state is to assume that the initial slip velocity v_i is uniform and it operates at the creep rate that one could further consider as the reference slip rate v_0. The initial stress state is then encapsulated in the initial state variable θ_i. Assuming the latter as uniform as well, one can readily show by dimensional analysis that the slip rate (the primary unknown in this model together with the state variable) depends in addition to dimensionless space $r b \sigma'_0 / d_c \mu$ and time $t v_0 / d_c$, on the following five non-dimensional parameters: a/b, $\Delta p_* / \sigma'_0$, α / α_c, f_0 / b and θ_i / θ_0, where $\alpha_c = \mu^2 d_c v_0 / b^2 \sigma'^2_0$ is a characteristic diffusivity. We note that this rate-and-state version of our model has an increased complexity with two more dimensionless parameters than the slip-weakening model. $\Delta p_* / \sigma'_0$ is indeed our same overpressure ratio $\mathscr{P}$. a/b quantifies the degree of weakening ($a/b < 1$) or strengthening ($a/b > 1$) and, as discussed previously, it would relate to the the ultimate stability behavior of the fault. f_0 / b quantifies the constant part of the friction coefficient with regard to b which in turn relates to the strength drop (i.e., the decay from the peak to the residual friction). Finally, θ_i / θ_0 is where the initial shear stress or pre-stress ratio $\mathscr{S}$ of the slip-weakening model would equivalently emerge. In fact, by multiplying equation (5.65) by σ'_0 and then expressing it at the initial conditions v_i and θ_i, the resulting dimensionless form of such equation reads as $\ln(\theta_i / \theta_0) = (f_0 / b)(\tau_0 / f_0 \sigma'_0 - 1)$. The dimensionless parameter θ_i / θ_0 can be then alternatively chosen as $\tau_0 / f_0 \sigma'_0$, which is similar to the pre-stress ratio of the slip-weakening model.

5.8   Concluding remarks

We have investigated the propagation of fluid-driven slow slip and earthquake nucleation on a slip-weakening circular fault subjected to fluid injection at a constant volume rate. Despite

some simplifying assumptions in our model, our investigation has revealed a very broad range of aseismic slip behaviors, from frustrated dynamic instabilities to unconditionally stable slip, from ruptures that move much faster than the diffusion of pore pressure to ruptures that move much slower than that. The circular fault geometry is likely the simplest one enabling quantitative comparisons with field observations thanks to its three-dimensional nature. It is thus also useful for preliminary engineering design of hydraulic stimulations in geo-energy applications. In addition to the effect of a non-zero Poisson's ratio that will elongate the shape of the rupture along the direction of principal shear, changes in lithologies as commonly encountered in the upper Earth's crust will alter the dynamics of an otherwise unbounded rupture as the one we have examined here. In particular, the effect of layering might promote containment of the reactivated fault surface within certain lithologies, similar to what is observed for hydraulic fractures (Bunger & Lecampion, 2017). This effect may be important in some cases and would require further quantification.

5.9 Supplementary material 1: Eigenvalue problem at the instability time for unlimited linear weakening of friction

5.9.1 Generalized eigenvalue problem

Following Uenishi and Rice (2002) and Garagash and Germanovich (2012), we extend their eigenvalue-based stability analysis, valid for unlimited linear weakening of friction under either in-plane shear (II) or anti-plane shear (III) mode of sliding, to the case of a circular rupture propagating under mixed-mode (II+III) conditions.

Equilibrium dictates that within the slipping region $r \leq R(t)$, the fault strength τ_s (5.3) must be locally equal to the fault shear stress τ (5.6). Equating the two previous equations and then differentiating with respect to time, leads to

$$v(r,t)\frac{\mathrm{d}f}{\mathrm{d}\delta}\sigma'(r,t) + f(\delta)\frac{\partial\sigma'(r,t)}{\partial t} = \frac{\partial\tau_0(r,t)}{\partial t} - \frac{\mu}{2\pi}\int_0^{R(t)} F(r,\xi)\frac{\partial v(\xi,t)}{\partial\xi}\mathrm{d}\xi, \tag{5.66}$$

where $v = \partial\delta/\partial t$ is the fault slip rate. When differentiating the integral term previously, we have considered Leibniz's integral rule and applied the condition $\partial\delta(R(t),t)/\partial r = 0$ which guarantees non-singular shear stresses along the rupture front.

In our problem, the effective normal stress $\sigma'(r,t) = \sigma'_0 - \Delta p(r,t)$ decreases from the initial uniform value σ'_0 due to overpressure $\Delta p(r,t)$ associated with fluid injection, whereas the shear stress that would be present on the fault if no slip occurs is a uniform and constant value τ_0. Nevertheless, for the sake of generality, we keep utilizing the generic terms $\sigma'(r,t)$ and $\tau_0(r,t)$. Indeed, $\sigma'(r,t)$ generally contains not only the initial effective normal stress and changes in pore pressure but also possible changes in total normal stress from the far field, as $\sigma' = \sigma - p$. Similarly, $\tau_0(r,t)$ could be a summation of both the initial shear stress and far-field shear loading. Far-field loads may be due to, for instance, tectonic forces and seasonal

variations of stress, among many others. Note that $\sigma'(r,t)$ and $\tau_0(r,t)$ are both axisymmetric in magnitude and at least one of them must be locally peaked around the origin in order to initiate slip at $r = 0$ at a certain time $t = t_0$. Equation (5.66) is then valid at any time $t > t_0$ and, as mentioned in the main text, it assumes a Poisson's ratio $v = 0$.

Let us scale equation (5.66) by introducing the following non-dimensional quantities: $\bar{r} = r/R$, $\bar{\xi} = \xi/R$, and $\bar{v} = v/v_{\text{rms}}$, where

$$v_{\text{rms}}(t) = \sqrt{\frac{1}{R(t)} \int_0^{R(t)} v^2(r,t)\mathrm{d}r} \tag{5.67}$$

is the root mean square of the slip rate distribution, such that $\int_0^1 \bar{v}^2(\bar{r})\mathrm{d}\bar{r} = 1$. Note that for the linear-weakening friction law (5.4), $\mathrm{d}f/\mathrm{d}\delta = -(f_p - f_r)/\delta_c$. The latter has the strong assumption that the residual friction coefficient f_r has not been reached yet at any point within the rupture. Otherwise, wherever $f = f_r$, $\mathrm{d}f/\mathrm{d}\delta = 0$. Moreover, for the exponential-weakening friction law (5.5), the same expression for $\mathrm{d}f/\mathrm{d}\delta$ is approximately valid in the range of small slip $\delta \ll \delta_c$, to first order in δ/δ_c.

Considering the previous quantities plus the relation (5.36) $\mu\delta_c = (f_p - f_r)\sigma'_0 R_w$, we nondimensionalize equation (5.66) to obtain

$$-\frac{R}{R_w}\bar{v}(\bar{r})\frac{\sigma'(\bar{r}R)}{\sigma'_0} + \frac{R}{\mu v_{\text{rms}}}f(\delta)\frac{\partial\sigma'(\bar{r}R)}{\partial t} = \frac{R}{\mu v_{\text{rms}}}\frac{\partial\tau_0(\bar{r}R)}{\partial t} - \frac{1}{2\pi}\int_0^1 F(\bar{r},\bar{\xi})\frac{\partial\bar{v}(\bar{\xi})}{\partial\bar{\xi}}\mathrm{d}\bar{\xi}. \tag{5.68}$$

In the previous equation, we dropped the explicit dependence on time t of the various variables for simplicity in the notation.

Following Uenishi and Rice (2002), at the instability time t_c, the slip rate diverges all over the fault plane, such that the root mean square of the slip rate distribution $v_{\text{rms}}(t_c) \to \infty$. The only non-vanishing terms of (5.68) lead to the following generalized eigenvalue problem:

$$\frac{R}{R_w}\bar{v}(\bar{r})\frac{\sigma'(\bar{r}R)}{\sigma'_0} = \frac{1}{2\pi}\int_0^1 F(\bar{r},\bar{\xi})\frac{\partial\bar{v}(\bar{\xi})}{\partial\bar{\xi}}\mathrm{d}\bar{\xi}, \tag{5.69}$$

which corresponds to the mixed-mode, circular rupture version of equation (14) in Garagash and Germanovich (2012).

Given a normalized distribution of effective normal stress at the instability time, $\sigma'(r,t_c)/\sigma'_0$, equation (5.69) can be solved to obtain the corresponding generalized eigenvalues and eigenfunctions. Moreover, what is more important is to calculate the smallest eigenvalue that would be related to the instabilities we observe in the full numerical solutions. In our problem, $\sigma'(r,t_c)$ is set by the distribution of overpressure at the time of instability, which does not allow us to obtain a purely analytical insight as the instability time is generally unknown and, more importantly, information about one of the problem parameters, the pre-stress ratio $\mathscr{S}$, is lost when deriving the eigenproblem (5.69). The only scenario in which equation (5.69) is inde-

pendent of t_c is when $\sigma'(r, t_c)$ is uniform, which in turn leads to a regular eigenvalue problem. Furthermore, in the particular case of $\sigma'(r, t) = \sigma'_0$, we obtain the circular rupture version of the eigenvalue problem of Uenishi and Rice (2002), which will give the corresponding universal nucleation radius of their problem.

5.9.2   Eigenvalue problem in the critically stressed and marginally pressurized limits

Let us come back to our particular problem where $\sigma'(r, t) = \sigma'_0 - \Delta p(r, t)$ and assume a rather general but self-similar injection scenario such that the overpressure can be written in the similarity form: $\Delta p(r, t) = \Delta p_w(t) \Pi(\xi)$, where $\Delta p_w(t)$ is the overpressure at the fluid source, and $\Pi(\xi)$ is the spatial distribution of overpressure with the properties: $\Pi(0) = 1$ and $\Pi(\infty) \to 0$. Note that such a self-similar injection scenario is possible only if one assumes a line source of fluids such that no length scale associated with the fluid source is introduced into the problem. For a discussion about the line-source approximation, see Section 5.10. Introducing the previous relations for the effective normal stress into (5.69), the generalized eigenvalue problem becomes

$$\frac{R}{R_w} \bar{v}(\bar{r}) \left(1 - \frac{\Delta p_w}{\sigma'_0} \Pi(\lambda \bar{r}) \right) = \frac{1}{2\pi} \int_0^1 F\left(\bar{r}, \bar{\xi} \right) \frac{\partial \bar{v}(\bar{\xi})}{\partial \bar{\xi}} \mathrm{d}\bar{\xi}, \tag{5.70}$$

where $\lambda(t_c) = R(t_c) / \sqrt{4\alpha t_c}$ is the so-called amplification factor at the instability time. We recall that the dependence of the various variables in the previous equation on t_c is omitted for simplicity.

Consider now the critically stressed limit: $\tau_0 \to f_p \sigma'_0$, where the rupture front largely outpaces the overpressure front at the time of instability, such that $\lambda(t_c) \gg 1$. In view of the properties of $\Pi(\xi)$, the term $(\Delta p_w / \sigma'_0) \Pi(\lambda \bar{r}) \ll 1$ so that, if neglected, equation (5.70) further simplifies to

$$\frac{R}{R_w} \bar{v}(\bar{r}) = \frac{1}{2\pi} \int_0^1 F\left(\bar{r}, \bar{\xi} \right) \frac{\partial \bar{v}(\bar{\xi})}{\partial \bar{\xi}} \mathrm{d}\bar{\xi}. \tag{5.71}$$

The previous equation is a regular eigenvalue problem. It corresponds indeed to the circular rupture version of the eigenvalue problem of Uenishi and Rice (2002). Derivation of equation (5.71) can be alternatively done by following the reasoning of Garagash and Germanovich (2012) that in the critically stressed limit, the effective normal stress over the slipping region is largely unchanged so that $\sigma'(r, t_c) \approx \sigma'_0$, except for a very small region of approximate size $\sqrt{4\alpha t_c}$ near the rupture center that at spatial scales in the order of the rupture size can be neglected. Replacing $\sigma'(r, t_c) \approx \sigma'_0$ into (5.69) leads equivalently to (5.71).

Let us now examine the marginally pressurized limit: $f_p \Delta p_w \approx f_p \sigma'_0 - \tau_0$, where the rupture front significantly lags the overpressure front at the instability time, so that $\lambda(t_c) \ll 1$. We refer to Section 5.10 for a discussion about the marginally pressurized limit and its relation to the line-source approximation. Particularly, we note that the property $\Pi(0) = 1$ cannot be

rigorously defined but, still, it can be established in an order of magnitude sense. Furthermore, for injection at a constant volumetric rate, the prefactor is quite close to one for all practical purposes (see Figure 5.11b). It is therefore convenient for practical applications to define the marginally pressurized limit in an approximate sense. Hence, we approximate the fluid over-pressure within the rupture as $\Delta p_w \Pi(\lambda \bar{r}) \approx \sigma'_0 - \tau_0/f_p$. After substituting the previous relation into (5.70), we obtain the following regular eigenvalue problem for marginally pressurized cases,

$$\frac{R}{R_w} \frac{\tau_0}{f_p \sigma'_0} \bar{v}(\bar{r}) = \frac{1}{2\pi} \int_0^1 F\left(\bar{r}, \bar{\xi}\right) \frac{\partial \bar{v}(\bar{\xi})}{\partial \bar{\xi}} \mathrm{d}\bar{\xi}. \tag{5.72}$$

It is important to mention that the critically stressed and marginally pressurized limits are both characterized by small slip at the instability time: $\delta(r = 0, t_c) \ll \delta_c$. This is observed in our numerical solutions and was also established by Garagash and Germanovich (2012) in the two-dimensional problem. The latter is very important since it implies that the approximation of the exponential-weakening friction law by a linear relation is valid, as well as the assumption of unlimited linear-weakening of friction (never reaching the residual strength of the fault). Finally, as a last comment, we have established the eigenvalue problems in both limits for a general (self-similar) injection scenario, not restricted to the constant-volumetric rate case that we solve in the main text. However, in the marginally pressurized limit, we have implicitly assumed that the overpressure at the fluid source at the instability time is approximately equal to the overpressure at the time of activation of slip. Such approximation is reasonable in the case of the constant-volumetric rate as the increase of overpressure at the fluid source is slowly logarithmic (see Figure 5.11b) and assumed to be approximately constant, equal to Δp_c, for practical applications. This approximation has to be carefully considered when dealing with other injection scenarios (see, for instance, Garagash and Germanovich, 2012; Ciardo and Lecampion, 2019; Ciardo and Rinaldi, 2021).

5.9.3   Numerical solution of the regular eigenvalue problem

In the critically stressed and marginally pressurized limits, the eigen equations (5.71) and (5.72) can be recast as:

$$\frac{1}{2\pi} \int_0^1 F\left(\bar{r}, \bar{\xi}\right) \frac{\partial \bar{v}(\bar{\xi})}{\partial \bar{\xi}} \mathrm{d}\bar{\xi} = \beta \bar{v}(\bar{r}), \tag{5.73}$$

with the eigenvalue

$$\beta = \frac{R}{R_w} \cdot \begin{cases} 1 & \text{for critically stressed faults } \mathscr{T}_p \ll 1 \\ \tau_0/f_p \sigma'_0 & \text{for marginally pressurized faults } \mathscr{T}_p \sim 10. \end{cases} \tag{5.74}$$

We calculate the eigenvalues β_k and eigenfunctions $\bar{v}_k$ of (5.73), with $k = 1, 2, ..., \infty$, by discretizing the linear integral operator on the left-hand side via a collocation boundary element

k	Number of boundary elements N		
	100	1000	10000
1	0.998912	1.002648	1.003018
2	2.551356	2.561554	2.562539
3	4.111055	4.128215	4.129803
4	5.671338	5.696629	5.698843
5	7.230949	7.265725	7.268573

Table 5.1: Eigenvalues β_k as a function of the number of boundary elements N.

method employing ring 'dislocations' with piece-wise constant slip rate. The details of such implementation can be found in the supplementary material of Sáez and Lecampion (2023b). For the numerical calculations, it is convenient to express the discretized form of the eigen equation (5.73) in matrix-vector form as

$$\mathbf{E}\bar{\boldsymbol{v}}_k = \beta_k \bar{\boldsymbol{v}}_k, \tag{5.75}$$

where $\bar{\boldsymbol{v}}_k \in \mathbb{R}^N$ are the discretized eigenfunctions with $k = 1, 2, ..., N$, where N is the number of ring-dislocation elements, and $\mathbf{E} \in \mathbb{R}^{N \times N}$ is a non-dimensional matrix that is equivalent to the collocation boundary element matrix of a circular shear crack of unit radius and unit shear modulus (see Sáez and Lecampion, 2023b). By collocation boundary element matrix, we mean that the product between $\mathbf{E}$ and a given vector representing a discretized slip distribution $\boldsymbol{\delta}$, would give as a result the corresponding discretized shear stress distribution $\boldsymbol{\tau}$ that is in quasi-static equilibrium with $\boldsymbol{\delta}$, in an infinite and otherwise unstressed solid.

We solve the discretized eigen equation (5.75) with the standard Wolfram Mathematica functions *Eigenvalues* and *Eigenvectors* which can be instructed to search only for the smallest eigenvalues and their corresponding eigenvectors. We do not intend here to conduct an extensive analysis of the eigenvalues and eigenfunctions as our unique goal in this work is to determine the smallest eigenvalue that we expect to give the nucleation radii for the critically stressed and marginally pressurized regimes. Nevertheless, we do report the first five (smaller) eigenvalues and their eigenvectors in Table 5.1 and Figure 5.10, respectively. The eigenfunctions are normalized such that $\int_0^1 \bar{\boldsymbol{v}}_k^2(\bar{r}) \mathrm{d}\bar{r} = 1$, meaning that the normalized eigenvectors from (5.75) must be divided by $\sqrt{1/N}$. It is interesting to note that the smallest eigenvalue β_1 is for all practical purposes equal to 1. Also, we note that the eigenfunctions are not orthogonal as the matrix $\mathbf{E}$ is non-symmetric.
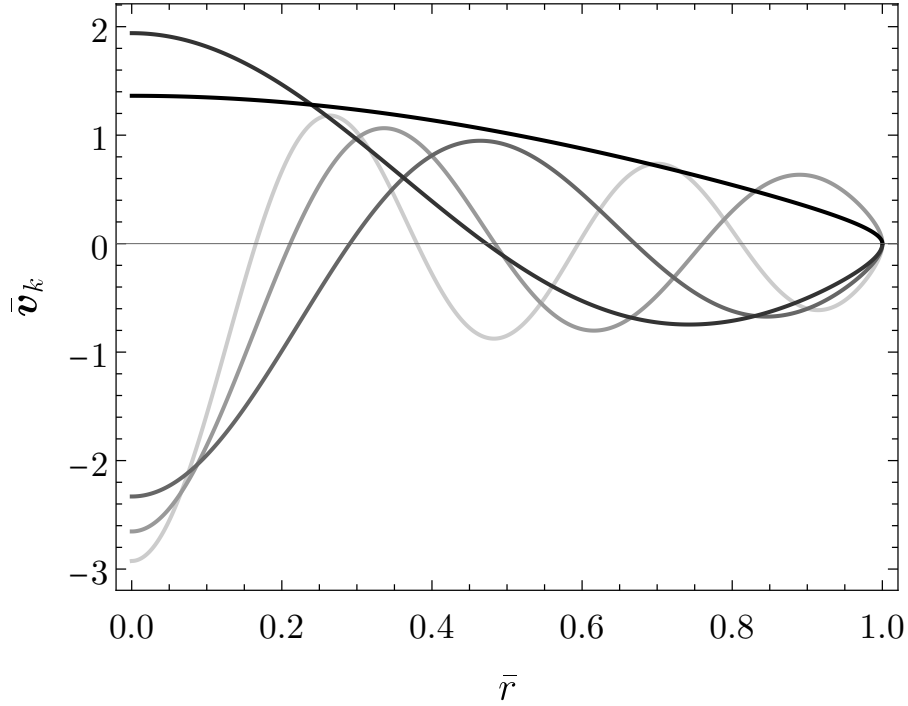
Figure 5.10: Normalized eigenfunctions $\bar{v}_k$ for $N = 10000$.

5.9.4 Universal nucleation radius of Uenishi and Rice for tensile and shear circular rupture instabilities

The eigen equation (5.71) for the critically stressed limit corresponds to the penny-shaped version of the eigen equation of Uenishi and Rice (2002). The nucleation radius (5.59) in the main text, is, therefore, the nucleation radius of a dynamic instability in the conditions analyzed by Uenishi and Rice (2002). In our circular configuration, the tectonic shear loading that drives the quasi-static phase of the rupture must be considered to be unidirectional, locally peaked around $r = 0$, and axisymmetric in magnitude. Moreover, this result is not only valid for a mixed-mode (II+III) shear rupture (with $v = 0$), but also for a cohesive tensile (mode I) crack. In this latter case, the nucleation radius is valid for any value of v as long as the shear modulus μ is replaced by $E'/2$, where $E' = E/(1 - v^2)$ is the plane-strain Young's modulus. Note that similarly to the shear rupture case, here the far-field tensile load driving the quasi-static growth of the mode-I rupture must be also locally peaked at $r = 0$ (in order to initiate fracture yielding at the origin) and axisymmetric in magnitude.

157

5.10   Supplementary material 2: A note on the line-source approximation of the fluid injection and the marginally pressurized limit

In our model, we idealize the fluid injection as a line source. Such approximation is of course valid for times $t \gg r_s^2/\alpha$, where r_s is the characteristic size of the actual fluid source. This is graphically shown in Figure 5.11a, where the line-source approximation is compared to the solution for a finite circular source of radius r_s. The latter is calculated from the known solution in the Laplace domain (section 13.5, equation 16, Carslaw and Jaeger, 1959) that we then invert numerically using the Stehfest's method (Stehfest, 1970). Figure 5.11a shows clearly how at large times the line-source and finite-source solutions become asymptotically equal at distances $r \geq r_s$. In particular, the overpressure at the fluid source can be approximated at large times by simply evaluating $\Delta p(r, t)$ (equation (5.1)) at $r = r_s$. By doing so, the argument of the exponential integral function is very small, $r_s^2/4\alpha t \ll 1$, and the overpressure at the fluid source can be asymptotically approximated as

$$\Delta p(r = r_s, t) \approx \frac{\Delta p_c}{4\pi} \left(-\gamma - \ln\left(\frac{r_s^2}{4\alpha t} \right) \right), \tag{5.76}$$

where $\gamma = 0.577216...$ is the Euler-Mascheroni's constant.

Equation (5.76) indicates that the overpressure at the fluid source increases logarithmically with time. This is further displayed in Figure 5.11b, where the temporal evolution of $\Delta p(r_s, t)$ is plotted for both the line-source and finite-source solutions. From this figure, we observe that the line-source approximation is already quite accurate for times $\alpha t/r_s^2 \gtrsim 10$. Furthermore, Figure 5.11b shows that the characteristic overpressure Δp_c (equation (5.2)) is in the order of magnitude of the overpressure at the fluid source for a wide range of practically relevant times. Consider, for instance, the case of geo-energy applications where fluid injections are conducted through a wellbore of radius $r_s \sim 10$ cm. By assuming plausible values of hydraulic diffusivity in the range 10^{-5} to 1 m^2/s, the characteristic time r_s^2/α takes values between 1000 down to 0.01 seconds which are much smaller than typical fluid injection duration in geo-energy applications. The large time limit is therefore commonly satisfied.

Note that we had already introduced Δp_c in a previous work (Sáez & Lecampion, 2023b) with the purpose of defining the marginally pressurized limit in a form that is more convenient for practical applications than in Sáez et al. (2022). We recall that the marginally pressurized limit is defined by the condition that the overpressure at the fluid source Δp_w is just sufficient to activate fault slip, $f_p \Delta p_w \approx f_p \sigma_0' - \tau_0$. As we have seen, we can approximate Δp_w quite well through a line source, yet its magnitude is not constant but rather increases with time. This increase is nevertheless logarithmically slow, so one could think in approximating Δp_w as constant and equal to the characteristic overpressure Δp_c. Indeed, the pre-factor in the order-of-magnitude relation $\Delta p_w \sim \Delta p_c$ is quite close to unity over a wide range of times (see Figure 5.11b). We therefore enforce $\Delta p_w \approx \Delta p_c$ with the aim of defining the marginally
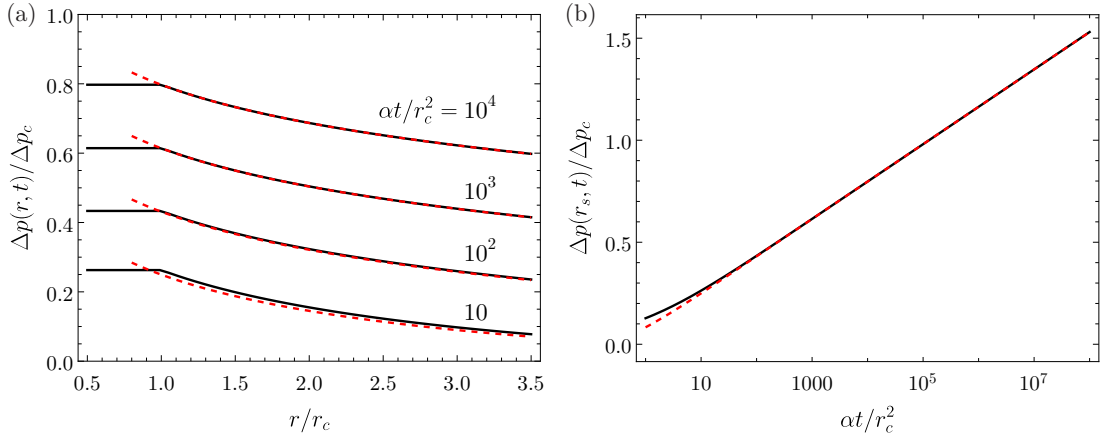
Figure 5.11: Finite source (solid black) versus line-source approximation (dashed red). (a) Spatial profile of normalized overpressure. (b) Normalized temporal evolution of the overpressure at the fluid source.

pressurized limit in the more practically convenient manner: $f_p \Delta p_c \approx f_p \sigma'_0 - \tau_0$. In this way, we essentially avoid introducing the length scale of the fluid source r_s into the problem that, we think, would unnecessary complexify the model and its practical applications. This subtle 'assumption' is all over the main text. Moreover, because the so-called intensity of the injection is $\Delta p_* = \Delta p_c / 4\pi$, the factor 4π is usually approximated by 10.

5.11   Supplementary material 3: Some remarks on the numerical solution

The numerical solutions are obtained through the axisymmetric numerical solver described in Chapter 2, with the adaptive time-stepping scheme described in the Supplementary Material of Chapter 4. The parameter β that controls the number of elements that the front advances during one time step is fixed for most simulations as 2.5, which results in a front advancement of 2 to 3 elements per time step. To resolve properly the cohesive zone, we consider no less than 100 elements covering the elasto-frictional length scale R_w.

6 Spatiotemporal signatures of seismic swarms driven by fluid injections and induced aseismic slip

Seismic swarms are often attributed to be driven by either the diffusion of pore pressure or the propagation of aseismic slip. In this chapter, we present a theoretical framework in which these two scenarios emerge as end members of a more general model in which earthquake swarms are driven by a combination of both mechanisms. We consider well-documented cases of anthropogenic seismic swarms which serve as a natural laboratory to test the theory, as the fluid sources underlying the seismic swarms are relatively well-constrained. We find that a likely general feature of the seismicity clouds is to be driven by pore pressure diffusion at early times of the injection and by stress transfer due to aseismic slip later on. The conditions controlling the transition between both regimes are theoretically established. While in the pore-pressure-driven regime, a square-root-of-time pattern of seismic swarm migration is expected, in the aseismic-slip-driven regime the predicted patterns are strongly connected to the injection flow rate history of the fluid source. Specifically, under well-defined conditions, the predicted pattern follows the square root of the current total volume of injected fluid. This theoretical prediction is found to be in good agreement with available field observations. Moreover, in the aseismic-slip-driven regime, the migration of the seismicity front is very sensitive to and contains important information on in-situ conditions such as the background stress state. Our model can notably explain seismic swarms with square-root-of-time migration patterns and characterized by unrealistically high hydraulic diffusivities as being driven by aseismic-slip stress transfer, meaning that the fluid source operates at an approximately constant volume rate. We also show that the back-front of seismicity frequently associated with the termination of fluid injections is a signature that is theoretically expected under the presence of aseismic slip as well.

This chapter is a modified version of the following scientific article:

Sáez, A. & Lecampion, B. Spatio-temporal signatures of seismic swarms driven by fluid injections and induced aseismic slip. *In preparation.*

Contributions of Alexis Sáez (CRediT, Contributor Roles Taxonomy)

Conceptualization, Methodology, Validation, Formal analysis, Investigation, Writing - Original Draft, Visualization, Funding acquisition.

6.1　Introduction

Earthquake swarms are seismic sequences that are strongly clustered in space and time and do not follow typical mainshock-aftershock behavior well-explained by the empirical Omori's law (Utsu, 1961). Seismic swarms are observed in a broad range of geological settings such as volcanic and geothermal regions (e.g., Wicks et al., 2011; Yukutake et al., 2011), tectonic plate interfaces (e.g., Holtkamp and Brudzinski, 2011; Nishikawa and Ide, 2017), stable continental regions (e.g., Sharma et al., 2020), and geological reservoirs subjected to borehole fluid injections (e.g., Healy et al., 1968; Cornet et al., 1997; Wei et al., 2015). The spatio-temporal patterns of earthquake swarms are commonly attributed to the signature of an underlying physical mechanism. The most common physical processes in seismic swarms are the diffusion of pore pressure and the propagation of aseismic slip. Pore pressure diffusion is often associated with a squared-root-of-time pattern and swarm migration velocities that are relatively slow in the sense that they feature realistic values of hydraulic diffusivity (e.g., Parotidis et al., 2005; Chen et al., 2012; Z. E. Ross and Cochran, 2021). Besides, the so-called back-front of seismicity is sometimes considered as a signature of pore pressure transients (e.g., Parotidis et al., 2004; Sirorattanakul et al., 2022). Conversely, the spatio-temporal patterns of seismic swarms driven by aseismic slip are much less understood. Yet it is commonly thought that high migration speeds (high with respect to the diffusion of pore pressure) are a possible signature of underlying aseismic slip transients (e.g., Lohman and McGuire, 2007).

A growing body of evidence suggests that whenever fluids are injected into the Earth's crust, the activation of not only seismic but also aseismic fault slip is present (Hamilton & Meehan, 1971; Scotti & Cornet, 1994; Cornet et al., 1997; Bourouis & Bernard, 2007; Guglielmi et al., 2015; Wei et al., 2015; Cappa et al., 2022). Furthermore, the increasing availability of geodetic data and advancements in data processing techniques are recently improving the detection of slow slip events behind seismic swarms, with coupled fluid flow and aseismic slip processes being now often invoked to explain more complete data sets (e.g., Sirorattanakul et al., 2022; Yukutake et al., 2022; Nishimura et al., 2023). In this work, we develop a theoretical framework for understanding what spatiotemporal signatures of seismic swarm migration are expected under the combined effect of pore pressure diffusion due to fluid injections and induced aseismic slip. We consider well-documented cases of anthropogenic seismic swarms which serve as a natural laboratory to test the theory, as the fluid sources underlying the seismic swarms are relatively well-constrained.

6.2 Theory

6.2.1 Model

We consider fluid injection into a porous fault zone from a localized line source of fluids (Figure 6.1) under the assumptions of the hydro-mechanical model presented recently by Sáez and Lecampion (2023a). In this model, the resulting spatiotemporal evolution of pore pressure follows a linear diffusion equation. In 2D, the line source is contained entirely within the fault zone; it has an infinite extent along the out-of-the-plane direction of Figure 6.1a, and produces a one-dimensional flow along the x axis. In 3D, the line source crosses the fault zone perpendicularly to the fault plane, providing a more realistic localized source of fluids and conditions for radial, axisymmetric flow (Figure 6.1b). Solutions of the linear diffusion equation under both conditions are self-similar (Carslaw & Jaeger, 1959),

$$\Delta p(s, t) = \Delta p_*(t) \cdot \Pi\left(\frac{s}{\sqrt{4\alpha t}}\right), \tag{6.1}$$

where s is a generalized spatial coordinate, equal to the Cartesian coordinate x in 2D, and the radial coordinate r in 3D, $\Delta p_*(t)$ is the intensity of the injection with units of pressure that may generally depend on time, $\Pi(\xi)$ is the self-similar spatial profile of overpressure which is function of the similarity coordinate $\xi = s/\ell_d(t)$, with $\ell_d(t) = \sqrt{4\alpha t}$ the classical diffusion length scale and α the fault hydraulic diffusivity. The function Π is such that $\Pi(0) \approx 1$ and $\Pi(s \to \infty) \to 0$. In this way, $\Delta p_*(t)$ is approximately the overpressure at the fluid source at any time $t > 0$, and the overpressure vanishes at infinity. The condition $\Pi(0) \approx 1$ cannot be achieved in 3D for injection from a line source, yet an approximation at the relevant time scales of the model can be made to define $\Delta p_*(t)$ as the fluid-source overpressure (Sáez & Lecampion, 2023a).

The injection of fluids has the effect of reducing the fault strength owing to the increase of pore-fluid pressure which decreases the effective normal stress. Such pore pressure increase will be eventually sufficient to activate fault slip when the fault strength equates to the pre-injection shear stress τ_0, which marks the onset of a fault rupture nucleating at the injection point. We consider that quasi-static, aseismic slip propagates on a planar slip-weakening fault interface. Our focus is on the case of unconditionally stable ruptures (Sáez & Lecampion, 2023a), which satisfy the relation $\tau_0 < f_r \sigma_0'$ (Garagash & Germanovich, 2012; Sáez & Lecampion, 2023a), where f_r is the residual friction coefficient and σ_0' the pre-injection effective normal stress. Such ruptures are characterized by four distinct and successive stages: (i) an initial phase in which the slip transients are well approximated by a fault obeying a constant friction coefficient equal to the peak value f_p, (ii) an acceleration phase of the rupture front due to the weakening of friction at rupture length scales that are comparable with the cohesive zone size, (iii) a crack-like phase in which the dynamics of the rupture front is controlled by an energy balance of the Griffith's type, and (iv) an ultimate regime in which the rupture propagates as if it were governed by a constant friction coefficient equal to the residual value f_r.
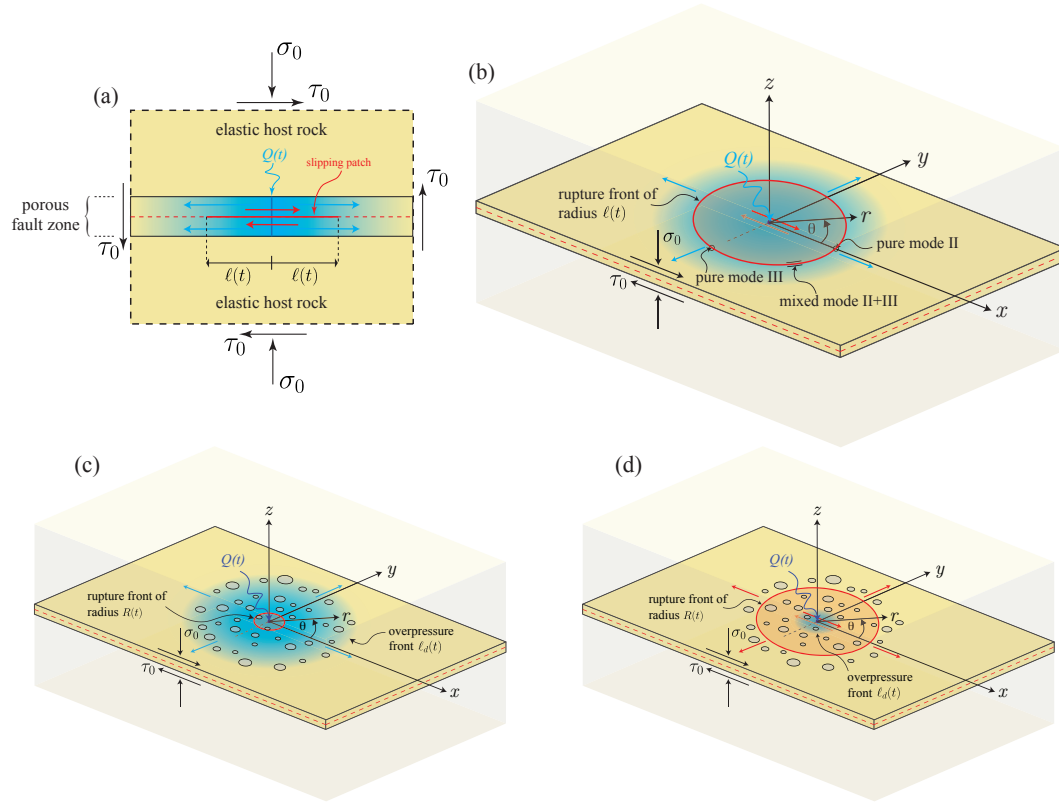
Figure 6.1: Model schematics. (a) and (b), fluid is injected into a permeable fault zone via an infinitesimal source with an arbitrary history of volume rate. The fault is planar and embedded in an unbounded linearly elastic impermeable host rock. The pre-injection stress state is uniform. (a) Two-dimensional plane-strain model. (b) Three-dimensional circular rupture model. (c) Pore-pressure-driven regime. (d) Aseismic-slip-driven regime. Gray areas in (c) and (d) represent unstable fault patches producing seismicity.

In this work, we assume that the rupture size is greater than the cohesive zone size, thereby focusing on stages (iii) and (iv). Sáez and Lecampion (2023a) examined recently a particular yet insightful case of ruptures that are driven by injection at a constant volume rate. Here, we generalize their model to account for fairly arbitrary injection rate histories as described by equation (6.1). For the sake of generality, we construct the physical model under two-dimensional plane-strain conditions (Figure 6.1a) as it has been done previously for similar models (Dublanchet, 2019; Garagash, 2021; Viesca, 2021; Yang & Dunham, 2021), as well as in a more realistic three-dimensional configuration. In the latter, we focus on the case of axisymmetric circular ruptures (Figure 6.1b) as they capture the most essential aspects of the dynamics of unbounded ruptures in three dimensions (Sáez et al., 2022; Sáez & Lecampion, 2023a, 2023b).

Let us define $\ell(t)$ as the position of the slip front, equal to the half-rupture length in 2D and the rupture radius in 3D (Figure 6.1). The fraction of the energy dissipated per unit area of rupture growth within the cohesive zone that is relevant for rupture advancement, known as fracture energy G_c, can be approximated both in 2D and 3D as (Garagash & Germanovich, 2012; Sáez & Lecampion, 2023a)

$$G_c \approx \left[\sigma_0' - \Delta p(\ell, t)\right]\left(f_p - f_r\right)\frac{\delta_c}{2}, \quad K_c = \sqrt{2\mu G_c},$$ (6.2)

where K_c is the so-called 'fracture' toughness. The fracture energy must equal the influx of elastic energy into the edge region G, also known as energy release rate, leading to (Garagash & Germanovich, 2012; Sáez & Lecampion, 2023a)

$$\frac{2\ell^\beta}{\sqrt{\pi}} \int_0^\ell \frac{f_r \Delta p(s, t)}{\sqrt{\ell^2 - s^2}} s^\gamma \mathrm{d}s + \frac{2\psi}{\sqrt{\pi}}\left(\tau_0 - f_r\sigma_0'\right)\sqrt{\ell} = K_c(\ell, t),$$ (6.3)

with the coefficients ψ, β and γ given by:

$$\{\psi, \beta, \gamma\} = \begin{cases} \{\pi/2, 1/2, 0\}, & \text{in 2D} \\ \{1, -1/2, 1\}, & \text{in 3D.} \end{cases}$$ (6.4)

Equation (6.3) summarizes in a compact way the competing physical mechanisms that take place during the propagation of fluid-driven stable ruptures in our model. The first term of the left-hand side is a stress intensity factor associated with the continuous reduction of fault strength due to fluid injection which unclamps the fault. This term is always positive and thus supplies energy to the rupture tip to promote rupture growth. The right-hand side is the rupture toughness, proportional to the fracture energy. This local term is associated with the dissipation of energy at the rupture front, thus resisting rupture advancement. The second term of the left-hand side is a stress intensity factor associated with a constant 'drop' of stress from the pre-stress τ_0 to the in-situ residual fault strength $f_r\sigma_0'$. This quantity is negative; a necessary condition for the rupture to be unconditionally stable. It corresponds to a term that 'consumes' energy in a non-local manner, and thus resists rupture advancement.

6.2.2 Swarm migration front and end-member regimes

Our model is characterized by three intrinsic length scales, namely, the slip front $\ell(t)$, an overpressure front that is classically chosen in diffusion problems as $\ell_d(t) = \sqrt{4\alpha t}$ (Carslaw & Jaeger, 1959), and an elasto-frictional length scale equal to $\ell_* = \mu \delta_c / (f_p - f_r) \sigma'_0$. The latter is associated with the cohesive zone size, where the dissipation of fracture energy happens. The former two are the ones naturally related to the migration patterns of seismic swarms as we explain below.

When $\ell_d(t) \gg \ell(t)$, the migration pattern of seismic swarms is expected to be dominated by pore pressure diffusion (Figure 6.1c). It should thus show a characteristic square-root-of-time dependence. This is because the diffusion front $\ell_d(t) \propto \sqrt{t}$ tracks an isobar of overpressure $\Pi(1) \sim 1\%$ of the current value of overpressure at the fluid source $\Delta p_*(t)$. The latter can be interpreted as a minimum Coulomb's stress change (threshold) required to trigger frictional instabilities. If such a threshold exists, it is certainly expected to be strongly site-dependent. Therefore, it does not seem possible to define in a sufficiently general and physically rigorous manner a diffusion front that can be representative of a 'seismicity front' without accepting a certain degree of arbitrariness. Indeed, a slightly different front than $\ell_d(t)$ yet of the same order of magnitude has been widely used for interpreting seismic swarms as if they were purely driven by pore pressure diffusion (S. Shapiro et al., 1997). However, if the structural discontinuities hosting micro-seismic events are, for example, misoriented with regard to the in-situ stress field, the Coulomb's stress threshold associated with $\ell_d(t)$ may be too small to be representative of a seismicity front (Wang & Dunham, 2022).

On the other hand, when $\ell(t) \gg \ell_d(t)$, the migration pattern of seismic swarms is expected to be dominated by aseismic-slip stress transfer (Figure 6.1d). In this case, the Coulomb's stress increase is maximum at the slip front and decays ahead of it. If one defines the seismicity front based on a threshold of Coulomb's stress change (subjected to the same degree of arbitrariness discussed previously), such a front must be at some distance ahead of the slip front. Moreover, if we adopt the simplifying assumption that the relative position of this front is approximately invariant with regard to the location of the slip front, seismic swarms should migrate according to the spatiotemporal patterns set by the dynamics of the slip front $\ell(t)$. Furthermore, if the offset between these two fronts is of smaller order than the rupture size, one can still consider the slip front as a proxy for the seismicity front, at least for the purpose of defining the limiting regimes of the model. Nevertheless, when constraining our model against field observations, we will always position the slip front behind the seismicity front to recognize the above.

With the previous considerations in mind, we define a convenient non-dimensional quantity that relates the two relevant fronts of the problem (Bhattacharya & Viesca, 2019),

$$\lambda(t) = \frac{\ell(t)}{\ell_d(t)}. \tag{6.5}$$

The so-called amplification factor λ provides a unified framework to understand what the nec-

essary conditions for the previous two distinct regimes of seismic swarm migration to emerge are, besides allowing us to identify the conditions under which a rather even combination of the two mechanisms will control the migration of swarms, $\lambda(t) \sim 1$.

6.2.3   Pore-pressure-driven regime

When either the current fluid-source overpressure is not yet sufficient to activate fault slip, $f_p \Delta p_*(t) < f_p \sigma_0' - \tau_0$, or slip has been activated but $\lambda(t) \ll 1$, the migration of seismic swarms is expected to be dominated by pore pressure diffusion and the square-root-of-time pattern. Moreover, as the rupture size is very small in comparison to the pressurized area, the overpressure over the slipping region and particularly along the cohesive zone can be approximated by the overpressure at the fluid source, $\Delta p_*(t)$. The fracture energy (6.2) can be thus approximated in this regime as

$$G_c(t) \approx \left(f_p - f_r\right) \frac{\delta_c}{2} \left(\sigma_0' - \Delta p_*(t)\right), \tag{6.6}$$

which depends on time but no longer on the position of the slip front. Let us now define the following non-dimensional integral,

$$\Psi(\lambda) = \int_0^1 \frac{\Pi(\lambda\eta)}{\sqrt{1-\eta^2}} \eta^\gamma \mathrm{d}\eta, \tag{6.7}$$

which in view of the properties of Π satisfies the following limiting behaviors: $\Psi \sim 1$ when $\lambda \ll 1$, and $\Psi \ll 1$ when $\lambda \gg 1$.

Considering the scaling of the model in the case $\lambda(t) \ll 1$ (Sáez & Lecampion, 2023a), we obtain the dimensionless form of the energy balance (6.3) in the pore-pressure-driven regime as

$$\Psi(\lambda) - \psi \mathcal{T}_r(t) = \frac{\sqrt{\pi}}{2} \mathcal{K}_d(t), \tag{6.8}$$

where,

$$\mathcal{T}_r(t) = \frac{f_r \sigma_0' - \tau_0}{f_r \Delta p_*(t)}, \text{ and } \mathcal{K}_p(t) = \frac{K_c(t)}{f_r \Delta p_*(t)\sqrt{\ell(t)}}, \tag{6.9}$$

are the so-called residual stress-injection parameter and dimensionless toughness, respectively. Unlike the case of injection at a constant rate where the parameter $\mathcal{T}_r$ is constant (Sáez & Lecampion, 2023a), here $\mathcal{T}_r$ is time-dependent owing to the arbitrary injection rate histories under consideration.

6.2.4   Aseismic-slip-driven regime

When $\lambda(t) \gg 1$, the migration of seismic swarms is expected to be dominated by aseismic-slip stress transfer and a migration pattern to be understood. Moreover, since the rupture front is far ahead of the fluid-pressurized region, the overpressure along the cohesive zone can be neglected. Hence, we approximate the fracture energy (6.2) in the aseismic-slip-driven regime simply as

$$G_c \approx \left(f_p - f_r\right)\frac{\delta_c}{2}\sigma_0', \tag{6.10}$$

which is notably constant and corresponds to the 'in-situ' fracture energy. In this regime, the dimensionless form of the energy balance (6.3) is (Sáez & Lecampion, 2023a)

$$\frac{1}{\mathscr{T}_r(t)}\Psi(\lambda) - \psi = \frac{\sqrt{\pi}}{2}\mathscr{K}_s(t), \text{ with } \mathscr{K}_s(t) = \frac{K_c}{(f_r\sigma_0' - \tau_0)\sqrt{\ell(t)}}, \tag{6.11}$$

where $\mathscr{K}_s(t)$ corresponds to the so-called nearly-unstable dimensionless toughness (Sáez & Lecampion, 2023a).

6.2.5   General solution: the two dimensionless parameters

As demonstrated by equations (6.8) and (6.11), our proxy to quantify the relative contributions of pore pressure and aseismic slip to the driving forces controlling the migration of seismic swarms, the amplification factor λ, is a function of only two time-dependent dimensionless parameters, $\mathscr{T}_r$ and $\mathscr{K}$. The latter comes in two choices depending on the relevant regime, either $\mathscr{K}_p$ or $\mathscr{K}_s$. The dimensionless toughness $\mathscr{K}$ quantifies how much the fracture energy contributes to resisting the advancement of the rupture at a given time t. Since any physically admissible quasi-static solution of the model must be such that the position of the rupture front $\ell(t)$ increases monotonically with time, the dimensionless toughnesses $\mathscr{K}_s(t)$ and $\mathscr{K}_p(t)$ always decrease with time. In the pore-pressure-driven regime, $\mathscr{K}_p(t)$ decreases even faster than $\mathscr{K}_s(t)$ if one considers a non-decreasing fluid-source overpressure with time. This means that the rupture always accelerates in time with regard to the overpressure front due to the diminishing effect of the fracture energy in the rupture-front energy balance, a result that was previously found for the particular case of injection at a constant rate in 2D (Garagash, 2021) and 3D (Sáez & Lecampion, 2023a), and is now generalized for arbitrary injection rate histories in 2D and 3D.

According to equation (6.3), the fluid-injection integral term whose intensity is $f_r\Delta p_*(t)$ is what 'feeds' the rupture to advance, whereas the term $\sim (f_r\sigma_0' - \tau_0)\sqrt{\ell}$ has the effect of resisting rupture growth. The competition between both non-local 'energy' terms is quantified by the residual stress-injection parameter $\mathscr{T}_r$, equation (6.9). The smaller the negative stress 'drop' $\tau_0 - f_r\sigma_0'$, the less opposition the rupture has to grow; whereas the higher the intensity of the injection, the faster the rupture propagates. Hence, decreasing values of $\mathscr{T}_r$ will always result

in faster aseismic ruptures. Moreover, as shown in Section 6.5.1, the parameter $\mathcal{T}_r$ is bounded as

$$\mathcal{T}_{\min} = 1 - \frac{\tau_0}{f_r \sigma_0'} < \mathcal{T}_r(t) < \frac{\sigma_0' - \tau_0/f_r}{\sigma_0' - \tau_0/f_p} = \mathcal{T}_{\max}. \tag{6.12}$$

Its maximum value $\mathcal{T}_{\max}$ is associated with the minimum possible fluid-source overpressure, that is, the amount that is just sufficient to activate fault slip, $\sigma_0' - \tau_0/f_p$. On the other hand, its minimum value $\mathcal{T}_{\min}$ is attained at the moment in which the fault is about to open when the fluid-source overpressure approaches the in-situ effective normal stress. Note that if we assume an injection rate history that produces a fluid-source overpressure $\Delta p_*(t)$ which increases monotonically with time, then $\mathcal{T}_r(t)$ will always evolve from $\mathcal{T}_{\max}$ to $\mathcal{T}_{\min}$. Therefore, such fluid injections which one may quite frequently expect, always tend to accelerate aseismic ruptures in time with regard to the overpressure front due to the decreasing values of $\mathcal{T}_r$. We highlight that our model is not limited to non-decreasing overpressures in time; fluid injections can be quite arbitrary as long as a possible depressurization of pore fluids does not change the propagation mode of the rupture from crack-like to pulse-like mode. The latter kind of injection-induced aseismic ruptures has been examined recently by Sáez and Lecampion (2023b).

So far, all of our results are general and not restricted to any specific injection rate history. To illustrate the quantitative predictions that our model can make, let us prescribe a particular injection scenario. Consider, for instance, axisymmetric radial flow with an injection rate that increases linearly with time: $Q(t) = R_q t$, where R_q is the (constant) rate of change of the injection rate. Closed-form expressions for $\Delta p_*(t)$ and $\Pi(\xi)$ are calculated in Section 6.5.2 for this case. The solution in the aseismic-slip-driven regime, equation (6.11), is displayed in Figure 6.2a in terms of $\lambda(\mathcal{T}_r, \mathcal{K}_s)$. Note that all the previous general results such as the acceleration of the slip front with regard to the overpressure front in time due to the decreasing values of both $\mathcal{T}_r$ and $\mathcal{K}_s$ are present in this particular solution. Moreover, the transition between the pore-pressure-driven regime and the aseismic-slip-driven regime could be interpreted in this plot as the contour line $\lambda = 1$, which is a one-to-one relation between $\mathcal{T}_r$ and $\mathcal{K}_s$.

6.2.6   Ultimate zero-fracture-energy regime and family of solutions

It can be readily shown from the definitions of the dimensionless toughnesses $\mathcal{K}_p$ and $\mathcal{K}_s$, that the ultimate regime of any unconditionally stable rupture ($t \to \infty$, $\ell \to \infty$) is such that $\mathcal{K} \to 0$. Hence, ultimately all ruptures behave to leading order as having zero fracture energy. This result had been already obtained for injection at a constant rate in 2D (Garagash, 2021) and 3D (Sáez & Lecampion, 2023a), and it is now generalized for arbitrary injection rate histories. In this ultimate zero-fracture-energy regime, the rupture-front energy balance further simplifies to

$$\Psi(\lambda) = \psi \mathcal{T}_r(t), \tag{6.13}$$
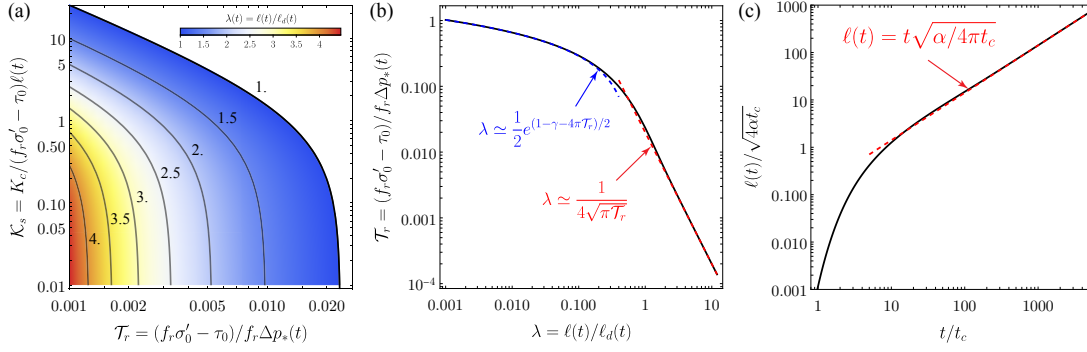
Figure 6.2: The main features of the model, as exemplified by the particular case of injection at a linearly increasing volume rate with time. (a) Aseismic-slip-driven regime. Amplification factor λ as a function of the two dimensionless parameters $\mathcal{T}_r$ and $\mathcal{K}_s$. (b) Zero-fracture-energy solution, $\lambda(\mathcal{T}_r, \mathcal{K}_s = 0)$, and asymptotic solutions for the pore-pressure-driven (blue) and aseismic-slip-driven (red) regimes. (c) Zero-fracture-energy solution in terms of the normalized rupture radius versus dimensionless time. Aseismic-slip-driven regime is characterized by a slip front moving at a constant rupture speed.

which is notably valid for both the pore-pressure-driven and aseismic-slip-driven regimes. Equation (6.13) admits closed-form solutions under various practically useful injection scenarios such as injection at a constant volume rate, constant overpressure, and linearly increasing rate of injection with time. A family of solutions for (6.13) is reported in Section 6.5.2. Moreover, in the case of the linearly increasing rate of injection that we analyzed previously, the ultimate zero-fracture-energy solution is displayed in Figure 6.2b. Such a solution is recast in a more intuitive manner in Figure 6.2c, where the evolution of the slip front in time ultimately reaches a steady stage characterized by a constant rupture speed. This rupture speed is a function of the fault hydraulic diffusivity and the time scale t_c given by equation (6.19), derived in Section 6.5.2.

6.2.7 Slip front as function of accumulated fluid volume in the aseismic-slip-driven regime

In the aseismic-slip-driven regime $\lambda(t) \gg 1$, the rupture surface is much bigger than the fluid pressurized area, hence, the equivalent shear load due to fluid injection can be approximated as a point force (Garagash & Germanovich, 2012; Viesca, 2021; Sáez et al., 2022; Sáez & Lecampion, 2023a),

$$f_r \Delta p(s, t) \approx f_r \Delta P(t) \frac{\delta^{\text{dirac}}(s)}{(2\pi s)^\gamma}, \quad \text{with} \quad \Delta P(t) = 2^{1-\gamma} \int_0^\infty \Delta p(s, t) (2\pi s)^\gamma \, \mathrm{d}s. \tag{6.14}$$

Substituting the previous equation into (6.3) leads after some manipulations to

$$\frac{f_r \Delta P(t)}{(\pi \ell)^{\gamma + 1/2}} + \frac{2\psi}{\sqrt{\pi}} \left[\tau_0 - f_r \sigma_0' \right] \sqrt{\ell} = K_c, \tag{6.15}$$

with $K_c = \sqrt{2\mu G_c}$ and G_c given by (6.10).

Previous studies concerned with the problem of injection-induced seismicity have attempted to link the size of fault rupture events with a specific operational parameter: the volume of injected fluid (McGarr, 2014; Galis et al., 2017; Garagash, 2021). Following the reasoning of prior works (McGarr, 2014; Galis et al., 2017; Garagash, 2021), we can relate the temporal evolution of the point force $\Delta P(t)$ to the current amount of injected volume $V(t)$ as (see Section 6.5.3)

$$\Delta P(t) = \frac{V(t)}{Sw}, \tag{6.16}$$

where S is the so-called oedometric storage coefficient representing the variation of fluid content caused by a unit pore pressure change under uniaxial strain condition (Detournay & Cheng, 1993), and w is the fault zone width. S is given by equation (6.25) and it accounts for the effects of fluid, pore, and bulk compressibilities in the fault zone. In (6.16), $V(t)$ has units of m^3 in 3D, and units of m^2 in 2D (volume per unit length of injection line). Note that the relevant compressibility-like parameter in our model is S, whereas in prior works is either the inverse of the bulk modulus (McGarr, 2014; Galis et al., 2017) or the pore compressibility (Garagash, 2021).

Substituting (6.16) in (6.15), we obtain after some manipulations,

$$\mathcal{V}(\ell, t) = 2\mathcal{T}_r^* \left(\frac{\sqrt{\pi}}{2} \mathcal{K}_s(\ell) + \psi \right), \quad \text{with} \quad \mathcal{V}(\ell, t) = \frac{V(t)}{\pi^\gamma w \ell^{\gamma+1}} \quad \text{and} \quad \mathcal{T}_r^* = \frac{f_r \sigma_0' - \tau_0}{f_r S^{-1}}, \tag{6.17}$$

where $\mathcal{V}$ is a dimensionless volume equal to the volume of injected fluid divided by the volume of fault whose slip surface has ruptured, and $\mathcal{T}_r^*$ is a small $\mathcal{T}_r$-like parameter. Equation (6.17) is an implicit equation for ℓ as a function of the current injected volume of fluid. Moreover, since ultimately $\mathcal{K}_s \to 0$, one can obtain a closed-form explicit expression for the position of the slip front $\ell(t)$ as a function of $V(t)$ in the ultimate zero-fracture-energy regime, which reads as

$$\ell(t) = c \left[\frac{V(t)}{w \mathcal{T}_r^*} \right]^\xi, \quad \text{with} \quad \xi = \begin{cases} 1, & \text{in 2D} \\ 1/2, & \text{in 3D}, \end{cases} \tag{6.18}$$

and the pre-factor $c = (2\pi^\gamma \psi)^{-\xi}$, equal to $1/\pi \approx 0.318310...$ in 2D, and $1/\sqrt{2\pi} \approx 0.398942...$ in 3D.

6.3 Application to the 1993 hydraulic stimulation at the Soultz geothermal site, France

We test our model against the well-documented case of the September 1993 hydraulic stimulation at the Soultz geothermal site in France, where direct evidence of injection-induced

aseismic slip exists (Cornet et al., 1997). The history of injection flow rate and accumulated volume of injected water is displayed in Figure 6.3a. Approximately 25,000 m^3 of water were injected through the so-called GPK1 well into a hot granite formation during a period of about 15 days. The fluid injection was conducted in a step incremental manner that reached a maximum of 36 l/s along the 550 m open-hole section located at depths between 2,850 m and 3,400 m. Figure 6.3b shows the spatiotemporal evolution of seismicity of the more than 10,000 events recorded during the injection test, before and after shut-in (Baria et al., 1996).

Prior works have suggested that this injection test stimulated a set of fractures (Evans, Moriya, et al., 2005), whereas our model considers the stimulation of only one single planar fault. Nevertheless, recent physics-based simulations of injection-induced aseismic slip in a two-dimensional fracture network have demonstrated that the same patterns predicted by a single fracture in two dimensions emerge collectively for a fracture network if it operates under critically stressed conditions (Ciardo & Lecampion, 2023). Since the fractures intersecting the open-hole section of the GPK1 well are known to be critically stressed (Evans, 2005), we make the assumption that the response of the fracture network can be approximated by an equivalent single planar fault.

Based on estimates of aseismic slip from borehole-wall deformations of up to 4.7 cm by Cornet et al. (1997), an equivalent hydraulic diffusivity of $\alpha \approx 0.06$ m^2/s has been estimated by Sáez and Lecampion (2023b). Figure 6.3b displays the corresponding overpressure front $\ell_d(t)$ together with the micro-seismicity in a distance-versus-time plot. The injection 'point' has been located according to the analysis of S. A. Shapiro et al. (1999). We observe that pore pressure diffusion alone does not seem to be able to explain the migration of micro-seismicity, especially in the second half of the stimulation period, where a square-root-of-time pattern appears inconsistent with the data. Because of the known occurrence of aseismic slip, the triggering of instabilities due to quasi-static stress transfer has already been suggested as a significant contributing factor (Cornet, 2016), making this case particularly suitable for the application of our hydro-mechanical model.

We first note that the injection rate history can be well approximated by a linear increase in injection rate with time (Figure 6.3a). We estimate the slope of the injection ramp-up by equating the actual volume of injected fluid, resulting in $Q(t) = R_q t$ with $R_q \approx 2.92 \times 10^{-5}$ l/s^2 as illustrated in Figure 6.3a. Assuming that the effect of the fracture energy in determining the position of the slip front can be neglected, we note that a steadily rising injection rate leads to a linear expansion of the slip front over time in the aseismic-slip-driven regime (Figure 6.2). This theoretical prediction aligns well with the observed pattern of micro-seismicity giving us confidence to pursue this route. The zero-fracture-energy regime is governed by two parameters, namely, the equivalent hydraulic diffusivity α, and the time scale (Section 6.5.2)

$$t_c = \frac{f_r \sigma_0' - \tau_0}{f_r R_q \eta / k w} \tag{6.19}$$

that is associated with the activation time of fault slip. Assuming that the amplification of
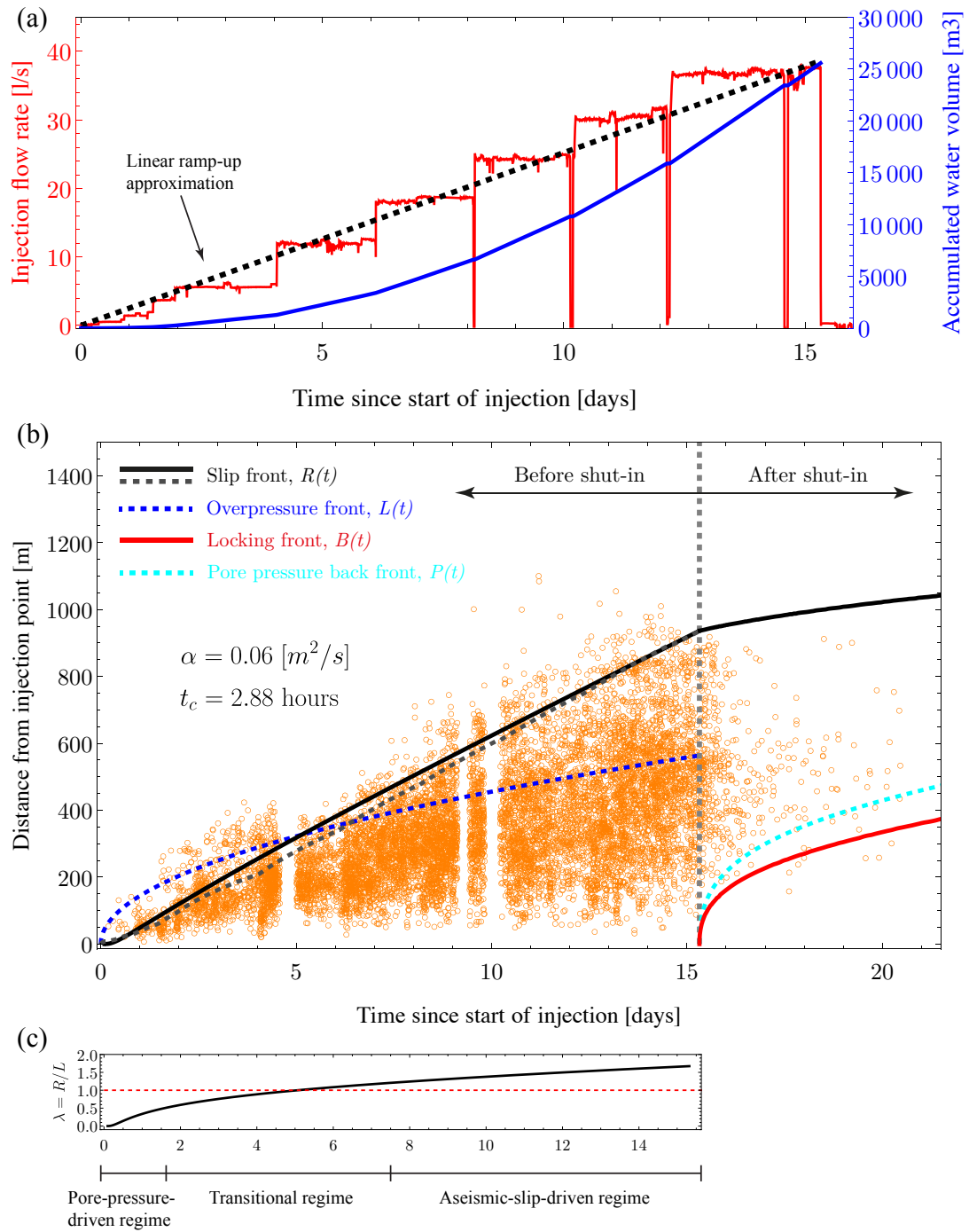
Figure 6.3: Application of our model to the 1993 hydraulic stimulation of the GPK1 well at the Soultz-sous-Forêts geothermal site in France. (a) Injection flow rate history and accumulated water volume in time. (b) Migration of seismicity in a distance versus time plot. For the slip front (black), the solid line corresponds to the solution of the zero-fracture-energy limit, equation (6.13), with the linear ramp-up approximation shown in panel (a). The dashed line further assumes a point-force approximation for the fluid injection, resulting in a relation with the accumulated volume, equation (6.18). (c) Amplification factor λ over time, highlighting the different regimes/stages driving the migration of the seismic swarm.

Coulomb's stress ahead of the slip front dominates the evolution of the seismicity front in the second part of the stimulation period, we find $t_c \approx 2.9$ hours to explain well the migration of seismicity (Figure 6.3b). In the previous estimate, we recognize that the rupture front must lag the seismicity front to some extent. The hydraulic transmissivity has been estimated at the highest pressures of the test in approximately 1.7×10^{-12} m^3 (Evans, Genter, et al., 2005). Assuming a water dynamic viscosity of $\eta = 3.5 \times 10^{-4}$ Pa·s, equation (6.19) constrains the stress 'distance' to the stability limit, $\sigma_0' - \tau_0 / f_r \approx 0.06$ MPa. Note that our parameter estimates give also a wellbore overpressure $\Delta p_*(t)$, equation (6.21), of about 10 MPa at the latest part of the injection, which is very close to the actual downhole overpressure measured at 2,850 m depth at these same times, equal to 9.1 MPa (Cornet et al., 1997).

By assuming that the seismic swarm operates in the aseismic-slip-driven regime at all times, we can use equation (6.18) that relates the position of the slip front to the current total volume of injected fluid. The history of accumulated volume is approximately quadratic in time (Figure 6.3a), so that (6.18) predicts an approximately linear pattern of migration with time. Knowing the accumulated volume in time, this model has the benefit of having only one parameter. We fit the model with the results displayed in Figure 6.3b. The interpretation of these results is part of an ongoing research.

6.4 Discussions

The application of our model to the September 1993 Soultz case shows a clear transition from the pore-pressure-driven regime at early times (the first one to three days of injection) to the aseismic-slip-driven regime at late times (starting from day 7 or 8). Indeed, our model predicts that whenever aseismic slip becomes the dominant mechanism, an early pore-pressure-driven regime and thus a transitional regime too, are expected to occur. The reason is that in a Coulomb's failure sense, a finite minimum amount of overpressure is always required to activate fault slip. Hence, before this activation time, the only mechanism present is pore pressure diffusion. Additionally, a gradual increase in overpressure is likely to happen in most fluid injections, particularly in the one analyzed here. Hence, both the dimensionless toughness $\mathcal{K}$ and residual stress-injection parameter $\mathcal{T}_r$ would decrease in time, so that an acceleration of the slip front with regard to the overpressure front is expected and thus a transition from the pore-pressure-driven regime to the aseismic-slip-driven regime is always a latent possibility.

According to our model, the linear pattern of migration featured by the 1993 Soultz case is strongly related to the approximately linear ramp-up of injection rate; a common injection protocol in hydraulic stimulation operations. We observe that other anthropogenic seismic swarms induced by the same kind of fluid-injection ramp-ups show systematically similar linear patterns of migration. An example of them is the 2013 hydraulic stimulation of the GRT-1 well at the Rittershoffen geothermal site in France, which is displayed in Figure 6.4a. Also, the 2006 hydraulic stimulation at the Basel geothermal project in Switzerland (e.g., figure

3a in Goertz-Allmann et al., 2011) shows a relatively linear pattern of migration. Yet we are still in the process of further testing our model against these observations; our preliminary results are encouraging.

On the other hand, it has been recently shown by Sáez and Lecampion (2023b) that seismicity after shut-in is expected to be triggered approximately in a region between the rupture front and locking front of the post-injection aseismic pulses that characterized the propagation of stable slip after shut-in (Sáez & Lecampion, 2023b). Using the model and procedure described in Sáez and Lecampion (2023b), we calculate the evolution of both fronts in time, including the pore-pressure back front (eq. 3.1 in Sáez and Lecampion, 2023b) that has been proposed to explain the so-called back front of seismicity sometimes observed after the termination of fluid injections (Parotidis et al., 2004). Based on the application of our model to the 1993 Soultz case after shut-in, as shown in Figure 6.3b, the back front signature seems also compatible with the propagation of aseismic slip and its contribution to the delayed triggering of seismicity (Sáez & Lecampion, 2023b).

Finally, seismic swarms are often considered to be driven by pore pressure diffusion due to the classical square-root-of-time migration pattern (S. Shapiro et al., 1997; S. Shapiro et al., 2005). However, in some occasions, the equivalent hydraulic diffusivity that is inferred from distance-versus-time plots of seismicity clouds could result in unrealistically high values. An example of those cases is the 2010-2011 seismic swarm at the Guy-Greenbrier fault in central Arkansas, US, associated with the disposal of wastewater coming from oil and gas production (Park et al., 2020). The migration of the seismicity cloud along the strike of the fault is displayed in Figure 6.4b. We observe that equation (6.18) predicts that a square-root-of-time pattern due to aseismic slip is also possible (see also section 6.5.2). Specifically, a square-root-of-time pattern corresponds to fluid sources with an approximately constant injection flow rate. If aseismic-slip stress transfer were the mechanism dominating the migration pattern of this kind of seismic swarm, estimates of hydraulic diffusivity α based on the seismicity clouds might be rather related to the quantity $\alpha\lambda^2$, with $\lambda \gg 1$ (see, Sáez et al., 2022, for further details about this particular case).

6.5 Supplemental material

6.5.1 Limiting values of $\mathcal{T}_r$

The limiting values of $\mathcal{T}_r$ are associated with meaningful scenarios. Its minimum value $\mathcal{T}_{\min}$ is given by the maximum possible overpressure at the fluid source, σ'_0. Note that if σ'_0 is surpassed, the fault walls would open (hydraulic fracturing), a condition that we do not intend to explore here. On the other hand, its maximum value $\mathcal{T}_{\max}$ comes from the minimum possible fluid-source overpressure. The latter corresponds to the amount of overpressure that is required to activate fault slip, $\sigma'_0 - \tau_0/f_p$. These two limiting conditions provide the range of possible values for the residual stress-injection parameter:
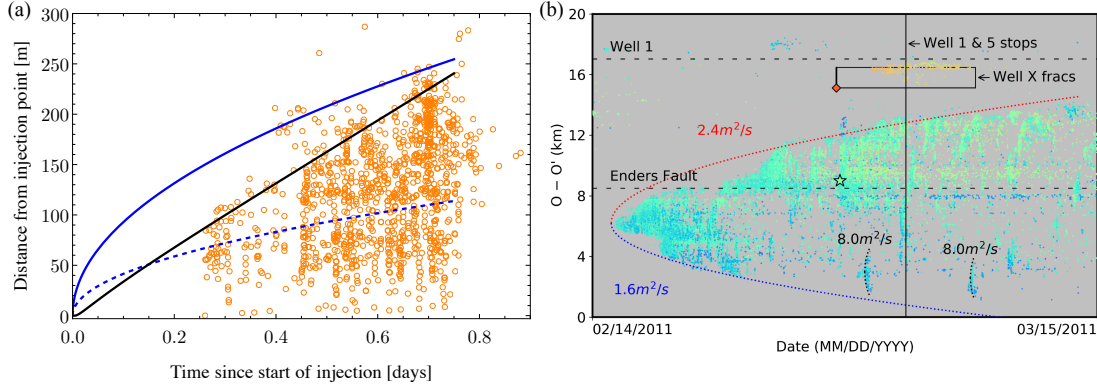
Figure 6.4: (a) Seismicity at the Rittershoffen geothermal site, France (Lengliné et al., 2017). The black solid line is the fitting of the slip front considering a linear injection ramp-up. The blue dashed line corresponds to an overpressure front with $\alpha = 0.05$ m^2/s, and the blue solid line $\alpha = 0.25$ m^2/s. (b) Seismicity at the Guy-Greenbrier fault in central Arkansas, US, associated with the disposal of wastewater coming from oil and gas production. The seismic swarm shows a strong square-root-of-time pattern, yet a relatively high equivalent hydraulic diffusivity (modified from Park et al., 2020).

One can show that $0 < \mathcal{T}_{\min} \leq 1$. The near-zero limit is approached when $\tau_0 \approx f_r \sigma_0'$. This condition corresponds to the so-called nearly unstable limit of slip-weakening faults (Sáez & Lecampion, 2023a). Nearly unstable ruptures are aseismic ruptures that are very close to becoming unstable but will never do. The one limit is, on the other hand, approached when the fault has almost no pre-stress, $\tau_0 \approx 0$. Similarly, one can also show that $0 < \mathcal{T}_{\max} \leq 1$. The near-zero limit is again related to the nearly unstable condition, $\tau_0 \approx f_r \sigma_0'$, whereas the one limit occurs this time when the slip-weakening friction law degenerates into the Coulomb's friction law, $f_r \approx f_p$.

6.5.2   Family of solutions

Given an explicit expression for $\Delta p(s, t)$, equation (6.13) can be used to obtain analytical solutions for λ in the so-called ultimate zero-fracture-energy regime. In fact, under the assumption of a constant friction coefficient, equation (6.13) has been already solved in 2D for ruptures driven by injection at constant overpressure (Bhattacharya & Viesca, 2019) and constant injection rate (Sáez et al., 2022), whereas in 3D, equation (6.13) has been also solved by Sáez et al. (2022) for the same two injection scenarios. These solutions are still valid here, as long as the constant friction coefficient is interpreted as the residual friction value of the slip-weakening model f_r (Sáez & Lecampion, 2023a). Moreover, they are also valid in the early-time Coulomb's friction stage (not examined here, see further details in Sáez and Lecampion, 2023a) with a constant peak friction coefficient f_p.

We complete this set of solutions by including a relevant injection scenario for hydraulic stimulation operations, where the injection rate increases linearly with time. In 3D (axisymmetric

Fluid source	2D - Mode II or III	3D - Mixed mode II+III
$Q(t)$ constant	Early times: $\ell(t) \propto \left(t - \sqrt{t}\right)$ (1) Large times: $\ell(t) \propto t$ (1)	$\ell(t) \propto \sqrt{t}$ (1)
$Q(t) \propto t$	Early times $\ell(t) \propto \left(t^{3/2} - 1\right)/t$ Large times: $\ell(t) \propto t^2$ (2)	Early times: $\ell(t) \propto \sqrt{t}e^{-t}$ (2) Large times: $\ell(t) \propto t$ (2)
$\Delta p(t)$ constant	$\ell(t) \propto \sqrt{t}$ (3)	$\ell(t) \propto t^\beta$ (1)(4)

Table 6.1: Temporal patterns of the rupture front $\ell(t)$ for different modes of propagation and types of fluid source in the zero-fracture-energy regime. (1) Solutions derived by Sáez et al. (2022). (2) Solutions derived here. (3) Solution derived by Bhattacharya and Viesca (2019). (4) β is between 0 and 1/2 (Sáez et al., 2022).

radial flow), the overpressure solution is obtained by convolution

$$\Delta p(s, t) = \int_0^t \frac{dQ(\tau)}{d\tau} G_p(s, t - \tau)d\tau, \tag{6.20}$$

where G_p is the Green's function for overpressure due to a unit rate of injection $Q(t) = 1$, given by $G_p(s, t) = \left(\eta/4\pi k w\right) E_1\left(s^2/4\alpha t\right)$. For linearly increasing rate, $Q(t) = R_q t$, where R_q is the rate of injection rate, the resulting overpressure solution is

$$\Delta p_*(t) = \frac{R_q \eta}{k w} t, \quad \Pi(\xi) = \frac{1}{4\pi}\left[\left(\xi^2 + 1\right)E_1\left(\xi^2\right) - \exp\left(-\xi^2\right)\right]. \tag{6.21}$$

Substituting equation (6.21) into (6.13), we obtain after integration the following implicit equation for λ,

$$1 - \gamma + \frac{2}{9}\left(8 - 3\gamma\right)\lambda^2 + \frac{2}{3}\lambda^2{}_2F_2\left[\begin{array}{cc} 1 & 1 \\ 2 & 5/2 \end{array}; -\lambda^2\right] + \frac{4}{15}\lambda^4{}_2F_2\left[\begin{array}{cc} 1 & 1 \\ 2 & 7/2 \end{array}; -\lambda^2\right]$$
$$- \ln(4\lambda^2) - \frac{4}{3}\lambda^2\ln(2\lambda) = 4\pi\mathscr{T}_r(t), \tag{6.22}$$

where the residual stress-injection parameter takes now the specific form of a dimensionless time: $\mathscr{T}_r(t) = (t/t_c)^{-1}$, with

$$t_c = \frac{f_r \sigma_0' - \tau_0}{f_r R_q \eta/k w} \tag{6.23}$$

a characteristic time that relates to the time of activation of slip.

The solution in 2D can be obtained likewise. We do not report it here because it has limited practical applications. Yet we do report the temporal patterns associated with it in Table 6.1.

6.5.3   Point force-volume relation

Under the assumptions of our model (Sáez et al., 2022; Sáez & Lecampion, 2023a, 2023b), the displacement field induced by the fluid injection into the poroelastic fault zone is irrotational. Therefore, the fluid content ζ relates to the pore-fluid pressure p according to the following local relation (eq. 96, Detournay and Cheng, 1993),

$$\zeta = S\Delta p, \tag{6.24}$$

where S is the so-called oedometric storage coefficient representing the variation of fluid content caused by a unit pore pressure change under uniaxial strain condition (Detournay & Cheng, 1993). S accounts for the effects of fluid, pore, and bulk compressibilities of the fault zone, and is given by

$$S = \frac{1}{M} + \frac{\alpha^2(1-2\nu)}{2(1-\nu)\mu}, \tag{6.25}$$

where M is the Biot's modulus and α the Biot's coefficient. The latter is not to be confused with hydraulic diffusivity.

We recall the definition of ζ which corresponds to the variation of fluid volume per unit volume of porous material. Hence, after integrating the linear relation (6.24) over the entire fault-zone volume $A_{\text{fault}}\,w$, we obtain

$$V(t) = Sw \int_{A_{\text{fault}}} \Delta p(s,t)\mathrm{d}A. \tag{6.26}$$

Note that in our case the fault zone extent is infinite yet for practical purposes, it corresponds to the volume affected by fluid overpressure. By recognizing that the integral in (6.26) is the strength of the point force $\Delta P(t)$ in (6.14), we can write the relation (6.16) in the main text.

7 On the maximum size and moment magnitude of injection-induced slow slip events

A growing body of literature suggests that a significant part of the moment release during subsurface fluid injections is due to aseismic motions. Understanding the size and moment magnitude of injection-induced slow slip events is thus important to better assess the seismic hazard associated with these operations. In this chapter, we present a theoretical estimate based on rupture physics and supported by numerical simulations, for an upper bound of the maximum size and moment magnitude of induced aseismic ruptures. We show that such an upper bound depends strongly on in-situ conditions such as the background stress state and frictional and hydraulic properties of the fault, and scales as a 3/2-power law with the injected volume of fluids, which is notably the only relevant operational parameter in the formula. We gather estimates of moment release due to aseismic slip and injected volumes coming from fluid injections that vary in size from laboratory experiments to industrial applications. Our preliminary results show good agreement between our theoretical estimate and these observations.

This chapter is a modified version of the following scientific article:

Sáez, A. & Lecampion, B. On the maximum size and moment magnitude of injection-induced slow slip events. *In preparation.*

Contributions of Alexis Sáez (CRediT, Contributor Roles Taxonomy)

Conceptualization, Methodology, Software, Validation, Formal analysis, Investigation, Writing - Original Draft, Visualization, Funding acquisition.

7.1 Introduction

Subsurface fluid injections have been long recognized to increase the risk of inducing earthquakes (Healy et al., 1968). While most of the time these earthquakes are harmless micro-

seismicity, they can sometimes be of a relatively large magnitude which poses a serious hazard for the geo-energy industry. Some examples of subsurface engineering technologies facing this issue are the disposal of wastewater from oil and gas activities (Yeck et al., 2017), the development of enhanced geothermal systems (Ellsworth et al., 2019), and hydraulic fracturing of unconventional oil and gas reservoirs (Bao & Eaton, 2016). The disposal of oil wastewater has induced, for instance, some of the largest injection-induced earthquakes in the US, namely, the Prague M_w 5.7 earthquake in 2011 (Keranen et al., 2013), and the Pawnee M_w 5.8 earthquake in 2016 (Yeck et al., 2017). On the other hand, the development of an enhanced geothermal system in Pohang, South Korea, induced in 2017 a M_w 5.5 earthquake which led to the shutdown of the project (Ellsworth et al., 2019), whereas hydraulic fracturing operations in Canada have induced earthquakes of magnitudes of up to 4.6 (Babaie Mahani et al., 2017; Babaie Mahani et al., 2019).

Subsurface fluid injections can induce not only earthquakes but also slow, aseismic slip events. This has been known since the 1960s when a slow surface fault rupture was causally linked to fluid injection operations of an oil field in LA (Hamilton & Meehan, 1971). Since then, a growing number of studies have either inferred or directly measured episodes of injection-induced aseismic slip during large-scale fluid injections in the field (Scotti & Cornet, 1994; Cornet et al., 1997; Bourouis & Bernard, 2007; Wei et al., 2015; Eyre et al., 2019), in-situ experiments (Guglielmi et al., 2015; Cappa et al., 2022), and laboratory experiments (Passelègue et al., 2020; Cebry et al., 2022). Moreover, the largest "earthquake" induced by hydraulic fracturing operations in Canada is, to this day, a slow slip event of magnitude 5.0 (Eyre et al., 2022), which is comparable to the largest injection-induced earthquakes. Releasing elastic strain energy through aseismic rather than seismic slips during industrial fluid injections is, in most cases, preferable to avoid hazardous elastodynamic waves. Understanding what leads to one mode of fault sliding or the other and the factors controlling the maximum size and moment release of these human-induced fault ruptures is crucial to better assess the seismic hazard associated with fluid injection operations.

In particular, the relation between operational fluid-injection parameters and the maximum magnitude of induced earthquakes is an active area of research (McGarr, 2014; van der Elst et al., 2016; Galis et al., 2017; Li et al., 2021). Essentially, one would like to know what are the consequences of using a certain injection protocol in the seismic hazard associated with that operation. Current approaches to estimating the moment release due to fluid injections either neglect aseismic slips (McGarr, 2014; van der Elst et al., 2016; Galis et al., 2017) or do not incorporate rupture physics (McGarr & Barbour, 2018). The latter leads to estimates that are insensitive to the background stress state of a fault which is known to control the elastic energy available for rupture growth and thus the dynamics of aseismic ruptures (Garagash & Germanovich, 2012; Sáez et al., 2022). Building up on our previous studies (Sáez et al., 2022; Sáez & Lecampion, 2023a, 2023b), we derive a theoretical upper bound of the maximum size and moment magnitude of injection-induced slow slip events. We show that such an upper bound depends on only one operational parameter: the accumulated volume of injected fluids. Nonetheless, it also depends strongly on in-situ conditions, namely, the background
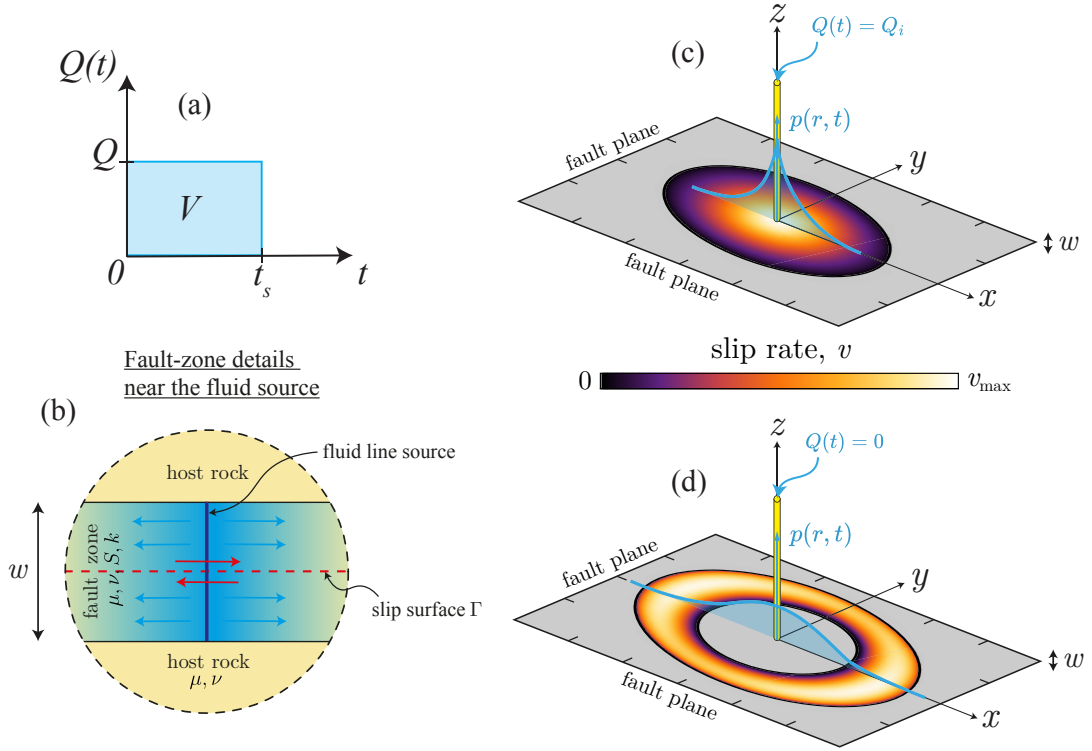
Figure 7.1: Summary of fault response during and after fluid injection. (a) Fluid is injected at a constant rate Q until $t = t_s$ at which the injection is instantaneously stopped. (b) Details of the fault zone near the fluid source. (c) Crack-like rupture during the pressurization stage. (d) Pulse-like rupture during the depressurization stage.

stress state and frictional and hydraulic properties of the fault. We gather estimates of moment release due to aseismic slip and injected volumes coming from fluid injections that vary in size from laboratory experiments to industrial applications. These observations are in good agreement with our physics-based scaling relation.

7.2   Results

7.2.1   Model

We consider aseismic ruptures nucleated by a localized increase of pore-fluid pressure due to the direct injection of fluids into a permeable fault zone (Figure 7.1b). We begin by examining a fluid injection conducted at a constant rate Q over a finite period of time t_s, followed by a sudden stop of the injection (Figure 7.1a). This results in two distinct injection stages: a pressurization or continuous-injection stage, and a depressurization or shut-in stage; which allows for investigating ruptures in all its stages, from nucleation to arrest (Sáez & Lecampion, 2023b). We consider a planar infinite fault obeying a slip-weakening friction law. The host rock is considered as purely elastic, and impermeable at the relevant time scales of the injection.

The resulting displacement field due to the fluid injection is irrotational (Marck et al., 2015). Fluid flow within the fault zone is then governed by an axisymmetric linear diffusion equation (Detournay & Cheng, 1993). This hydro-mechanical model has been investigated in detail by ourselves in a prior work (Sáez & Lecampion, 2023a), which is itself an extension to three dimensions of the two-dimensional plane-strain model of Garagash and Germanovich (2012). Here, we focus on the case of ruptures that are unconditionally stable or aseismic (Garagash & Germanovich, 2012; Sáez & Lecampion, 2023a). In particular, the uniform background shear stress τ_0 must be lower than the in-situ residual fault strength $f_r \sigma_0'$, where f_r is the residual (dynamic) friction coefficient and σ_0' is the uniform initial effective normal stress. We assume that τ_0 and σ_0' are the result of long-term tectonic loading. As shown recently by Sáez and Lecampion (2023a), under these conditions, unconditionally stable ruptures evolve always between two similarity solutions, one at early times where the fault interface behaves as being governed by a constant friction coefficient equal to the peak (static) value f_p, and the other one at late times where the fault interface behaves to leading order as if it were governed by a constant residual friction coefficient f_r and negligible fracture energy $G_c \approx 0$. The late-time solution, which is the ultimate asymptotic regime of any rupture, is an upper bound for the rupture size during the entire lifetime of the event, as it predicts the largest possible rupture extent at any given time since the start of the injection.

7.2.2   Maximum size of injection-induced slow slip events

To keep the analytical derivations tractable, we approximate the rupture as being circular. Strictly speaking, this is valid only when the Poisson's ratio $v = 0$. Nevertheless, we quantify the effect of rupture non-circularity when $v \neq 0$ through numerical calculations. During the pressurization stage ($t < t_s$), the axisymmetric overpressure $\Delta p(r, t) = p(r, t) - p_0$, with p_0 the uniform initial pore pressure, is given by $\Delta p(r, t) = \Delta p_* \cdot E_1 \left(r^2 / 4\alpha t \right)$, where $\Delta p_* = Q\eta / 4\pi k w$ is the intensity of the injection with units of pressure, η is the fluid dynamic viscosity, and $k w$ and α are the fault hydraulic transmissivity and diffusivity, respectively. As stated previously, an upper bound for the rupture radius R comes from assuming that the rupture surface operates at a constant residual friction coefficient with zero fracture energy. Under these conditions, the evolution of the rupture radius is governed by an energy balance of the Griffith's type (Sáez & Lecampion, 2023a):

$$\frac{2}{\sqrt{\pi}} \frac{f_r \Delta p_*}{\sqrt{R}} \int_0^R \frac{E_1 \left(r^2 / 4\alpha t \right)}{\sqrt{R^2 - r^2}} r \, \mathrm{d}r = \frac{2}{\sqrt{\pi}} \left[f_r \sigma_0' - \tau_0 \right] \sqrt{R}. \tag{7.1}$$

According to this energy balance, the fluid-injection integral term of the left-hand side whose stress scale is $f_r \Delta p_*$ supplies elastic energy for the rupture to grow while continuously reducing the fault strength. Conversely, in the absence of a local dissipation mechanism as the fracture energy, the term of the right-hand side $\sim (f_r \sigma_0' - \tau_0) \sqrt{R}$, non-local in nature, is responsible alone for resisting rupture advancement. The previously assumed condition $\tau_0 < f_r \sigma_0'$ is then essential to ensure the stability of the rupture, as otherwise the quasi-static energy balance has ultimately no solution (Sáez & Lecampion, 2023a), that is, a run-away

dynamic rupture occurs (Garagash & Germanovich, 2012; Galis et al., 2017; Sáez & Lecampion, 2023a). The competition between both 'energy' terms in (7.1) is quantified by one single dimensionless number, the so-called residual stress-injection parameter (Sáez & Lecampion, 2023a),

$$\mathcal{T}_r = \frac{f_r \sigma_0' - \tau_0}{f_r \Delta p_*}. \tag{7.2}$$

Intuitively, one expects that the smaller the negative stress 'drop' $f_r \sigma_0' - \tau_0$, the less opposition the rupture has to grow, whereas the higher the intensity of the injection $f_r \Delta p_*$, the faster the rupture would propagate. Hence, decreasing values of $\mathcal{T}_r$ will always result in faster aseismic ruptures. Equation (7.1) admits analytical solution in the form (Sáez et al., 2022),

$$R(t) = \lambda (\mathcal{T}_r) \cdot L(t), \tag{7.3}$$

where λ is the so-called amplification factor (Bhattacharya & Viesca, 2019), and $L(t) = \sqrt{4\alpha t}$ is the classical diffusion length scale, also taken as the nominal position of the overpressure front . Owing to self-similarity, λ is time-invariant and depends only on the parameter $\mathcal{T}_r$. This analytical solution (Figure 7.2a) was derived first by Sáez et al. (2022) for an interface with constant friction, which is notably valid for our upper-bound solution as long as the constant friction coefficient is replaced by f_r. Figure 7.2a provides deep insights. When $\mathcal{T}_r \ll 1$, aseismic ruptures break regions much further away than the pressurized fault zone, $\lambda \gg 1$. This is the so-called nearly unstable regime (Sáez & Lecampion, 2023a) as when $\tau_0 \rightarrow f_r \sigma_0'$ the rupture approaches the ultimate stability condition. Conversely, when $\mathcal{T}_r \sim 10$, aseismic ruptures are confined well within the overpressurized region, a regime known as marginally pressurized because it relates to a scenario in which the fluid injection provides just the minimum amount of overpressure that is sufficient to activate fault slip (Garagash & Germanovich, 2012; Sáez & Lecampion, 2023a).

Upon the stop of the fluid injection ($t > t_s$), pore-fluid pressure drops quickly near the fluid source while it keeps increasing away from it (Figure 7.1d). This latter increase is what further drives the propagation of aseismic ruptures after shut-in. Since we want to provide an upper bound for the rupture size, we adopt the simplifying assumption of neglecting the fracture energy and assume that slip propagates at a constant residual friction value f_r. The propagation and arrest of aseismic slip in a constant-friction fault have been extensively investigated (Sáez & Lecampion, 2023b). In this model, ruptures transition from a crack-like propagation style during the pressurization stage (Figure 7.2c) to a pulse-like mode after shut-in (Figure 7.2d). Furthermore, based on the analysis of Sáez and Lecampion (2023b), one can readily show here that the propagation of the slip pulses in our upper-bound configuration is controlled by the same dimensionless number that controls crack-like propagation during the pressurization stage, $\mathcal{T}_r$. This is shown in Figure 7.2b for an exemplifying case displaying the evolution of the locking and rupture fronts for a circular rupture. Slip arrests when the locking front catches the rupture front. Although perhaps more insightfully, the rupture front stops when it is caught by the so-called pore-pressure back front (Sáez & Lecampion, 2023b). This latter means that
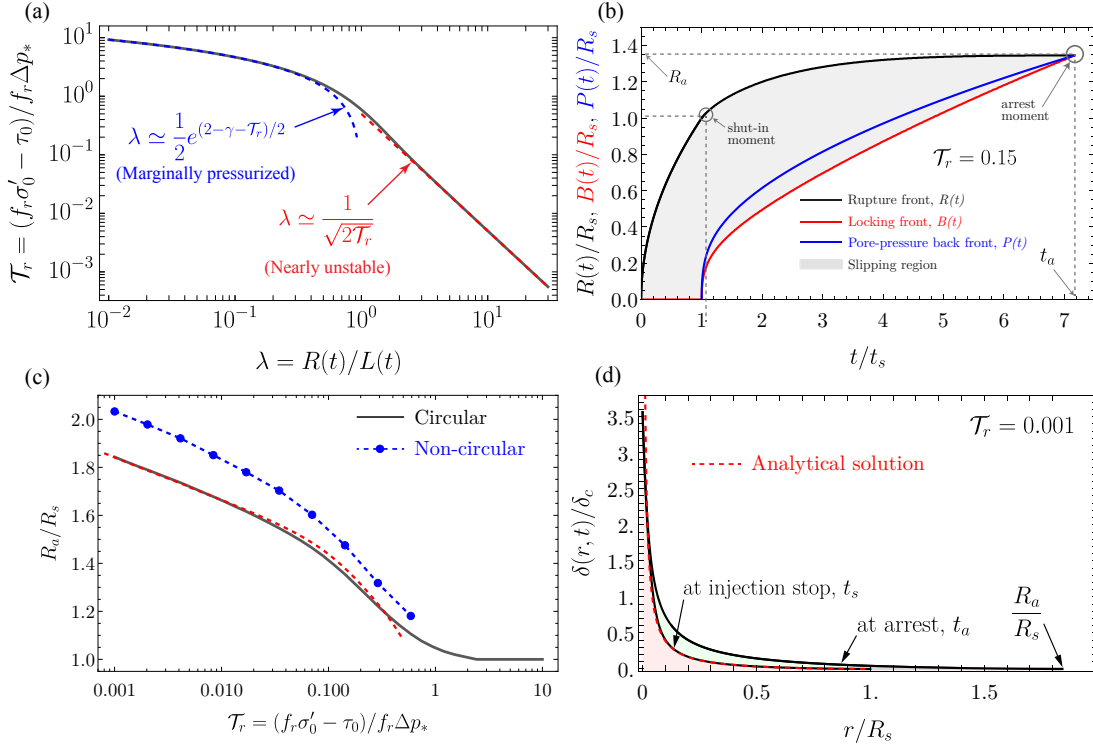
Figure 7.2: An upper bound for the maximum size of injection-induced slow slip events. (a) Amplification factor as a function of the residual stress-injection parameter $\mathcal{T}_r$. Blue and red dashed lines correspond to asymptotic limiting behaviors for small and large λ. (b) Normalized position of the relevant fluid and slip fronts as a function of normalized time. (c) Maximum run-out distance as a function of the parameter $\mathcal{T}_r$. Non-circular solutions is for a Poisson's ratio $\nu = 0.25$. (d) Normalized slip distribution at the moment the injection stops, and at the moment the rupture arrests.

there is no further increase of pore pressure within the rupture pulse that can ever sustain the propagation of slip. This, in addition to the energy balance (7.1) expressed at the time of arrest t_a, provides a complete physical understanding of how, when, and where injection-induced aseismic ruptures arrest.

The residual stress-injection parameter $\mathcal{T}_r$, injection duration t_s, and fault hydraulic diffusivity α, control the upper bound for the arrest time t_a and maximum rupture run-out distance R_a (Figure 7.2c). When ruptures are marginally pressurized ($\mathcal{T}_r \sim 10$), the slip pulses arrest almost immediately after the injection stops. Conversely, when ruptures are nearly unstable ($\mathcal{T}_r \ll 1$), they are predicted to propagate for several orders of magnitude the injection duration and grow up to approximately twice the size of the ruptures at the moment the injection stops. The effect of a Poisson's ratio $\nu \neq 0$ is such that it slightly increases both the arrest time and maximum rupture run-out distance (Figure 7.2c). Furthermore, in the nearly unstable regime that produces the largest ruptures, these upper-bound quantities can be estimated simply as (Sáez & Lecampion, 2023b):

$$\frac{t_a}{t_s} \approx a\mathcal{T}_r^{-b}, \quad \text{and} \quad R_a \approx \left[4\alpha t_a \left(\frac{t_a}{t_s} - 1 \right) \ln \left(\frac{t_a}{t_a - t_s} \right) \right]^{1/2}, \tag{7.4}$$

in the circular rupture case, with $a = 0.946876$ and $b = 1.084361$. Equations (7.2) and (7.4) show that the arrest time and maximum size of aseismic ruptures are controlled by the following factors: (i) how close to the background shear stress τ_0 the in-situ residual strength of the fault $f_r \sigma_0'$ drops, (ii) how intensively the fluid injection is conducted according to Δp_*, (iii) how long the duration of the injection t_s is, and (iv) how large the fault hydraulic diffusivity α is. Moreover, the contribution of the depressurization stage to the maximum run-out distance is approximately a factor of two at most. The order of magnitude of the maximum size is given by the rupture radius, equation (7.3), evaluated at the moment the injection stops.

7.2.3   Maximum magnitude of injection-induced slow slip events

The scalar moment release M_0 at a given time t is given by (Aki & Richards, 2002),

$$M_0(t) = \mu \iint_{A_r(t)} \delta(x, y, t) \mathrm{d}x \mathrm{d}y, \tag{7.5}$$

where μ is the bulk shear modulus, δ is the current slip distribution, and A_r is the current rupture surface. In the pressurization stage ($t < t_s$), an upper bound for the spatiotemporal evolution of fault slip can be obtained analytically for the end-member cases of nearly unstable and marginally pressurized ruptures (see Section 7.4.1). To highlight how significant is to analyze the end-member cases, we note that their asymptotes for the rupture radius nearly overlap and thus quantify together almost any rupture scenario (Figure 7.2a). The slip distribution of nearly unstable ruptures is remarkably peaked around the injection point (Figure 7.2d). Its analytical solution is indeed singular at the injection point; a boundary layer must be resolved at distances $r \sim L(t)$ (Garagash & Germanovich, 2012). Although this
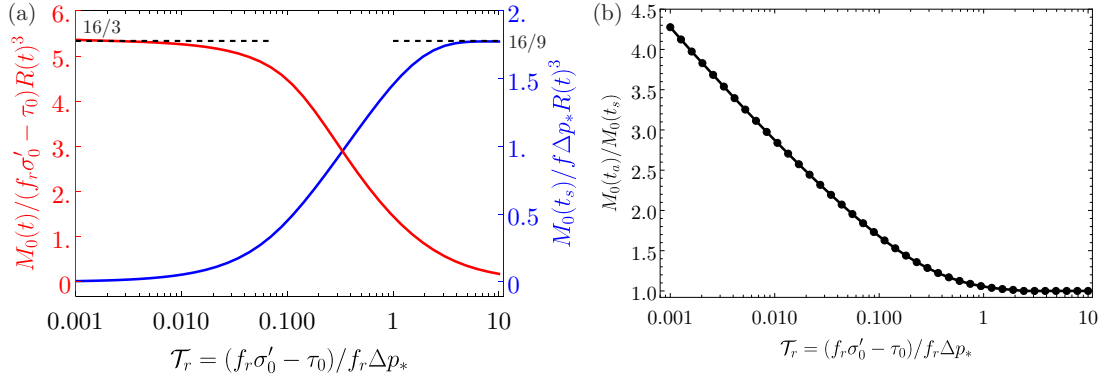
Figure 7.3: An upper bound for the moment release of injection-induced slow slip events. (a) Normalized moment release during the pressurization stage as a function of the parameter $\mathcal{T}_r$ for nearly unstable ruptures (red) and marginally pressurized ruptures (blue). Dashed lines correspond to asymptotic analytical solutions. Solid lines correspond to full numerical solutions. (b) Normalized moment release during the depressurization stage as a function of the parameter $\mathcal{T}_r$.

boundary layer has no consequences in estimating the moment release. After integration of the slip profiles, equation (7.5) leads to an upper bound for the moment release M_0 at a given time $t \leq t_s$ as,

$$M_0(t) \simeq \begin{cases} \frac{16}{3}\left(f_r \sigma_0' - \tau_0\right) R(t)^3 & \text{for nearly unstable ruptures, } \mathcal{T}_r \ll 1, \\ \frac{16}{9} f_r \Delta p_* R(t)^3 & \text{for marginally pressurized ruptures, } \mathcal{T}_r \sim 10, \end{cases} \tag{7.6}$$

with $R(t)$ known analytically from equation (7.3). Owing to self-similarity, the normalized moment release depends uniquely on the parameter $\mathcal{T}_r$ for circular ruptures. We compare the previous analytical estimates for M_0 (dashed lines) against the full numerical solution of the upper-bound model (solid lines) in Figure 7.3a.

To make the link between the moment release M_0 and the operational parameters of the fluid injection, namely, the injection rate and injection duration (one could alternatively choose the injected volume $V(t) = Qt$ in replacement of one of the other parameters), we use the asymptotes for λ (Figure 7.2a) plus equation (7.3) to recast equation (7.6) as

$$M_0(t) = A \cdot V(t)^{3/2}, \quad \text{with} \quad A = \begin{cases} \frac{16}{3\sqrt{f_r \sigma_0' - \tau_0}}\left(\frac{f_r}{wS}\right)^{3/2} & \text{for } \mathcal{T}_r \ll 1, \\ \frac{32}{9\pi} \frac{f_r \eta}{kw} \frac{\lambda^3 \alpha^{3/2}}{Q^{1/2}} & \text{for } \mathcal{T}_r \sim 10. \end{cases} \tag{7.7}$$

It is interesting that in the marginally pressurized regime ($\mathcal{T}_r \sim 10$), the moment release depends on the injected volume (or injection duration) and the injection rate, whereas in the nearly unstable regime ($\mathcal{T}_r \ll 1$) which is the case that produces the largest ruptures, the only operational parameter that controls the moment release is the current injected volume.

In the depressurization stage ($t > t_s$), the propagation and ultimate arrest of the aseismic pulses result in a further accumulation of fault slip as exemplified in Figure 7.2d, and thus an increase in the final moment release and magnitude of the events. Again, an upper bound for the further accumulation of slip can be calculated by neglecting the fracture energy. By dimensional considerations, one can readily show that such a contribution of the depressurization stage to the final moment release as quantified by the ratio $M_0(t_a)/M_0(t_s)$, depends only on the residual stress-injection parameter $\mathcal{T}_r$ plus a small correction due to non-circularity when $\nu \neq 0$. We calculate this contribution numerically (Figure 7.3b). The final moment release is at most 4 times the moment release at the moment the injection stops in the more nearly unstable cases (smallest values of $\mathcal{T}_r$). Moreover, the moment magnitude can be calculated from the moment release evaluated at the time of arrest t_a as (Hanks & Kanamori, 1979),

$$M_w = \frac{2}{3}\log_{10}(M_0) - 6.07. \tag{7.8}$$

7.2.4 Generalization to an arbitrary history of injection rate

By analyzing the particular and insightful case of injection at a constant volume rate in the previous sections, we developed a time-dependent upper bound for the rupture size and moment release that accounts for the entire lifetime of injection-induced slow slip events, from nucleation to arrest. An important characteristic of this model is that aseismic ruptures can grow much further away than the fluid-pressurized region ($\lambda \gg 1$) or be well confined within it ($\lambda \ll 1$). An aseismic rupture that breaks non-pressurized fault regions is a possibility that always emerges when incorporating rupture physics (Garagash & Germanovich, 2012; Sáez & Lecampion, 2023a), even in the absence of frictional weakening owing to simple long-range elastostatic stress transfer effects (Bhattacharya & Viesca, 2019; Sáez et al., 2022). Such a regime has been observed in laboratory experiments (Cebry et al., 2022), inferred to have occurred in in-situ experiments (Guglielmi et al., 2015; Bhattacharya & Viesca, 2019) and field cases (Eyre et al., 2019). It seems likely that the slow slip events that have been detected so far belong to this regime, as not only the ruptures of the largest extent are predicted to occur under such conditions but also the greater amount of slip. Nearly unstable ruptures ($\mathcal{T}_r \ll 1$, $\lambda \gg 1$) seem then to provide the upper bound of most practical interest. In this section, we generalize such an upper bound to account for a history of injection flow rate that is arbitrary.

When ruptures are nearly unstable, because the slip front largely outpaces the overpressure front, the reduction of strength due to fluid injection can be approximated as a point force,

$$f_r \Delta p(r,t) \approx f_r \Delta P(t)\frac{\delta^{\text{dirac}}(r)}{2\pi r}, \quad \text{with} \quad \Delta P(t) = 2\pi \int_0^\infty \Delta p(r,t)r\,\mathrm{d}r, \tag{7.9}$$

whose strength $\Delta P(t)$ relates to the current volume of injected fluid as (see Chapter 6, Section 6.2.7)

$$\Delta P(t) = \frac{V(t)}{Sw}, \tag{7.10}$$

where S is the so-called oedometric storage coefficient representing the variation of fluid content caused by a unit pore pressure change under uniaxial strain condition (Detournay & Cheng, 1993), and w is the fault zone width. S is given by equation (6.25) and it accounts for the effects of fluid, pore, and bulk compressibilities in the fault zone. Evaluating the double integral (7.16) (see Section 7.4.1) prior substitution of (7.17), (7.9), (7.10), leads to

$$\delta(r,t) = \frac{4}{\pi} \frac{\left(f_r \sigma_0' - \tau_0 \right)}{\mu} R(t) \left[\frac{1}{2\mathscr{T}_r^*} \frac{V(t)}{w\pi R(t)^2} \frac{\arccos(\bar{r})}{\bar{r}} - \sqrt{1-\bar{r}^2} \right]. \tag{7.11}$$

The condition that the rupture propagates with no stress singularity along its front (Barenblatt, 1962)

$$\lim_{r \to R^-} \frac{\partial \delta(r,t)}{\partial r} \sqrt{R-r} = 0, \tag{7.12}$$

requires that

$$R(t) = \left[\frac{V(t)}{2\pi w \mathscr{T}_r^*} \right]^{1/2}, \tag{7.13}$$

which is an alternative way of deriving equation (6.18) in Chapter 6. Furthermore, substituting (7.13) into (7.11) one obtains

$$\delta(r,t) = \frac{4}{\pi} \frac{\left(f_r \sigma_0' - \tau_0 \right)}{\mu} \left[\frac{\arccos(\bar{r})}{\bar{r}} - \sqrt{1-\bar{r}^2} \right] \left[\frac{V(t)}{2\pi w \mathscr{T}_r^*} \right]^{1/2}. \tag{7.14}$$

Finally, we can calculate the moment release (7.5) as a function of the injected volume. After integration, we obtain

$$M_0(t) = \frac{16}{3} \left(f_r \sigma_0' - \tau_0 \right) \left[\frac{V(t)}{2\pi w \mathscr{T}_r^*} \right]^{3/2}, \tag{7.15}$$

which is identical to equation (7.7) when $\mathscr{T}_r \ll 1$ if we substitute $\mathscr{T}_r$ given by equation (7.2).

7.3   Discussion

Our results provide upper-bound estimates for the maximum size and moment magnitude of injection-induced slow slip events that are either confined to the pressurized region or grow much further away than that. The latter scenario seems to be the more relevant practically. However, so far the only existing estimate for the moment release accounting for aseismic slip is based on assumptions that the rupture is confined within the pressurized region (McGarr & Barbour, 2018). McGarr and Barbour (2018) proposed indeed a linear relation between the cumulative moment release and V, which differs importantly from our 3/2-power law scaling. To test their relation, they considered two data points of aseismic moment release and injected volume in their study. One was related to the in-situ experiments by Guglielmi et al. (2015), and the other one estimated from laboratory experiments of hydraulic fracturing
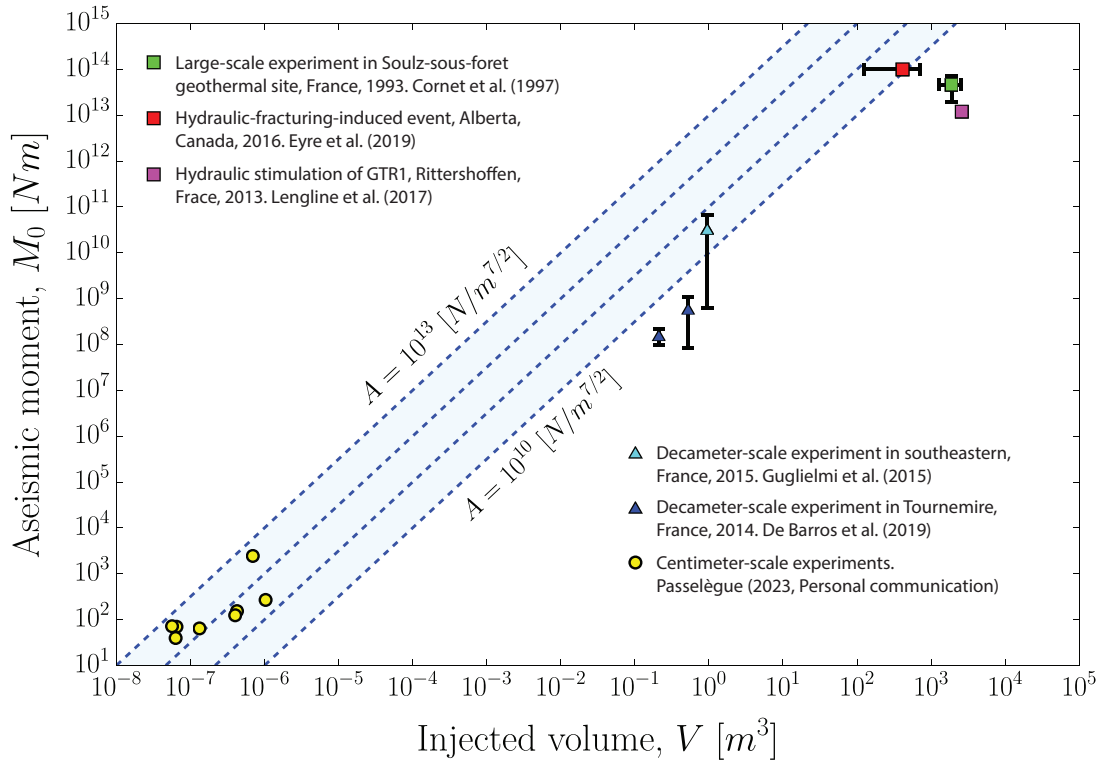
Figure 7.4: Preliminary comparison of the theoretical upper bound for the moment release due to aseismic slip for 4 values of the pre-factor A, with data points from volumes of different sizes ranging from laboratory experiments to large fluid injections in the field (references in the plot).

(Goodfellow et al., 2015). However, the physics of hydraulic fracturing (Detournay, 2016) differs significantly from its shear rupture counterpart. Indeed, one can readily show that the moment release by hydraulic fractures scales linearly with the injected volume as the integral of the fracture width over the crack area is equal to the fracture volume. Assuming that the injected fluid fulfills such a volume in a hydraulic fracture, equation (7.5) implies that $M_0 \propto V$ in that case. We therefore keep the one point by Guglielmi et al. (2015) but discard the hydraulic-fracturing data point as it corresponds to a different problem. In order to test our upper-bound estimate, we collect additional data from available information coming from laboratory and in-situ experiments, as well as large-scale fluid injections in the field. Our preliminary results are shown in Figure 7.4 together with the upper bound estimate, equation (7.7) for $\mathscr{T}_r \ll 1$, for four values of the factor A considering realistic parameters for it. The comparison with observations is an ongoing work. We are currently gathering more data points to be included in Figure 7.4.

7.4   Supplementary material

7.4.1   Slip profiles for nearly unstable and marginally pressurized ruptures

Consider the quasi-static elastic equilibrium that relates the fault slip distribution δ to the change of shear stress $\Delta\tau$ within an axisymmetric circular shear crack (Sneddon, 1951):

$$\delta(r,t) = \frac{4R(t)}{\pi\mu} \int_{\bar{r}}^{1} \frac{\xi\,\mathrm{d}\xi}{\sqrt{\xi^2 - \bar{r}^2}} \int_{0}^{1} \frac{\Delta\tau(s\xi R(t),t)\,s\,\mathrm{d}s}{\sqrt{1-s^2}}, \tag{7.16}$$

where $\bar{r} = r/R(t)$ is the normalized radial coordinate. In the limiting regime of a rupture propagating with zero fracture energy and at the residual friction level which provides the upper bound for the moment release, the change of shear stress is simply

$$\Delta\tau(r,t) = \tau_0 - f_r\left[\sigma_0' - \Delta p(r,t)\right] = \tau_0 - f_r\sigma_0' + f_r\Delta p(r,t). \tag{7.17}$$

For injection at a constant volume rate, the slip profiles for the end-member cases of nearly unstable and marginally pressurized ruptures can be calculated following the procedure of Sáez et al. (2022) as long as we interpret their constant friction coefficient as f_r. An upper bound for the spatiotemporal evolution of slip is then,

$$\delta(r,t) \simeq \frac{\sqrt{8}}{\pi} \frac{f_r\Delta p_*}{\mu} L(t)\sqrt{\mathcal{T}_r} \left[\frac{\arccos(\bar{r})}{\bar{r}} - \sqrt{1-\bar{r}^2}\right], \tag{7.18}$$

for nearly unstable ruptures ($\mathcal{T}_r \ll 1$), and

$$\delta(r,t) \simeq \frac{8}{\pi} \frac{f_r\Delta p_*}{\mu} R(t) \left[\sqrt{1-\bar{r}^2} - \bar{r}\cdot\arccos(\bar{r})\right], \tag{7.19}$$

for marginally pressurized ruptures ($\mathcal{T}_r \sim 10$). Integration of the previous slip profiles over the rupture area leads to the asymptotes for the moment release M_0 during the pressurization stage, equation (7.6).

8 Conclusions

8.1 Summary

This doctoral thesis investigated the mechanics of three-dimensional fluid-driven frictional ruptures and their implications for the phenomenon of injection-induced seismicity —a critical concern in the geo-energy industry. Below, we summarize the main findings and conclusions of our research.

We examined the propagation of fluid-driven stable frictional ruptures using minimal physical ingredients to reproduce such a phenomenon, including a constant friction coefficient at a single planar fault interface. We considered fluid injections conducted at a constant volumetric rate and a constant overpressure. We found that a dimensionless number equal to the ratio between the stress criticality or distance to failure under ambient conditions and the intensity of the fluid injection controls the dynamics of the interfacial ruptures. Insightful self-similar and non-self-similar analytical solutions for the particular case of circular ruptures which occur in the limit of a Poisson's ratio equal to zero were derived, whereas the more general case of non-circular ruptures was solved via numerical calculations. Two end-member regimes were identified, namely, critically stressed faults that are about to fail (slide) before the injection starts, and marginally pressurized faults that are characterized by an injection that provides just the minimum amount of fluid pressure required to activate fault slip. Critically stressed faults produce ruptures that expand much further away than the fluid-pressurized region. Conversely, marginally pressurized faults host ruptures that are well confined within the diffusively expanding region affected by the pressurization of pore fluids. We determined the equilibrium shape of fluid-driven aseismic ruptures which were found to be quasi-elliptical. The ruptures are more elongated for increasing values of the Poisson's ratio and, perhaps more interestingly, for faults that are closer to the critically stressed regime. This, our first investigation, provided for the first time a basic understanding of how injection-induced aseismic ruptures propagate in a fully three-dimensional configuration.

By extending our previous hydro-mechanical model to account for a shut-in period or stop of the fluid injection, we found that aseismic slip not only keeps propagating after shut-in but

191

also develops a in very distinct mode: as a pulse of slip. The conditions determining the propagation in pulse-like mode and, more importantly, the conditions determining when and where exactly fluid-driven aseismic ruptures arrest, were fully established. The same dimensionless number identified during the continuous injection stage in our first investigation was found to control the dynamics of the aseismic slip pulses. In particular, we found that marginally pressurized faults produce ruptures that arrest almost immediately upon shut-in, whereas critically stressed faults host ruptures that can propagate for several orders of magnitude the injection duration and reach up to approximately twice the size of the ruptures at the moment that the injection stops. We consequently argue that the persistent stressing of increasingly larger rock volumes caused by post-injection aseismic slip is a plausible mechanism for the triggering of post-injection seismicity. Seismicity after shut-in is a critical concern in the geo-energy industry, as a growing number of cases show that the stop of fluid injection activities does not necessarily guarantee the cessation of seismicity. Furthermore, it is not rare that the largest events of injection-induced seismic sequences occur in the post-injection stage. Using field observations of post-injection-induced seismicity, we elaborated via theoretical arguments and numerical calculations on the characteristics of this triggering mechanism and found quantitative agreement between our model and field observations.

We then extended our former constant-friction fault model to account for a friction coefficient that weakens with slip. This enabled the model to develop a proper cohesive zone besides incorporating a finite amount of fracture energy, both ingredients absent in the former model. To do so, we considered two friction laws characterized by a linear and an exponential weakening of friction respectively. We focused on the particular case of axisymmetric circular shear ruptures as they were found in our previous investigations to capture the most essential aspects of the dynamics of unbounded ruptures in three dimensions. It was shown that fluid-driven aseismic slip can occur in two distinct modes in this model: as an interfacial rupture that is unconditionally stable, or as the quasi-static nucleation phase of an otherwise dynamic rupture. The conditions determining whether the interface slides in one way or the other were fully established. For ruptures that are unconditionally stable, we found that fault slip undergoes four distinct stages in time. Initially, ruptures are self-similar in a diffusive manner and the fault interface behaves as if it were governed by a constant friction coefficient equal to the peak (static) friction value. Slip then accelerates due to frictional weakening while the cohesive zone develops. Once the latter gets properly localized, a finite amount of fracture energy emerges along the interface, and the rupture dynamics is governed by an energy balance of the Griffith's type. We showed that in this stage, fault slip always transitions from a large-toughness to a small-toughness regime due to the diminishing effect of the fracture energy in the near-front energy budget as the rupture grows. Moreover, while slip grows likely confined within the pressurized region in prior stages, here the rupture front can largely outpace the pressurization front if the fault is close to the stability limit. Ultimately, self-similarity is recovered and the fault behaves again as possessing a constant friction coefficient, but this time equal to the residual (dynamic) friction value. It was shown that in this ultimate regime, the fault interface operates to leading order with zero fracture energy.

On the other hand, when aseismic slip propagates as the nucleation phase of a dynamic rupture, fault slip also initiates in a self-similar manner and the interface operates at a constant peak friction coefficient. The maximum size that aseismic ruptures can reach before becoming unstable (inertially dominated) was found to be as small as a critical nucleation radius equal to the shear modulus divided by the slip-weakening rate, and as large as infinity when faults are close to the stability limit. The former case corresponds to faults that are critically stressed before the injection starts, in which case ruptures always expand much further away than the pressurized region. The larger the critical nucleation radius is with regard to the cohesive zone size, the longer ruptures can accelerate aseismically before becoming unstable. When the nucleation radius is smaller than the cohesive zone size, aseismic ruptures accelerate upon departing from the self-similar response due to continuous frictional weakening over the entire slipping region, undergoing nucleation unaffected by the residual fault strength. Conversely, when the nucleation radius is (much) larger than the cohesive zone size, aseismic ruptures transition towards a stage controlled by a front-localized energy balance and undergo nucleation in a 'crack-like' manner. We provided analytical and numerical solutions for the problem solved over its full dimensionless parameter space, as well as expressions for relevant length and time scales characterizing the transition between different stages and regimes. In this more comprehensive picture of injection-induced fault slip, we notably found that our former constant-friction model is an asymptotic solution that emerges at both early and late times of the fluid injection, where the constant friction coefficient is either the peak or residual friction value respectively.

Since we realized very early in our research that the temporal patterns of aseismic slip growth were strongly dependent on the boundary condition associated with the fluid injection, we investigated the mechanistic origins of this dependence in some important regimes of fault slip propagation. By considering a fairly arbitrary history of injection flow rate, we found that two time-dependent dimensionless numbers, one of them corresponding to a generalization of the dimensionless number found in our first investigation, control the dynamics of unconditionally stable ruptures. Moreover, various properties of aseismic ruptures that were found in the slip-weakening model for injection at a constant volume rate were generalized here for arbitrary histories of injection flow rate. Some of these properties are the transition from a large-toughness to a small-toughness regime and an ultimate asymptotic regime in which the fault interface operates to leading order with zero fracture energy. In the limit in which the rupture surface is much bigger than the fluid-pressurized region, an insightful analytical relation between the position of the slip front and the accumulated volume of injected fluid was found. In this regime, the only parameter of the fluid injection that matters to estimate the position of the slip front is indeed the accumulated volume of injected fluid.

We then used the above findings to develop a theoretical framework for understanding seismic swarms. Seismic swarms are often attributed to be driven by either the diffusion of pore pressure or the propagation of aseismic slip. We proposed a theoretical model in which these two scenarios emerge as end-member solutions of a more general case in which earthquake swarms are driven by a combination of both mechanisms. We considered well-documented

cases of anthropogenic seismic swarms which serve as a natural laboratory to test the theory, as the fluid sources underlying the seismic swarms are relatively well-constrained. We found that a likely general feature of the seismicity clouds is to be driven by pore pressure diffusion at early times of the injection and by stress transfer due to aseismic slip later on. The conditions controlling the transition between both regimes were theoretically established. While in the pore-pressure-driven regime, a square-root-of-time pattern of seismic swarm migration is expected, in the aseismic-slip-driven regime the predicted patterns are strongly connected to the injection flow rate history of the fluid source. Specifically, under the conditions described in the above paragraph, the predicted pattern follows the square root of the current volume of injected fluid. This theoretical prediction was found to be in good agreement with available field observations. Moreover, in the aseismic-slip-driven regime, the migration of the seismicity front is very sensitive to and contains important information on in-situ conditions such as the background stress state. Our model was shown to be notably able to explain seismic swarms with square-root-of-time migration patterns and characterized by unrealistically high hydraulic diffusivities as being driven by aseismic-slip stress transfer, meaning that the underlying fluid source operates at an approximately constant volume rate. We also demonstrated that the back-front of seismicity frequently associated with the termination of fluid injections is a signature that is theoretically expected under the presence of aseismic slip as well.

The moment release (and associated earthquake magnitude) due to subsurface fluid injections is an important parameter for seismic hazard analysis in the geo-energy industry. A growing body of literature suggests that a significant part of the moment release during fluid injections is due to aseismic, rather than seismic motions. The occurrence of predominantly aseismic slip in these operations is indeed considered a highly favorable outcome, as earthquakes of a relatively large magnitude can pose a significant risk to the success of geo-energy projects. Most of the current approaches to estimating the moment release due to fluid injections either neglect the aseismic part or do not incorporate rupture physics. To contribute to filling this gap of knowledge, we built up on all our above investigations to provide a theoretical estimate supported by numerical calculations, for an upper bound of the maximum size and moment magnitude of induced aseismic ruptures. We showed that such an upper bound depends strongly on in-situ conditions such as the background stress state and frictional and hydraulic properties of the fault, and scales as a 3/2-power law with the injected volume of fluids, which is notably the only relevant operational parameter in the formula. We gathered estimates of moment release due to aseismic slip and injected volumes coming from fluid injections that vary in size from laboratory experiments to industrial applications. Our preliminary results show good agreement between our theoretical estimate and available observations.

Finally, we would like to mention that an important contribution of this doctoral research was the development of an efficient numerical solver to simulate frictional slip and fault opening in 3D networks of discontinuities of arbitrary shapes. In our solver, these localized deformations can be driven not only by variations in interfacial fluid pressure as explored in this work but also by total stresses applied either on the discontinuities' faces or the far field. The capabilities of the solver are therefore much more general than what we exploited here.

We expect this scientific output to become a very important tool for future investigations.

8.2 Perspectives

This doctoral research offers for the first time a quantitative and conceptual framework to understand various problems associated with transients of frictional slip induced by either natural or anthropogenic fluid injections in the Earth's crust, arising both in subsurface engineering applications and earthquake science. In addition, our research opens a number of likely fruitful research directions to which we provide some guidelines and perspectives below.

8.2.1 Incorporating further complexities

Incorporating further complexities into the model is an interesting research direction by itself. For instance, all of our models assume that fluid flow occurs within a permeable interface characterized by constant hydraulic properties. It has been however suggested for a long time that variations of effective normal stress may induce permeability changes in fractures (e.g., Witherspoon et al., 1980) and faults (e.g., Rice, 1992). Also, it is known that frictional slip may be accompanied by dilatant (or contracting) fracture/fault-gouge behavior that would inevitably induce changes in fluid flow and thus in the propagation of fault slip (e.g., Ciardo and Lecampion, 2019; Yang and Dunham, 2021). The effect of such hydro-mechanical couplings on the propagation of fault slip remains to be investigated in 3D and requires the solution of a fully-coupled hydro-mechanical problem. In addition, poroelastic effects in the surrounding medium around the fracture/fault may be relevant in some cases (e.g., Heimisson et al., 2022). Accounting for a permeable host rock would notably allow for fluid mass exchange between the slipping region and the bulk, whose effects on the propagation of fault slip remain poorly understood.

In terms of material (e.g., elastic constants and frictional properties) and stress heterogeneities, changes in lithologies as commonly encountered in the upper Earth's crust would certainly alter the dynamics of the otherwise unbounded ruptures that we have examined here. In particular, the effect of layering might cause containment of the reactivated fault surface within certain lithologies thus promoting the development of elongated ruptures, similar to what is observed for hydraulic fractures (Bunger & Lecampion, 2017).

8.2.2 Further applications of the models

In this thesis, we have already explored in detail some of the implications of our modeling results, particularly for the phenomenon of injection-induced seismicity. Yet a much broader range of applications can be potentially investigated. For instance, one could further explore the implications of our models for natural seismic swarms. Unlike the anthropogenic seismic

swarms that we examined here where the fluid source is relatively well-constrained, possible natural sources of fluids activating aseismic and seismic slip during swarm episodes are of course much less constrained. Nevertheless, there are a number of observables that one could consider to make both qualitative and quantitative comparisons with our models, such as (to mention just a few of them) spatial and/or temporal distributions of seismic moment release and stress drops, as well as aseismic slip when, for instance, geodetic data is available to conduct kinematic inversions (e.g., Sirorattanakul et al., 2022; Yukutake et al., 2022; Nishimura et al., 2023). Also, analyzing global scaling relations of seismic swarms may help to better constrain the underlying physical processes.

On the other hand, another interesting phenomena that could be analyzed in light of our results are slow slip events in subduction zones (Bürgmann, 2018). There is general consensus that fluids are involved in the mechanics of slow slip events (Behr & Bürgmann, 2021), with several lines of evidence suggesting that they occur at depths where pore fluids are inferred to be overpressurized up to near lithostatic pressures (Shelly et al., 2006; Kato et al., 2010; Behr & Bürgmann, 2021). The common view is that they initiate as dynamic instabilities in a similar manner to regular earthquakes (e.g., Liu and Rice, 2007), yet a mechanism that prevents the slip rate from reaching levels that would radiate strong seismic waves is invoked (e.g., Segall et al., 2010). An alternative model could consider that slow slip events are not frustrated dynamic instabilities, but rather the result of unconditionally stable sliding. In this view, the driving force that makes them emerge, propagate, and perhaps arrest, is transient episodes of pressurization and depressurization of pore fluids (Warren-Smith et al., 2019; Perez-Silva et al., 2023), which in turn induce episodes of aseismic slip that can propagate much faster than the diffusion of pore pressure. Metamorphic dehydration reactions in the oceanic slab may, for instance, induce hydraulic fractures that could transport fluids at the time scales that are relevant for slow slip events. Fluid flow could be further modulated by spatiotemporal variations of permeability due to fault-valving behavior (Zhu et al., 2020). The characteristics of their seismic signature, so-called tremors and low-frequency earthquakes (Obara, 2002; Katsumata & Kamaya, 2003), could provide important information to constrain such a model, as well as global scaling relations (Ide et al., 2007; Frank & Brodsky, 2019; Michel et al., 2019).

8.2.3 Laboratory experiments

Our results provide a means for characterizing the conditions under which distinct regimes and stages of injection-induced fault slip are expected to emerge not only in the field but also under well-controlled and achievable conditions in the laboratory. Fluid injection experiments where the notion of a finite rupture growing on a simulated interface exists (Passelègue et al., 2020; Gori et al., 2021; Cebry et al., 2022) are particularly promising to investigate and validate the mechanistic understanding we have obtained in this thesis. Our research can help guide the design of these experimental works.

Appendices

A A collocation boundary element method for elastostatic crack problems in three dimensions

A.1 Introduction

In order to solve numerically the boundary integral equations of linear elasticity, the so-called boundary element methods (BEM) have been successfully developed over the past few decades (Bonnet, 1999). BEMs are roughly categorized in two: collocation BEM and Galerkin BEM (Bonnet, 2017). Among the applications for crack problems, one of the most widely used methods is a type of collocation BEM called the displacement discontinuity method (DDM) (Crouch & Starfield, 1983). The DDM is indeed our choice to relate the displacement discontinuity distribution over a set of arbitrary-shaped fractures to the corresponding tractions applied on the crack faces that are in elatostatic equilibrium, as required by the mechanical solver developed in Chapter 2. Note that in this appendix, we make use of the term 'crack' to refer to any pre-existing geological discontinuity.

One key ingredient of the DDM is to know the solution for the elastic fields (displacement vector and stress tensor) due to a dislocation loop of a certain shape in a usually infinite solid. The numerical method is then built, in simple words, by the superposition of multiple dislocation loops that can geometrically represent the cracks under consideration via spatial discretization. The most common dislocation loops used in the context of BEMs are rectangular and triangular loops. For the general case of arbitrary-shaped cracks, triangular dislocation loops are preferred due to the greater versatility for the discretization of general non-planar surfaces. For that reason, we adopt a triangular dislocation loop here.

The general solution for the elastic fields due to a dislocation over a general bounded plane area in an infinite solid was first derived by Rongved (Rongved, 1957). Rongved's solution is given in terms of surface integrals that have to be solved by integrating over specific dislocation regions (shapes). In our case of interest, the solution for a generic triangular dislocation loop is known (Crouch & Starfield, 1983; Kuriyama & Mizuta, 1993) and is expressed in terms of multiple hypersingular, singular, and quasi-singular integrals. One of the major challenges

in the computation of the elastic fields and the implementation of the DDM is to calculate those integrals in an accurate and efficient manner. Several numerical techniques have been proposed in the literature to efficiently deal with these integrals (e.g., Lachat and Watson, 1976). Moreover, analytical integration techniques have been more recently developed and provide exact yet cumbersome closed-form analytical expressions (e.g., Kuriyama and Mizuta, 1993; Nintcheu Fata, 2009).

In this work, we use the recent contribution of Nintcheu Fata (2009, 2011) who developed and applied a new integration technique to solve analytically for three-dimensional boundary integrals of potential theory which appear explicitly in the elastic field solutions due to a generic triangular dislocation loop in an isotropic, homogeneous, and infinite medium (Kuriyama & Mizuta, 1993). One key aspect of our work here is to make the link between Nintcheu Fata's integrals and the elastic fields induced by a triangular dislocation loop. We note that the explicit formulae obtained by Nintcheu Fata facilitate numerical implementations because they are written in a recursive manner with regard to each edge of the triangular loop. Besides, the treatment of the singularities for BEM applications is easier to deal with, as it will become clear later.

A.2   A triangular dislocation loop in an infinite solid

A.2.1   The solution for the elastic fields

This section is based on the description of the elastic flieds due to a triangular dislocation loop as described by Kuriyama and Mizuta (1993) plus some definitions and notations used by Nintcheu Fata (2009, 2011) that will facilitate the link between both works in the following section.

Consider a Cartesian frame $\{\mathbf{0}; \boldsymbol{i}_1, \boldsymbol{i}_2, \boldsymbol{i}_3\}$ and the triplet $\{\boldsymbol{y}^1, \boldsymbol{y}^2, \boldsymbol{y}^3\} \subset \mathbb{R}^3$ that corresponds to the position vectors of the vertices of a generic triangular dislocation loop E (see Figure A.1, left). Let us define the local reference system $\{\boldsymbol{y}^1; \boldsymbol{e}_1, \boldsymbol{e}_2, \boldsymbol{e}_3\}$ for E with origin at $\boldsymbol{y}^1$, where $\boldsymbol{e}_1$ is parallel (and pointing in the direction of) the triangle edge defined by the segment $[\boldsymbol{y}^1, \boldsymbol{y}^2]$, $\boldsymbol{e}_2 = \boldsymbol{e}_3 \times \boldsymbol{e}_1$, and $\boldsymbol{e}_3$ is normal to the plane of E spanned by $\{\boldsymbol{e}_1, \boldsymbol{e}_2\}$. The local reference system is associated with the local coordinate system $\{\boldsymbol{y}^1; \xi, \zeta, \eta\}$.

Let $\boldsymbol{x} \in \mathbb{R}^3$ be an arbitrary observation point that when expressed in the local coordinate system of E is

$$\boldsymbol{x}^o_{y^1} = \boldsymbol{x} - \boldsymbol{y}^1 = \xi^o \boldsymbol{e}_1 + \zeta^o \boldsymbol{e}_2 + \eta^o \boldsymbol{e}_3. \tag{A.1}$$

Following Kuriyama and Mizuta (1993), the displacement u_i and stress σ_{ij} fields induced at the arbitrary point $\boldsymbol{x} \in \mathbb{R}^3$ due to a dislocation characterized by a constant displacement

discontinuity vector d_i ($i = 1, 2, 3$) acting over the triangle E can be written as,

$$u_i = a_{ij} d_j, \quad \sigma_{ij} = b_{ijk} d_k, \quad (i, j, k = 1, 2, 3) \tag{A.2}$$

where a_{ij} and b_{ijk} are the so-called influence coefficients and the displacement discontinuity vector is defined as $d_i = u_i(\xi, \zeta, \eta = 0^-) - u_i(\xi, \zeta, \eta = 0^+)$.

According to Kuriyama and Mizuta (1993), the influence coefficients can be expressed in terms of the partial derivatives of the following integral function f, which is integrated over the triangle E and evaluated at the arbitrary observation point $\boldsymbol{x} \in \mathbb{R}^3$,

$$f(\xi^o, \zeta^o, \eta^o) = \int_E \frac{d\xi' d\zeta'}{\sqrt{(\xi' - \xi^o)^2 + (\zeta' - \zeta^o)^2 + (\eta^o)^2}}. \tag{A.3}$$

By defining first $a_{ij} = \alpha \tilde{a}_{ij}$, the displacement influence coefficients take the following form,

$$
\begin{aligned}
\tilde{a}_{11} &= 2(1 - \nu) f_3 - \eta^o f_{11} & \tilde{a}_{12} &= -\eta^o f_{12} & \tilde{a}_{13} &= -\left[(1 - 2\nu) f_1 + \eta^o f_{13}\right] \\
\tilde{a}_{21} &= -\eta^o f_{12} & \tilde{a}_{22} &= 2(1 - \nu) f_3 - \eta^o f_{22} & \tilde{a}_{23} &= -\left[(1 - 2\nu) f_2 + \eta^o f_{23}\right] \\
\tilde{a}_{31} &= (1 - 2\nu) f_1 - \eta^o f_{13} & \tilde{a}_{32} &= (1 - 2\nu) f_2 - \eta^o f_{23} & \tilde{a}_{33} &= 2(1 - \nu) f_3 - \eta^o f_{33}
\end{aligned} \tag{A.4}
$$

Similarly, by defining $b_{ijk} = \beta \tilde{b}_{ijk}$, the stress influence coefficients are determined by the following expressions,

$$
\begin{aligned}
\tilde{b}_{111} &= 2 f_{13} - \eta^o f_{111} & \tilde{b}_{112} &= 2\nu f_{23} - \eta^o f_{112} & \tilde{b}_{113} &= f_{33} + (1 - 2\nu) f_{22} - \eta^o f_{113} \\
\tilde{b}_{221} &= 2\nu f_{13} - \eta^o f_{122} & \tilde{b}_{222} &= 2 f_{23} - \eta^o f_{222} & \tilde{b}_{223} &= f_{33} + (1 - 2\nu) f_{11} - \eta^o f_{223} \\
\tilde{b}_{331} &= -\eta^o f_{133} & \tilde{b}_{332} &= -\eta^o f_{233} & \tilde{b}_{333} &= f_{33} - \eta^o f_{333} \\
\tilde{b}_{121} &= (1 - \nu) f_{23} - \eta^o f_{112} & \tilde{b}_{122} &= (1 - \nu) f_{13} - \eta^o f_{122} & \tilde{b}_{123} &= -(1 - 2\nu) f_{12} - \eta^o f_{123} \\
\tilde{b}_{231} &= -\nu f_{12} - \eta^o f_{123} & \tilde{b}_{232} &= f_{33} + \nu f_{11} - \eta^o f_{223} & \tilde{b}_{233} &= -\eta^o f_{233} \\
\tilde{b}_{131} &= f_{33} + \nu f_{22} - \eta^o f_{113} & \tilde{b}_{132} &= -\nu f_{12} - \eta^o f_{123} & \tilde{b}_{133} &= -\eta^o f_{133}
\end{aligned} \tag{A.5}
$$

Where α and β are prefactors given by,

$$\alpha = \frac{1}{8\pi(1 - \nu)}, \quad \beta = \frac{\mu}{4\pi(1 - \nu)}, \tag{A.6}$$

with μ and ν the shear modulus and Poisson's ratio, respectively.

In equations (A.4) and (A.5), the partial derivatives of f are denoted as $f_1, f_2, ..., f_{333}$, where each corresponding suffix means taking a partial derivative with respect to one of the local coordinates of E, such that $\xi = 1$, $\zeta = 2$ and $\eta = 3$.
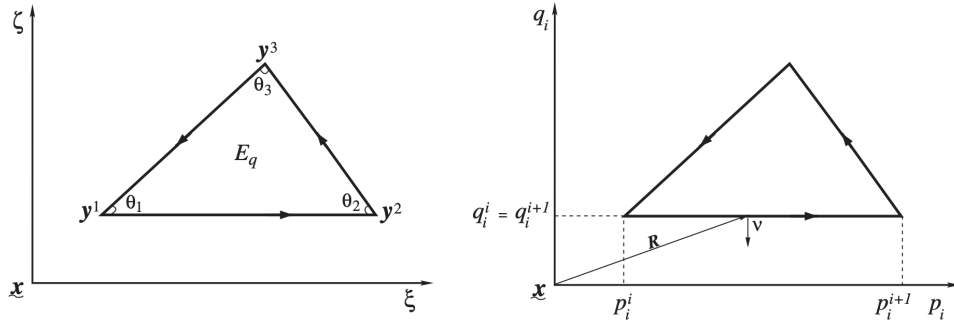
Figure A.1: Local coordinate systems associated with a generic triangle E. Taken from Nintcheu Fata (2009).

A.2.2   The link between the elastic fields and the generic integrals of potential theory

In this section, we link the work of Nintcheu Fata (2009, 2011) to the computation of the partial derivatives of f that give the elastic fields as defined in the previous section through equations (A.4) and (A.5). Following Nintcheu Fata (2009), let P_E be the plane of E spanned by $\{e_1, e_2\}$ and $y \in P_E$ an arbitrary field point that expressed in the local coordinate system of E takes the following form,

$$y_{y^1} = y - y^1 = \xi' e_1 + \zeta' e_2. \tag{A.7}$$

Let us now define the local coordinate system $\{x; e_1, e_2, e_3\}$ with origin at the observation point $x \in \mathbb{R}^3$ (see Figure A.1). In $\{x; e_1, e_2, e_3\}$, the position vector r of the arbitrary field point $y \in P_E$ can be expressed as,

$$r = y - x = \xi e_1 + \zeta e_2 + \eta e_3, \tag{A.8}$$

so that the distance between the observation point $x \in \mathbb{R}^3$ and the field point $y \in P_E$ is $r = \|y - x\| = \sqrt{\xi^2 + \zeta^2 + \eta^2}$, with

$$\xi = \xi' - \xi^o, \quad \zeta = \zeta' - \zeta^o, \quad \eta = -\eta^o. \tag{A.9}$$

With these definitions, the integral function f given by equation (A.3) can be recast simply as

$$f(x) = \int_E \frac{ds_y}{\|y - x\|} = \int_E \frac{ds}{r}, \tag{A.10}$$

so that the partial derivatives of f can be now calculated easily. After performing the respective differentiation, the first and second partial derivatives of f take the following form,

$$f_1 = \int_E \frac{\xi}{r^3} ds \qquad\qquad f_2 = \int_E \frac{\zeta}{r^3} ds \qquad\qquad f_3 = \int_E \frac{\eta}{r^3} ds$$

$$f_{11} = -\int_E \frac{1}{r^3} ds + 3\int_E \frac{\xi^2}{r^5} ds \quad f_{22} = -\int_E \frac{1}{r^3} ds + 3\int_E \frac{\zeta^2}{r^5} ds \quad f_{33} = -\int_E \frac{1}{r^3} ds + 3\eta^2 \int_E \frac{1}{r^5} ds$$

$$f_{12} = 3\int_E \frac{\xi\zeta}{r^5} ds \qquad\qquad f_{13} = 3\eta \int_E \frac{\xi}{r^5} ds \qquad\qquad f_{23} = 3\eta \int_E \frac{\zeta}{r^5} ds, \qquad (A.11)$$

whereas the third partial derivatives are given by

$$f_{111} = -9\int_E \frac{\xi}{r^5} ds + 15\int_E \frac{\xi^3}{r^7} ds \qquad\qquad f_{222} = -9\int_E \frac{\zeta}{r^5} ds + 15\int_E \frac{\zeta^3}{r^7} ds$$

$$f_{333} = -9\eta \int_E \frac{1}{r^5} ds + 15\eta^3 \int_E \frac{1}{r^7} ds \qquad\qquad f_{123} = 15\eta \int_E \frac{\xi\zeta}{r^7} ds$$

$$f_{112} = -3\int_E \frac{\zeta}{r^5} ds + 15\int_E \frac{\xi^2 \zeta}{r^7} ds \qquad\qquad f_{122} = -3\int_E \frac{\xi}{r^5} ds + 15\int_E \frac{\xi\zeta^2}{r^7} ds$$

$$f_{113} = -3\eta \int_E \frac{1}{r^5} ds + 15\eta \int_E \frac{\xi^2}{r^7} ds \qquad\qquad f_{223} = -3\eta \int_E \frac{1}{r^5} ds + 15\eta \int_E \frac{\zeta^2}{r^7} ds$$

$$f_{133} = -3\int_E \frac{\xi}{r^5} ds + 15\eta^2 \int_E \frac{\xi}{r^7} ds \qquad\qquad f_{233} = -3\int_E \frac{\zeta}{r^5} ds + 15\eta^2 \int_E \frac{\zeta}{r^7} ds. \qquad (A.12)$$

At this point, we note that the integrals that define the partial derivatives of f in equations (A.11) and (A.12) are exactly some of the generic integrals for the elastic surface potentials solved analytically by Nintcheu Fata (2011). Following Nintcheu Fata's notation, we can rewrite the partial derivatives of f, equations (A.11) and (A.12), as

$$f_1 = I_3^\xi, \qquad\qquad f_2 = I_3^\zeta, \qquad\qquad f_3 = \eta I_3$$

$$f_{11} = -I_3 + 3I_5^{\xi\xi}, \qquad\qquad f_{22} = -I_3 + 3I_5^{\zeta\zeta}, \qquad\qquad f_{33} = -I_3 + 3\eta^2 I_5$$

$$f_{12} = 3I_5^{\xi\zeta}, \qquad\qquad f_{13} = 3\eta I_5^\xi, \qquad\qquad f_{23} = 3\eta I_5^\zeta, \qquad (A.13)$$

and

$$f_{111} = -9I_5^\xi + 15I_7^{\xi\xi\xi} \qquad\qquad\qquad f_{222} = -9I_5^\zeta + 15I_7^{\zeta\zeta\zeta}$$

$$f_{333} = -9\eta I_5 + 15\eta^3 I_7 \qquad\qquad\qquad f_{123} = 15\eta I_7^{\xi\zeta}$$

$$f_{112} = -3I_5^\zeta + 15I_7^{\xi\xi\zeta}, \qquad\qquad\qquad f_{122} = -3I_5^\xi + 15I_7^{\xi\zeta\zeta}$$

$$f_{113} = -3\eta I_5 + 15\eta I_7^{\xi\xi} \qquad\qquad\qquad f_{223} = -3\eta I_5 + 15\eta I_7^{\zeta\zeta}$$

$$f_{133} = -3I_5^\xi + 15\eta^2 I_7^\xi, \qquad\qquad\qquad f_{233} = -3I_5^\zeta + 15\eta^2 I_7^\zeta, \qquad (A.14)$$

respectively.

Note that the notation for the generic integrals (e.g., $I_7^{\xi\zeta\zeta}$) is such that the subscript represents the exponent of the integrand's denominator and the superscript represents directly the

integrand's numerator.

A.2.3   Exact formulae for generic integrals

We describe now the procedure to compute the generic integrals appearing in equations (A.13) and (A.14). We also discuss very briefly some relevant details of the analytical integration technique used by Nintcheu Fata (2009, 2011).

One can define the local orthogonal companion basis $\{e_1, e_2, e_3\}$ of the generic triangle E as a function of the the triplet $\{y^1, y^2, y^3\}$ that represents the position vectors of the triangle vertices as follows,

$$\sigma = \frac{\left(y^3 - y^1\right) \cdot \left(y^2 - y^1\right)}{\left\|y^2 - y^1\right\|^2}, \tag{A.15}$$

$$e_1 = \frac{\left(y^2 - y^1\right)}{\left\|y^2 - y^1\right\|}, \quad e_2 = \frac{\left(y^3 - y^1\right) - \sigma\left(y^2 - y^1\right)}{\left\|\left(y^3 - y^1\right) - \sigma\left(y^2 - y^1\right)\right\|}, \quad e_3 = e_1 \times e_2. \tag{A.16}$$

Plus, the following geometric parameters of E (see Figure A.1, left),

$$b = \left(y^2 - y^1\right) \cdot e_1, \quad a = \left(y^3 - y^1\right) \cdot e_2, \quad c = \left(y^3 - y^1\right) \cdot e_1 \tag{A.17}$$

$$\theta_1 = \arccos\left(\frac{c}{\sqrt{c^2 + a^2}}\right), \quad \theta_2 = \arccos\left(\frac{b - c}{\sqrt{(b - c)^2 + a^2}}\right), \quad \theta_3 = \pi - (\theta_1 + \theta_2). \tag{A.18}$$

By using the previous definitions, one can define the coordinates of the vertex '1' of E in $\{x; e_1, e_2, e_3\}$ plus the auxiliary angles α_i,

$$\xi_1 = \left(y^1 - x\right) \cdot e_1, \quad \zeta_1 = \left(y^1 - x\right) \cdot e_2, \quad \eta = \left(y^1 - x\right) \cdot e_3, \tag{A.19}$$

$$\alpha_1 = 0, \quad \alpha_2 = \pi - \theta_2, \quad \alpha_3 = \pi + \theta_1. \tag{A.20}$$

Using the auxiliary angles α_i, one can now define a set of useful local reference systems $\{x; e_{p_i}, e_{q_i}, e_3\}$ with origin at the observation point $x \in \mathbb{R}^3$, which are associated with each i-th edge $L_i = [y^i, y^{i+1}]$ of E ($i = 1, 2, 3$ and the superscript '4' must be replaced by '1'), where the unit vector e_{p_i} is parallel (and points in the direction of) the corresponding triangle edge L_i (see Figure A.1, right). These three local reference systems $\{x; e_{p_i}, e_{q_i}, e_3\}$ induce three local coordinate systems $\{x; p_i, q_i, \eta\}$ such that,

$$p_i = \xi \cos(\alpha_i) + \zeta \sin(\alpha_i), \tag{A.21}$$

$$q_i = -\xi \sin(\alpha_i) + \zeta \cos(\alpha_i). \tag{A.22}$$

The analytical integration technique used by Nintcheu Fata (2009, 2011) makes extensive use of the previously defined local reference and coordinate systems. We also highlight that in his work, the generic integrals are classified in two categories. In one group, application of the Stokes' theorem is needed to transform surface integrals in contour integrals, whereas

in a second group, integration can be performed directly as surface integrals. Notably, the application of the Stokes' theorem for the first group of integrals requires a special treatment for the case in which the projection of the observation point $\boldsymbol{x} \in \mathbb{R}^3$ over the plane P_E in the direction of $\boldsymbol{e}_3$ (i.e., perpendicular to P_E) lies inside E.

Let us call such projection of the observation point as $\widetilde{\boldsymbol{x}} \in P_E$. As described carefully by Nintcheu Fata (2009), the application of the Stokes' theorem leads to different values of the integrals of the first group depending on the following sub-cases: $\widetilde{\boldsymbol{x}} \in P_E \setminus E$ (strictly outside the triangle), $\widetilde{\boldsymbol{x}} \in \{\boldsymbol{y}^1, \boldsymbol{y}^2, \boldsymbol{y}^3\}$ (over a triangle vertex), $\widetilde{\boldsymbol{x}} \in L_1 \cup L_2 \cup L_3 \setminus \{\boldsymbol{y}^1, \bar{\boldsymbol{y}^2}, \boldsymbol{y}^3\}$ (over a triangle edge but not over a triangle vertex), and $\widetilde{\boldsymbol{x}} \in E$ (strictly inside the triangle). This is the reason why equation (A.33) is in the form of a piece-wise function.

The use of the local coordinate systems $\{\boldsymbol{x}; p_i, q_i, \eta\}$, equation (A.21), and the transformation of surface integrals into contour integrals, provides notably the chance to write the exact expressions for the generic integrals of the first group as a sum of analytic formulae over the sides L_i of E (see appendix in Nintcheu Fata, 2011) that significantly facilitates the numerical implementation. Furthermore, the second group of integrals that are solved directly as surface integrals can be also expressed exactly as a sum of analytic formulae over the sides L_i, after using equation (A.21), and performing some algebraic manipulations (Nintcheu Fata, 2009).

The exact formulae for the generic integrals appearing in equations (A.13) and (A.14) can be found in the appendix of Nintcheu Fata (2011). These formulae are written in terms of the following functions that have to be evaluated for every edge L_i of E,

$$\tilde{\rho}_i(\boldsymbol{x}) = \rho_i - \rho_{i+1}, \quad \tilde{\phi}_i(\boldsymbol{x}) = p_i^i \rho_i - p_i^{i+1} \rho_{i+1}, \quad \chi_i(\boldsymbol{x}) = \ln(p_i^i + \rho_i) - \ln(p_i^{i+1} + \rho_{i+1})$$

$$\delta_i(\boldsymbol{x}) = \frac{p_i^i}{\rho_i} - \frac{p_i^{i+1}}{\rho_{i+1}}, \quad \mathscr{L}_i(\boldsymbol{x}) = \frac{1}{\rho_i} - \frac{1}{\rho_{i+1}}, \quad \mathscr{D}_i(\boldsymbol{x}) = \frac{p_i^i}{(\rho_i)^3} - \frac{p_i^{i+1}}{(\rho_{i+1})^3}, \quad \Lambda_i(\boldsymbol{x}) = \frac{1}{(\rho_i)^3} - \frac{1}{(\rho_{i+1})^3}$$

$$\gamma_i(\boldsymbol{x}) = \arctan\left(\frac{-2 p_i^i q_i \eta \rho_i}{(q_i)^2 (\rho_i)^2 - (p_i^i)^2 \eta^2}\right) - \arctan\left(\frac{-2 p_i^{i+1} q_i \eta \rho_{i+1}}{(q_i)^2 (\rho_{i+1})^2 - (p_i^{i+1})^2 \eta^2}\right), \tag{A.23}$$

where again, the superscript and subscript '4' must be replaced by '1'. The previous functions require the computation of the local coordinates (p_i^j, q_i^j, η) of the j-th vertex of E that are endpoints of each i-th edge $L_i = [\boldsymbol{y}^i, \boldsymbol{y}^{i+1}]$. These coordinates can be calculated as,

$$p_1^1 = \xi_1, \quad p_1^2 = b + \xi_1, \quad q_1^1 = q_1^2 = q_1 = \zeta_1 \tag{A.24}$$

$$p_2^2 = (b + \xi_1) \cos(\alpha_2) + \zeta_1 \sin(\alpha_2), \quad p_2^3 = (c + \xi_1) \cos(\alpha_2) + (a + \zeta_1) \sin(\alpha_2) \tag{A.25}$$

$$q_2^2 = q_2^3 = q_2 = -(b + \xi_1) \sin(\alpha_2) + \zeta_1 \cos(\alpha_2) \tag{A.26}$$

$$p_3^3 = (c + \xi_1) \cos(\alpha_3) + (a + \zeta_1) \sin(\alpha_3), \quad p_3^1 = \xi_1 \cos(\alpha_3) + \zeta_1 \sin(\alpha_3) \tag{A.27}$$

$$q_3^3 = q_3^1 = q_3 = -\xi_1 \sin(\alpha_3) + \zeta_1 \cos(\alpha_3). \tag{A.28}$$

$$\tag{A.29}$$

Equation (A.24) gives the local coordinates of the endpoints $\boldsymbol{y}^1$ and $\boldsymbol{y}^2$ of edge L_1, equations

(A.25) and (A.26) give the local coordinates of the endpoints $\boldsymbol{y}^2$ and $\boldsymbol{y}^3$ of edge L_2, and equations (A.27) and (A.28) the local coordinates of the endpoints $\boldsymbol{y}^3$ and $\boldsymbol{y}^1$ of edge L_3. In addition, the distance between the observation point $\boldsymbol{x}$ and the vertex $\boldsymbol{y}^j$ can be computed via these local coordinates simply as,

$$\rho_1 = \sqrt{(p_1^1)^2 + (q_1)^2 + \eta^2}, \quad \rho_2 = \sqrt{(p_2^2)^2 + (q_2)^2 + \eta^2}, \quad \rho_3 = \sqrt{(p_3^3)^2 + (q_3)^2 + \eta^2}. \quad \text{(A.30)}$$

Finally, when evaluating displacement and traction vectors on the solid's boundary,

$$\theta(\boldsymbol{x}) = \begin{cases} \frac{1}{2} \sum_{k=1}^{3} \gamma_k(\boldsymbol{x}) + \theta_0(\boldsymbol{x}), & \text{if } \eta > 0 \\ \frac{1}{2} \sum_{k=1}^{3} \gamma_k(\boldsymbol{x}) - \theta_0(\boldsymbol{x}), & \text{if } \eta \leq 0 \end{cases} \quad \text{(A.31)}$$

whereas in the case of evaluating displacement vectors at interior points of the solid,

$$\theta(\boldsymbol{x}) = \begin{cases} \frac{1}{2} \sum_{k=1}^{3} \gamma_k(\boldsymbol{x}) + \theta_0(\boldsymbol{x}), & \text{if } \eta \geq 0 \\ \frac{1}{2} \sum_{k=1}^{3} \gamma_k(\boldsymbol{x}) - \theta_0(\boldsymbol{x}), & \text{if } \eta < 0. \end{cases} \quad \text{(A.32)}$$

In the previous two equations, $\theta_0(\boldsymbol{x})$ depends on the location of the projection of $\boldsymbol{x}$ over the plane P_E in the direction $\boldsymbol{e}_3$ that we call $\widetilde{\boldsymbol{x}}$. This is,

$$\theta_0(\boldsymbol{x}) = \begin{cases} 0, & \text{if } \widetilde{\boldsymbol{x}} \in P_E \setminus \bar{E} \\ \theta_i, & \text{if } \widetilde{\boldsymbol{x}} = \boldsymbol{y}^i \, (i = 1, 2, 3) \\ \pi & \text{if } \widetilde{\boldsymbol{x}} \in L_1 \cup L_2 \cup L_3 \setminus \{\boldsymbol{y}^1, \boldsymbol{y}^2, \boldsymbol{y}^3\} \\ 2\pi & \text{if } \widetilde{\boldsymbol{x}} \in E. \end{cases} \quad \text{(A.33)}$$

A.2.4   Computational implementation in C++

On the basis of the definitions of the previous section, the generic integrals given in the appendix of Nintcheu Fata (2011) can be calculated via recursive formulae associated with each edge L_i of the triangle E. We implemented the numerical calculation of the generic integrals that appear in the partial derivatives of f, equations (A.13) and (A.14), and the subsequent computation of the elastic fields that are function of these partial derivatives through equations (A.4) and (A.5).

The computational implementation was done in C++. The algorithm used for the computation of the elastic fields is summarized below:

1. Assume $\boldsymbol{x}$, $\{\boldsymbol{y}^1, \boldsymbol{y}^2, \boldsymbol{y}^3\}$ and $d_i (i = 1, 2, 3)$ as known.
2. Compute the vectors $\{\boldsymbol{e}_1, \boldsymbol{e}_2, \boldsymbol{e}_3\}$, the geometric parameters a, b, c, and θ_i, the local coordinates (p_i^j, q_i^j, η), and the distances ρ_i, using equations (A.15) to (A.20), and equations (A.24) to (A.30).
3. Compute the functions $\tilde{\rho}_i(\boldsymbol{x})$, $\tilde{\phi}_i(\boldsymbol{x})$, $\chi_i(\boldsymbol{x})$, $\delta_i(\boldsymbol{x})$, $\mathscr{L}(\boldsymbol{x})$, $\mathscr{D}(\boldsymbol{x})$, $\Lambda_i(\boldsymbol{x})$ and $\theta(\boldsymbol{x})$ using equa-

tions (A.23), (A.33), and (A.31) or (A.32) depending on the location of the observation point.

4. Compute the following generic integrals I_k, I_k^ξ, I_k^ζ ($k = 3, 5, 7$), $I_k^{\xi\xi}$, $I_k^{\xi\zeta}$, $I_k^{\zeta\zeta}$ ($k = 5, 7$), $I_7^{\xi\xi\xi}$, $I_7^{\zeta\zeta\zeta}$, $I_7^{\xi\xi\zeta}$ and $I_7^{\xi\zeta\zeta}$, as defined in the appendix of Nintcheu Fata (2011).

5. Compute the partial derivatives f_1, f_2, ..., f_{333}, using equations (A.13) and (A.14).

6. Compute the displacement a_{ij} and stress b_{ijk} ($i, j, k = 1, 2, 3$) influence coefficients, using equations (A.4) to (A.6).

7. Finally, compute the the displacement u_i and stress σ_{ij} components using equation (A.2).

Note that the elastic fields given by the previous algorithm are expressed in the local reference system of the generic triangular dislocation loop E (see Figure A.1).

A.2.5   Verification

We tested our implementation for the computation of the generic integrals (steps 1 to 4 in the algorithm described in the previous section) against numerical integration performed via Wolfram Mathematica for observation points located outside the dislocation loop (otherwise the integrals are singular and regular numerical integration procedures may loose precision). This is done for a unit triangle with vertices given by $\boldsymbol{y}^1 = (0, 0, 0)$, $\boldsymbol{y}^2 = (1, 0, 0)$, and $\boldsymbol{y}^3 = (0, 1, 0)$, and at different observation points $\boldsymbol{x} \in \mathbb{R}^3$. The results of this verification are summarized in Table A.1. Many other cases for different triangular geometries were tested. The results were systematically consistent.

A.3   The displacement discontinuity method

A.3.1   Formulation

As anticipated, the displacement and stress fields induced by a triangular dislocation loop in an infinite solid can be used to develop an efficient numerical solver for boundary value problems involving multiple arbitrary-shaped cracks in three dimensions. In our case, we aim specifically at obtaining an expression that relates the distribution of displacement discontinuity components through the cracks to the distribution of the corresponding traction components that need to be applied at the crack surfaces in order to satisfy elastostatic equilibrium. We are interested here only in the case of an infinite solid, even though the extension of the method to finite solids is straightforward (Crouch & Starfield, 1983).

Consider a discretization of an arbitrary-shaped crack surface Γ via a triangulation made out of flat triangles such that $\Gamma = \cup_{i=1}^{N_E} E_i$, where E_i is the i-th triangular dislocation loop element and N_E is the total number of elements in the mesh. Consider now a constant displacement discontinuity vector $\boldsymbol{d}^j$ with components (d_1^j, d_2^j, d_3^j) existing at every j-th

	Observation point $= (1, 0, 0.3)^T$		Observation point $= (0.3, 0.3, 0.7)^T$	
	Exact formulae	Numerical integration	Exact formulae	Numerical integration
I_5	9.52059207	9.52059207	1.95541660	1.95541660
I_5^{ξ}	-2.35037195	-2.35037195	0.03421098	0.03421098
I_5^{ζ}	0.98559934	0.98559934	0.03421097	0.03421097
$I_5^{\zeta\zeta}$	0.20505000	0.20505000	0.07934980	0.07934980
$I_5^{\xi\zeta}$	-0.35156588	-0.35156588	-0.02808261	-0.02808261
I_7	64.55805175	64.55805175	3.47682764	3.47682764
I_7^{ξ}	-11.53353531	-11.53353531	0.04665346	0.04665346
$I_7^{\xi\xi}$	3.02978475	3.02978475	0.12588554	0.12588554
$I_7^{\xi\zeta}$	-1.18701740	-1.18701740	-0.03915187	-0.03915187
$I_7^{\xi\xi\xi}$	-1.08743779	-1.08743779	0.01658548	0.01658548

Table A.1: Verification of some generic integrals. Analytical versus numerical integration.

triangle E_j ($j = 1, ..., N_E$) and expressed in the local reference system of E_j as defined in the previous section. Let us analyze the interaction between two dislocation loops E_i and E_j.

First, let $\{e_1^j, e_2^j, e_3^j\}$ be the local orthogonal companion basis of the triangle E_j. One can define the rotation matrix $R^j = [e_1^j, e_2^j, e_3^j] \in \mathbb{R}^{3 \times 3}$ (composed by column-vectors) and the following transformation rule $\sigma^g = R^j \sigma^l (R^j)^T$ to transform the stress tensor from the local reference system of E_j to the global Cartesian reference system $\{0; i_1, i_2, i_3\}$. Likewise, the rotation matrix associated with the triangle E_i can be defined as $R^i = [e_1^i, e_2^i, e_3^i] \in \mathbb{R}^{3 \times 3}$ and an analogous transformation rule can be established. Furthermore, one can define the rotation matrix $R \in \mathbb{R}^{3 \times 3}$ that characterizes the transition from the local reference system of E_j to the local reference system of E_i as,

$$R = (R^i)^T R^j. \tag{A.34}$$

Let $t^{ij} \in \mathbb{R}^3$ be the traction vector at the centroid[1] of E_i induced by the constant displacement discontinuity vector d^j acting over the triangular dislocation E_j, and expressed in the local reference system of E_i. Since the elastic fields derived in section A.2 are expressed in the local reference system of the applied dislocation loop (in our case E_j), one can show by using equation (A.2), the corresponding transformation rules of $R \in \mathbb{R}^{3 \times 3}$, and the definition of the

---

[1]The selection of the centroid is arbitrary, in principle, it can be any point inside the triangle except at the edges where the traction components are singular.

Cauchy stress tensor $\boldsymbol{t} = \boldsymbol{\sigma} \cdot \boldsymbol{n}$, that $\boldsymbol{t}^{ij}$ takes the following form,

$$\boldsymbol{t}^{ij} = \boldsymbol{T}^{ij} \boldsymbol{d}^j \, (\text{no sum on } j), \tag{A.35}$$

where $\boldsymbol{T}^{ij} \in \mathbb{R}^{3 \times 3}$ is the stress influence matrix given by

$$\boldsymbol{T}^{ij} = [\boldsymbol{s}_1, \boldsymbol{s}_2, \boldsymbol{s}_3], \tag{A.36}$$

with the column-vectors s_i

$$\boldsymbol{s}_1 = \boldsymbol{R}\boldsymbol{B}_1\boldsymbol{n}, \quad \boldsymbol{s}_2 = \boldsymbol{R}\boldsymbol{B}_2\boldsymbol{n}, \quad \boldsymbol{s}_3 = \boldsymbol{R}\boldsymbol{B}_3\boldsymbol{n}. \tag{A.37}$$

In the previous equation, $\boldsymbol{B_i} \in \mathbb{R}^{3 \times 3}$ ($i = 1, 2, 3$) are matrices whose entries are given by the coefficients b_{ijk} ($i, j, k = 1, 2, 3$), equations (A.5) and (A.6), and $\boldsymbol{n}$ is the unit normal vector of E_i expressed in the local reference system of E_j, such that $\boldsymbol{n} = \boldsymbol{R}^j \boldsymbol{e}_3^i$.

Finally, the traction vector at the centroid of the i-th triangular dislocation loop element $\boldsymbol{t}^i \in \mathbb{R}^3$ due to the constant displacement discontinuities $\boldsymbol{d}^j \in \mathbb{R}^3$ ($j = 1, ..., N_E$) of all the N_E triangular dislocation loop elements can be computed by invoking the principle of superposition of linear systems. Summing up the individual contribution given by equation (A.35), we obtain

$$\boldsymbol{t}^i = \sum_{j=1}^{N_E} \boldsymbol{T}^{ij} \boldsymbol{d}^j. \tag{A.38}$$

Repeating the same procedure for every i-th triangular dislocation loop element, one can arrive to the final matrix-vector equation,

$$\boldsymbol{t} = \boldsymbol{E}\boldsymbol{d}, \tag{A.39}$$

where $\boldsymbol{t} \in \mathbb{R}^{3N_E}$ is a vector containing the three components of all the individual traction vectors evaluated at the centroid of each triangular dislocation loop element, $\boldsymbol{E} \in \mathbb{R}^{3N_E \times 3N_E}$ is a dense, fully-populated matrix accounting for the interaction and contribution of all triangular elements, and $\boldsymbol{d} \in \mathbb{R}^{3N_E}$ is a vector containing the three components of all the individual displacement discontinuity vectors.

Note that equation (A.38) can be use to compute the traction vector at any arbitrary point in $\mathbb{R}^3$ given a unit normal vector. A similar expression to (A.38) can be obtained to compute the displacement vector and the stress tensor at any arbitrary point in $\mathbb{R}^3$.

A.3.2   Computational implementation in C++

On the basis of the definitions of the previous section, we implemented the computation of the fully-populated elasticity matrix $\boldsymbol{E} \in \mathbb{R}^{3N_E \times 3N_E}$ in C++, in order to solve general boundary value problems in linear elasticity involving cracks of any shape in three dimensions, via equation

(A.39). Note that both the traction vector $\boldsymbol{t} \in \mathbb{R}^{3N_E}$ and the displacement discontinuity vector $\boldsymbol{d} \in \mathbb{R}^{3N_E}$ are expressed in (A.39) at the local reference systems of the corresponding triangular dislocation loop elements.

A.4 Supplementary material: Axisymmetric boundary element matrix

For the particular case of our planar axisymmetric circular rupture model ($\nu = 0$), we implement the displacement discontinuity method using ring-dislocation boundary elements with piece-wise uniform displacement discontinuity (see Gordeliy and Detournay, 2011, for example). The two relevant displacement discontinuity components are fault slip and fault opening. Note that in our axisymmetric model, the slip is axisymmetric in terms of magnitude but not in terms of direction. Fault slip is indeed unidirectional. The stress influence factors E_{ij} that compose the collocation boundary element matrix $\mathbf{E}$ are obtained by subtracting two concentric circular dislocation loops of different radii; a prismatic dislocation loop for fault opening, and a glide dislocation loop for fault slip. The shear (or normal) stress E_{ij} at the i-th collocation point located at r_i due to the j-th ring-dislocation boundary element of width $\Delta x_j = R_j - R_{j-1}$, where R_j and R_{j-1} are the outer and inner radii of the ring, are thus calculated by superposition as $E_{ij} = F_j^i - F_{j-1}^i$, where F_j^i represents the shear (or normal) stress at the i-th collocation point due to a circular dislocation loop of radius R_j. The analytical expression for F_j^i is given by (see appendix B in Gordeliy and Detournay, 2011),

$$F_j^i = \mu^* \frac{k\left(\rho_{ij}\right)}{8\pi\sqrt{\rho_{ij}}R_j} \left(\frac{k\left(\rho_{ij}\right)^2 \left(1-\rho_{ij}^2\right)}{4\rho_{ij}k_1\left(\rho_{ij}\right)^2} E\left(k\left(\rho_{ij}\right)^2\right) + K\left(k\left(\rho_{ij}\right)^2\right) \right), \tag{A.40}$$

where $\mu^* = 2\mu$ for the shear (slip) component and $\mu^* = E'$ (the plane-strain Young's modulus, which is equal to the Young's modulus when $\nu = 0$) for the normal (opening) component, $\rho_{ij} = r_i / R_j$, $k(x) = 2\sqrt{x} / (1 + x)$, $k_1(x) = (1 - x) / (1 + x)$, and $K(\cdot)$ and $E(\cdot)$ are the complete elliptic integrals of the first and second kind, respectively.

In the implementation of the displacement discontinuity method, we consider an equal number of ring-dislocation boundary elements and collocation points, such that $\mathbf{E}$ is a squared matrix of size $2N \times 2N$ with N the number of boundary elements. The collocation points are chosen to be located at the centroid of their respective elements.

Bibliography

Aki, K., & Richards, P. (2002). *Quantitative Seismology* (2nd edition).

Ampuero, J.-P., & Rubin, A. M. (2008). Earthquake nucleation on rate and state faults – aging and slip laws. *Journal of Geophysical Research: Solid Earth, 113*(B1).

Andrews, D. J. (1976). Rupture propagation with finite stress in antiplane strain. *Journal of Geophysical Research (1896-1977), 81*(20), 3575–3582.

Azad, M., Garagash, D., & Satish, M. (2017). Nucleation of dynamic slip on a hydraulically fractured fault. *Journal of Geophysical Research: Solid Earth, 122*(4), 2812–2830.

Babaie Mahani, A., Kao, H., Atkinson, G. M., Assatourians, K., Addo, K., & Liu, Y. (2019). Ground-Motion Characteristics of the 30 November 2018 Injection-Induced Earthquake Sequence in Northeast British Columbia, Canada. *Seismological Research Letters, 90*(4), 1457–1467.

Babaie Mahani, A., Schultz, R., Kao, H., Walker, D., Johnson, J., & Salas, C. (2017). Fluid Injection and Seismic Activity in the Northern Montney Play, British Columbia, Canada, with Special Reference to the 17 August 2015 Mw 4.6 Induced Earthquake. *Bulletin of the Seismological Society of America, 107*(2), 542–552.

Baisch, S., Koch, C., & Muntendam-bos, A. (2019). Traffic light systems: to what extent can induced seismicity be controlled? *Seismological Research Letters, 90*(3), 1145–1154.

Bandis, S., Lumsden, A., & Barton, N. (1983). Fundamentals of rock joint deformation. *International Journal of Rock Mechanics and Mining Sciences & Geomechanics Abstracts, 20*(6), 249–268.

Bao, X., & Eaton, D. (2016). Fault activation by hydraulic fracturing in western canada. *Science, 354*(6318), 1406–1409.

Barenblatt, G. (1962). The mathematical theory of equilibrium cracks in brittle fracture. *Advances in Applied Mechanics, 7*, 55–129.

Barenblatt, G. (1996). *Scaling, self-similarity, and intermediate asymptotics* (1st edition). Cambridge University Press.

Baria, R., Baumgartner, J., & Gérard., A. (1996). *European hot dry rock programme 1992-1995. extended summary of the final report to ec (dgxii), contract jou2-ct92-0115.* (tech. rep.).

Barton, C., Zoback, M., & Moos, D. (1995). Fluid flow along potentially active faults in crystalline rock. *Geology*, *23*(8), 683–686.

Baujard, C., Genter, A., Dalmais, E., Maurer, V., Hehn, R., Rosillette, R., Vidal, J., & Schmittbuhl, J. (2017). Hydrothermal characterization of wells grt-1 and grt-2 in rittershoffen, france: implications on the understanding of natural flow systems in the rhine graben. *Geothermics*, *65*, 255–268.

Bayart, E., Svetlizky, I., & Fineberg, J. (2016). Slippery but tough: the rapid fracture of lubricated frictional interfaces. *Physical Review Letters*, *116*, 194301.

Bear, J. (2013). *Dynamics of fluids in porous media*. Courier Corporation.

Behr, W. M., & Bürgmann, R. (2021). What's down there? the structures, materials and environment of deep-seated slow slip and tremor. *Philosophical Transactions of the Royal Society A: Mathematical, Physical and Engineering Sciences*, *379*(2193), 20200218.

Bhattacharya, P., & Viesca, R. (2019). Fluid-induced aseismic fault slip outpaces pore-fluid migration. *Science*, *364*(6439), 464–468.

Bonnet, M. (1999). *Boundary integral equation methods for solids and fluids*. John Wiley & Sons, Ltd.

Bonnet, M. (2017). Boundary integral equation methods for elastic and plastic problems. John Wiley & Sons, Ltd.

Bosl, W., & Nur, A. (2002). Aftershocks and pore fluid diffusion following the 1992 Landers earthquake. *Journal of Geophysical Research: Solid Earth*, *107*(B12), ESE 17.

Bourouis, S., & Bernard, P. (2007). Evidence for coupled seismic and aseismic fault slip during water injection in the geothermal site of Soultz (France), and implications for seismogenic transients. *Geophysical Journal International*, *169*(2), 723–732.

Boyet, A., De Simone, S., Ge, S., & Vilarrasa, V. (2023). Poroelastic stress relaxation, slip stress transfer and friction weakening controlled post-injection seismicity at the basel enhanced geothermal system. *Communications Earth & Environment*, *4*(1), 104.

Broberg, K. B. (1999). *Cracks and fracture*. Academic Press.

Bunger, A. P., & Lecampion, B. (2017). Four critical issues for successful hydraulic fracturing applications. In X.-T. Feng (Ed.), *Rock mechanics and engineering*. CRC Press/Balkema.

Bürgmann, R. (2018). The geophysics, geology and mechanics of slow fault slip. *Earth and Planetary Science Letters*, *495*, 112–134.

Campillo, M., & Ionescu, I. R. (1997). Initiation of antiplane shear instability under slip dependent friction. *Journal of Geophysical Research: Solid Earth*, *102*(B9), 20363–20371.

Cappa, F., Scuderi, M., Collettini, C., Guglielmi, Y., & Avouac, J. (2019). Stabilization of fault slip by fluid injection in the laboratory and in situ. *Science Advances*, *5*(3).

Cappa, F., Guglielmi, Y., Nussbaum, C., De Barros, L., & Birkholzer, J. (2022). Fluid migration in low-permeability faults driven by decoupling of fault slip and opening. *Nature Geoscience, 15*(9), 747–751.

Carslaw, H., & Jaeger, J. (1959). *Conduction of heat in solids* (2nd edition). Oxford: Clarendon Press.

Castellano, M., Lorez, F., & Kammer, D. S. (2023). Nucleation of frictional slip: a yielding or a fracture process? *Journal of the Mechanics and Physics of Solids, 173*, 105193.

Cebry, S. B. L., Ke, C.-Y., & McLaskey, G. C. (2022). The role of background stress state in fluid-induced aseismic slip and dynamic rupture on a 3-m laboratory fault. *Journal of Geophysical Research: Solid Earth, 127*(8), e2022JB024371.

Cebry, S. B. L., & McLaskey, G. C. (2021). Seismic swarms produced by rapid fluid injection into a low permeability laboratory fault. *Earth and Planetary Science Letters, 557*, 116726.

Chen, X., Nakata, N., Pennington, C., Haffener, J., Chang, J., He, X., Zhan, Z., Ni, S., & Walter, J. (2017). The Pawnee earthquake as a result of the interplay among injection, faults and foreshocks. *Scientific Reports, 7*(1), 4945.

Chen, X., Shearer, P., & Abercrombie, R. (2012). Spatial migration of earthquakes within seismic clusters in Southern California: evidence for fluid diffusion. *Journal of Geophysical Research: Solid Earth, 117*(B4).

Ciardo, F., & Lecampion, B. (2019). Effect of dilatancy on the transition from aseismic to seismic slip due to fluid injection in a fault. *Journal of Geophysical Research: Solid Earth, 124*(4), 3724–3743.

Ciardo, F., Lecampion, B., Fayard, F., & Chaillat, S. (2020). A fast boundary element based solver for localized inelastic deformations. *International Journal for Numerical Methods in Engineering, 121*, 5696–5718.

Ciardo, F., & Rinaldi, A. P. (2021). Impact of injection rate ramp-up on nucleation and arrest of dynamic fault slip. *Geomechanics and Geophysics for Geo-Energy and Geo-Resources, 8*(1), 28.

Ciardo, F., & Lecampion, B. (2023). Injection-induced aseismic slip in tight fractured rocks. *Rock Mech. Rock Eng.*

Clements, D., & Ang, W. (1988). Stress intensity factors for the circular annulus crack. *Int. J. Eng. Sci., 26*(4), 325–329.

Cocco, M., & Bizzarri, A. (2002). On the slip-weakening behavior of rate- and state dependent constitutive laws. *Geophysical Research Letters, 29*(11), 11-1-11–4.

Cornet, F. (2016). Seismic and aseismic motions generated by fluid injections. *Geomechanics for Energy and the Environment, 5*, 42–54.

Cornet, F., Helm, J., Poitrenaud, H., & Etchecopar, A. (1997). Seismic and aseismic slips induced by large-scale fluid injections. *Pure and Applied Geophysics, 150*, 563–583.

Crouch, S., & Starfield, A. (1983). *Boundary element methods in solid mechanics: with applications in rock mechanics and geological engineering* (1st edition). George Allen; Unwin.

David, L., & Lazarus, V. (2022). On the key role of crack surface area on the lifetime of arbitrarily shaped flat cracks. *International Journal of Fatigue, 154*, 106512.

Deichmann, N., & Giardini, D. (2009). Earthquakes induced by the stimulation of an enhanced geothermal system below Basel (Switzerland). *Seismological Research Letters, 80*(5), 784–798.

Dempsey, J. P., Tan, L., & Wang, S. (2010). An isolated cohesive crack in tension. *Continuum Mechanics and Thermodynamics, 22*(6), 617–634.

de Souza Neto, E., Perić, D., & Owen, D. (2008). *Computational methods for plasticity: theory and applications* (1st edition). John Wiley; Sons, Ltd.

Detournay, E. (2016). Mechanics of hydraulic fractures. *Annual Review of Fluid Mechanics, 48*(1), 311–339.

Detournay, E., & Cheng, A. (1993). Fundamentals of poroelasticity. Elsevier.

Dieterich, J. (1994). A constitutive law for rate of earthquake production and its application to earthquake clustering. *Journal of Geophysical Research: Solid Earth, 99*(B2), 2601–2618.

Dieterich, J. (1979). Modeling of rock friction: 1. experimental results and constitutive equations. *J. Geophys. Res. Solid Earth, 84*(B5), 2161–2168.

Dublanchet, P. (2019). Fluid driven shear cracks on a strengthening rate-and-state frictional fault. *Journal of the Mechanics and Physics of Solids, 132*, 103672.

Duboeuf, L., De Barros, L., Cappa, F., Guglielmi, Y., Deschamps, A., & Seguy, S. (2017). Aseismic motions drive a sparse seismicity during fluid injections into a fractured zone in a carbonate reservoir. *Journal of Geophysical Research: Solid Earth, 122*(10), 8285–8304.

Ellsworth, W. (2013). Injection-induced earthquakes. *Science, 341*(6142).

Ellsworth, W., Giardini, D., Townend, J., Ge, S., & Shimamoto, T. (2019). Triggering of the Pohang, Korea, earthquake (Mw 5.5) by enhanced geothermal system stimulation. *Seismological Research Letters, 90*(5), 1844–1858.

Evans, K. F. (2005). Permeability creation and damage due to massive fluid injections into granite at 3.5 km at soultz: 2. critical stress and fracture strength. *Journal of Geophysical Research: Solid Earth, 110*(B4).

Evans, K. F., Genter, A., & Sausse, J. (2005). Permeability creation and damage due to massive fluid injections into granite at 3.5 km at soultz: 1. borehole observations. *Journal of Geophysical Research: Solid Earth*, *110*(B4).

Evans, K. F., Moriya, H., Niitsuma, H., Jones, R. H., Phillips, W. S., Genter, A., Sausse, J., Jung, R., & Baria, R. (2005). Microseismicity and permeability enhancement of hydrogeologic structures during massive fluid injections into granite at 3 km depth at the Soultz HDR site. *Geophysical Journal International*, *160*(1), 388–412.

Eyre, T., Eaton, D., Garagash, D., Zecevic, M., Venieri, M., Weir, R., & Lawton, D. (2019). The role of aseismic slip in hydraulic fracturing-induced seismicity. *Science Advances*, *5*(8).

Eyre, T., Samsonov, S., Feng, W., Kao, H., & Eaton, D. W. (2022). Insar data reveal that the largest hydraulic fracturing-induced earthquake in canada, to date, is a slow-slip event. *Scientific Reports*, *12*(1), 2043.

Eyre, T., Zecevic, M., Salvage, R. O., & Eaton, D. W. (2020). A long-lived swarm of hydraulic fracturing-induced seismicity provides evidence for aseismic slip. *Bulletin of the Seismological Society of America*, *110*(5), 2205–2215.

Fabrikant, V. (1989). *Applications of potential theory in mechanics: a selection of new results*. Kluwer Academic Publishers The Netherlands.

Favier, E., Lazarus, V., & Leblond, J. (2006). Coplanar propagation paths of 3d cracks in infinite bodies loaded in shear. *International Journal of Solids and Structures*, *43*(7), 2091–2109.

Frank, W. B., & Brodsky, E. E. (2019). Daily measurement of slow slip from low-frequency earthquakes is consistent with ordinary earthquake scaling. *Science Advances*, *5*(10), eaaw9386.

Fredriksson, B. (1976). Finite element solution of surface nonlinearities in structural mechanics with special emphasis to contact and fracture mechanics problems. *Computers & Structures*, *6*(4), 281–290.

Galis, M., Ampuero, J., Mai, P., & Cappa, F. (2017). Induced seismicity provides insight into why earthquake ruptures stop. *Science Advances*, *3*(12).

Gao, H. (1988). Nearly circular shear mode cracks. *International Journal of Solids and Structures*, *24*(2), 177–193.

Garagash, D. I. (2012). Seismic and aseismic slip pulses driven by thermal pressurization of pore fluid. *J. Geophys. Res. Solid Earth*, *117*(B4), B04314.

Garagash, D. (2021). Fracture mechanics of rate-and-state faults and fluid injection induced slip. *Philosophical Transactions of the Royal Society A: Mathematical, Physical and Engineering Sciences*, *379*(2196), 20200129.

Garagash, D., & Germanovich, L. (2012). Nucleation and arrest of dynamic slip on a pressurized fault. *Journal of Geophysical Research: Solid Earth*, *117*(B10).

Goebel, T., & Brodsky, E. (2018). The spatial footprint of injection wells in a global compilation of induced earthquake sequences. *Science, 361*(6405), 899–904.

Goertz-Allmann, B. P., Goertz, A., & Wiemer, S. (2011). Stress drop variations of induced earthquakes at the basel geothermal site. *Geophysical Research Letters, 38*(9).

Goodfellow, S. D., Nasseri, M. H. B., Maxwell, S. C., & Young, R. P. (2015). Hydraulic fracture energy budget: insights from the laboratory. *Geophysical Research Letters, 42*(9), 3179–3187.

Gordeliy, E., & Detournay, E. (2011). Displacement discontinuity method for modeling axisymmetric cracks in an elastic half-space. *International Journal of Solids and Structures, 48*(19), 2614–2629.

Gori, M., Rubino, V., Rosakis, A. J., & Lapusta, N. (2021). Dynamic rupture initiation and propagation in a fluid-injection laboratory setup with diagnostics across multiple temporal scales. *Proceedings of the National Academy of Sciences, 118*(51).

Guglielmi, Y., Cappa, F., Avouac, J., Henry, P., & Elsworth, D. (2015). Seismicity triggered by fluid injection-induced aseismic slip. *Science, 348*(6240), 1224–1226.

Hackbusch, W. (2015). *Hierarchical matrices: algorithms and analysis* (1st edition). Springer Berlin, Heidelberg.

Hacker, B., Peacock, S., Abers, G., & Holloway, S. (2003). Subduction factory 2. Are intermediate-depth earthquakes in subducting slabs linked to metamorphic dehydration reactions? *Journal of Geophysical Research: Solid Earth, 108*(B1).

Hainzl, S., Fischer, T., Čermáková, H., Bachura, M., & Vlček, J. (2016). Aftershocks triggered by fluid intrusion: evidence for the aftershock sequence occurred 2014 in West Bohemia/Vogtland. *Journal of Geophysical Research: Solid Earth, 121*(4), 2575–2590.

Hamilton, D., & Meehan, R. (1971). Ground Rupture in the Baldwin Hills. *Science, 172*(3981), 333–344.

Hanks, T. C., & Kanamori, H. (1979). A moment magnitude scale. *Journal of Geophysical Research: Solid Earth, 84*(B5), 2348–2350.

Hatch, R., Abercrombie, R., Ruhl, C., & Smith, K. (2020). Evidence of aseismic and fluid-driven processes in a small complex seismic swarm near Virginia City, Nevada. *Geophysical Research Letters, 47*(4), e2019GL085477.

Healy, J., Rubey, W., Griggs, D., & Raleigh, C. (1968). The Denver earthquakes. *Science, 161*(3848), 1301–1310.

Heimisson, E. R., Liu, S., Lapusta, N., & Rudnicki, J. (2022). A spectral boundary-integral method for faults and fractures in a poroelastic solid: simulations of a rate-and-state fault with dilatancy, compaction, and fluid injection. *Journal of Geophysical Research: Solid Earth, 127*(9), e2022JB024185.

Hills, D., Kelly, P., Dai, D., & Korsunsky, A. (1996). *Solution of Crack Problems - The Distributed Dislocation Technique* (1st edition, Vol. 44). Springer Netherlands.

Holtkamp, S., & Brudzinski, M. (2011). Earthquake swarms in circum-pacific subduction zones. *Earth and Planetary Science Letters*, *305*(1), 215–225.

Ida, Y. (1972). Cohesive force across the tip of a longitudinal-shear crack and griffith's specific surface energy. *Journal of Geophysical Research*, *77*(20), 3796–3805.

Ide, S., Beroza, G., Shelly, D., & Uchide, T. (2007). A scaling law for slow earthquakes. *Nature*, *447*(7140), 76–79.

Irwin, G. R. (1958). Fracture. *Elasticity and Plasticity*, 551–590.

Jacquey, A. B., & Viesca, R. C. (2023). Nucleation and arrest of fluid-induced aseismic slip. *Geophysical Research Letters*, *50*(4), e2022GL101228.

Jaeger, J. (1955). Numerical values for the temperature in radial heat flow. *Journal of Mathematics and Physics*, *34*, 316–321.

Kato, A., Iidaka, T., Ikuta, R., Yoshida, Y., Katsumata, K., Iwasaki, T., Sakai, S., Thurber, C., Tsumura, N., Yamaoka, K., Watanabe, T., Kunitomo, T., Yamazaki, F., Okubo, M., Suzuki, S., & Hirata, N. (2010). Variations of fluid pressure within the subducting oceanic crust and slow earthquakes. *Geophysical Research Letters*, *37*(14).

Katsumata, A., & Kamaya, N. (2003). Low-frequency continuous tremor around the moho discontinuity away from volcanoes in the southwest japan. *Geophysical Research Letters*, *30*(1), 20-1-20–4.

Keranen, K., Savage, H., Abers, G., & Cochran, E. (2013). Potentially induced earthquakes in Oklahoma, USA: Links between wastewater injection and the 2011 Mw 5.7 earthquake sequence. *Geology*, *41*(6), 699–702.

Keranen, K., Weingarten, M., Abers, G., Bekins, B., & Ge, S. (2014). Sharp increase in central Oklahoma seismicity since 2008 induced by massive wastewater injection. *Science*, *345*(6195), 448–451.

King, G. C., Stein, R. S., & Lin, J. (1994). Static stress changes and the triggering of earthquakes. *Bulletin of the Seismological Society of America*, *84*(3), 935–953.

Kuriyama, K., & Mizuta, Y. (1993). Three-dimensional elastic analysis by the displacement discontinuity method with boundary division into triangular leaf elements. *International Journal of Rock Mechanics and Mining Sciences and Geomechanics Abstracts*, *30*(2), 111–123.

Lachat, J. C., & Watson, J. O. (1976). Effective numerical treatment of boundary integral equations: a formulation for three-dimensional elastostatics. *International Journal for Numerical Methods in Engineering*, *10*(5), 991–1005.

Lai, Y., Movchan, A., & Rodin, G. (2002). A study of quasi-circular cracks. *International Journal of Fracture*, *113*(1), 1–25.

Lapusta, N., Rice, J. R., Ben-Zion, Y., & Zheng, G. (2000). Elastodynamic analysis for slow tectonic loading with spontaneous rupture episodes on faults with rate- and state-dependent friction. *Journal of Geophysical Research: Solid Earth*, *105*(B10), 23765–23789.

Larochelle, S., Lapusta, N., Ampuero, J.-P., & Cappa, F. (2021). Constraining fault friction and stability with fluid-injection field experiments. *Geophysical Research Letters*, *48*(10), e2020GL091188.

Lawn, B. (1993). *Fracture of brittle solids* (2nd edition). Cambridge University Press.

Lebihain, M., Roch, T., & Molinari, J.-F. (2022). Quasi-static crack front deformations in cohesive materials. *Journal of the Mechanics and Physics of Solids*, *168*, 105025.

Lengliné, O., Boubacar, M., & Schmittbuhl, J. (2017). Seismicity related to the hydraulic stimulation of GRT1, Rittershoffen, France. *Geophysical Journal International*, *208*(3), 1704–1715.

Li, Z., Elsworth, D., Wang, C., Boyd, L., Frone, Z., Metcalfe, E., Nieto, A., Porse, S., Vandermeer, W., Podgorney, R., Huang, H., McLing, T., Neupane, G., Chakravarty, A., Cook, P. J., Dobson, P. F., Doughty, C. A., Guglielmi, Y., Hopp, C., . . . EGS-Collab. (2021). Constraining maximum event magnitude during injection-triggered seismicity. *Nature Communications*, *12*(1), 1528.

Liu, Y., & Rice, J. R. (2007). Spontaneous and triggered aseismic deformation transients in a subduction fault model. *Journal of Geophysical Research: Solid Earth*, *112*(B9).

Lohman, R. B., & McGuire, J. J. (2007). Earthquake swarms driven by aseismic creep in the salton trough, california. *Journal of Geophysical Research: Solid Earth*, *112*(B4).

Marck, J., Savitski, A. A., & Detournay, E. (2015). Line source in a poroelastic layer bounded by an elastic space. *Int. J. Numer. Anal. Methods Geomech.*, *39*(14), 1484–1505.

Marone, C. (1998). Laboratory-derived friction laws and their application to seismic faulting. *Annual Review of Earth and Planetary Sciences*, *26*(1), 643–696.

McGarr, A. (2014). Maximum magnitude earthquakes induced by fluid injection. *Journal of Geophysical Research: solid earth*, *119*(2), 1008–1019.

McGarr, A., & Barbour, A. (2018). Injection-induced moment release can also be aseismic. *Geophysical Research Letters*, *45*(11), 5344–5351.

Michalowski, R., & Mroz, Z. (1978). Associated and non-associated sliding rules in contact friction problems. *Archiwum Mechaniki Stosowanej*, *30*(3), 259–276.

Michel, S., Gualandi, A., & Avouac, J.-P. (2019). Similar scaling laws for earthquakes and cascadia slow-slip events. *Nature*, *574*(7779), 522–526.

Miller, S. (2020). Aftershocks are fluid-driven and decay rates controlled by permeability dynamics. *Nature Communications, 11*(1), 5787.

Miller, S., Collettini, C., Chiaraluce, L., Cocco, M., Barchi, M., & Kaus, B. (2004). Aftershocks driven by a high-pressure co2 source at depth. *Nature, 427*(6976), 724–727.

Mogilevskaya, S. G. (2014). Lost in translation: crack problems in different languages. *International Journal of Solids and Structures, 51*(25), 4492–4503.

Möri, A., & Lecampion, B. (2021). Arrest of a radial hydraulic fracture upon shut-in of the injection. *International Journal of Solids and Structures, 219-220*, 151–165.

Mroz, Z., & Giambanco, G. (1996). An interface model for analysis of deformation behavior of discontinuities. *International Journal for Numerical and Analytical Methods in Geomechanics, 20*, 1–33.

Nintcheu Fata, S. (2009). Explicit expressions for 3d boundary integrals in potential theory. *International Journal for Numerical Methods in Engineering, 78*(1), 32–47.

Nintcheu Fata, S. (2011). Explicit expressions for three-dimensional boundary integrals in linear elasticity. *Journal of Computational and Applied Mathematics, 235*(15), 4480–4495.

Nishikawa, T., & Ide, S. (2017). Detection of earthquake swarms at subduction zones globally: insights into tectonic controls on swarm activity. *Journal of Geophysical Research: Solid Earth, 122*(7), 5325–5343.

Nishimura, T., Hiramatsu, Y., & Ohta, Y. (2023). Episodic transient deformation revealed by the analysis of multiple gnss networks in the noto peninsula, central japan. *Scientific Reports, 13*(1), 8381.

Norbeck, J., & Horne, R. (2018). Maximum magnitude of injection-induced earthquakes: a criterion to assess the influence of pressure migration along faults. *Tectonophysics, 733*, 108–118.

Obara, K. (2002). Nonvolcanic deep tremor associated with subduction in southwest japan. *Science, 296*(5573), 1679–1681.

Paglialunga, F., Passelègue, F., Latour, S., Gounon, A., & Violay, M. (2023). Influence of viscous lubricant on nucleation and propagation of frictional ruptures. *Journal of Geophysical Research: Solid Earth, 128*(4), e2022JB026090.

Paglialunga, F., Passelègue, F. X., Brantut, N., Barras, F., Lebihain, M., & Violay, M. (2022). On the scale dependence in the dynamics of frictional rupture: constant fracture energy versus size-dependent breakdown work. *Earth and Planetary Science Letters, 584*, 117442.

Palmer, A., & Rice, J. (1973). The growth of slip surfaces in the progressive failure of over-consolidated clay. *Proceedings of the Royal Society of London. A. Mathematical and Physical Sciences, 332*(1591), 527–548.

Park, Y., Mousavi, S. M., Zhu, W., Ellsworth, W. L., & Beroza, G. C. (2020). Machine-learning-based analysis of the guy-greenbrier, arkansas earthquakes: a tale of two sequences. *Geophysical Research Letters, 47*(6), e2020GL087032.

Parotidis, M., Shapiro, S. A., & Rothert, E. (2004). Back front of seismicity induced after termination of borehole fluid injection. *Geophysical Research Letters, 31*(2).

Parotidis, M., Shapiro, S., & Rothert, E. (2005). Evidence for triggering of the vogtland swarms 2000 by pore pressure diffusion. *Journal of Geophysical Research: Solid Earth, 110*(B5).

Passelègue, F. X., Almakari, M., Dublanchet, P., Barras, F., Fortin, J., & Violay, M. (2020). Initial effective stress controls the nature of earthquakes. *Nature Communications, 11*(1), 5132.

Peacock, S. M. (2009). Thermal and metamorphic environment of subduction zone episodic tremor and slip. *Journal of Geophysical Research: Solid Earth, 114*(B8).

Perez-Silva, A., Kaneko, Y., Savage, M., Wallace, L., & Warren-Smith, E. (2023). Characteristics of slow slip events explained by rate-strengthening faults subject to periodic pore fluid pressure changes. *Journal of Geophysical Research: Solid Earth, 128*(6), e2022JB026332.

Perfettini, H., & Avouac, J.-P. (2007). Modeling afterslip and aftershocks following the 1992 landers earthquake. *Journal of Geophysical Research: Solid Earth, 112*(B7).

Plesha, M. E. (1987). Constitutive models for rock discontinuities with dilatancy and surface degradation. *International Journal for Numerical and Analytical Methods in Geomechanics, 11*(4), 345–362.

Rice, J. (1968). Mathematical analysis in the mechanics of fracture. *Fracture: an advanced treatise, 2*, 191–311.

Rice, J. (1992). Fault stress states, pore pressure distributions, and the weakness of the San Andreas fault. In B. Evans & T.-f. Wong (Eds.), *Fault mechanics and transport properties of rocks* (pp. 475–503). Academic Press.

Rice, J. (1993). Spatio-temporal complexity of slip on a fault. *Journal of Geophysical Research: Solid Earth, 98*(B6), 9885–9907.

Rice, J. (2006). Heating and weakening of faults during earthquake slip. *Journal of Geophysical Research: Solid Earth, 111*(B5).

Rogers, G., & Dragert, H. (2003). Episodic tremor and slip on the cascadia subduction zone: the chatter of silent slip. *Science, 300*(5627), 1942–1943.

Rongved, L. (1957). Dislocation over a bounded plane area in an infinite solid. *J. Appl. Mech, 24*, 252–254.

Ross, Z. E., & Cochran, E. S. (2021). Evidence for latent crustal fluid injection transients in southern california from long-duration earthquake swarms. *Geophysical Research Letters, 48*(12), e2021GL092465.

Ross, Z., Cochran, E., Trugman, D., & Smith, J. (2020). 3d fault architecture controls the dynamism of earthquake swarms. *Science, 368*(6497), 1357–1361.

Ross, Z., Rollins, C., Cochran, E., Hauksson, E., Avouac, J., & Ben-Zion, Y. (2017). Aftershocks driven by afterslip and fluid pressure sweeping through a fault-fracture mesh. *Geophysical Research Letters, 44*(16), 8260–8267.

Rubin, A. M., & Ampuero, J.-P. (2005). Earthquake nucleation on (aging) rate and state faults. *Journal of Geophysical Research: Solid Earth, 110*(B11).

Ruina, A. (1983). Slip instability and state variable friction laws. *J. Geophys. Res. Solid Earth, 88*(B12), 10359–10370.

Rutqvist, J., & Stephansson, O. (2003). The role of hydromechanical coupling in fractured rock engineering. *Hydrogeology Journal, 11*(1), 7–40.

Sáez, A., & Lecampion, B. (2023a). Fluid-driven slow slip and earthquake nucleation on a slip-weakening circular fault. *Submitted to Journal of the Mechanics and Physics of Solids.*

Sáez, A., & Lecampion, B. (2023b). Post-injection aseismic slip as a mechanism for the delayed triggering of seismicity. *Proceedings of the Royal Society A: Mathematical, Physical and Engineering Sciences, 479*(2273), 20220810.

Sáez, A., Lecampion, B., Bhattacharya, P., & Viesca, R. C. (2022). Three-dimensional fluid-driven stable frictional ruptures. *Journal of the Mechanics and Physics of Solids, 160,* 104754.

Salamon, N., & Dundurs, J. (1971). Elastic fields of a dislocation loop in a two-phase material. *Journal of Elasticity, 1*(2), 153–164.

Salamon, N., & Dundurs, J. (1977). A circular glide dislocation loop in a two-phase material. *Journal of Physics C: Solid State Physics, 10*(4), 497–507.

Scholz, C. (2019). *The mechanics of earthquakes and faulting* (3rd edition). Cambridge University Press.

Scotti, O., & Cornet, F. (1994). In situ evidence for fluid-induced aseismic slip events along fault zones. *International Journal of Rock Mechanics and Mining Sciences and Geomechanics Abstracts, 31*(4), 347–358.

Scuderi, M., & Collettini, C. (2016). The role of fluid pressure in induced vs. triggered seismicity: insights from rock deformation experiments on carbonates. *Scientific Reports, 6*(1), 24852.

Segall, P., Rubin, A. M., Bradley, A. M., & Rice, J. R. (2010). Dilatant strengthening as a mechanism for slow slip events. *Journal of Geophysical Research: Solid Earth, 115*(B12).

Shapiro, S., Huenges, E., & Borm, G. (1997). Estimating the crust permeability from fluid-injection-induced seismic emission at the KTB site. *Geophysical Journal International, 131*(2), F15–F18.

Shapiro, S., Rentsch, S., & Rothert, E. (2005). Characterization of hydraulic properties of rocks using probability of fluid-induced microearthquakes. *Geophysics, 70*(2), F27–F33.

Shapiro, S. A., Audigane, P., & Royer, J.-J. (1999). Large-scale in situ permeability tensor of rocks from induced microseismicity. *Geophysical Journal International, 137*(1), 207–213.

Sharma, V., Wadhawan, M., Rana, N., Sreejith, K., Agrawal, R., Kamra, C., Hosalikar, K., Narkhede, K. V., Suresh, G., & Gahalaut, V. K. (2020). A long duration non-volcanic earthquake sequence in the stable continental region of india: the palghar swarm. *Tectonophysics, 779*, 228376.

Shelly, D. R., Beroza, G. C., Ide, S., & Nakamula, S. (2006). Low-frequency earthquakes in shikoku, japan, and their relationship to episodic tremor and slip. *Nature, 442*(7099), 188–191.

Sibson, R. (1992). Implications of fault-valve behaviour for rupture nucleation and recurrence. *Tectonophysics, 211*(1-4), 283–293.

Sibson, R. (2020). Preparation zones for large crustal earthquakes consequent on fault-valve action. *Earth, Planets and Space, 72*(1), 31.

Sirorattanakul, K., Ross, Z. E., Khoshmanesh, M., Cochran, E. S., Acosta, M., & Avouac, J.-P. (2022). The 2020 westmorland, california earthquake swarm as aftershocks of a slow slip event sustained by fluid flow. *Journal of Geophysical Research: Solid Earth, 127*(11), e2022JB024693.

Sneddon, I. (1951). *Fourier transforms*. McGraw-Hill, New York.

Stehfest, H. (1970). Numerical inversion of laplace transforms. *Communications of the ACM, 13*(1), 47–49.

Stupkiewicz, S., & Mróz, Z. (2001). Modeling of friction and dilatancy effects at brittle interfaces for monotonic and cyclic loading. *Journal of Theoretical and Applied Mechanics, 39*, 707–739.

Svetlizky, I., Bayart, E., & Fineberg, J. (2019). Brittle fracture theory describes the onset of frictional motion. *Annual Review of Condensed Matter Physics, 10*(1), 253–273.

Svetlizky, I., & Fineberg, J. (2014). Classical shear cracks drive the onset of dry frictional motion. *Nature, 509*(7499), 205–208.

Tada, H., Paris, P. C., & Irwin, G. R. (2000). *The stress analysis of cracks handbook* (3rd edition). ASME Press.

Terzaghi, K. (1923). Die berechning deer durchlassigkeitziffer des tonesaus dem verlauf spannungserscheinungen, akad. *Der Wissenchafen in Wien, Sitzung-sberichte. Mathematisch-naturwissenschafttliche Klasse. Part lia, 142*(3/4), 125–138.

Tse, S. T., & Rice, J. R. (1986). Crustal earthquake instability in relation to the depth variation of frictional slip properties. *Journal of Geophysical Research: Solid Earth, 91*(B9), 9452–9472.

Uenishi, K., & Rice, J. (2002). Universal nucleation length for slip-weakening rupture instability under non-uniform fault loading. *J. Geophys. Res., 108*.

Uenishi, K. (2018). Three-dimensional fracture instability of a displacement-weakening planar interface under locally peaked nonuniform loading. *Journal of the Mechanics and Physics of Solids, 115*, 195–207.

Utsu, T. (1961). A statistical study on the occurrence of aftershocks. *Geophys. Mag., 30*, 521–605.

van der Elst, N., Page, M., Weiser, D., Goebel, T., & Hosseini, S. M. (2016). Induced earthquake magnitudes are as large as (statistically) expected. *Journal of Geophysical Research: Solid Earth, 121*(6), 4575–4590.

Viesca, R. C. (2021). Self-similar fault slip in response to fluid injection. *Journal of Fluid Mechanics, 928*, A29.

Vilarrasa, V., & Carrera, J. (2015). Geologic carbon storage is unlikely to trigger large earthquakes and reactivate faults through which CO_2 could leak. *Proceedings of the National Academy of Sciences, 112*(19), 5938–5943.

Wang, T. A., & Dunham, E. M. (2022). Hindcasting injection-induced aseismic slip and microseismicity at the cooper basin enhanced geothermal systems project. *Scientific Reports, 12*(1), 19481.

Warren-Smith, E., Fry, B., Wallace, L., Chon, E., Henrys, S., Sheehan, A., Mochizuki, K., Schwartz, S., Webb, S., & Lebedev, S. (2019). Episodic stress and fluid pressure cycling in subducting oceanic crust during slow slip. *Nature Geoscience, 12*(6), 475–481.

Wei, S., Avouac, J., Hudnut, K., Donnellan, A., Parker, J., Graves, R., Helmberger, D., Fielding, E., Liu, Z., Cappa, F., & Eneva, M. (2015). The 2012 Brawley swarm triggered by injection-induced aseismic slip. *Earth and Planetary Science Letters, 422*, 115–125.

Wibberley, C. A. J., & Shimamoto, T. (2003). Internal structure and permeability of major strike-slip fault zones: the median tectonic line in mie prefecture, southwest japan. *Journal of Structural Geology, 25*(1), 59–78.

Wicks, C., Thelen, W., Weaver, C., Gomberg, J., Rohay, A., & Bodin, P. (2011). Insar observations of aseismic slip associated with an earthquake swarm in the columbia river flood basalts. *Journal of Geophysical Research: Solid Earth, 116*(B12).

Witherspoon, P., Wang, J., Iwai, K., & Gale, J. (1980). Validity of cubic law for fluid flow in a deformable rock fracture. *Water Resources Research, 16*(6), 1016–1024.

Wong, T., Ko, S., & Olgaard, D. (1997). Generation and maintenance of pore pressure excess in a dehydrating system 2. theoretical analysis. *Journal of Geophysical Research: Solid Earth, 102*(B1), 841–852.

Wriggers, P. (2006). *Computational contact mechanics* (2nd edition). Springer.

Yang, Y., & Dunham, E. M. (2021). Effect of porosity and permeability evolution on injection-induced aseismic slip. *Journal of Geophysical Research: Solid Earth, 126*(7), e2020JB021258.

Yeck, W. L., Hayes, G. P., McNamara, D. E., Rubinstein, J. L., Barnhart, W. D., Earle, P. S., & Benz, H. M. (2017). Oklahoma experiences largest earthquake during ongoing regional wastewater injection hazard mitigation efforts. *Geophysical Research Letters, 44*(2), 711–717.

Yukutake, Y., Yoshida, K., & Honda, R. (2022). Interaction between aseismic slip and fluid invasion in earthquake swarms revealed by dense geodetic and seismic observations. *Journal of Geophysical Research: Solid Earth*, e2021JB022933.

Yukutake, Y., Ito, H., Honda, R., Harada, M., Tanada, T., & Yoshida, A. (2011). Fluid-induced swarm earthquake sequence revealed by precisely determined hypocenters and focal mechanisms in the 2009 activity at hakone volcano, japan. *Journal of Geophysical Research: Solid Earth, 116*(B4).

Zhu, W., Allison, K., Dunham, E., & Yang, Y. (2020). Fault valving and pore pressure evolution in simulations of earthquake sequences and aseismic slip. *Nature Communications, 11*(1), 4833.

Zoback, M., & Gorelick, S. (2012). Earthquake triggering and large-scale geologic storage of carbon dioxide. *Proceedings of the National Academy of Sciences, 109*(26), 10164–10168.

Alexis Sáez

PhD Student

Swiss Federal Institute of Technology Lausanne (EPFL)

EPFL-ENAC-IIC-GEL, Station 18, CH-1015, Lausanne, Switzerland
Phone: (+41) 78 941 0404, E-mail: alexis.saez@epfl.ch

Education

Swiss Federal Institute of Technology Lausanne (EPFL), Switzerland

2019-2023 Ph.D. in Mechanics. Advisor: Brice Lecampion

- *Subfield:* Geomechanics.

- *Holder of a Swiss Government Excellence Scholarship for Foreign Students* 2019-2023 to conduct research on the subject: injection-induced seismicity.

University of Chile, Chile

2014 Professional Title of Civil Engineer.

- *Awarded as the Best Graduate Engineer of 2014 Class.*

2014 M.Sc.E. in Earthquake Engineering.

- *Holder of the Full Tuition-Fee Waiver Scholarship.* This scholarship is given once per year to one outstanding civil engineering's student to pursue the master program in earthquake engineering.

2010 B.Sc.E. in Civil Engineering.

- *Awarded the Outstanding Student Prize* consecutively from 2006 to 2010. This award recognizes undergraduate students belonging to the 6% of higher grades of the School of Engineering.

Professional Experience

06/2019-Now   *Doctoral Assistant* at Geo-energy Laboratory, Civil Engineering Institute, School of Architecture, Civil and Environmental Engineering (ENAC), Swiss Federal Institute of Technology Lausanne (EPFL), Switzerland.

09/2022-02/2023   *Visiting PhD Student* at Earthquake Research Institute, the University of Tokyo, Japan. (Host Professor: Aitaro Kato)

- *Awarded the EPFL Doc.Mobility Grant* to conduct a 6-months research stay on the subject: the role of fluids in slow earthquakes.

01/2013-12/2016   *Project Engineer* at Corporación Nacional del Cobre de Chile (CODELCO), Santiago, Chile. Structural, geotechnical and seismic revisions for large mining projects and tailings dams.

- *Fellow of the Graduate Program* which focuses on developing technical capabilities and leadership skills of young talented engineers to drive the transformation of the mining of the future for Chile.

Teaching Experience

Swiss Federal Institute of Technology Lausanne (EPFL), Switzerland

2019-2021   *Teaching Assistant for Computational Geomechanics (CIVIL-423),* Civil Engineering Institute.
Master's course on poroelasticity theory and its numerical solution via the continuous Galerkin finite element method.

2020-2021   *Teaching Assistant for Geotechnical Engineering (CIVIL-306),* Civil Engineering Institute.
Bachelor's course on fundamentals of soil mechanics and engineering design of soil structures.

Publications

PhD articles – published or under review:

1. **Sáez, A.**, Lecampion, B., Bhattacharya, P. & Viesca, R.C. (2022). Three-dimensional fluid-driven stable frictional ruptures. *Journal of the Mechanics and Physics of Solids*, 132, 103672. https://doi.org/10.1016/j.jmps.2021.104754

2. **Sáez, A.** & Lecampion, B. (2023). Post-injection aseismic slip as a mechanism for the delayed triggering of seismicity. *Proceedings of the Royal Society A: Mathematical, Physical and Engineering Sciences*, 479, 20220810. http://doi.org/10.1098/rspa.2022.0810

3. **Sáez, A.** & Lecampion, B. Fluid-driven slow slip and earthquake nucleation on a slip-weakening circular fault. Under review in *Journal of the Mechanics and Physics of Solids.* [Accepted with minor modifications; October 7, 2023]. https://doi.org/10.48550/arXiv.2309.04567

4. Lecampion, B., **Sáez, A.** & Gupta, A. (2023). Shearing and opening of a pre-existing discontinuity in response to fluid injection. *57th U.S. Rock Mechanics/Geomechanics Symposium*, Atlanta, Georgia, USA, June 25-28. https://doi.org/10.56952/ARMA-2023-0721

PhD articles – in preparation:

5. **Sáez, A.** & Lecampion, B. Maximum magnitude of injection-induced slow slip events. [Preliminary results presented at AGU Fall Meeting 2021, New Orleans, USA] https://www.authorea.com/doi/full/10.1002/essoar.10509487.1

6. **Sáez, A.** & Lecampion, B. Spatiotemporal signatures of seismic swarms driven by fluid injections and induced aseismic slip. [Preliminary results presented at EGU General Assembly 2022, Vienna, Austria] https://meetingorganizer.copernicus.org/EGU22/EGU22-11943.html

7. **Sáez, A.** & Lecampion, B. Extraction of fluids to mitigate the seismic risk associated with post-injection-induced seismicity. [Preliminary results presented at EGU General Assembly 2023, Vienna, Austria] https://meetingorganizer.copernicus.org/EGU23/EGU23-15861.html

Master's articles – conferences proceedings (peer-reviewed):

8. **Sáez, A.**, Moroni, M. O. & Sarrazín, M. (2012), "Contributions to the Chilean Code for Seismic Design of Buildings with Energy Dissipation Devices", Proceedings of the 15th World Conference on Earthquake Engineering, Lisbon, Portugal.
https://www.iitk.ac.in/nicee/wcee/article/WCEE2012_5761.pdf

9. **Sáez, A.**, Moroni, M. O. & Sarrazín, M. (2014), "Correction Factor for Estimating The Maximum Relative Velocity Based on Pseudo Velocity", 10th U.S. National Conference on Earthquake Engineering, Alaska, EEUU.
https://datacenterhub.org/resources/12484/download/10NCEE-001144.pdf   226

Invited talks

02/2023	Seismology and Rock Mechanics groups, National Research Institute for Earth Science and Disaster Prevention (NIED), Japan. "Fluid-driven stable fault slip: nucleation, propagation and arrest", Tsukuba, Japan. (Host: Prof. Eiichi Fukuyama)
02/2023	Seismology and Physics of the Earth's interior group, Department of geophysics, Kyoto University. "Fluid-driven stable fault slip: nucleation, propagation and arrest", Kyoto, Japan. (Host: Prof. Yoshihiro Kaneko)
08/2022	Seismological Laboratory, Caltech - Brown Bag Seminar. "Fluid-driven stable fault slip: nucleation, propagation and arrest", Pasadena, CA, USA. (Host: Dr. Mateo Acosta)
08/2022	Earth Resources Laboratory, MIT. "Fluid-driven stable fault slip in 3D: nucleation, propagation and arrest", Cambridge, MA, USA. (Host: Dr. Ekaterina Bolotskaya)
08/2022	Schlumberger-Doll Research. "Fluid-driven stable fault slip: nucleation, propagation and arrest", Cambridge, MA, USA. (Host: Dr. Romain Prioul)
05/2022	Geoazur Laboratory, Université de Côte d'Azur. "Post-injection pulse-like aseismic ruptures", Sophia Antipolis, France. (Host: Dr. François Passelègue)
06/2021	Applied and Earthquake Seismology Research Group, Department of Earth Sciences, Freie Universität Berlin. "Three-dimensional aseismic ruptures driven by fluid injection", Berlin, Germany. (Host: Prof. Serge Shapiro) Online.
05/2021	Seismology Group, Department of Geophysics, University of Chile,. "Three-dimensional aseismic ruptures driven by fluid pressure diffusion", Santiago, Chile. (Host: Prof. Sergio Ruiz) Online.
04/2021	GFZ German Research Centre for Geosciences - Section 4.1 Lithosphere Dynamics. "Three-dimensional aseismic ruptures driven by fluid injection", Potsdam, Germany. (Host: Dr. Matthias Rosenau) Online.

Oral presentations

05/2023	European Geosciences Union (EGU) - General Assembly 2023. "Extraction of fluids to mitigate the seismic risk associated with post-injection aseismic slip", Vienna, Austria.
12/2022	American Geophysical Union (AGU) - Fall Meeting 2022. "Pulse-like aseismic ruptures upon the cessation of fluid injections: regimes of propagation and arrest in 3D", Chicago, IL, USA. Online.
07/2022	11th European Solid Mechanics Conference (ESMC). "Three-dimensional fluid-driven stable frictional ruptures", Galway, Ireland.
05/2022	European Geosciences Union (EGU) - General Assembly 2022. "Spatio-temporal patterns of fluid-driven aseismic slip transients: implications for seismic swarms", Vienna, Austria.
05/2022	European Geosciences Union (EGU) - General Assembly 2022. "2D and 3D numerical modeling of fluid-driven frictional crack growth for geothermal hydraulic stimulation", Vienna, Austria.
05/2021	European Geosciences Union (EGU) - General Assembly 2021. "Three-dimensional aseismic ruptures driven by fluid injection", Vienna, Austria. Online.

Peer reviewer

2022-Now   Rock Mechanics and Rock Engineering

2023-Now   Geophysical Journal International

Awards

2014   *Best Graduate Engineer of 2014 Class Award*, given by the Chilean Society of
            Engineers to the best graduate civil engineer of the 2014 class of the Division
            of Structures, Construction and Geotechnics, Department of Civil
            Engineering, University of Chile.

2006-2010   *Outstanding Student Award*, granted by the School of Engineering and
            Sciences, University of Chile, to undergraduate students belonging to the 6%
            of higher grades of the faculty.

Grants and Scholarships

2019-2023   *Swiss Government Excellence Scholarship for Foreign Students*, granted by
            the Swiss Confederation to conduct research at EPFL on the topic of
            injection-induced seismicity as part of the PhD program in Mechanics.
            Amount: ∼75,000 USD.

2022-2023   *EPFL Doc.Mobility Grant*, given by EPFL to carry out a doctoral research
            stay of 6 months in the Earthquake Research Institute of the University of
            Tokyo, on the topic of the role of fluids in slow earthquakes.
            Amount: ∼10,000 USD.

2022   *EPFL-ETH Zürich Summer School Grant*, given by EPFL and ETH Zürich
            to organize an international summer course for PhD students: "Mechanics of
            earthquakes and aseismic slip", held in Zürich, Switzerland, July 2022.
            https://earthquake-mechanics-2022.ethz.ch
            Amount: ∼20,000 USD.

2010   *Full Tuition Fee Waiver Scholarship*, given by the Department of Civil
            Engineering, University of Chile, once per year to one outstanding student to
            study the master program in earthquake engineering.
            Amount: ∼4,000 USD.

2006   *Bicentenario Scholarship*, given by the Chilean government to students with
            financial difficulties and outstanding results in the admission exam to public
            universities.
            Amount: ∼5,000 USD.

Organizing Committees

2022   Creator and principal organizer of the international summer course for PhD students:
        "Mechanics of earthquakes and aseismic slip", Zürich, Switzerland, 18-21 July 2022.
        https://earthquake-mechanics-2022.ethz.ch

2012   Member of conference organizing committee: Behavior of Steel Structures in Seismic
        Areas (STESSA) 7th International Conference, Santiago, Chile.

2010   Member of conference organizing committee: Proceedings of the 10th Chilean Conference
        on Seismology and Earthquake Engineering, Santiago, Chile.

Technology Transfer

2014   Development of a proposal of national code for the seismic design of buildings with passive energy dissipation systems. This proposal was the main output of my master's thesis and provided the basis for the now official national code NCh3411 of the Standardization National Institute of Chile.

Memberships

- European Mechanics Society (EUROMECH).
- European Geosciences Union (EGU).
- American Geophysical Union (AGU).

Programming languages

- Proficient in C++, Python, Wolfram Mathematica, and Matlab.

Languages

- Fluent in English, Portuguese and Spanish (native).

Career Breaks

2017-2018   Trip around the world for two years (Australia, China, Brasil, Myanmar, among many other countries).